

UNIVERSITY OF SEVILLE

DOCTORAL THESIS

---

**Wheel-rail contact force measurement.  
A comparison between distance laser  
and strain gauges measuring technology**

---

*Author:*

Pedro URDA GÓMEZ

*Supervisor:*

Dr. José L. ESCALONA

FRANCO and Dr. Sergio

MUÑOZ MORENO

*A thesis submitted in fulfilment of the requirements  
for the degree of Philosophiæ Doctor (PhD)*

*in the*

University of Seville

Department of Mechanical and Manufacturing Engineering

October 2019





# *Abstract*

The development of this PhD thesis is focus on the wheel/rail contact force measurement on a 1 : 10 scaled railway vehicle. To that end, the author has designed and manufactured a dynamometric wheelset instrumented with several sensors for the direct measurement of forces applied on the instrumented wheel. Two different technologies have been used for the wheelset instrumentation: On the one hand, a set of strain gauges measure the radial strains experienced by the wheel-web when a lateral load is applied on the wheel. On the other hand, three high precision lasers have been installed on the axel that measure the lateral deflection experienced by the wheel due to the applied lateral loads. Normal contact forces are measured independently throughout the deflection experienced by the primary suspension. This is also measured with laser distance sensors. After being instrumented, the wheelset has been submitted to a calibration process. A calibration test bench where controlled loads can be applied to the wheelset has been also designed and manufactured. Finally the instrumented wheelset has been installed on the scaled vehicle and tested on a 5 *inches* wide scale track. The force measurements obtained in the experiments with both set of sensors have been compared with numerical results drawn from a computational model of the vehicle. A novel procedure to measure the track irregularities applied to the scaled track has been also include as part of this thesis.

**Keywords:** Multibody systems, railways dynamics simulations, railway vehicle design, track irregularities, dynamometric wheelset, wheel/rail contact force measurement, track irregularities measurement, dynamometric wheelset calibration.



# *Resumen*

El desarrollo de esta tesis se centra en la medición experimental de fuerzas de contacto rueda carril en un vehículo ferroviario a escala 1 : 10. Para ello, el autor ha diseñado y fabricado un eje dinamométrico instrumentado con múltiples sensores para la medición directa de las fuerzas aplicadas en las ruedas. Para la instrumentación del sistema se han utilizado dos tecnologías distintas: Por un lado se dispone de un conjunto de bandas extensométricas que miden las deformaciones radiales experimentadas por el velo de la rueda debidas a la carga lateral aplicada en la misma. Por otro lado se han instalado tres láseres de alta precisión que miden la deflexión experimentada por la rueda debidas también a las cargas lateral aplicadas. Las fuerzas normales a las que se ve sometida la rueda son calculadas a través de la medición de la deflexión experimentada por la suspensión primaria del vehículo, siendo también medida mediante sensores de distancia láser. Tras la instrumentación el eje dinamométrico ha sido sometido a un proceso de calibración, para el cual se ha diseñado y fabricado un banco de pruebas a escala donde pueden aplicarse cargas al eje de forma controlada y conocer la respuesta de los sensores. Finalmente el mencionado eje dinamométrico ha sido instalado en el vehículo a escala y su funcionamiento ha sido probado en una vía a escala de 5 *inches* de ancho. En los experimentos realizados se han contrastado las mediciones de fuerzas realizadas por ambos sensores y comparado con resultados numéricos obtenidos de un modelo multicuerpo de simulación del vehículo. Como parte de esta tesis se incluye también la descripción del novedoso proceso de auscultación y cálculo de irregularidades realizado en del trazado ferroviario a escala.

**Palabras clave:** Sistemas multicuerpo, simulación de la dinámica ferroviaria, diseño de vehículos ferroviarios, irregularidades de vía, eje dinamométrico, medición fuerzas de contacto rueda/carril, auscultación de vía, calibración eje dinamométrico.



## *Acknowledgements*

En primer lugar quisiera agradecer a mi directo el Dr. José Luis Escalona Franco por haberme dado la oportunidad de realizar esta tesis doctoral, haciendo realidad este hito en mi carrera académica. Gracias por todos tus enseñanzas, directrices y sobre todo tu gran paciencia durante estos cuatro últimos años. En segundo lugar agradecer a mi codirector el Dr. Sergio Muñoz Moreno por toda la ayuda prestada en esta etapa. Agradecerte tus consejos y sobre todo tus ánimos en los momentos más duros de esta tesis. Gracias tamibién al Dr. Javier Fernández Aceituno por sus buenos consejos. Agradecer también la ayuda económica prestada por el Ministerio de Economía y Competitividad a través de las becas FPI que ha hecho posible costear esta investigación.



# Contents

<b>Abstract</b>	<b>iii</b>
<b>Resumen</b>	<b>v</b>
<b>Acknowledgements</b>	<b>vii</b>
<b>Contents</b>	<b>viii</b>
<b>List of Figures</b>	<b>xiii</b>
<b>List of Tables</b>	<b>xix</b>
<b>Abbreviations</b>	<b>xxi</b>
<b>Symbols</b>	<b>xxiii</b>
<b>1 Introduction</b>	<b>1</b>
1.1 Literature review . . . . .	1
1.2 Outline of the thesis . . . . .	14
<b>2 Experimental Scaled Track</b>	<b>17</b>
2.1 Scaled track design . . . . .	17
2.2 Ideal track geometry . . . . .	19
2.3 Track irregularities . . . . .	24
2.3.1 Modeling of track irregularities . . . . .	24
2.4 Experimental scaled track measurement . . . . .	27
2.4.1 Track centre line measurement . . . . .	28
2.4.1.1 Track centre line calculation algorithm . . . . .	32
2.4.1.2 Data synchronization . . . . .	34
2.4.1.3 Synchronization procedure . . . . .	35

2.4.2	Measurement of track gauge and cant angle . . . . .	39
2.5	Track geometry optimization . . . . .	41
2.6	Calculation of track irregularities . . . . .	45
<b>3</b>	<b>Scaled Dynamometric Wheelset: Strain Gauges Method</b>	<b>55</b>
3.1	Dynamometric wheelsets . . . . .	55
3.2	Design of the scaled dynamometric wheelset . . . . .	56
3.2.1	Instrumentation of the scaled dynamometric wheelset with strain gauges . . . . .	60
3.2.2	Strain gauges installation . . . . .	62
3.2.3	Lateral force estimation based on wheel-web radial strains . . . . .	66
3.2.4	Numerical validation of the radial strains method . . . . .	76
3.3	Calibration of the scaled dynamometric wheelset . . . . .	79
3.3.1	Static calibration test bench . . . . .	80
3.3.1.1	Strain gauges calibration in the test bench . . . . .	81
<b>4</b>	<b>Scaled Dynamometric Wheelset: Distance Lasers Approach</b>	<b>89</b>
4.1	Dynamometric wheelset instrumented with non-contact distance sensors . . . . .	89
4.2	Lateral force estimation based on wheel-web deflections . . . . .	91
4.3	Primary suspension lasers calibration . . . . .	95
4.4	Calibration of the lateral precision lasers . . . . .	97
<b>5</b>	<b>Numerical Modelling</b>	<b>107</b>
5.1	Introduction . . . . .	107
5.2	Multibody model with weakly coupled vertical and lateral dynamics . . . . .	108
5.2.1	Coordinates and frames in the multibody model . . . . .	108
5.2.2	Kinematics notation of the multibody model . . . . .	111
5.2.3	Kinematics of the track . . . . .	112
5.2.4	Kinematics of the rail head centrelines . . . . .	114
5.2.5	Kinematics of arbitrary vehicle bodies . . . . .	115
5.2.6	Kinematics of a wheelset . . . . .	116
5.2.7	Wheel-rail contact kinematics constraints . . . . .	117
5.2.8	Generalized coordinates of the equations of motion . . . . .	120
5.2.9	Equations of motion of vertical dynamics . . . . .	121
5.2.10	Equations of motion of lateral dynamics . . . . .	123
5.2.11	Wheel rail contact forces . . . . .	124
5.3	Full 3D railroad multibody model . . . . .	130
5.3.1	Coordinates and frames . . . . .	130
5.3.2	Kinematics of the track . . . . .	132
5.3.3	Kinematics of the vehicle . . . . .	134
5.3.4	Contact constraints . . . . .	137



5.3.5	Equations of motion . . . . .	138
5.4	Scaled vehicle modelling . . . . .	141
<b>6</b>	<b>Comparison Between Measured and Simulated Wheel-Rail Contact Forces</b>	<b>143</b>
6.1	Simulation to experiment comparison . . . . .	143
6.1.1	Vehicle instrumentation for the experiments . . . . .	144
6.1.2	Experiments on the track . . . . .	148
6.1.3	Forward movement experiments . . . . .	148
6.1.3.1	Experiment 1 contact force measurements . . . . .	159
6.1.3.2	Experiment 2 contact force measurements . . . . .	160
6.1.3.3	Experiment 3 contact force measurements . . . . .	162
6.1.4	Backward movement experiments . . . . .	163
6.1.4.1	Experiment 4 contact force measurements . . . . .	173
6.1.4.2	Experiment 5 contact force measurements . . . . .	175
6.1.4.3	Experiment 6 contact force measurements . . . . .	177
<b>7</b>	<b>Closure</b>	<b>179</b>
7.1	Closure . . . . .	179
7.1.1	Summary . . . . .	179
7.1.2	Conclusions . . . . .	180
7.1.3	Publications . . . . .	182
7.1.3.1	Journal papers . . . . .	182
7.1.3.2	Conference papers . . . . .	183
	<b>Bibliography</b>	<b>185</b>



# List of Figures

2.1	Sunset at the scale track . . . . .	18
2.2	Moving sleeper mechanism . . . . .	19
2.3	Moving sleeper mechanism assembly . . . . .	20
2.4	Supporting table . . . . .	20
2.5	Scale rail section . . . . .	21
2.6	Rail junction . . . . .	22
2.7	Schematic track definition . . . . .	22
2.8	Scale track plan view . . . . .	23
2.9	Reference track vs real track . . . . .	25
2.10	Track irregularities . . . . .	26
2.11	Irregularities of alignment and gauge variation . . . . .	27
2.12	Irregularities of cross level and vertical profile . . . . .	27
2.13	Track recording trolley . . . . .	29
2.14	Total station Leica Nova MS50 . . . . .	30
2.15	Track centre line elliptical plate meter . . . . .	30
2.16	Ellipse self centering property . . . . .	31
2.17	Ellipsoidal plate meter placed on the track . . . . .	32
2.18	Measured centre line coordinate X . . . . .	33
2.19	Scaled track centre line measuring process . . . . .	34
2.20	Scaled track centre line measuring process . . . . .	35
2.21	Synchronization points on calibrated bars . . . . .	36
2.22	Measured track centre line vs designed track centre line . . . . .	38
2.23	Measured track height vs designed track height . . . . .	39
2.24	Track gauge and cant angle meter . . . . .	40
2.25	Track gauge and cant angle meter final assembly . . . . .	41
2.26	Track gauge and cant angle measuring procedure . . . . .	42
2.27	Measured track gauges . . . . .	43
2.28	Measured track cant angles . . . . .	44
2.29	Measured, optimized and initial estimation track centre lines . . . . .	46
2.30	Measured, optimized and initial estimation track centre line heights . . . . .	46
2.31	Track sections . . . . .	47

2.32 Gauge track irregularity . . . . .	48
2.33 Track cant angle . . . . .	48
2.34 Cross level track irregularity . . . . .	49
2.35 Alignment and vertical profile calculation procedure . . . . .	50
2.36 Alignment track irregularity . . . . .	51
2.37 Vertical profile track irregularity . . . . .	51
2.38 Components of track irregularity . . . . .	52
2.39 Components of track irregularity . . . . .	52
3.1 Original Scaled Bogie Design . . . . .	57
3.2 Original (left) and new (right) scaled wheel . . . . .	58
3.3 Original (up) and New (down) Scaled Wheel Section . . . . .	58
3.4 ANSYS Finite Elements Model . . . . .	59
3.5 FEM Element Size Analysis . . . . .	60
3.6 New scaled bogie design . . . . .	61
3.7 Mounting of Strain Gauges . . . . .	62
3.8 Half-bridge Configuration . . . . .	63
3.9 Radial strain state of the wheel . . . . .	64
3.10 Loads applied to the wheel . . . . .	64
3.11 Simulated radial strain in different measuring radius . . . . .	65
3.12 Datatel transmitters and receiver . . . . .	66
3.13 Final assembly of the scaled dynamometric wheelset . . . . .	66
3.14 Measuring points, radial lines and measuring circumference . . . . .	67
3.15 Synthesized strains when lateral and vertical loads are applied on the wheel . . . . .	77
3.16 Simulated vs estimated applied lateral load . . . . .	78
3.17 Simulated vs estimated applied vertical load . . . . .	78
3.18 Deformed shape when a unitary lateral load is applied on the wheel . . . . .	79
3.19 Luccini Rolling Rig . . . . .	80
3.20 Scaled Static Test Bench . . . . .	81
3.21 Calibration Test Bench Instrumentation . . . . .	81
3.22 Test Bench Load Cells . . . . .	82
3.23 FEM Experimental Validation . . . . .	83
3.24 Effect of the Normal Load Applied on the Wheel . . . . .	84
3.25 Normal load effect on the measured radial strains. Track experiment . . . . .	85
3.26 Normal load effect on the measured radial strains, experimental validation . . . . .	85
3.27 Points of application of the force in the wheel tread . . . . .	86
3.28 Influence of the contact point on the radial strain measurements . . . . .	87
4.1 Vertical lasers mounting on the bogie frame . . . . .	91
4.2 Lateral lasers mounting on the left bearing box . . . . .	92

4.3	Final assembly of the dynamometric wheelset . . . . .	92
4.4	Laser based method kinematic assumptions . . . . .	93
4.5	Deformed wheel web shaped when a unitary lateral load is applied . . . . .	95
4.6	Right Side Vertical Laser Calibration . . . . .	96
4.7	Left Side Vertical Laser Calibration . . . . .	97
4.8	Lateral deflection vs applied lateral load, experimental validation . . . . .	98
4.9	Influence of the contact point on the lateral lasers measurements . . . . .	99
4.10	Lateral deflection vs applied lateral load, experimental validation . . . . .	100
4.11	Upper Laser Raw Measurement . . . . .	101
4.12	Central Laser Raw Measurement . . . . .	101
4.13	Lower Laser Raw Measurement . . . . .	102
4.14	Upper Laser Irregularity Pattern . . . . .	102
4.15	Central Laser Irregularity Pattern . . . . .	103
4.16	Lower Laser Irregularity Pattern . . . . .	103
4.17	Upper Laser Raw and Corrected Measurement . . . . .	104
4.18	Central Laser Raw and Corrected Measurement . . . . .	105
4.19	Lower Laser Raw and Corrected Measurement . . . . .	105
5.1	Frames of reference used in the railroad modelling . . . . .	109
5.2	Wheelset-track frame, wheelset frame and wheelset intermediate frame . . . . .	110
5.3	Rail-head frames . . . . .	111
5.4	Track frame at centreline . . . . .	114
5.5	Kinematic description of an arbitrary vehicle body . . . . .	116
5.6	Geometry of wheelset-track knife-edge contact constraints . . . . .	118
5.7	Forces and torque on a wheelset . . . . .	124
5.8	Kinematics of the bodies of a railway vehicle with relative body-track frame coordinates . . . . .	131
5.9	Railroad vehicle as a set of open-chain mechanisms . . . . .	133
5.10	Wheel profile and rail profile geometry . . . . .	134
5.11	Real and equivalent wheel profiles . . . . .	138
5.12	Multibody model main elements . . . . .	141
6.1	Instrumented scaled bogie on the track. Front view . . . . .	145
6.2	Instrumented scaled bogie on the track. Left side view . . . . .	146
6.3	Instrumented scaled bogie on the track. Right side view . . . . .	146
6.4	Track beacon . . . . .	147
6.5	LabVIEW user control interface . . . . .	147
6.6	Forward velocity profile in Experiment 3 . . . . .	149
6.7	Longitudinal acceleration $a_x$ of the instrumented wheelset . . . . .	150
6.8	Lateral acceleration $a_y$ of the instrumented wheelset . . . . .	151
6.9	Vertical acceleration $a_z$ of the instrumented wheelset . . . . .	151

6.10 Angular velocity $\omega_x$ of the instrumented wheelset . . . . .	152
6.11 Angular velocity $\omega_y$ of the instrumented wheelset . . . . .	152
6.12 Angular velocity $\omega_z$ of the instrumented wheelset . . . . .	153
6.13 Longitudinal acceleration $a_x$ of the bogie frame . . . . .	154
6.14 Lateral acceleration $a_y$ of the bogie frame . . . . .	154
6.15 Vertical acceleration $a_z$ of the bogie frame . . . . .	155
6.16 Angular velocity $\omega_x$ of the bogie frame . . . . .	155
6.17 Angular velocity $\omega_y$ of the bogie frame . . . . .	156
6.18 Angular velocity $\omega_z$ of the bogie frame . . . . .	156
6.19 Continuous flange contact in the sharp radius curve . . . . .	158
6.20 Normal force experiment 1, methods comparison . . . . .	159
6.21 Lateral force experiment 1, methods comparison . . . . .	159
6.22 Lateral force experiment 1, methods comparison . . . . .	160
6.23 Normal force experiment 2, methods comparison . . . . .	160
6.24 Lateral force experiment 2, methods comparison . . . . .	161
6.25 Lateral force experiment 2, methods comparison . . . . .	161
6.26 Normal force experiment 3, methods comparison . . . . .	162
6.27 Lateral force experiment 3, methods comparison . . . . .	162
6.28 Lateral force experiment 3, methods comparison . . . . .	163
6.29 Forward velocity profile in experiment 6 . . . . .	164
6.30 Longitudinal acceleration $a_x$ of the instrumented wheelset . . . . .	164
6.31 Lateral acceleration $a_y$ of the instrumented wheelset . . . . .	165
6.32 Vertical acceleration $a_z$ of the instrumented wheelset . . . . .	165
6.33 Angular velocity $\omega_x$ of the instrumented wheelset . . . . .	166
6.34 Angular velocity $\omega_y$ of the instrumented wheelset . . . . .	166
6.35 Angular velocity $\omega_z$ of the instrumented wheelset . . . . .	167
6.36 Longitudinal acceleration $a_x$ of the bogie frame . . . . .	167
6.37 Lateral acceleration $a_y$ of the bogie frame . . . . .	168
6.38 Vertical acceleration $a_z$ of the bogie frame . . . . .	168
6.39 Angular velocity $\omega_x$ of the bogie frame . . . . .	169
6.40 Angular velocity $\omega_y$ of the bogie frame . . . . .	169
6.41 Angular velocity $\omega_z$ of the bogie frame . . . . .	170
6.42 Normal force experiment 4, methods comparison . . . . .	173
6.43 Lateral force experiment 4, methods comparison . . . . .	173
6.44 Lateral force experiment 4, methods comparison . . . . .	174
6.45 Normal force experiment 5, methods comparison . . . . .	175
6.46 Lateral force experiment 5, methods comparison . . . . .	175
6.47 Lateral force experiment 5, methods comparison . . . . .	176
6.48 Normal force experiment 6, methods comparison . . . . .	177
6.49 Lateral force experiment 6, methods comparison . . . . .	177

---

6.50 Lateral force experiment 6, methods comparison . . . . .	178
---	-----





# List of Tables

2.1	Target distance vs distance from the station . . . . .	31
2.2	Horizontal track definition input parameters example . . . . .	43
2.3	Vertical track definition input parameters example . . . . .	44
2.4	Horizontal optimization parameters initial estimation . . . . .	47
2.5	Optimized horizontal parameters . . . . .	53
2.6	Vertical optimization parameters initial estimation . . . . .	53
2.7	Optimized vertical parameters . . . . .	54
3.1	FEM Convergence and Efficiency Analysis . . . . .	60
5.1	Horizontal profile description . . . . .	113
5.2	Vertical profile description . . . . .	113
5.3	Body frames initial position and orientation . . . . .	142
5.4	Mass and inertia properties of bodies . . . . .	142
5.5	Primary suspension elements . . . . .	142
5.6	Traction rods . . . . .	142
6.1	Instruments equipped on the vehicle . . . . .	145
6.2	Second curve average lateral force . . . . .	171



# Abbreviations

<b>ANN</b>	<b>A</b> rtificial <b>N</b> eural <b>N</b> etwork
<b>MSD</b>	<b>M</b> ultibody <b>S</b> ystems <b>D</b> ynamic
<b>MBS</b>	<b>M</b> ultibody <b>S</b> ystem
<b>MBCM</b>	<b>M</b> odel <b>B</b> ase <b>C</b> ondition <b>M</b> onitoring
<b>PVDF</b>	<b>P</b> oly <b>V</b> inyl <b>D</b> ene <b>F</b> luoride
<b>EKF</b>	<b>E</b> xtended <b>K</b> alman <b>F</b> ilter
<b>MEMS</b>	<b>M</b> icro <b>E</b> lectrical <b>M</b> echanical <b>S</b> ystems
<b>VRA</b>	<b>V</b> ehicle <b>R</b> esponse <b>A</b> nalysis
<b>FEM</b>	<b>F</b> inite <b>E</b> lement <b>M</b> ethod
<b>DOF</b>	<b>D</b> egree <b>O</b> f <b>F</b> reedom
<b>COG</b>	<b>C</b> enter <b>O</b> f <b>G</b> ravity
<b>GF</b>	<b>G</b> lobal <b>F</b> rame
<b>TF</b>	<b>T</b> rack <b>F</b> rame
<b>BF</b>	<b>B</b> ody <b>F</b> rame
<b>BTF</b>	<b>B</b> ody <b>T</b> rack <b>F</b> rame
<b>WF</b>	<b>W</b> heelset <b>F</b> rame
<b>WT</b>	<b>W</b> heelset <b>T</b> rack frame
<b>WIF</b>	<b>W</b> heelset <b>I</b> ntermediate <b>F</b> rame
<b>VTF</b>	<b>V</b> ehicle <b>T</b> rack <b>F</b> rame
<b>LPF</b>	<b>L</b> eft <b>P</b> rofile <b>F</b> rame
<b>RPF</b>	<b>R</b> ight <b>P</b> rofile <b>F</b> rame

---

<b>NE</b>	<b>N</b> ewton- <b>E</b> uler
<b>DAE</b>	<b>D</b> ifferential <b>A</b> lgebraic <b>E</b> quation
<b>ODE</b>	<b>O</b> rdinary <b>D</b> ifferential <b>E</b> quation
<b>PSD</b>	<b>P</b> ower <b>S</b> pectral <b>D</b> ensity
<b>IMU</b>	<b>I</b> nternal <b>M</b> easurement <b>U</b> nit
<b>DC</b>	<b>D</b> irect <b>C</b> urrent
<b>TCL</b>	<b>T</b> rack <b>C</b> enter <b>L</b> ine
<b>DAQ</b>	<b>D</b> ata <b>A</b> cquisition software

# Symbols

$x$	Longitudinal Cartesian coordinate
$y$	Lateral Cartesian coordinate
$z$	Vertical Cartesian coordinate
$\varphi$	Roll Euler angle
$\theta$	Pitch Euler angle
$\psi$	Yaw Euler angle
$\mathbf{R}$	Position vector which origin coincides with the GF
$\mathbf{r}$	Position vector which origin coincides with the TF
$\mathbf{u}$	Position vector which origin coincides with the BF, WF and WIF
$\mathbf{w}$	Position vector which origin coincides with the BTF and WTF
$\Phi$	Euler angles in vector form
$\mathbf{A}$	Transformation matrix
$\boldsymbol{\omega}$	Angular velocity vector
$\boldsymbol{\alpha}$	Angular acceleration vector
$\mathbf{q}$	$6 \times 1$ vector of coordinates
$\mathbf{H}$	Partial derivative: $\partial \mathbf{R} / \partial \mathbf{q}$
$\mathbf{h}$	Partial derivative: $\partial \dot{\mathbf{R}} / \partial \mathbf{q}$
$\mathbf{G}$	Partial derivative: $\partial \boldsymbol{\omega} / \partial \dot{\mathbf{q}}$
$\mathbf{g}$	Partial derivative: $\partial \boldsymbol{\omega} / \partial \mathbf{q}$
$\mathbf{I}$	Inertia tensor

---

<b>F</b>	Force vector
<b>T</b>	Torque vector
<b>M</b>	Mass matrix
<b>C</b>	Damping matrix
<b>K</b>	Stiffness matrix
<b>Q</b>	Generalized force vector
<b>a</b>	Vector of Cartesian and angular accelerations
<b>L</b>	Jacobian matrix: $\begin{bmatrix} \mathbf{H} & \mathbf{G} \end{bmatrix}^T$
<b>l</b>	Jacobian matrix: $\begin{bmatrix} \mathbf{h} & \mathbf{g} \end{bmatrix}^T$
$k$	Stiffness parameter
$c$	Damping parameter
$l$	Suspension element length
$l_0$	Suspension element initial length
$\dot{l}$	Suspension element deformation rate
$f_s$	Suspension element scalar force
$\varepsilon$	Vector of creepages
$F_f^T$	Tangential flange contact scalar force
$F_f^N$	Normal flange contact scalar force
$s$	Trajectory coordinate
<b>C</b>	Vector of constraints
<b>C<sub>q</sub></b>	Jacobian matrix of the constraints
<b><math>\dot{\mathbf{C}}_q</math></b>	Time derivative of the Jacobian matrix
<b>C<sub>t</sub></b>	First partial-time derivative of the vector of constraints
<b>C<sub>tt</sub></b>	Second partial-time derivative of the vector of constraints
$\mathbf{s}^w$	Vector of wheel surface parameters
$\mathbf{s}^r$	Vector of rail surface parameters
<b>t</b>	Tangent vector
<b>n</b>	normal of constraints

---

$\boldsymbol{\lambda}$	Vector of Lagrange multipliers
$u_z$	Vertical track irregularity
$u_y$	Lateral track irregularity
$d$	Track gauge
$d'$	Irregular track gauge
$\mathbf{f}$	Function vector





*A mi abuelo Pedrín, allá donde estés...*



# Chapter 1

## Introduction

### 1.1 Literature review

The first application of the rail as an element of support and guidance for vehicles was in Great Britain in the 16th century. These were mining vehicles that moved on wooden rails that would later be covered with steel. In the year 1804, an incredible event took place that would change the course of history forever, the invention of the steam engine. Not long after in 1814, the first steam-powered locomotive appeared on the scene followed by the first passenger train in 1825. The railway boom allowed for the development of once isolated regions, becoming a state issue for countries such as the United States, Canada, Russia and China. Railways dominated until the 19th century when the turbine motor was invented and the internal combustion engine was developed. Currently, the overuse of the internal combustion engine with all of the environmental problems that it creates is once again bringing attention to railways as a mode of transportation due to their high safety reliability, high degree of automation and smaller impact on the environment. Unfortunately, the infrastructure costs for railways are very high, around 7-10 million Euros per kilometre using the most modern construction. Its large volume represents a difficulty in integrating it into metropolitan transport networks, and thus it is necessary to resort to lighter systems such as metros, trams or buses. In spite of this, it can be said that the 21st century railway has become

a means of transport with as many comforts as the car and a clear direct competitor of the plane over medium distances.

The increase in the service speed of rail transport during the last decades has increased not only the comfort of the vehicles but also the mechanics and security of both the vehicles and the rails. Under these circumstances, the life cycle of many railway components has grown shorter causing a significant increase in the maintenance costs. The wheel-rail interaction is the principal factor that determines the dynamic behaviour of a vehicle, which is why the study of this interaction has become very important for the scientific and technological community. Although the advance of mathematical models and measuring instruments has been fundamental for the knowledge/study of the physical processes that occur during the wheel-rail contact, many aspects are still unknown and thus, some of the practices used today are based on the experience and use of empirical methods. The immediate consequence of the use of these techniques results in the application of high safety coefficients, with more conservative designs and the use of traditional materials. In this regard, achieving more precise knowledge about wheel-rail contact forces is crucial for the development of new methodologies with impacts on the economic, environmental, and safety-related levels[1, 2].

Railway vehicle running safety criteria are based on wheel-rail contact force magnitudes. Recently, novel criteria have been proposed as that presented in [3] by Wei et al or presented by Braghin et al [4]. In the work by Braghin, the results obtained are compared with this new criterion where the instantaneous angle of attack of the wheel with the rail is taken into account with other traditional ones. (Weinstock [5] and Elkins-Wu [6]). This new criteria, that can be considered to be derived from Nadal's criteria [7], is more robust than the traditional one as it is based on parameters that depend on the wheel-rail geometry.

Despite the variety of existing criteria, the most commonly used safety criteria are [8]:

1. Nadal's derailment criteria: It establishes the limiting value of  $Y/Q$  to prevent derailment. This limit is related to the flange slope and the coefficient of friction..
2. Prud'homme's criteria: It establishes the track resistance against applied lateral loads. The resultant lateral force on each wheelset must be smaller than  $(10 + 2Q_0/3)$  kN, where  $Q_0$  is the static vertical force on a single wheel.

3. Roll-over safety criteria: It is obtained from the vertical loads on each wheel of the vehicle. Its magnitude must be above a certain value.
4. Discharge safety criteria: Discharge factor, that is a function of the static vertical load  $Q_0$  and the instantaneous vertical loads on the first and second wheelset of the bogie must be smaller than a certain value.

In view of these criteria that are well established within the railway industry, it can be seen that the knowledge of the wheel-rail contact forces turns out to be decisive in order to quantitatively assess the safety of the running of a railway vehicle.

The European standard EN-14363 [9] defines the tests for the acceptance of the dynamic behavior of railway vehicles. These tests must be carried out so that new design of vehicles, or vehicles with modified operating conditions can circulate through European railway networks. All of these tests require the measurement of wheel-rail forces (normal and vertical forces) although they do not specify the method to be used. The most precise way to obtain the values of the aforementioned contact forces is through the so-called dynamometric axels. In general, these are conventional axels instrumented with strain gauges for direct measurement of forces. These devices are expensive, due to the extreme precision required in the location of the gauges and the telemetry equipment necessary to transfer the signals to the acquisition system. Additionally, its accuracy for medium frequencies is not totally clear. Cazzulani et al. [10] studies the metrological properties of a dynamometric wheelset in order to verify whether it is really capable of measuring in the appropriate frequency range. In addition, various alternatives are suggested to better the precision of the measurement when the axel operates in extreme conditions. Bionda et al. [11] recently presented a study where the precision of the wheel-rail force measurement is analyzed, determining that it is necessary to use at least six independent sections of the wheel to obtain a correct measurement of the contact force.

Furthermore, it is important to note that prior to putting them into operation, dynamometric wheelsets must undergo a severe calibration process [12] where the response of the system is analyzed when different forces are applied to it. Calibration can be done on static [13] or dynamic benches [14], also known as rolling rigs. Some of these machines can test a full scale dynamometric wheelset up to 300 km/h while controlling

vertical and lateral loads and the relative wheelset-rail yaw angle. The rails are two rings machined with a conventional UIC profile. With a sophisticated test rig controller, it is possible to reproduce straight and curve running conditions, including acceleration and braking. Nevertheless, the dynamic operation of a wheelset on a roller rig differs from its behavior on a real rail. Bosso et al. [15] carried out a study comparing both scenarios and finding notable differences. Thus, the high cost of the dynamometric axles means that even for high-performance laboratory vehicles, such as the ADIF S  n  ca [16], they are prohibitive.

As an alternative to the use of dynamometric axels, there is the measurement of contact forces through indirect methods. These methods are based on the use of a computational model that describes the dynamics of the vehicle and the measurement of a series of inertial sensors installed on it. These types of techniques can be framed within what is known as Model-Based Condition Monitoring (MBCM) which is commonly used in machine maintenance. Within the railway industry, the application of MBCM techniques in the following fields is being actively researched:

1. Detection of derailment at its earliest stage. The works of Mattoto et al. [17], Boronenko et al. [18], Hubacher and Scheiber [19] and Zeng [20], use MBCM techniques for the timely detection of this phenomenon before reaching catastrophic situations. In light of these works, it can be seen that these methods are still far from being able to be implemented in a real system.
2. Estimation of the wheel and rail profile and detection of instabilities. It is known that excessive wear of the profiles causes loop instabilities (hunting) [21]. MBCM can be applied to avoid this effect as proposed by Charles et al. [22]. Again, these methods are still in development.
3. Condition monitoring of the suspension system of railway vehicles. This is the most innovative use of MBCM. It is currently under development, and it is known [21] that they have not been commercially implemented, which represents an opportunity to offer a product with competitive advantages in the market.

In scientific literature, numerous works can be found on the estimation of parameters and states of railway vehicles based on its instrumentation and the analysis of signals

of on-board systems. Goda and Goodall [23], Goodall and Kadiramanathan [24], Li et al. [25] and Hayashi et al. [26] present different studies where failures in vehicle suspension are detected based on the measurement of inertial sensors and Kalman filter-based estimators. Another interesting study is that presented by Charles and Goodall [27] where the estimate with Extended Kalman Filter (EKF) of creep forces is used as input in the vehicle's brake control system. Bruni et al. [28] presents a method based on Time Domain Signal Analysis for the evaluation of the unstable operation of the vehicle caused by excessive hunting. Finally, Xia et. al [29] presents a method for the detection of derailment and the control of the vehicle's operating speed based on the measurement of an accelerometer.

In the reference [30], the authors review the various condition monitoring techniques currently available, making a distinction between model-based techniques and signal-based techniques. In model-based techniques, Kalman or extended Kalman filters are generally applied according to whether or not the system is linear. The problem with this methodology lies in the uncertainties that exist when building the models. On the other hand, the technique based on signals is based on the instrumentation of the bogies, being there where any phenomenon that could jeopardize the safety of the vehicle can be detected more quickly.

Not all applications of condition monitoring are based on a model, there are also some so-called "model-free" applications. Xia et al. presents in [31] an inverse model of the wagon for the prediction of the contact forces from the dynamic response of the vehicle. This paper presents three different ways to address the problem, called: white-box inverse model, gray-box inverse model and black-box inverse model. In the white-box inverse model, there is a complete model of the vehicle with all its equations based on the physical laws. On the contrary, in the black-box inverse model, only a relationship between inputs and outputs of the system is available. The gray-box inverse model is presented as an intermediate solution between the previous two, being much more efficient.

It can be said that in general, in the field of instrumentation in Mechanical Engineering, a great advance is being experienced thanks to the tremendous decrease in the price of the sensors and the rise of the Micro-Electro-Mechanical-Sensors (MEMS). The precise knowledge of the state of a dynamic system should not be achieved so much by "brute

force”, that is, by using a large number of sensors, but by means of instrumentations based on system models being analysed [[32]-[33]]. In this sense, the Kalman filtering technique [34] and its variants provide the necessary technology to obtain the state of a system from an incomplete set of experimental measures. In addition, Kalman filtering allows theoretical models to be adjusted by obtaining the values of their parameters from experimental measurements. In the field of track measurement, Charles [35] has developed a method for the continuous monitoring of railway vehicles based on dynamic simulation. Using Kalman’s filtering technique, they manage to assess in real time an estimate of the wheel and rail profile and the coefficient of friction between the two surfaces to detect areas of low adhesion where long braking distances are necessary. Smith and Wu [36] propose combining displacement measurements, accurate for low frequencies, and acceleration, accurate for high frequencies, to obtain high precision displacement data using multichannel Kalman filtering. Ward et al. [37] proposes a method for estimating the tangential forces of wheel-rail contact based on Kalman filtering and a computational model of the lateral dynamics of the vehicle. It is assumed that the tangential forces are a function of pseudo-slip speeds (creepages) following the Polach model [38]. This study includes the tangential forces within the vector of vehicle states. In the publication of Naets et al. [39] they describe a method of estimating excitation forces in general in multibody systems based on the use of reduced models sub-system global model parametrization and the EKF method of estimation. This study also includes the excitation forces in the state vector. In this case, a model with stochastic variation is assumed. The system uses completely non-linear equations of multibody systems and shows that real-time estimates can be made.

The estimation of wheel-rail contact forces in the industry is nothing new. In 1891, one of the first dynamometric axes appears, built for the Southern Pacific Railroad [40]. The objective was to have an infrastructure where wrong wheel designs or possible manufacturing defects could be detected. The system consisted of two wheels mounted on an axle that supported some discs powered by a steam engine. By means of a system of springs and counterweights, the loads applied to the shaft were controlled. Reference [41] describes how in the 1980s in the Dutch rail network, a laboratory vehicle was already used for road maintenance that included the Vehicle Response Analysis (VRA) system. This system was able to estimate lateral and longitudinal contact forces and from these estimates, determining the coefficients of the Nadad and



Pruned'homme criteria in real time. The system was based on experimentally obtained transfer functions ("model free") and signal treatment with analog filters. More recently [42] a simulation model has been carried out to evaluate wheel-rail contact forces for irregularities of small wavelengths. The analytical model assumes that the movement of the axles is independent of the rest of the bodies of the vehicle and is stimulated by the irregularities of the road. Gullers et al. [43] presents an experimental wheel-rail force calculation model based on dynamometric axes and a finite axis model to estimate high frequency forces. In this study, they show that the contact forces in the range of 100-1250 Hz, which cannot be obtained with dynamometric axes based exclusively on sensors, contribute significantly to the dynamic response of the vehicle. Nielsen [44] conducts a similar study measuring high frequency vertical forces. In addition, an interesting study is carried out about the effect of the shock loads on the wheel and the influence of the corrugation of the rails on the vertical dynamics of the vehicle and the contact forces. The results are validated with field tests. In the work of Jönsson et al. [45], a comparison is made of contact forces obtained experimentally with those obtained by simulation, showing a strong agreement. This paper proposes the use of computer simulation together with irregularity measures obtained through auscultation for the validation of the new designs of railway vehicles. Sun et al. presents in [46] a bi-directional inverse model of a freight wagon where vertical contact forces are monitored from inertial measurements. Alternatively, Mehrpouyaa and Ahmadian employ in [47] a finite element model of a merchandise vehicle for the identification of the forces applied on the wheelsets. Xia and Cole present in [48] an inverse model of the vehicle for estimating contact forces based on the use of low-cost inertial sensors used at the industrial level. The results obtained are validated with VAMPIRE [49]. Ren and Chen [50] have recently presented a method for the continuous measurement of contact forces using a dynamometric wheelset and state space theory. The application of the theory of state space allows continuous monitoring of the contact forces with a simpler mounting of simple strain gauges. Lai Wei et al. presents in [51] an indirect method for the measurement of forces based on the placement of displacement sensors in the suspensions, accelerometers and strain gauges. Something similar is stated by Gialleonardo et al in [52] where dynamometric wheelset measurements are combined with suspension deflection measurements to estimate contact force.

The problem of estimating wheel-rail contact forces is intimately related with the precise

knowledge of the point or points of contact between the wheel and the rail. The position of the contact point will determine the direction of the forces applied to the wheels that will affect the dynamics of the vehicle. Various thesis can be found in the scientific literature focusing on the online analytical determination of the contact points during the kinematic simulation such as that presented by Malvezzi [53] who uses semi-analytical methods to determine the point of contact or the hybrid method presented by Sugiyama [54]. The latter uses look up tables [55] to determine the tire contact and online calculation when the contact passes to the flange. There are other experimental studies applied to the determination of the contact point as the one presented in [56] from the measurement of sensors installed in the wheel that can be found in the scientific literature.

As previously mentioned, the determination of the wheel-rail contact forces in the railway industry is generally based on the use of strain gauges which obtain the value of wheel-rail contact loads by measuring the strain of the points where they are placed. Depending on the position of the sensors used, the following are distinguished: methods based on the axle body, methods based on the wheel core, methods based on elements of the primary suspension and mixed methods that combine other previous methods. The first two are currently used the most.

The forces that exist at the wheel-rail contact point are divided into three types: vertical loads  $F_z$  ( $V$  o  $Q$ ), lateral loads  $F_y$  ( $L$  o  $Y$ ) and longitudinal loads  $F_x$ . Of the three aforementioned forces, the longitudinal forces are the simplest to measure through placing sensors on the shaft body. In [57] they obtain the longitudinal force from the torque applied to the shaft, which is measured by strain gauges. It should be noted that obtaining wheel-rail forces using sensors placed on the axle body can be affected by the variation in the position of the contact point as described by Elkins and Cartert [58]. In addition, the influence of the variation in the position of the contact point cannot be eliminated from the measurement of the lateral load. On the other hand, the inertia of the axle masses that lie between the contact point and the sensors are an additional source of error that must be eliminated. These methods also present space problems for placing the sensors between the grease boxes and the wheels.

On the other hand, several solutions have been developed to obtain wheel-rail forces with methods based on the placement of sensors in the wheel web. In general, all of

them have strain gauges whose angular and radial positions must be perfectly defined through previous studies. Angular parameters are used to eliminate the influence of wheel rotation on measurements, while radial parameters are used to decouple measurements of contact forces (normal, lateral and longitudinal). The connection of the extensometric sensors is usually carried out through the use of Wheatstone bridges. Different connection configurations can be made depending on the type of measurement [59]. In the work presented by Feng Yu [60], a method of placing the strain gauges at full bridge is analysed so that the measurement of the normal load is decoupled from the lateral load.

For the determination of the radial position of the sensors, a few different alternatives have been proposed. For example, as described by Kanehara and Fujioka [56], the sensors can be placed at points of the wheel web where the sensitivity to one of the forces is zero, or holes can be made in the wheel core and instrumented in nearby areas and inside the holes. These methods present problems because the hypotheses used further simplify the problems related to the decoupling of forces.

Regarding the angular positioning of the sensors to eliminate the influence of the rotation of the wheel on the measured signals, one of the most used strategies is to place the sensors in the same radial position separated by a specific angle. This is because the strains measured by the sensors vary periodically with the rotational movement of the wheel. If the number of sensors used is increased and their measurements are combined, the result is a data point that tends towards a continuous distribution of the deformation of these points with the variation of the angular position of the contact point. These techniques have certain disadvantages related to robustness, due to the high number of strain gauges necessary to eliminate the effects of ripple. They also present problems because the average sensitivities obtained from the measurement bridge are lower than the real ones. This last one is caused by the cycles of positive and negative deformations experienced by strain gauges during a complete turn of the wheel.

Another alternative to reduce the effect of angular variation of the contact point is based on measuring the deformation of the strain gauges when they pass through a specific angular position (Kanehara and Ohno [61]). This methodology eliminates the influence of the angular variation of the wheel, but reduces the bandwidth for the measurement

of the contact forces due to a decrease in the sampling frequency in the system. These solutions are not usually recommended due to the high number of gauges needed to achieve minimum sampling frequencies that ensure efficient data acquisition.

A third strategy for the configuration of strain gauges is usually to place two of them offset by an angle of  $90^\circ$  in the same radial position. The signals of these gauges are independent and are considered sinusoidal. Gomez et al. [62] describes an example of this technique used in a 1 : 2.6 scale model, analyzing the effects separately of applying a constant vertical force and a constant lateral force. It can be seen that the deformation signals at different radial positions follow a very different variation from one another. The data in the frequency domain is also analyzed, obtaining the amplitudes of the main harmonics for each of the radial positions. In most cases, the greatest amplitudes belong to the first harmonics, which together with the second harmonics are typically the most useful.

In this way, the actual variation in time of the applied force can be determined based on the variation in the amplitude of one of the harmonics. This is a strategy widely used in the methods based on the use of the wheel web, but the main problem of the instrumentation lies in the fact that it is not possible to eliminate high amplitudes of unwanted harmonics. Zang et al. proposes in [63] a complex analysis in frequency that allows to eliminate those components of the rotation that are independent of the fluctuations of the load from the signals acquired by the dynamometric wheelset. Acquiring information from instrumentation placed on the axis is always complex due to the high levels of vibration to which it is subjected.

Based on the described problems of the instrumentation technique of points of the veil of the wheel, Gomez et al. [[[62],[64]]] has proposed a positioning of the gauges that allow the elimination of unwanted harmonics. The methodology developed by the authors consists in placing a set of extensometric sensors so that the signals obtained with the deformation of the sensors are independent of their angular position with respect to the line of application of the load. The extensometric sensors contained in the same radial position constitute what they call measurement circles, being able to obtain different independent signals for each measurement circle. Each extensometric sensor belonging to the same measurement circle has another extensometric sensor positioned diametrically opposite to the first one, that is to say with a  $180^\circ$  offset, thus constituting

what the authors call measurement diameters. The signals of the extensometric sensors belonging to the same measurement diameter are combined with each other by adding or subtracting depending on whether they want to eliminate odd or even harmonics. At least two strain bridges are instrumented for each measuring circumference, one called a phase bridge and the other quadrature bridge. Both have the same configuration but out of phase  $90^\circ/k$ , where  $k$  indicates the pure harmonic on which the measurement is based. This would correspond to a  $90^\circ$  offset for the first harmonic and a  $45^\circ$  offset for the second. For example, pairs of sensors are placed at  $180^\circ$  to eliminate even harmonics of the signals that come from the deformation of the gauges and at  $90^\circ$  to eliminate the influence of the angle on the first harmonic of deformation.

Different configurations of this methodology are described in the patent ES 2 334 529 A1 of Gimenez and Gomez [65]. Here the authors propose a methodology to obtain the three components of the wheel-rail contact force in addition to locating the position of the contact point. For this, the implementation of at least three measurement circles is established. An alternative strain gauges location and electrical configuration is proposed by Garcia et al. in the patent ES 2 436 692 B1 [66]. Both alternatives have been already utilised in the industry.

On the other hand, Gutiérrez López and others [67], based on the study of the dynamic behavior of ground vehicles and given the importance of contact forces between the tire and the roadway, have developed a new method for measuring the forces and moments of contact between the road and the tires. Although the method described by the authors is applied to the wheels of car vehicles, their study is based on previous developments in the railway world (US Patent 5492002 from Higgins et al. and the patent ES 2 334 529 A1 from Giménez and Gómez) and can be adapted for the determination of wheel-rail contact forces.

The limitations presented by the geometry of the tires of the automobile vehicles prevented the use of the methodology proposed by Giménez and Gómez in the patent ES 2 334 529 A1, since in the case of the automobile tires it is almost never possible to place the extensometric sensors or strain gauges in the angular positions required by this methodology. In this way, Gutiérrez López and others [67] propose a more flexible methodology to obtain the forces and moments that act on the tire from signals that do not depend on the angular position of the sensors. In this method, as in the previous

case, the authors define circumferences of measurements and radial lines of measurements where the strain gauges are placed. At least three measuring circumferences and five radial lines are required, which is a total of 15 sensors. The aforementioned method divides the influence functions that describe the relationship between the different components of stresses and the deformations into two groups: symmetric and antisymmetric. These influence functions are subsequently decomposed as Fourier series whose coefficients (amplitudes) represent the sensitivities and remain constant for a wheel determination with specific measurement circumferences. These sensitivities are grouped into a matrix that forms the coefficient matrix of a system of linear equations from which the three components of the contact forces ( $F_x$ ,  $F_y$  and  $F_z$ ) and the three components of the contact moments ( $M_x$ ,  $M_y$  and  $M_z$ ) are obtained. This method has the advantage that for the same number of sensors, more harmonics can be eliminated than with the techniques currently used in the railway industry, thereby reducing the ripple effects.

Another application similar to that presented by Gutiérrez López [67] for the measurement of contact forces between wheels and the road can be found in Bastiaan's work [68]. In this case, instead of instrumentation with strain gauges, piezoelectric sensors are used. The algorithms used for force estimation are based on the use of artificial neural networks [69]. The algorithms presented are even capable of detecting wheel slides on the road with the idea to eventually be integrated into the vehicle's active safety system in the future. Dingqing et al. [70] presents a similar study for the estimation of contact forces based on track geometry with algorithms based on neural networks. As can be seen, artificial neural networks (ANN) are a very powerful and appropriate tool to solve these types of problems. In [[71]-[72]] the authors present a method based on ANN to determine the location and the energy associated with impacts that take place in the fuselage of airplanes, inputting into their system the measurements coming from piezoelectric sensors.

Until now it has been seen how the use of strain gauges is the most widespread practice for measuring contact forces on the wheel. Despite being a very reliable technology, as long as they are correctly installed and calibrated, they have the problem of being mounted on rolling parts, they need either telemetry equipment or sophisticated brush connectors to transmit the information to the acquisition system. Both solutions make

the manufacturing of the dynamometric axis enormously expensive. Matsumoto et al. presents in [[73]-[74]] a very interesting alternative to instrument a dynamometric wheel without using strain gauges. Instead, “Eddy-current” inductive displacement sensors capable of determining the distance to a magnetic surface through electromagnetic effects are used. These sensors are installed on fixed parts of the vehicle such as the grease boxes so that no more than a simple cable connection is needed to transmit the information. From the deflection experienced by the wheel, researchers are able to determine the lateral load applied to it. Due to the fact that the sensors are not installed directly on the wheel-web as strain gauges are, they would measure deflections caused not only by the load applied to the wheel but also by other mechanical effects such as clearances between the axle and the grease box, possible turns of the bearing itself or lack of perpendicularity between the axle and the wheel. For this reason, it is necessary to use, as explained in [[73]-[74]], a fusion of several sensors so that from a kinematic model of the system integrated by the axle and the grease box one can accurately extract the applied lateral load. Obviously this approach can only determine lateral loads. For the measurement of vertical forces, the researchers propose to use LVDT displacement sensors to measure the deflection of the suspensions and from them, the value of the load. The longitudinal forces as suggested by the researchers can be obtained from the longitudinal deformation experienced by the traction rods measured through strain gauges. A recent application of this method is found in the work done by Cheli et al. in [75] that presents a tram model developed for the estimation of forces on elastic wheels and whose results are experimentally validated.

As an alternative to the methods presented above, measurements of wheel-rail contact forces made by rail instrumentation instead of the axle or wheel can also be found in the scientific literature. This methodology has the advantage that it does not need any sophisticated acquisition or telemetry system, since the sensors are installed in the rails themselves. Obviously, the disadvantage lies in the fact that the measurement can only be carried out discreetly at specific points of the track. This approach is interesting when one wants to know, for example, the effect of the passage of the vehicle on changes in track or contra-lane areas in urban trains [76, 77]. Song et al. presented in [78] an innovative technique for measuring forces by implementing the rails using PVDF sensors (Poly Vinyl Dene Fluoride). These are sensors with piezoresistive technology that, unlike the strain gauges, are not affected by the presence of magnetic fields. In

[79] the development of an interesting sensor to also measure rail force is presented. This sensor is installed in the soul of the rail where a hole must have been previously made to house it. It has been taken into account that the perforations made in the soul of the rail do not affect the safety of the lane as opposed to any alteration made in the wheel veil that does compromises its safety.

The wheel-rail contact forces are not only of interest to the railway industry. The manufacturers of roller coasters also have a great interest in knowing the contact forces that appear in their vehicles to always guarantee maximum safety to their occupants and ensure the integrity of the attraction structure. It should be kept in mind that current roller coasters reach very high speeds, such as the famous Kingda Ka in the United States with a maximum speed of  $206\text{ km/h}$ . Generally the contact forces in this type of vehicles have been estimated from inertial models and measures of accelerometers placed in the vehicle itself and the structure [80]. Alternatively, direct measurements of the contact forces can be made from more sophisticated systems such as that presented by Simonis et al. in [81] where one of the vehicle's bearings is instrumented with strain gauges and piezoelectric sensors.

## 1.2 Outline of the thesis

The objective of this thesis is to develop a mechatronic system for the direct measurement of the contact forces in a 1 : 10 scale rail vehicle [82] developed by the Department of Mechanical and Manufacturing Engineering of the University of Seville. The vehicle runs on a 5 inches wide scale track. The scale track characteristics and the measurement of its real geometry is presented in Chapter 2. A dynamometric wheelset has been manufactured and instrumented in which two different technologies for the measurement of wheel-rail contact forces presented in the industry have been integrated, of which one would like to compare. The designed system has been carefully calibrated in a static test bench, where it has been subjected to different load applied in a controlled manner. During this process, the experimental validation of a finite element model of the dynamometric axis has also been carried out obtaining a good agreement between simulations and experiments. The design, instrumentation and calibration of the scale dynamometric wheelset is presented in Chapters 3 and 4. Finally, its operation has been



tested on the track. The force measurements obtained have been compared with the numerical results obtained from two multibody dynamic simulation models described in Chapter 5. The vehicle tested consists of a single bogie consisting of two wheelsets and a frame, connected by suspension elements. Vehicle's instrumentation and experimental results are presented in Chapter 6. The manuscript is closed by Chapter 7, where all the conclusions drawn from this research are summarized.

An important part of this PhD thesis is based on the use of a scale railway vehicle. Having a scale system represents a great advantage when it comes to carrying out experiments. It should be kept in mind that not all railway engineering research institutes have access to real vehicles and infrastructures to carry out their experimental campaigns. The use of systems at scale is a relatively economical way (due to its reduced size) and safe (by not compromising passenger safety or infrastructure) to carry out experiments with rail vehicles and facilities. The results obtained from the scale systems can then be normally extended to full scale systems.

The multibody simulation softwares used in this thesis have been developed over the past few years by this research group. This made in home software is an alternative to several railway simulation programs found in the market such as:

- GENESIS [83]
- NUCARS [84]
- ROBOTRAN [85]
- VAMPIRE [49]
- ADAMS-RAIL [[86], [87]]
- SIMPACK [[88], [89]]
- SAMS [90]

Having ones own simulation model is a great advantage over the mentioned commercial packages. In these packages, the configuration options are limited to the user. By using

---

ones own software, however, different models of wheel-rail contact [91, 92], integration methods, different ways of treating the track geometry[93] and its irregularities [94], etc. can be studied. In return, they require a great effort of programming and study until a robust system that delivers reliable results can be achieved.

## Chapter 2

# Experimental Scaled Track

### 2.1 Scaled track design

In railways multibody modelling, the track geometry is an essential input for the model. In order to get an accurate dynamic simulation, a correct and precise track description is needed. The more accurate that definition is, the better agreement between the simulated system and the real one will be reached. The track geometry has an essential role in the wheel-rail contact scenario. Taking into account that the main purpose of this thesis is the development of a railway multibody model for the estimation of the wheel-rail contact forces and its experimental validation, a perfect knowledge of the scaled track where the experimental vehicle moves is required.

The experimental campaigns accomplished in this project have been carried out in the scaled track facilities at the University of Seville. It is a 5 inches wide and 90 meters long open track located in the roof of the School of Engineering (see Fig. 2.1). It was built in 2017 covered through European Union funding. The manufacturing and final assembly of the scale track was accomplished by a private company selected by public tender, based on a previous design made by the Department of Mechanical Engineering of the University of Seville.

The original idea of the project was to build a track with variable geometry that allow the manual insertion of track irregularities. For that purpose a multi-degree of freedom



FIGURE 2.1: Sunset at the scale track

mechanism that allow track width, cant angle and relative position between rails variation has been designed (see Fig.2.2). For a better understanding of the mechanism functionality see Fig. 2.3. As it can be observed, the central base of the mechanism is separated in two parts that can move along a longitudinal slider. Turning the central nut, the track width can be modified. The two rails are supported by a couple of sub-mechanisms that can vary its relative position acting on three bolts. Finally, the lateral bolts and nuts modified the tilt angle of the entire mechanism changing this way the cant angle of the track. Every single part of the mechanism has been manufactured in high quality stainless steel to perfectly resist atmospheric corrosion. The maximum movement allowable by this design are:

- Track width:  $127 \pm 8$  mm.
- Rails relative height:  $0 \pm 5$  mm.
- Sleeper height:  $0 \pm 8$  mm.
- Cant angle:  $0 \pm 4.5$  degrees.



FIGURE 2.2: Moving sleeper mechanism

These mechanisms have been assembly every 100 mm along the track, fixed to a series of 47 iron welded tables (See Fig. 2.4) distributed on rooftop of the building. All of them are levelled by adjustable legs, getting a perfect alignment of table plane despite all the roof irregularities. Tables are rigidly connected between them to give the maximum robustness to the track.

The rail section has been carefully designed to emulate a real rail profile (see Fig. 2.5). As it can be observed the rail section has two notches, that are necessary to attach the rails to the moving sleeper mechanism. The rails have been milled in 3 meter long sections. To connect each section to the next one a joint mechanism has been also designed. Figure 2.6 shows the solution adopted. Parts number 1 and 3 are in charge of connecting two contiguous rail sections (part number 2).

## 2.2 Ideal track geometry

In the railway industry a real track definition is given by a horizontal and a vertical profile. In the horizontal plane, three different types of geometric forms can be found:

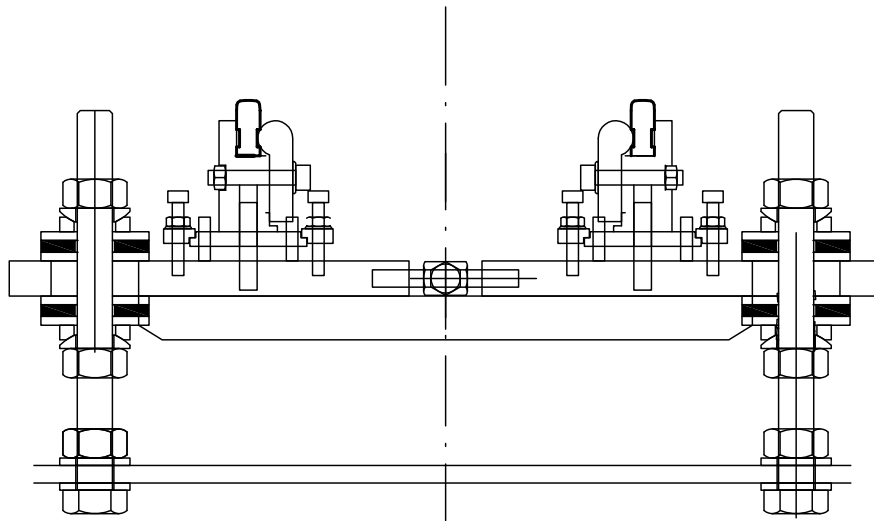


FIGURE 2.3: Moving sleeper mechanism assembly



FIGURE 2.4: Supporting table

- Tangent sections.
- Constant radius curves.
- Transition or variable radius curves.

Transitions connect tangent sections with constant curvature sections or two constant curvature sections with different curvature radius or direction. If transitions are not

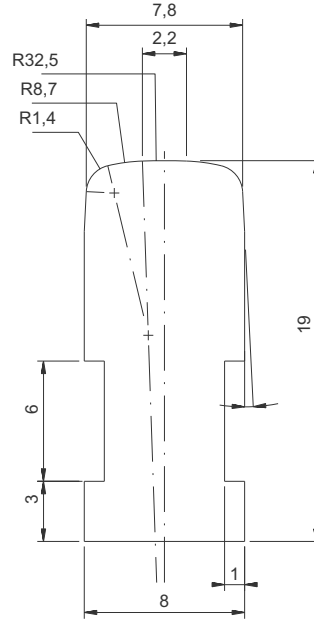


FIGURE 2.5: Scale rail section

used for the track definition, an instantaneous centrifugal force would appear in the connection point between the strait and constant curvature sections that compromise the safety and comfort of the vehicle at this point. Different transition curves can be utilised, however, the most common in railway and road track definition are the clothoids or Cornu spirals. Its main feature is the linear curvature variation with respect to the arc length coordinate.

Vertical profile can be defined in a similar manner. Constant slope and transition sections are its main elements. As mentioned above, transitions are necessary to connect both types of sections. In Fig. 2.7, a simplified horizontal and vertical definition of an ideal track are shown. Note that small radius of curvature sections are used to connect two constant slope sections.

The original idea of the scaled track project was to create an ideal geometry consisting of strait sections, transitions with variable curvature and constant radius curves. Figure 2.8 shows the proposed plan view of the track subjected to the available space on the rooftop of the building. As can be observed, a scaled railway bridge is also part of the railway circuit. It will allow to study the dynamic performance of the experimental

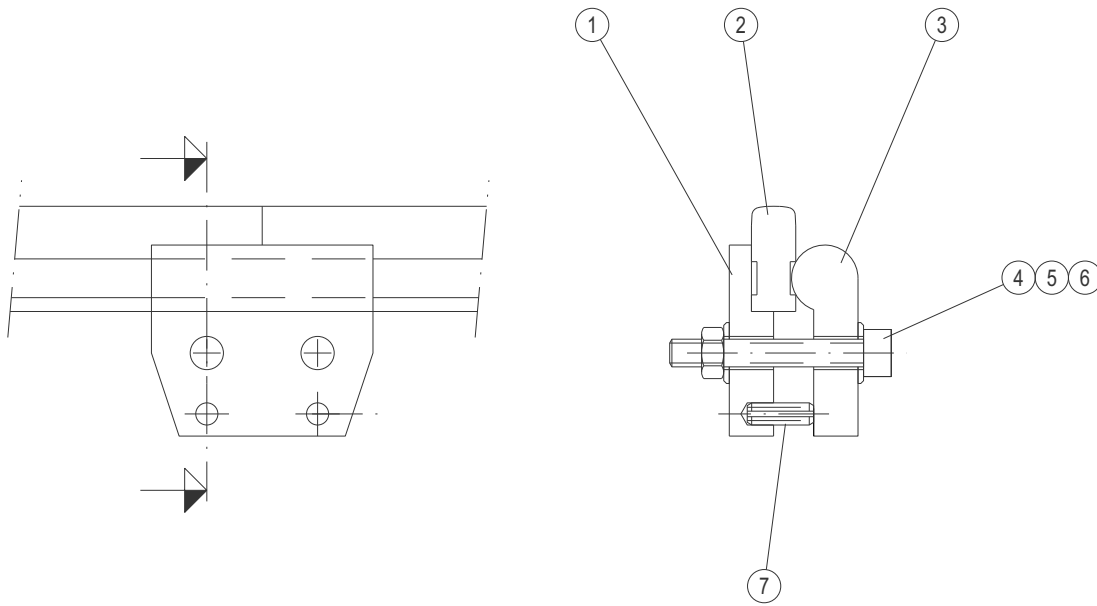


FIGURE 2.6: Rail junction

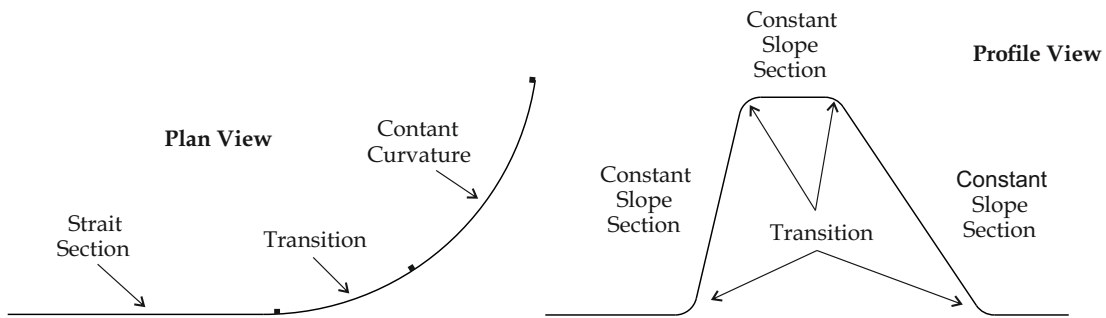


FIGURE 2.7: Schematic track definition

vehicle while passing over it. The list below enumerate the various types of section that theoretically should describe the scale track horizontal projection.

- A:** 20 meters long strait section (scale bridge included).
- B:** 3 meters long and 60 meters mean radius transition section.
- C:** 26 meters long and 24 meters constant radius section.
- D:** 3 meters long and 60 meters mean radius transition section.
- E:** 6 meters long strait section.



**F:** 3 meters long and 24 meters mean radius transition section.

**G:** 12 meters long and 6 meters constant radius section.

**H:** 3 meters long and 24 meters mean radius transition section.

**I:** 12 meters long strait section.

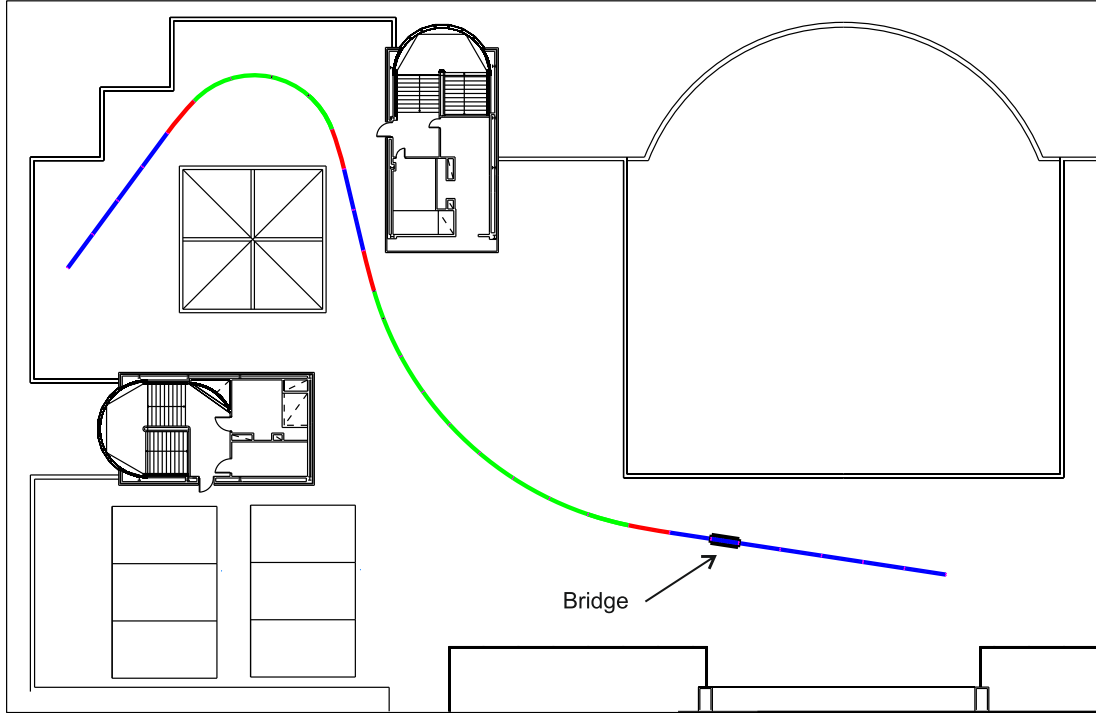


FIGURE 2.8: Scale track plan view

The track vertical profile has been described in a similar way. As previously explained two kind of sections can be found on it. The nodes ( points of connection between two different track sections) in the vertical profile, do not coincide with the number of nodes in the horizontal profile. A minimum radius of 20 meters is established for vertical transitions. Therefore, the sections present in the scale track vertical definition are:

**A:** 76 meters long horizontal section.

**B:** 4 meters long 3.75% ascending constant slope section.

**C:** 2 meters long horizontal section.

**D:** 3 meters long 5% descending constant slope section.

**E:** 2 meters long horizontal section.

## 2.3 Track irregularities

In the previous section an ideal track description has been presented. Predictably, getting this theoretical geometry is impossible due to possible errors in the assembly process. These differences between the reference track geometry and the real one are called track irregularities (see Fig. 2.9). Apart of being produced during the building process, they can also be result from usage operations or movements on the foundation. Track irregularities have great significance in railways operation. Depending on their magnitude, they might be only a matter of ride comfort or even compromise ride safety. Concerning to track comfort regulations, one can find the *British Railways* indexes for comfort and smoothness of railroad vehicles [95]. Another example is the European norm EN 12299 [96] that deals with passengers comfort in railroad vehicles. In addition, *The Association of American Railroad* establishes the so-called "Track safety standards" [97] for railroad vehicles. Large track irregularities may lead to a derailment scenario. Thus, a correct identification and characterization of track irregularities results an essential task in railways engineering.

### 2.3.1 Modeling of track irregularities

As mentioned in the previous section, track irregularities represent the difference between real position and orientation of rail cross sections with respect to their reference position (see Fig. 2.10). Although this is the formal way to define track irregularities, is not the most common way in the railways industry. An alternative definition is normally utilized. Two different types of geometry variations should be considered: distributed track irregularities and isolated track irregularities. Distributed track variations are characterized by the four independent magnitudes listed below. Figures 2.11 and 2.12 show graphically their effect on a track. Such geometric track variations represent a

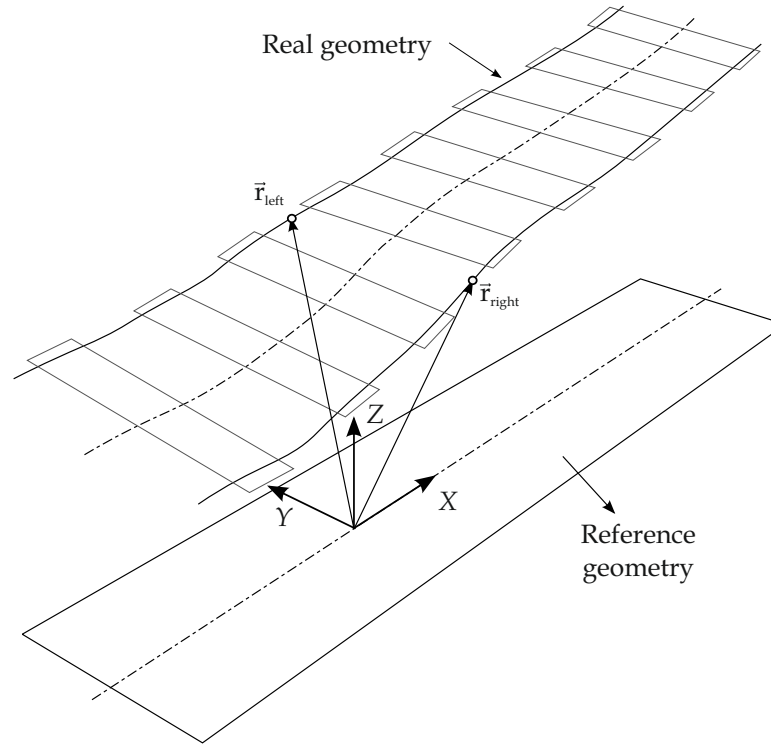


FIGURE 2.9: Reference track vs real track

very important information for railways operators, and they must be regularly measured using special track devices. Each of them defined below. Equation 2.1 represents their mathematical definition.

- **Alignment:** It is defined as the lateral displacement of the real track centre line with respect to its designed features as depicted in Figure 2.11. Its main effects usually appears as lateral vibrations at the vehicle. Crooked rails, incorrect maintenance procedures or high lateral wheel-rail contact forces are the major culprit.
- **Track gauge:** It represent the difference between the nominal track gauge and the measured one in every single point of the track (See Fig.2.11). It has noticeable effect in vehicle lateral stability. Likewise, crooked rails, incorrect maintenance procedures or high lateral wheel-rail contact forces are once again its origin.

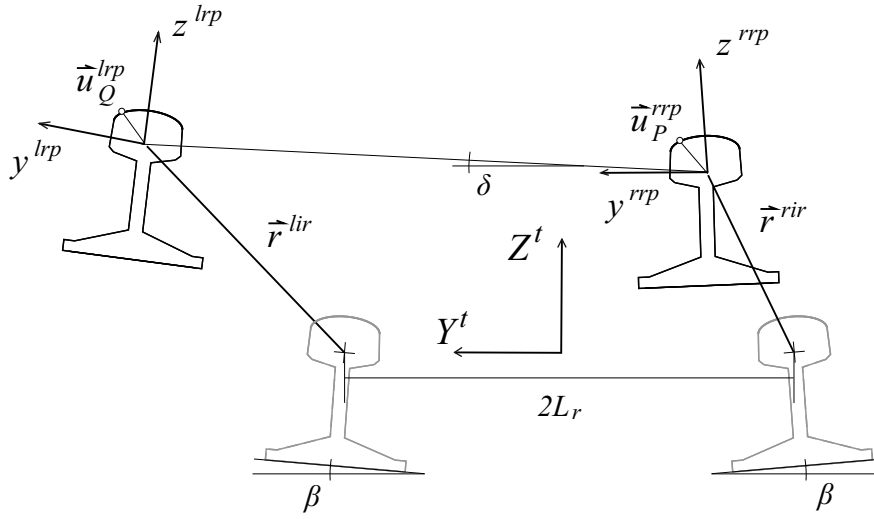


FIGURE 2.10: Track irregularities

- **Cross level:** It is defined as the relative vertical distance between left and right rails in an specific section of the track (See Fig. 2.12). It is mainly produced by track flexibility, excessive vehicle weights and thermal loads on the track. They have small effects on lateral vehicle dynamics.
- **Vertical profile:** It can be described as the difference of height between the reference track central line and the real track centre line. As in the previous phenomena, track flexibility, excessive vehicle weights and thermal loads on the track among others are its major causes.

Alignment and track gauge are considered horizontal track irregularities and cross level and vertical profile are vertical track irregularities. It is also important to note that alignment and vertical profile are absolute magnitudes while track gauge and cross level are relative magnitudes.

$$\begin{aligned}
 \text{Alignment} &= (y^{lir} + y^{rir})/2 \\
 \text{Gauge} &= (y^{lir} - y^{rir}) \\
 \text{Crosslevel} &= (z^{lir} - z^{rir}) \\
 \text{Verticalprofile} &= (z^{lir} - z^{rir})/2
 \end{aligned} \tag{2.1}$$

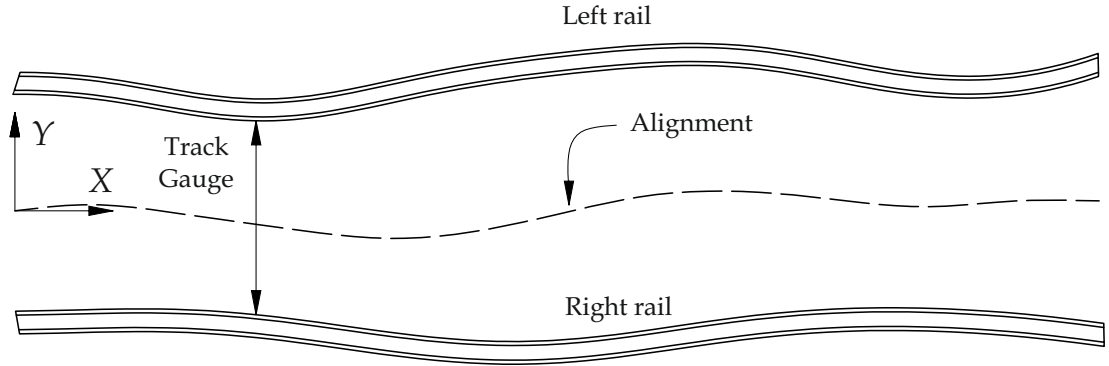


FIGURE 2.11: Irregularities of alignment and gauge variation

Finally, isolated track irregularities are the other form of track irregularity that can be found on the track. This form of track irregularity do not have to be underestimated since under certain conditions they can produce unsafe response in the vehicle. There is seven different kinds of analytical isolated defects listed as: Bump, cusp, plateau, jog, sinusoid, damped sinusoid and trough [41].

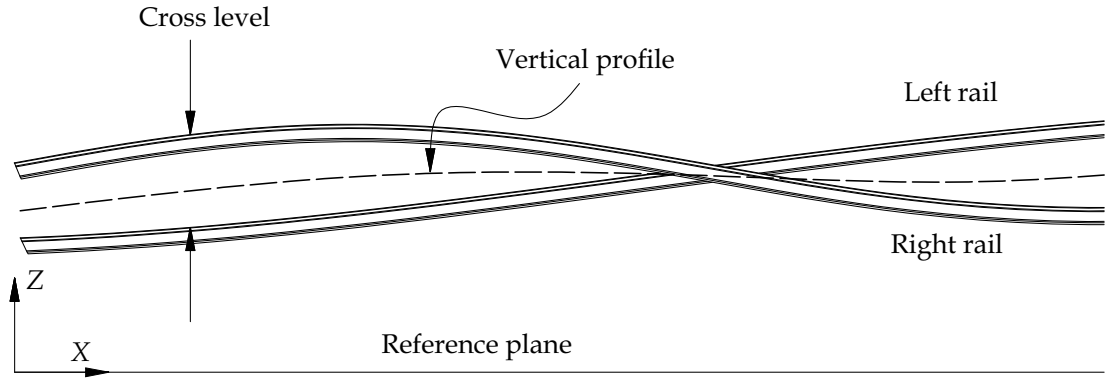


FIGURE 2.12: Irregularities of cross level and vertical profile

## 2.4 Experimental scaled track measurement

An ideal track geometry description and its irregularities have been presented in the previous sections. As it explained before, the main objective of this project is the experimental measurement of wheel-rail contact forces and its validation. For that purpose, a multibody model of the experimental scale vehicle has been developed. In addition to the correct definition of all the geometric, mass and inertial parameters

of the vehicle, it is equally important to introduce as a model input a precise track geometry definition. Thus, a highly precise track measurement has been carried out as part of this project. There is a lot of literature ([41], [98]) and standards about track measurement since it is a recurring task regularly done in the railways industry. However, not all of them can be directly applied to an scale track that is ten times smaller than a real one. For this reason, an alternative procedure has been developed in order to accomplish such important task.

### 2.4.1 Track centre line measurement

In a full scale track, the centre line is measured with the aid of a so-called track recording trolleys. Figure 2.13 shows one of this track measurement systems. As it can be seen, the trolley has one of its side faces fixed to one rail. A reflector is located over the trolley frame. So that the absolute rail position can be established with the aid of a *total station*. A distance measurement system and tilt sensor determine the track gauge and cant angle. A total station is an electronic instrument used in modern surveying and building construction that uses an electronic transit theodolite in conjunction with electronic distance meter. It is also integrated with a microprocessor, electronic data collector and storage system. The instrument is used to measure sloping distance of object to the instrument, horizontal angles and vertical angles.

Based on the design described above, a similar and equally effective equipment for an scaled track has been developed, with the feature that, track centre line is measured separately of track gauge and cant angle. This second part of the procedure will be explained in later sections. For the scale track centre line measurement, a high precision total station has been used. Not any kind of total station is suitable for such application, taking into account the small dimensions of the experimental scale track and the desirable expected precision. The machine selected is a Leica Nova MS50 (see Fig. 2.14) in combination with a high-precision 360° mini reflector. According to the supplier, the absolute device precision, provided good operation conditions, is between 0.2 to 0.5 mm. There is not other more precise device in the market based on interferometry. For smaller precisions a laser based system is required. This equipment is prohibitive in this project due to its extraordinary cost.



FIGURE 2.13: Track recording trolley

For the track centre line detection, fig 2.15 shows the designed elliptical plate meter designed. An ellipsoidal profile with 129.5 and 126 mm on its long and short semi-axis respectively has been machined on its base. An ellipse has the property that if it is placed in between two parallel lines and it contacts to both, the centre of the ellipse stays in the mid point of both lines (see Fig. 2.16). That means, if this elliptical plate is placed on the scale track and it contacts both rails, its centre will be always placed over the track centre line. The scenario where the elliptical plate is positioned in between two parallel lines is represented in fig. 2.16. But, what would happen if this plate is located between two constant curvature lines like the two rails in a constant curvature section of the track? This premise would not be valid unless the radius of curvature was large enough to despise its curvature against the scale track gauge. Considering that the track gauge is 127 mm and the minimum radius of curvature in the scaled track is 24 m, it can be accepted that the designed device will also work fine in curve sections. Figure 2.17 shows the current ellipsoidal plate meter used for the scale track centre line measurement. As it can be observed, the 360° mini-prism is screwed at its geometric centre.

The most important element of this centre line measuring system is the total station that has to be located at such point from where the reflector can be perfectly observed.



FIGURE 2.14: Total station Leica Nova MS50

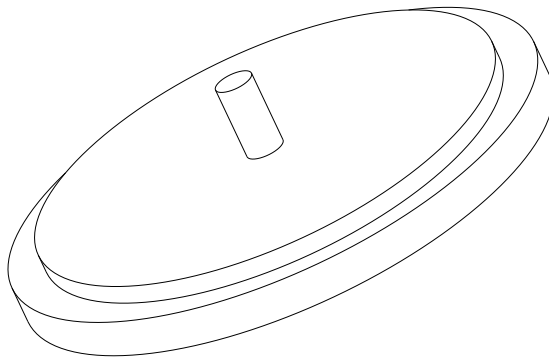


FIGURE 2.15: Track centre line elliptical plate meter

Given the almost 90 meter long scale track and its sinusoidal layout, the station can not be positioned in one single point and keep an eye on the reflector at the same time. It is also known that the precision of the measurement made by the total station is associated with its relative position to the target point. In addition, weather conditions also have a notorious influence in the measurement. Taking into account these external factors, several tests have been carried out before the scale track centre line is finally measured.

The first experiment performed was a distance-accuracy test. In this trial, a calibrated



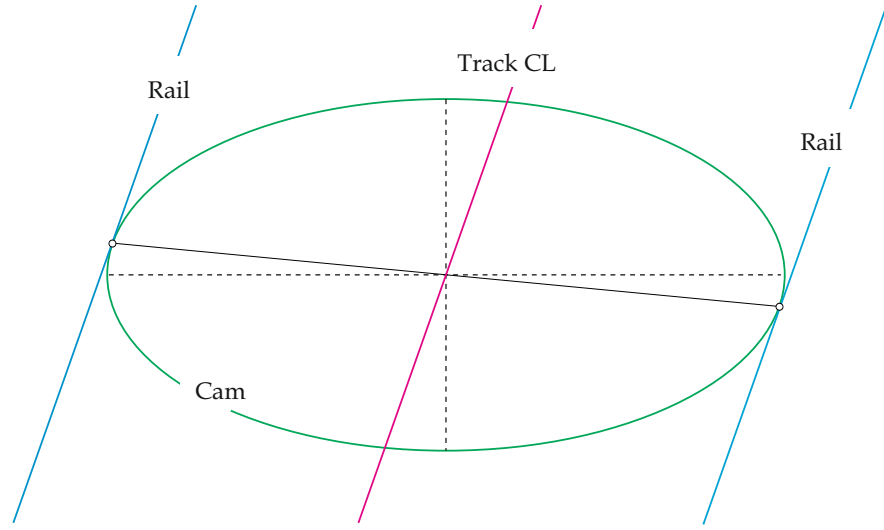


FIGURE 2.16: Ellipse self-centering property

rod with two threaded holes separated  $120 \pm 0.01$  mm where the mini-prism can be screwed, has been used. This bar has been placed in different positions, each of them further than the previous one. The distance between both holes has been measured in all these spots. Table 2.1 summarized the results obtained. In the light of them, a 15 meters range proves to be the most suitable gap between the total station and the track. Taking this into consideration, the total length of the track and the objects presents on the roof, the total station has to be placed in three different positions on the rooftop during the track measurement. That means, the centre line has to be measured in three sections, each of them with its own reference system that will be necessary to synchronize on a unique reference system located at the beginning of the track, having its X axis pointing to track centre line direction. This process will be explained in the next section.

TABLE 2.1: Target distance vs distance from the station

Distance (m)	Target length (mm)
5	120.4
15	120.2
25	120.5
60	98.1



FIGURE 2.17: Ellipsoidal plate meter placed on the track

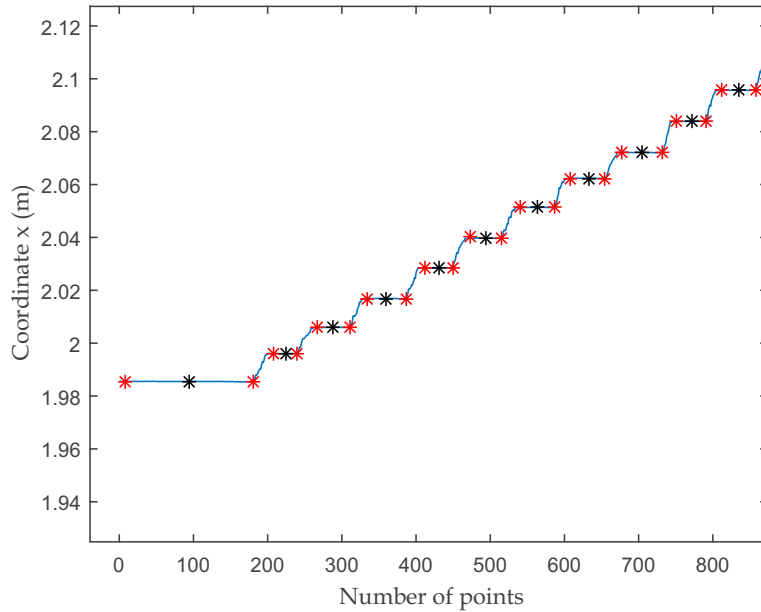
#### 2.4.1.1 Track centre line calculation algorithm

Once the equipment that is needed for the centre line measurement has been presented, in this section the algorithm used to determine the  $[x, y, z]$  coordinates of a centre line set of points is explained. First of all, the difference between the total station modes of operation must be established:

- **Discrete mode:** The station acquires the  $[x, y, z]$  coordinates of a single target point when the operator requests it.
- **Continuous mode:** By serial port communication with a computer, the station gets at a 20 Hz rate the  $[x, y, z]$  coordinates of the target points where the reflector is located.

In this case, the continuous mode has been selected. The absolute position of the reflector is continuously stored in the PC while the elliptical plate meter is moved along the track. This way, points are located alternatively over the sleepers and the

mid point between sleepers (separated 100 *mm*). According to Nyquist theorem, the minimum wave length noticeable in the track centre line will be 100 *mm* with the chosen space acquisition rate. Figure 2.18 shows coloured in blue the  $x$  coordinate measured by the total station before being processed by the centre line calculation algorithm. As it can be observed, it has an staircase shape where every flat region represents a point of the track centre line where the elliptical plate meter has been stopped during the measurement. During the measurement process the operator has to locate the elliptical plate over the rails and make it contact with them. Then the plate has to be moved in 50 *mm* steps. At each step the plate has to be static for a few second while the total station is acquiring its current position. The mentioned algorithm receives this information as input, not just the  $x$  coordinate but also the other two coordinates along the track and establish the indices of the measured vector among which the measurement has been stable for a few seconds. Red star points define the limits of this regions. Finally, the algorithm states the measured average value at each axis, obtaining as a result, the  $[x, y, z]$  coordinates of the track centre line.

FIGURE 2.18: Measured centre line coordinate  $x$ 

The mentioned algorithm, represents a fast way to calculate the track centre line from the data acquired by the total station, it also permits to detect any wrong measured

point and remove it from the set. Figure 2.19 shows the total station placed on the rooftop while the author moves the elliptical plate meter along the track centre line. The total station automatically follows the reflector and stores its position.



FIGURE 2.19: Scaled track centre line measuring process

#### 2.4.1.2 Data synchronization

As it has been mentioned before, the dimensions of the experimental track make it impossible to be measured in one go. The total station has to be placed in three different spots at the rooftop. That means, there will be three packages of track centre line coordinates, each of them with its own reference system. The following procedure has been developed to get the coordinates of the points referred to the same coordinate system. The track global coordinate system can be located in any point, but for the sake of simplicity it has been settled at the starting point of the track, having its  $X$  axis pointing along the track centre line.

Figure 2.20 helps to understand the synchronization process. Reference systems coloured in magenta, red and dark green are named:  $F_1 \equiv \langle O_1; X_1, Y_1, Z_1 \rangle$ ,  $F_2 \equiv \langle O_2; X_2, Y_2, Z_2 \rangle$  and  $F_3 \equiv \langle O_3; X_3, Y_3, Z_3 \rangle$  respectively. They represent the three

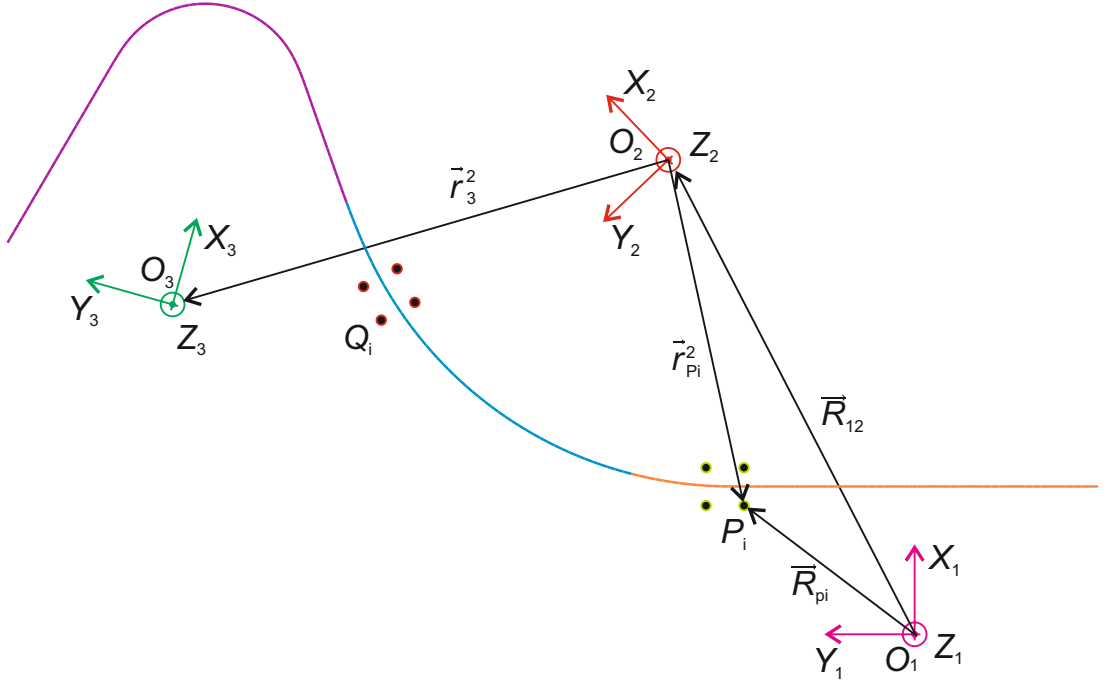


FIGURE 2.20: Scaled track centre line measuring process

positions at the rooftop where the total station has been located during the measuring process. Lines coloured in orange, blue and purple represent the three track sections independently measured. Points contained in the orange, blue and purple lines are expressed in reference systems  $F_1$ ,  $F_2$  and  $F_3$  respectively. To make section synchronization possible, two sets of points (coloured in black-green and black-red in Fig. 2.20) called synchronization points have been defined. These synchronization points are real points located in four calibrated bars distributed on the track and rigidly joined to the track supporting tables (see Fig. 2.21) where the elliptical meter plate can be precisely located.

#### 2.4.1.3 Synchronization procedure

Synchronization requires to find the position vector and orientation matrices of frames  $F_1$ ,  $F_2$  and  $F_3$ . The synchronization process consists in obtaining the coordinates of blue and purple track sections (see Fig. 2.20) in the  $F_1$  reference system. Thus, it is necessary to translate and rotate in a proper way this two sets of points. The first



FIGURE 2.21: Synchronization points on calibrated bars

step will be obtaining the absolute position vector  $\vec{\mathbf{R}}_{12}$  of the reference system  $F_2$  (the second spot where the station was located during the measuring process) expressed in reference system  $F_1$ . For that purpose, synchronization points set  $P_i$  has to be measured first from reference system  $F_1$  and then from  $F_2$ . They are the linkage between track sections orange and blue. Equation 2.2 states the vector relationship mentioned above. Equation 2.3 is the matrix form of eq. 2.2 where  $A^{1,2}$  is the rotation matrix from reference system  $F_2$  to  $F_1$ .

$$\vec{R}_{P_i} = \vec{R}_{12} + \vec{r}_{P_i}^2 \quad (2.2)$$

$$\mathbf{R}_{P_i} = \mathbf{R}_{12} + A^{1,2} \cdot \vec{r}_{P_i}^2 \quad (2.3)$$

$$A^{1,2} = A_{\psi}^{1,2} \cdot A_{\phi}^{1,2} \cdot A_{\theta}^{1,2} \quad (2.4)$$



$$\begin{aligned}
A_{\psi}^{1,2} &= \begin{bmatrix} \cos(\psi^{1,2}) & -\sin(\psi^{1,2}) & 0 \\ \sin(\psi^{1,2}) & \cos(\psi^{1,2}) & 0 \\ 0 & 0 & 1 \end{bmatrix} \\
A_{\psi}^{1,2} &= \begin{bmatrix} \cos(\psi^{1,2}) & -\sin(\psi^{1,2}) & 0 \\ \sin(\psi^{1,2}) & \cos(\psi^{1,2}) & 0 \\ 0 & 0 & 1 \end{bmatrix} \\
A_{\psi}^{1,2} &= \begin{bmatrix} \cos(\psi^{1,2}) & -\sin(\psi^{1,2}) & 0 \\ \sin(\psi^{1,2}) & \cos(\psi^{1,2}) & 0 \\ 0 & 0 & 1 \end{bmatrix}
\end{aligned} \tag{2.5}$$

Matrix expression 2.3 represents a three scalar equations with six unknown variables, where  $\mathbf{R}_{12} = [x_2, y_2, z_2]$  are the coordinates of  $F_2$  reference system origin and  $\phi_2^{1,2}$ ,  $\theta_2^{1,2}$  and  $\psi_2^{1,2}$  are its Euler orientation angles. Thus, a priori, measuring just two synchronization points from  $F_1$  and the same two points from  $F_2$  would be enough to find the position and orientation of reference system  $F_2$  with respect to  $F_1$ . However, a total of twelve synchronization points have been measured from each position of the station. The resulting set of equations is over determined and they can be solved using least squares method.

Once vector  $\mathbf{R}_{12}$  and matrix  $A^{1,2}$  have been determined, track blue section coordinates can be easily transformed from reference system  $F_2$  to reference system  $F_1$  by means of eq. 2.6, where  $\mathbf{R}_{S_i^2}$  represents coordinate vector of an arbitrary point of blue track centre line expressed in reference system  $F_1$  and  $\bar{r}_{S_i^2}^2$  is that same coordinate vector expressed in reference system  $F_2$ .

$$\mathbf{R}_{S_i^2} = \mathbf{R}_{12} + A^{2,1} \bar{r}_{S_i^2}^2 \tag{2.6}$$

This procedure can be equally applied to transform purple track centre line section coordinates from reference system  $F_3$  to reference system  $F_1$ . In this case, it is necessary to do an intermediate transformation from reference system  $F_3$  to  $F_2$  and finally from  $F_2$  to  $F_1$  as explained above. Synchronization points  $Q_i$  set has to be used to determine

$F_3$  coordinates and orientation angles expressed in  $F_2$ . Equation 2.7 summarizes this procedure, where  $\mathbf{R}_{S_i^3}$  are purple track centre line coordinates expressed in reference system  $F_1$ ,  $\bar{r}_{O_3}^2$  are the coordinates of reference system  $F_3$  expressed in  $F_2$ ,  $A^{1,3}$  is the orientation matrix from  $F_3$  to  $F_1$  and  $\bar{r}_{S_i^3}^3$  are the purple track centre line coordinates expressed in  $F_3$ .

$$\mathbf{R}_{S_i^3} = \mathbf{R}_{12} + A^{2,1} \cdot \bar{r}_{O_3}^2 + A^{3,1} \cdot \bar{r}_{S_i^3}^3 \quad (2.7)$$

As conclusion of this section, Figures 2.22 and 2.23 show the final track centre line obtained after the synchronization process. As it can be seen, there is a notorious difference between the expected and finally obtained track centre line. For this reason, a later optimization process have to be accomplished for the measuring of track centre line to obtain the ideal geometry that fits better with the measured one. The geometry optimization process will be treated in a later section of this chapter.

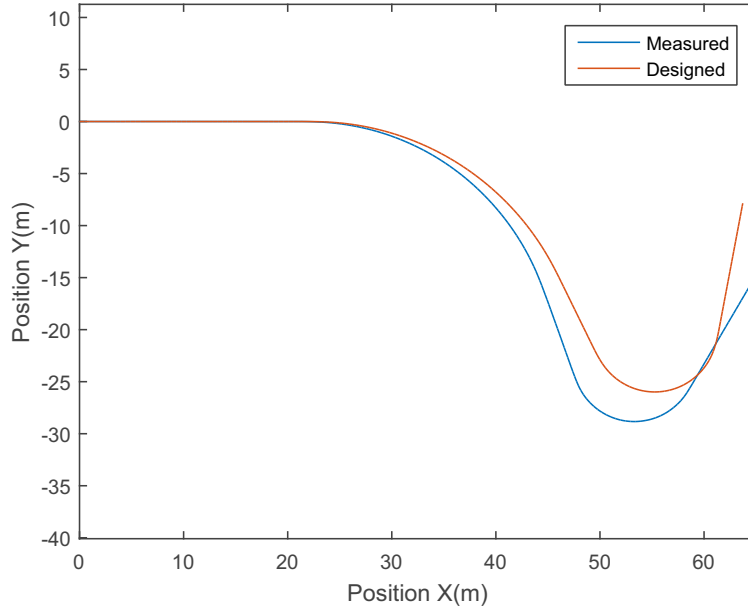


FIGURE 2.22: Measured track centre line vs designed track centre line



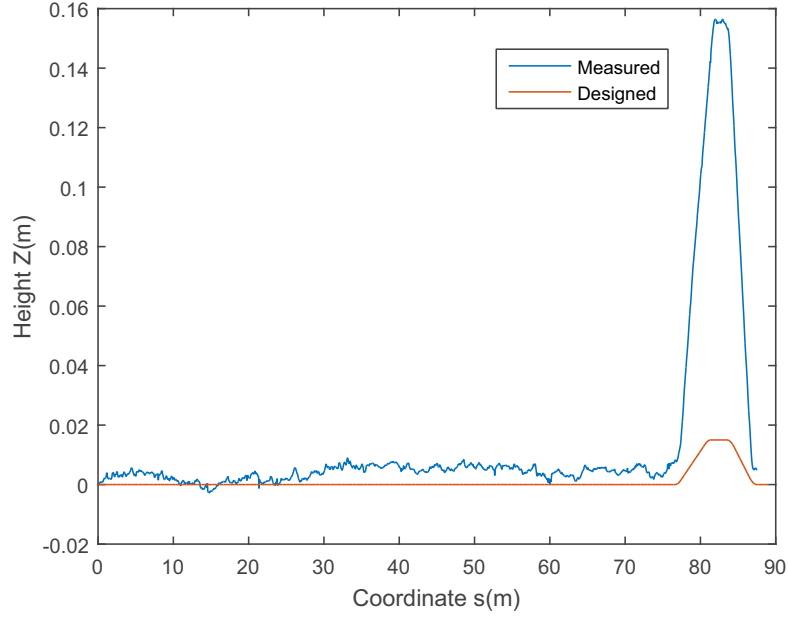


FIGURE 2.23: Measured track height vs designed track height

#### 2.4.2 Measurement of track gauge and cant angle

Once the scale track centre line has been properly measured, track gauges and cant angles should be measured to conclude track measurement. This final step prove to be simpler since it is not necessary to use the total station nor transform any coordinates. To measured track gauge and cant angle a novel device has been designed and manufactured (see fig 2.24). Measurer main two elements are a high-precision Linear Variable Differential Transformer (LVDT) and a high-precision inclinometer. On the one hand, Schreiber SM34 LVDT has a  $10mm$  total stroke and  $0.05\text{ mm}$  accuracy. On the other hand, TSC-22-10 dual-axis tilt sensor, has a measuring range of  $\pm 10^\circ$  and  $\pm 0.01^\circ$  resolution.

Figure 2.25 shows the final assembly of the meter device. Its performance is simple. Distance and tilt sensors are rigidly joined to the central bar which lies over the to rails. The angle part located under the bar, keep the bar perpendicular to one of the rails and the slider, pushed by LVDT inner spring, keeps in touch with the opposite rail. Thus, when the ruler is moved along the track by an operator, track gauge and cant

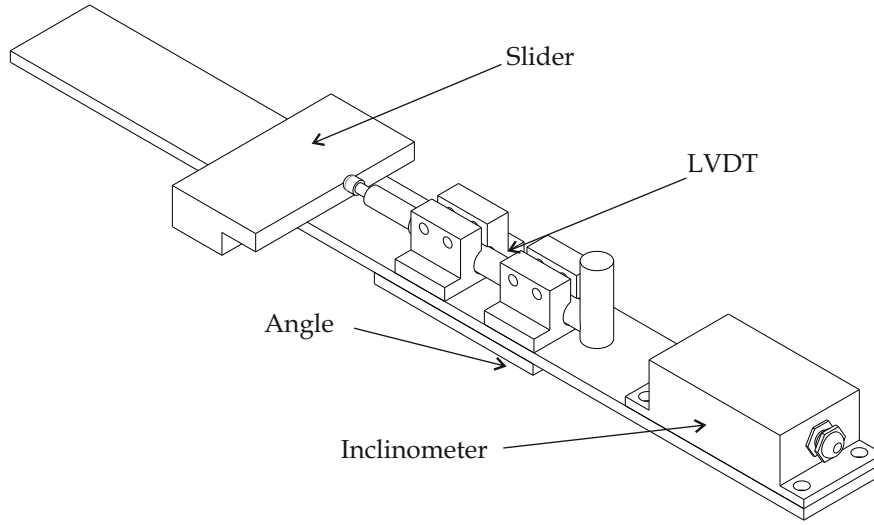


FIGURE 2.24: Track gauge and cant angle meter

angle are simultaneously measured. Figure 2.26 shows the track gauge and cant angle measuring procedure. As it was done with track centre line, gauge and tilt have been measured every  $50\text{ mm}$  along the track. It is important to note that the LVDT, unlike the tilt sensor, makes a relative measurement of track gauge. In fact, what LVDT is registering are gauge variations between measured spots on the track. Hence, a Vernier calliper must be used to measure a first track gauge and obtain the followings gauges from LVDT gauge variation measurement.

Figures 2.27 and 2.28 show measured track gauges and cant angles on the track. As it can be observed in Fig. 2.27 is about  $128\text{ mm}$  and differs from the expected  $127\text{ mm}$  designed track gauge. Inaccuracies made during the scale track assembly process are responsible for this phenomena. Figure 2.28 shows the tilt angle along the track. As it can be seen, tilt angle is not close to 0 between  $s = 21\text{ m}$  and  $s = 50\text{ m}$  that correspond with first curve section, and between  $s = 60\text{ m}$  and  $s = 75\text{ m}$  corresponding to the second curve section. In this two sections cant angle mean values are  $0.5^\circ$  and  $2.2^\circ$  respectively. They are the cant angle values that compensates the centrifugal force in the vehicle while moving at  $1.5\text{ m/s}$  along the curve. Expression 2.8 states the exact cant angle that eliminates the centrifugal effect on the vehicle, where  $V$  is the forward velocity,  $g$  is the constant of gravity and  $R$  is the curve radius.



FIGURE 2.25: Track gauge and cant angle meter final assembly

$$\alpha = \arcsin\left(\frac{V^2}{gR^2}\right) \quad (2.8)$$

## 2.5 Track geometry optimization

As explained in previous section, the final scale track geometry differs substantially from the design specifications listed in Section 2.2 and depicted in fig 2.22 and 2.23. Therefore, the ideal track geometry, that is the combination of straight sections, transitions and curves, that best fits with the measured scale track geometry has to be determined. To this end, an optimization algorithm has been developed. The algorithm, takes an initial estimation of the track geometry as input and optimizes its parameters until obtaining a good agreement with the measured geometry. On the hand, in the horizontal plane, these parameters are: the starting coordinate  $s$  of each section, radius of curvatures and cant heights. On the other hand, in the vertical plane optimized parameters are: the starting coordinate  $s$ , transition radius of curvature and initial slopes.



FIGURE 2.26: Track gauge and cant angle measuring procedure

Table 2.2 shows an example of horizontal track centre line definition parameters. First column is the coordinate  $s$  where each track section starts. There are three possible types of sections designated by numbers 1, 2 and 3 for tangent, transition and constant curvature sections respectively. In this example a 35 m long horizontal track is defined. It has a 10 m long tangent section followed by a 5 m long transition which curvature varies from  $0 \text{ m}^{-1}$  to  $0.1 \text{ m}^{-1}$ . After that, there is a 10 m long constant  $0.1 \text{ m}^{-1}$  curvature section and 0.001 m cant height, followed by a 10 m long transition section that goes progressively from the previously defined curvature to  $0 \text{ m}^{-1}$ . A final 10 m long tangent track is defined.

Vertical profile track definition is expressed in similar manner. Table 2.3 shows the vertical profile definition parameters of the same example track mentioned above. First column is newly the starting coordinate of each section (as explained in section 2.2 there are two kind of sections in the track vertical profile definition), second column is the radius of curvature of the transition that connect two constant slope section and the last column is the initial slope of the section.

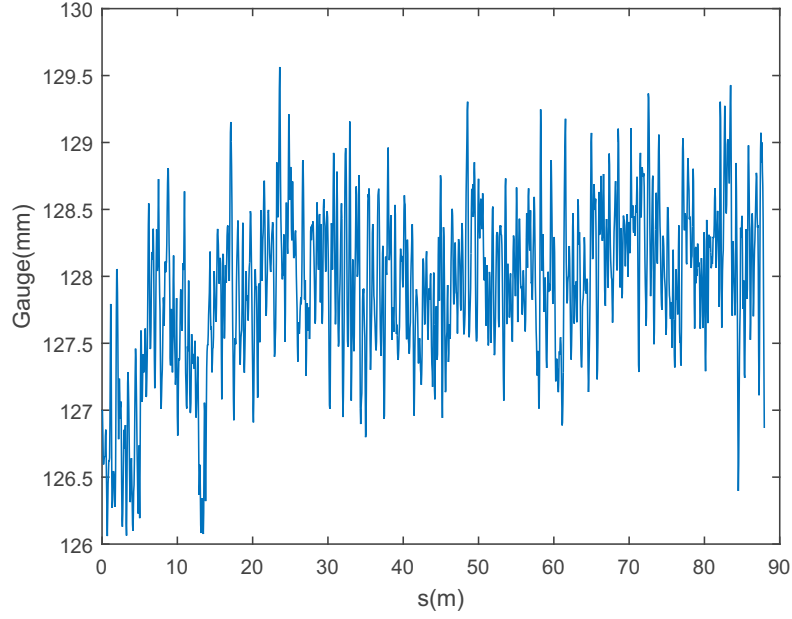


FIGURE 2.27: Measured track gauges

TABLE 2.2: Horizontal track definition input parameters example

s (m)	Section (-)	Curvature (1/m)	Cant (m)
0	1	0.0	0.0
10	2	0.0	0.0
15	3	0.1	0.001
25	2	0.1	0.0
35	1	0.0	0.0
45	1	0.0	0.0

The geometry optimization algorithm is based on the so-called *track preprocessor*. It is a software, that frequently accompanies any railways simulation programme and generates all track information needed for the multibody simulation. It operates in a preliminary phase before the dynamic simulation, and its results can be utilized by the simulation software any time during the integration process and later post processing phase. By using a track preprocessor, simulations become more efficient. The preprocessor calculates in a phase previous to the simulation lots of parameters such as track

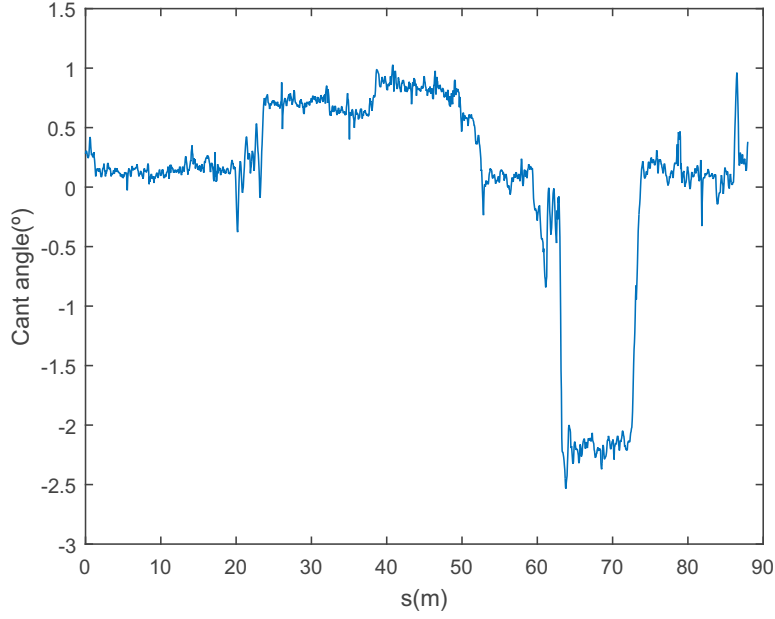


FIGURE 2.28: Measured track cant angles

TABLE 2.3: Vertical track definition input parameters example

s (m)	Curvature (m)	Slope (rad)
0	0.0	0.0
10	10.0	0.005
20	-10.0	0.0
30	-10.0	-0.005
40	10.0	0.0
45	0.0	0.0

centre line coordinates, track frame orientation matrices and track centre line tangent and normal vectors among others.

The track pre-processor used in this project was developed by the research group and it is entirely programmed in Matlab. It takes as input a text file with an specific structure as explained with tables 2.2 and 2.3 and all necessary parameters for track geometry description.

The track geometry optimization algorithm, calculates at each step the mean squared quadratic error of ideal and measured track geometry and modifies the parameters mentioned before to minimize that error. Actually, for the sake of simplicity and computer efficiency, the optimization is accomplished in two phases. First, the horizontal profile is optimized and after it, the vertical profile. Expression 2.9 estates the mentioned squared quadratic error where  $\mathbf{R}_i^{ideal}$  and  $\mathbf{R}_i^{measured}$  represent the  $(x, y, z)$  coordinates of the ideal and measured track centre line respectively. The number of points  $n$  utilized depends on the chosen track centre line discretization. Figures 2.29 and 2.30 show the optimized track centre line and heights resulting from the optimization algorithm. Tables 2.4, 2.5, 2.6 and 2.7 show initial and final values of the optimized parameters. As it can be seen, the optimized solution for the vertical profile (see Table 2.7) has more sections than the vertical profile initially estimated (see Table 2.6). That is because the track centre line optimization algorithm can find in this solution a better agreement with the measure done on the track. Figure 2.31 shows the different tangent, transition and curve sections that compound the optimized scale track geometry.

$$MSE = \frac{1}{n} \sum_{i=1}^n (\mathbf{R}_i^{ideal} - \mathbf{R}_i^{measured})^T (\mathbf{R}_i^{ideal} - \mathbf{R}_i^{measured}) \quad (2.9)$$

## 2.6 Calculation of track irregularities

After the scale track centre line has been measured and its ideal geometry has been found, the track irregularities calculation can be accomplished. As explained in Section 2.3 the difference between the measured and ideal geometry constitutes the so-called track irregularities. In this section, irregularities of alignment, gauge, cross level and vertical profile will be determined. Based on them, rails current position with respect to their ideal position will be calculated. System of equations 2.1 shows the relationship between these mentioned irregularities and the irregularity vector components  $y^{lir}$ ,  $z^{lir}$ ,  $y^{rir}$  and  $z^{rir}$  (see Fig 2.10).

Gauge and cross level irregularities can be easily obtained from the measurements made with the LVDT and the inclinometer (See Subsection 2.4.2). Gauge is defined as the

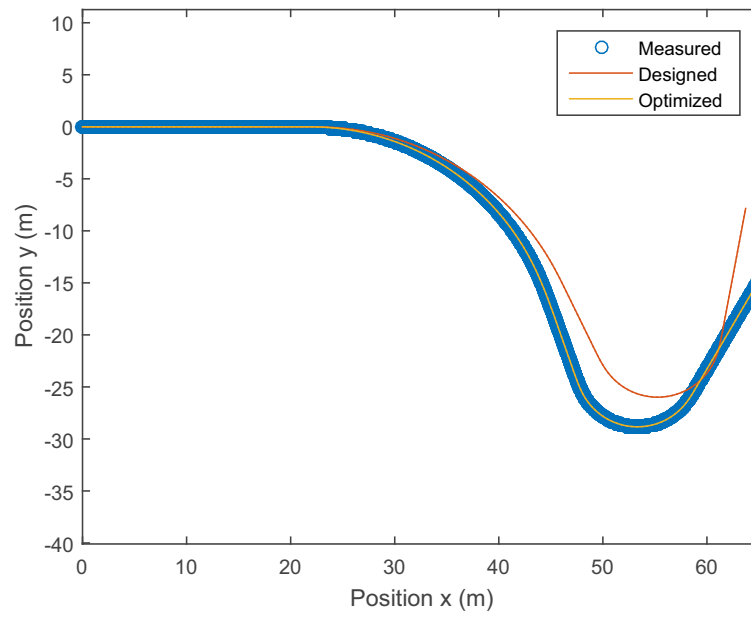


FIGURE 2.29: Measured, optimized and initial estimation track centre lines

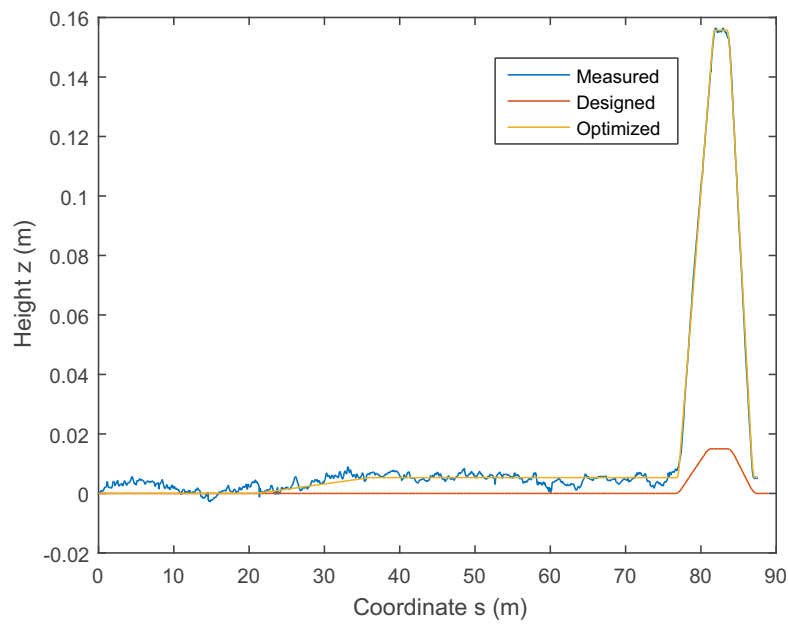


FIGURE 2.30: Measured, optimized and initial estimation track centre line heights



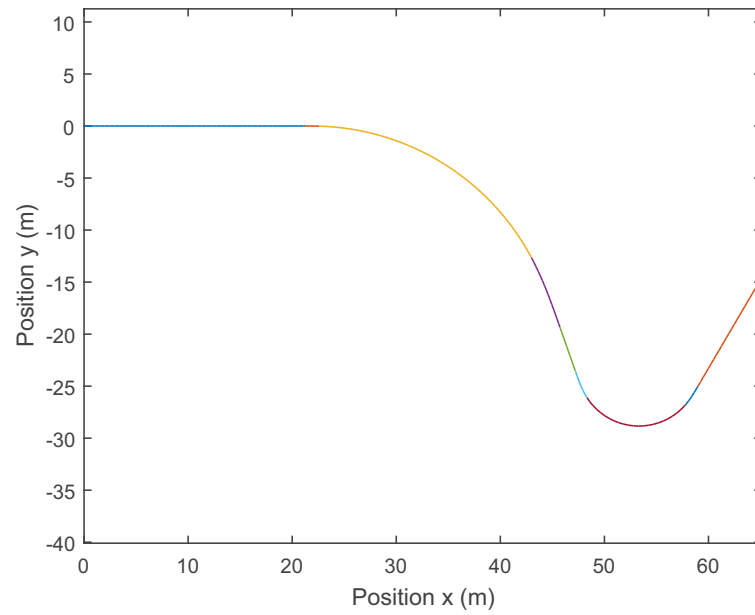


FIGURE 2.31: Track sections

TABLE 2.4: Horizontal optimization parameters initial estimation

s (m)	Curvature (1/m)	Cant (mm)
0	0.0	0.0
21	0.0	0.0
24	-0.0385	1.3
50	-0.0385	0.0
53	0.0	0.0
59	0.167	0.0
62	0.167	5.18
74	0.0	0.0
77	0.0	0.0
89	0.0	0.0

difference between real track gauge and its nominal value. In order to obtain a more reasonable value of gauge irregularity, the  $127.9 \text{ mm}$  mean track gauge value measured by the LVDT is going to be considered as nominal scale track gauge. Figure 2.32 shows the obtained track gauge irregularity. For the cross level calculation, observing fig 2.33, it can be seen that superelevation value named as  $h$ , is given by equation 2.10.

$$h = \sin(\alpha_{Inc}) \cdot d_{LVDT} \quad (2.10)$$

Where  $\alpha_{Inc}$  is the measured tilt angle and  $d_{LVDT}$  is the measured track gauge.

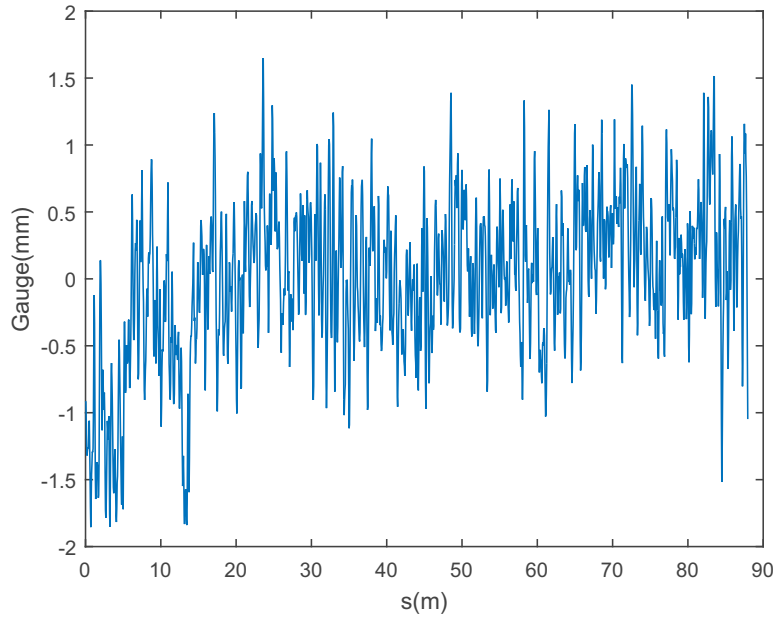


FIGURE 2.32: Gauge track irregularity

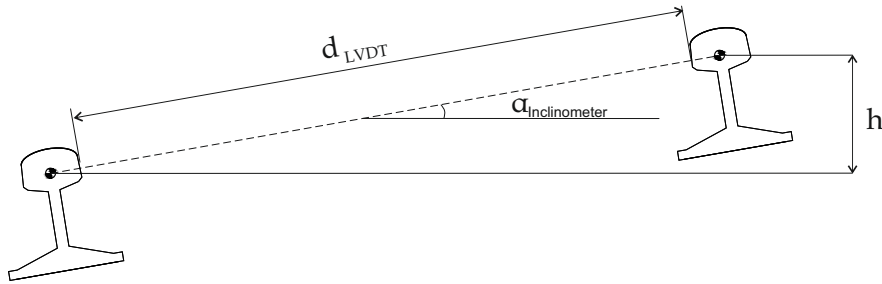


FIGURE 2.33: Track cant angle

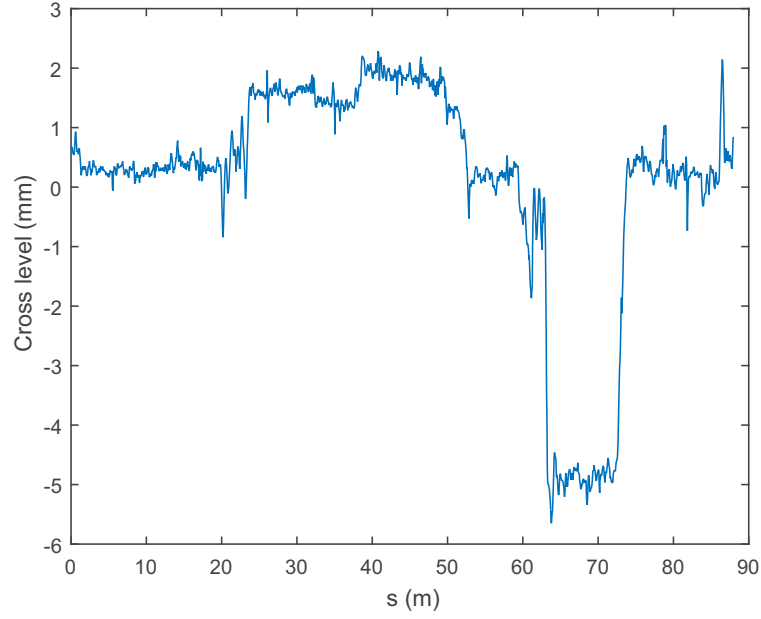


FIGURE 2.34: Cross level track irregularity

Alignment and vertical profile irregularities can not be obtained in such a direct way. The process needed to obtain these last two irregularities starts by determining the minimum distance between every track centre line measured point and the optimized track centre line. For that purpose, the track pre-processor is once again an useful tool. Let's see fig 2.35. Point  $P_i$  represent a measured real point on the track. Point  $Q_i$  could be any point belonging to the optimized track centre line. The minimum distance between both points will be the modulus of vector  $\vec{d}$ . Its components can be determined by expression 2.11, where  $\vec{R}_{Q_i}$  is the absolute position on one point of the optimized track centre line and  $\vec{R}_{P_i}$  is the absolute position of the measured point. Let define  $\vec{t}_{Q_i}$  as the tangent vector to the scale track ideal centre line at point  $Q_i$ . If vector  $\vec{d}$  is such minimum distance, it has to be perpendicular to  $\vec{t}_{Q_i}$ . Thus, equation 2.12 has to be fulfilled. The process concludes projecting vector  $\vec{d}$  on the track reference frame according to eq. 2.13. Second and third components of vector  $r^{irr}$  are the irregularities of alignment and vertical profile respectively (see fig 2.36 and 2.37). Once the four track irregularities have been determined, system of equations (2.1) can now be solved to obtain the irregularity vector components  $y^{lir}$ ,  $z^{lir}$ ,  $y^{rir}$  and  $z^{rir}$  (see fig 2.38 - 2.39). This components of track irregularities will constitute the input irregularity vector for

the multibody scale railway model developed in this project.

$$\vec{d} = \vec{R}_{Q_i} - \vec{R}_{P_i} \quad (2.11)$$

$$\vec{d} \cdot \vec{t}_{Q_i} = 0 \quad (2.12)$$

$$r^{irr} = (\mathbf{A}^t)^T \mathbf{d} \quad (2.13)$$

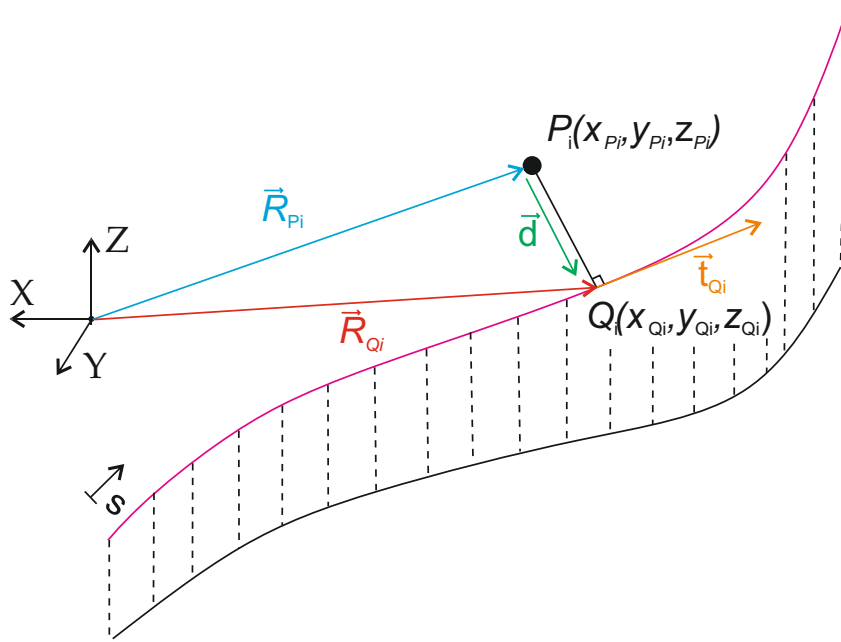


FIGURE 2.35: Alignment and vertical profile calculation procedure

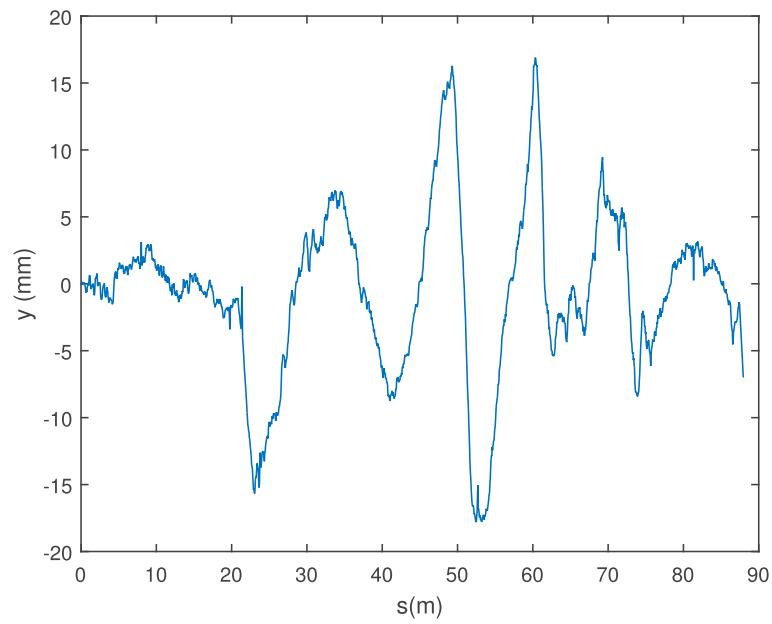


FIGURE 2.36: Alignment track irregularity

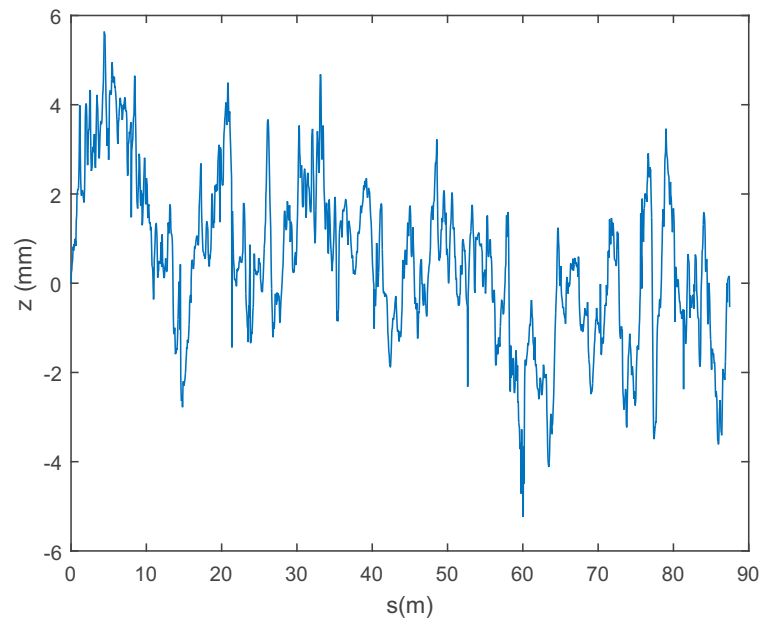


FIGURE 2.37: Vertical profile track irregularity

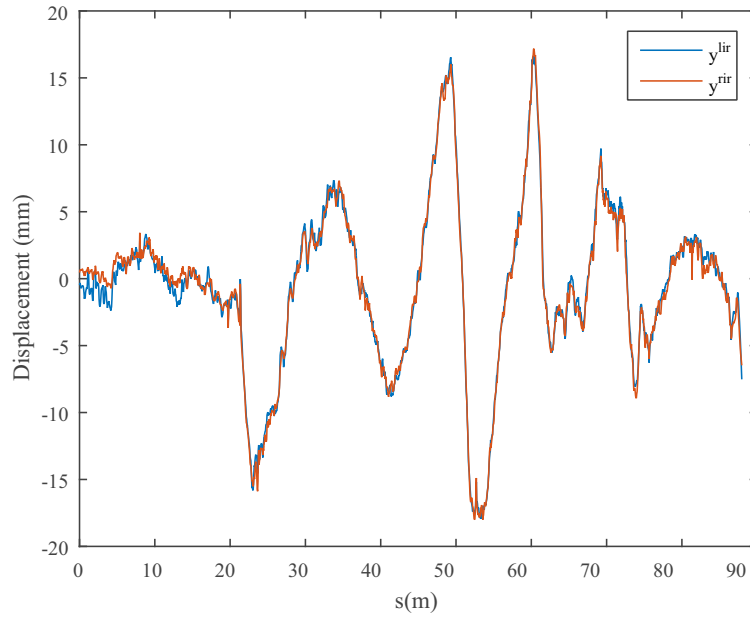
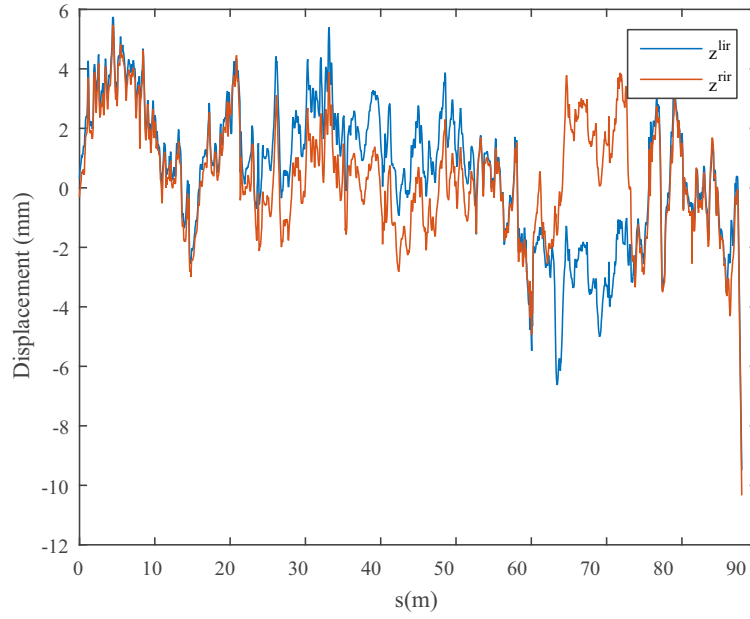
FIGURE 2.38: Component  $y^{lir}$  and  $y^{rir}$  of track irregularityFIGURE 2.39: Component  $z^{lir}$  and  $z^{rir}$  of track irregularity

TABLE 2.5: Optimized horizontal parameters

<b>s (m)</b>	<b>Curvature (1/m)</b>	<b>Cant (mm)</b>
0	0.0	0.0
21.235	0.0	0.0
22.593	-0.0419	1.3
47.732	-0.0419	0.0
54.990	0.0	0.0
59.473	0.169	0.0
62.239	0.169	5.18
73.228	0.0	0.0
75.397	0.0	0.0
89.957	0.0	0.0

TABLE 2.6: Vertical optimization parameters initial estimation

<b>s (m)</b>	<b>Transition radius (m)</b>	<b>Slope (rad)</b>
0	0.0	0.0
77.0	200.0	0.00375
81.0	-200.0	0.0
84.0	-200.0	-0.005
87.0	200.0	0.0
89.0	0.0	0.0

TABLE 2.7: Optimized vertical parameters

s (m)	Transition radius (m)	Slope (rad)
0	0.0	0.0
20.9	10.0	0.00035
36.1	0.0	0.0
77.0	10.4	0.032
81.7	-10.0	0.0
83.7	-10.5	-0.047
86.9	10.0	0.0
87.5	0.0	0.0



## Chapter 3

# Scaled Dynamometric Wheelset: Strain Gauges Method

### 3.1 Dynamometric wheelsets

In railways industry, the measured values of wheel-rail contact forces during vehicles operation is considered as information of incalculable value for any railway vehicle manufacturer or operating company. It is well known that wheel-rail contact forces are highly related to vehicle safety, ride comfort and track maintenance periods. Throughout modern railway history several approaches for measuring the wheel-rail contact force experimental have been carried out. Some of them are focus on the indirect contact force measurement as in [99], where inertial sensors located at the bearing boxes in conjunction with other sensors installed on the vehicle, are utilised to estimated the wheel-rail contact force from the dynamic response of the vehicle. These methods obviously need a precise dynamic model that reproduces the vehicle response in interaction with the track. On the other hand, methods based on the direct measurement of wheel-rail contact forces can also be found in the literature. They are based on the use of the so-called dynamometric wheelsets, non conventional wheelsets equipped with numerous sensors that make possible the direct measurement of the wheel-rail contact forces as explained for instance in [73] and [100].

Dynamometric wheelsets are a rare equipment for an ordinary railway vehicle. They are expensive, difficult to manufacture and complex to put into operation. They also require a sophisticated calibration process where an unequivocal relation between input forces and sensor outputs has to be established.

As mentioned in previous chapters, the main purpose of this PhD thesis is the experimental measurement of wheel-rail contact forces in a scaled railway vehicle designed and built by the Department of Mechanical and Manufacturing Engineering of the University of Seville. The scaling strategy followed on the scaled vehicle design process can be found in [82]. The reduced dimensions of the actual vehicle make the contact force measuring process even more difficult than in a full scaled vehicle. Although the current dynamic behaviour of the scaled vehicle is not representative of a full-scale one due to the great reduction in size, the contact measurement techniques shown in this PhD thesis can be extended to real vehicles meanwhile an equivalent calibration procedure to the one explained next was followed. To the author best knowledge, there are non existing precedents of this peculiar task in the scientific literature. In this third chapter, the design, manufacturing and calibration process of an scaled dynamometric wheelset instrumented with strain gauges is going to be covered. The algorithm needed to measure the wheel/rail contact forces from the sensors measurement is also discussed.

## 3.2 Design of the scaled dynamometric wheelset

In this section and on the following ones, the procedure of design, manufacturing and instrumentation is going to be explained. Figure 3.1 shows the original design of one of the two bogies that form the scaled vehicle [82]. To obtain the desired dynamometric wheelset, one of these axes has to be removed from the vehicle, it has to be equipped with sensors to measure the forces applied on the wheels, and subjected to a high precision calibration process.

As it can be observed, the reduced dimensions of the wheel (just 37.75 mm of nominal radius<sup>1</sup>) and its solid body make really difficult to execute any action on it. Firstly,

---

<sup>1</sup>Nominal radius: is the wheel rolling radius when the wheelset is centred on the track

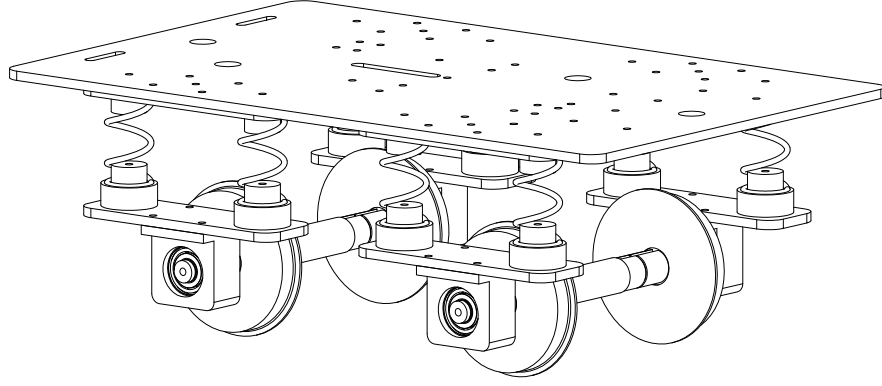


FIGURE 3.1: Original Scaled Bogie Design

because there is not enough space to install any sensor on the wheel web or the bearing box, and secondly, because even being able to install such sensors, the solid construction of the wheel makes the potential magnitudes to be measured (like wheel web deformations or lateral deflections) derisory. For this reason a redesign of the scaled wheelsets and their bearing boxes has been accomplished. The goal was to obtain a new geometry with larger and more slender wheels, making easy the installation of contact force measurement sensors.

Figure 3.2 shows the original and new design of the scaled wheel. The size difference can be observed. The new design has been machined in marine stainless steel in order to avoid corrosion and minimizing wear. Apart of the change in the nominal radius (now  $63.5 \text{ mm}$ ), the second big difference between both designs is the wheel cross section. As it can be seen in Fig. 3.3, the new scaled wheel cross section has a thinner wheel web with just  $2 \text{ mm}$  of thickness. Wheel conicity has also been increased from  $\lambda^w = 1/30$  to  $1/10$ , keeping the flange angle of attack of  $75^\circ$ . The new total tread length is  $12 \text{ mm}$  wide, that allows bigger lateral displacement of the axle on the rails before flange contact occurs.

The evolution of the scaled wheel design has been the result of a finite elements analysis with ANSYS Multi Physics where different wheel geometries and thickness have been simulated. The goal was to obtain such a geometry where the radial strains and lateral deflections on the wheel-web were large enough to be measured by industrial sensors. Thanks to this new design presented above, there is more available space to install sensors on the wheel and also bigger deformations and lateral deflections on the wheel

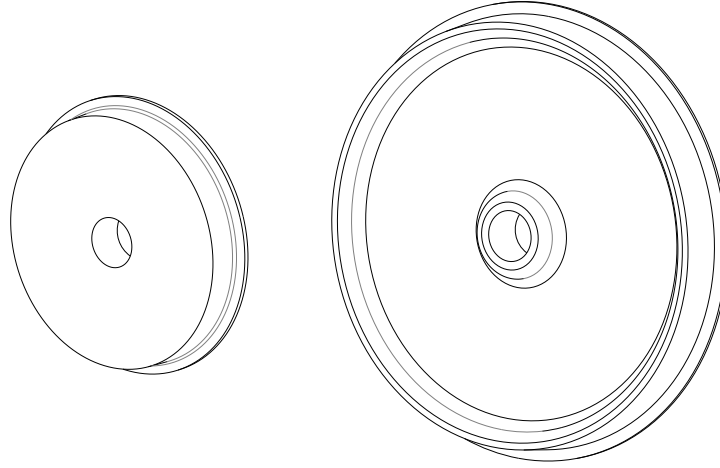


FIGURE 3.2: Original (left) and new(right) scaled Wheel

when forces are applied on it. The final assembly of the redesigned bogie is shown in Fig. 3.6.

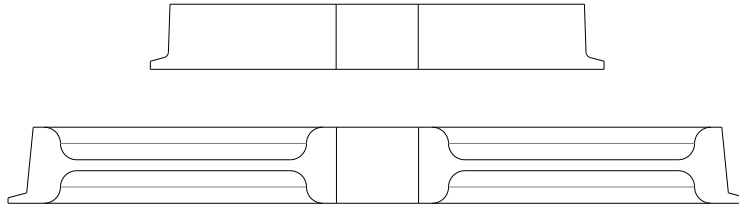


FIGURE 3.3: Original (up) and New (down) Scaled Wheel Section

Figure 3.4 shows the 3D models developed in ANSYS. Two separate FEM have been modelled: one single wheel and a complete wheelset. The complete wheelset model was originally used to evaluate the wheels radial strains distribution and lateral deflections in both wheels when different loads applied on them. As it is known, the large number of elements that form the model make it less efficient. For this reason a simplified single wheel model was created later. The FEMs are the perfect scenario to estimate the radial strains and lateral deflections that will appear on the wheels when running on the real

track. The FEM are used to select the most suitable sensors and its positions on the wheelset for the measurement of the wheel/rail contact forces. The type of element selected to build the model is *SOLID185*, defined by eight nodes with three degree of freedom at each node. This type of element proves to be suitable for 3D modelling of solid structures, apart of been computationally efficient. A convergence analysis has been carried out to determine the most efficient size of element. A  $600\ \mu\text{m}$  element size has been finally established resulting in a 1.98 million element model.

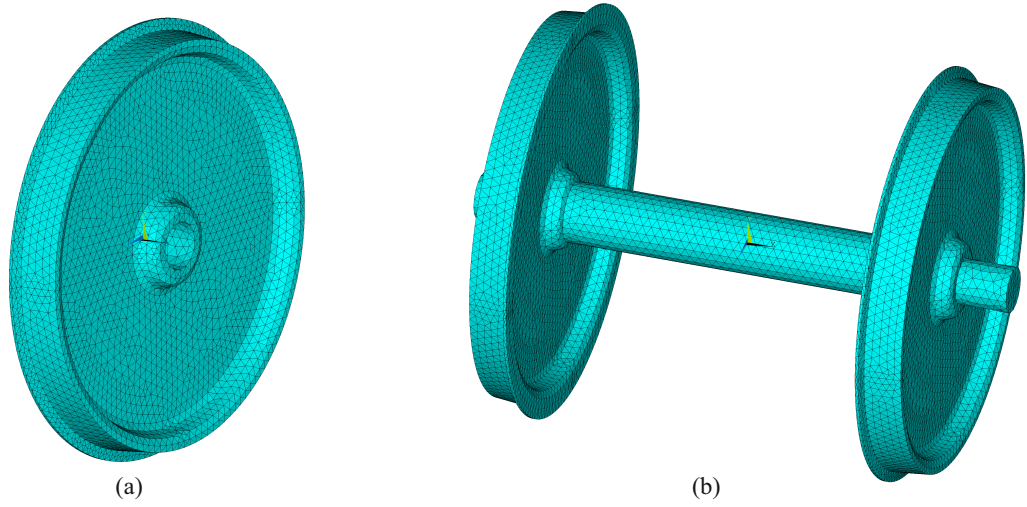


FIGURE 3.4: ANSYS Finite Elements Model

Figure 3.5 shows the deformed cross-sections of the scaled wheel using four different size of element. The wheel has been subjected to a  $100\ \text{N}$  normal load and a  $150\ \text{N}$  lateral. As it can be observed, the lateral deflections tend to be stable for element size of  $0.6\ \text{mm}$ , showing a variation smaller than 2.5% with respect to a finest  $0.4\ \text{mm}$  model. Table 3.1 shows a quantitative comparative between the four mentioned cases of analysis. Simulations have been carried out in an Intel Core i7-4930K CPU @  $3.40\ \text{GHz}$ ,  $3701\ \text{MHz}$  and 6 cores. After several trials the  $0.6\ \text{mm}$  element size results to be the most efficient without loss of precision.

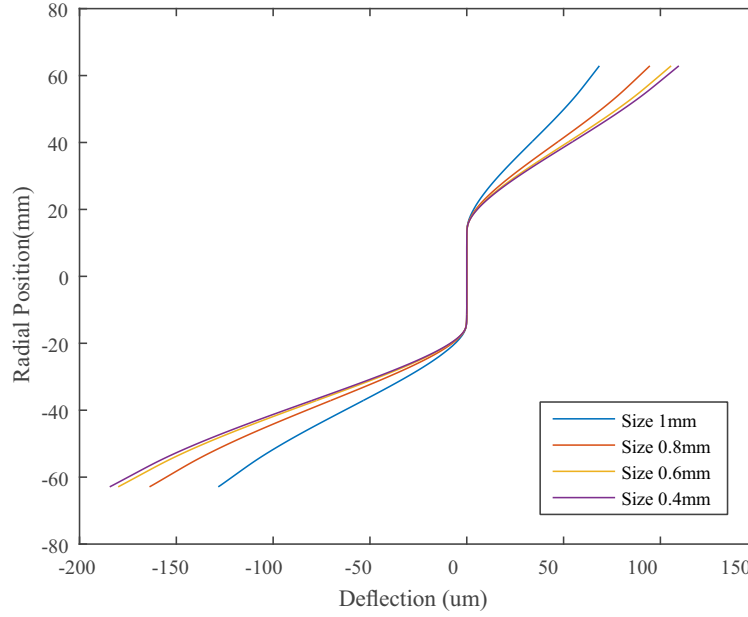


FIGURE 3.5: FEM Element Size Analysis

TABLE 3.1: FEM Convergence and Efficiency Analysis

Size (mm)	Elements (Million)	Max. Displ ( $\mu\text{m}$ )	Comp. Time (s)
1.0	0.42	128.3	45
0.8	0.87	163.9	62
0.6	1.98	180.0	366
0.4	6.20	184.0	1560

### 3.2.1 Instrumentation of the scaled dynamometric wheelset with strain gauges

The instrumentation of a full scale dynamometric wheelset normally represent a great challenge for engineers. Different strategies for the instrumentation of a dynamometric wheelset can be found in the literature. The most common are two: the use of strain gauges to measure radial strains on the wheel-web [100] and the use of non-contact sensors to measure the lateral deflection experienced by the wheels [73]. In this PhD thesis both technologies are going to be used for the instrumentation of the scaled

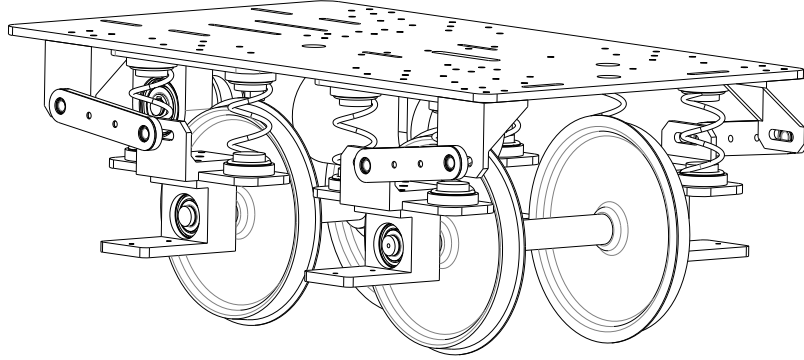


FIGURE 3.6: New scaled bogie design

dynamometric wheelset. The goal is to compare the force results obtained with both technologies and to determine the most suitable for such application. In this chapter the strain gauges approach is discussed, leaving the non-contact sensors approach for Chapter 4.

Dynamometric wheelsets based on strain gauge technology are the most commonly found in the literature. Despite being a straightforward method to measure wheel-rail contact forces, they have some disadvantages. First, strain gauges are delicate sensors that require a careful use and precise installation. Second, their life is limited and they have to be replaced regularly to guarantee the correct operation of the dynamometric wheelset. However, the data transmission represents the main challenge. Strain gauges should be installed in the axle or the wheel-web itself, taking into account that the wheelset is rolling, wire communication between sensors and data acquisition equipments is not a valid solution. Expensive and sophisticated technologies such as telemetry systems or high quality brush connectors must be used. For this reason, a dynamometric wheelset instrumented with strain gauges is an expensive and complex system for the measurement of wheel-rail contact forces.

### 3.2.2 Strain gauges installation

Due to the reduced available space for sensors and equipment in the scaled wheelset, a single wheel has been instrumented. A set of twelve strain gauges have been installed in the wheel, six on each side of the wheel-web (See Fig. 3.7). Each strain gauge has a twin unit at the opposite side, located at the same angular position, resulting on a total of six active strain bridges in the dynamometric wheelset.



FIGURE 3.7: Mounting of Strain Gauges

The bridges have been connected in a half-bridge configuration. This configuration has two active strain gauges and two passive variable resistors that balance the full bridge (see Fig. 3.8). Depending on how this four elements are interconnected in the Wheatstone half-bridge, the response of the system varies. There are two possibilities: if the two active strain gauges are located in opposite arms of the bridges, their measured strains are added, while if the active strain gauges are located in adjacent arms, their measurements are subtracted [59]. In addition, the half-bridge configuration also minimize the effect of temperature on the measurement. With both active strain gauges at the same temperature and mounted on the same material, any changes in the temperature affect the sensors in the same way. Figure 3.9 shows the strain field of the wheel considering that all nodes of the wheel hub are fixed. In this scenario a constant force has been applied at the wheel tread. As it can be observed, one side of the wheel is compressed while the other remains tensioned.



The strain measured by the internal and external strain gauge in one of the strain bridges are given by:

$$\begin{aligned}\varepsilon_{ext} &= \varepsilon_{ext}^Q + \varepsilon_{ext}^N \\ \varepsilon_{int} &= \varepsilon_{int}^Q + \varepsilon_{int}^N\end{aligned}\quad (3.1)$$

where  $\varepsilon_{ext}^Q$  and  $\varepsilon_{ext}^N$  are the radial strain produced by the lateral load  $Q$  and normal load  $N$  on the external face of the wheel respectively. Considering that the external load applied in the wheel is centred in the wheel tread (See Fig. 3.10), the measured strains due to the normal component of the applied force in both sides of the wheel  $\varepsilon_{ext}^N$  and  $\varepsilon_{int}^N$  are identical. Thus, if the strain bridges are connected in differential configuration, it yields,

$$\varepsilon_{tot} = \varepsilon_{ext} - \varepsilon_{int} = \varepsilon_{ext}^Q - \varepsilon_{int}^Q \quad (3.2)$$

where  $\varepsilon_{tot}$  represents the total strain measured in one of the strain bridges. As one can see, this configuration only allows the lateral load measurement. Thus this methodology is not valid for the applied normal load measurement. Another procedure explained later is used for the normal load measurement.

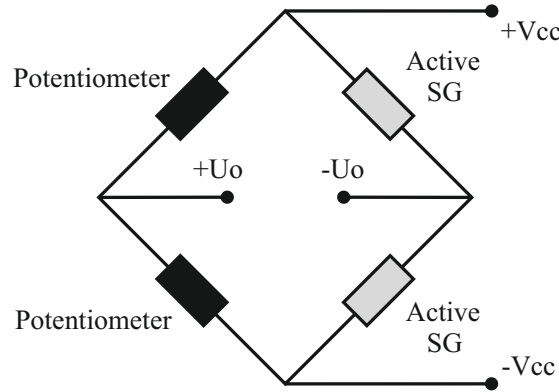


FIGURE 3.8: Half-bridge Configuration

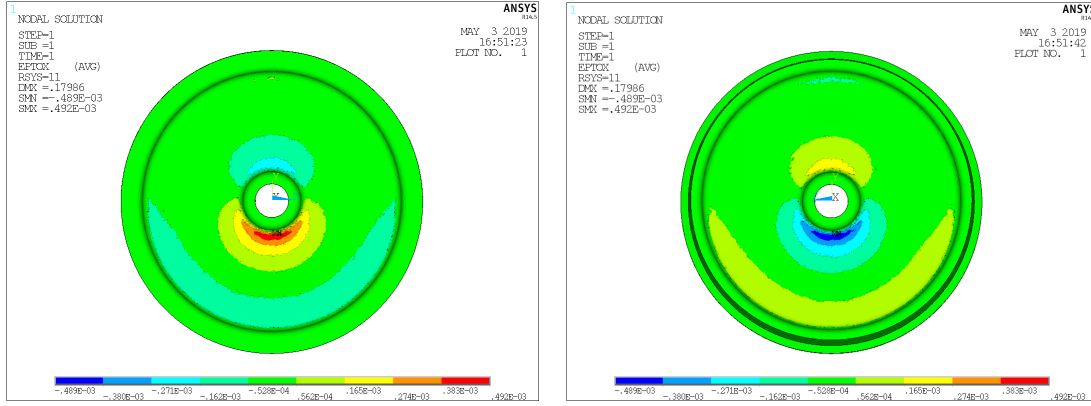


FIGURE 3.9: Radial strain state of the wheel

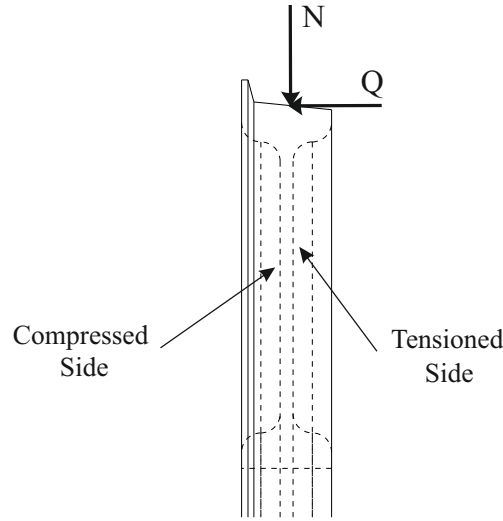


FIGURE 3.10: Loads applied to the wheel

As it can be observed in Fig. 3.7, the strain gauges have been installed in the vicinity of the wheel shaft because strains are bigger in that area. Figure 3.11 shows the numerical results obtained from the *FEM* when a 100 N lateral load is applied on the wheel.

As mentioned before in this section, the use of strain gauges requires the use of wireless communication between the sensors and the data acquisition system or brushed connectors. Both solutions can be found in the market being equally expensive. The use of a brushed connector was initially considered in this thesis, however the reduced dimensions of the axle and the numbers of signals to transmit made that solution unfeasible. It should be noted that this kind of connectors usually have a considerable level of noise

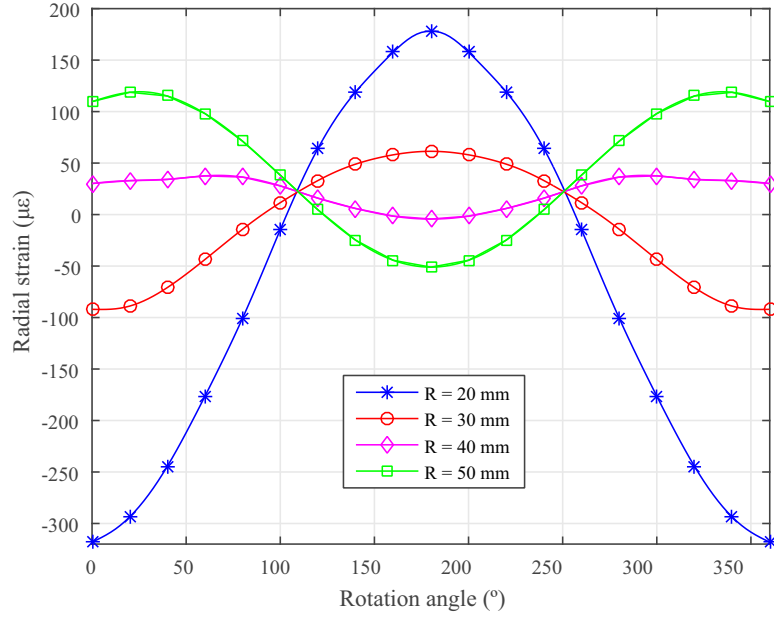


FIGURE 3.11: Simulated radial strain in different measuring radius

due to the sliding connections. In a full scale system where large loads are applied on the wheels, that noise could be neglected but not in such scaled system. Figure 3.12 shows on the left the three wireless transmitters installed on the instrumented wheelset. Each device has two measuring channels. They power the strain bridges, amplify and transmit the signal to the receiver. An external 9 V power supply is required to power the transmitters. Figure 3.12 shows on the right the receiver that conditions and amplify the signals sent by the wireless transmitters. These signals are then acquired by the DAQ system.

Figure 3.13 shows the final assembly of the dynamometric wheelset with the strain gauges and the telemetry system installed on it. Left wheel shown in the figure is the instrumented with the strain sensors. The assembly process of all the instruments in the dynamometric wheelset has been carefully accomplished to keep the wheelset balanced. An unbalance wheelset would introduce abnormal radial accelerations in the scaled vehicle.

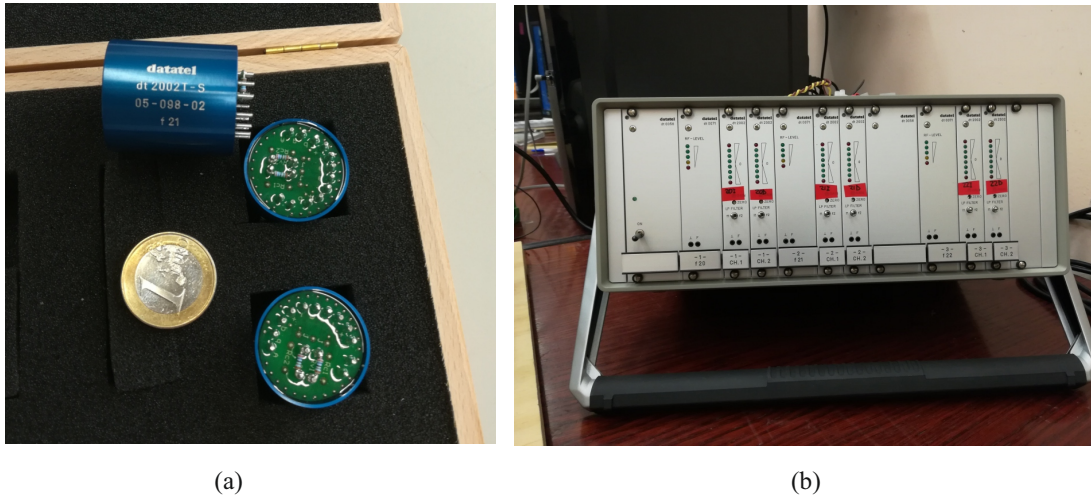


FIGURE 3.12: Datatel transmitters and receiver

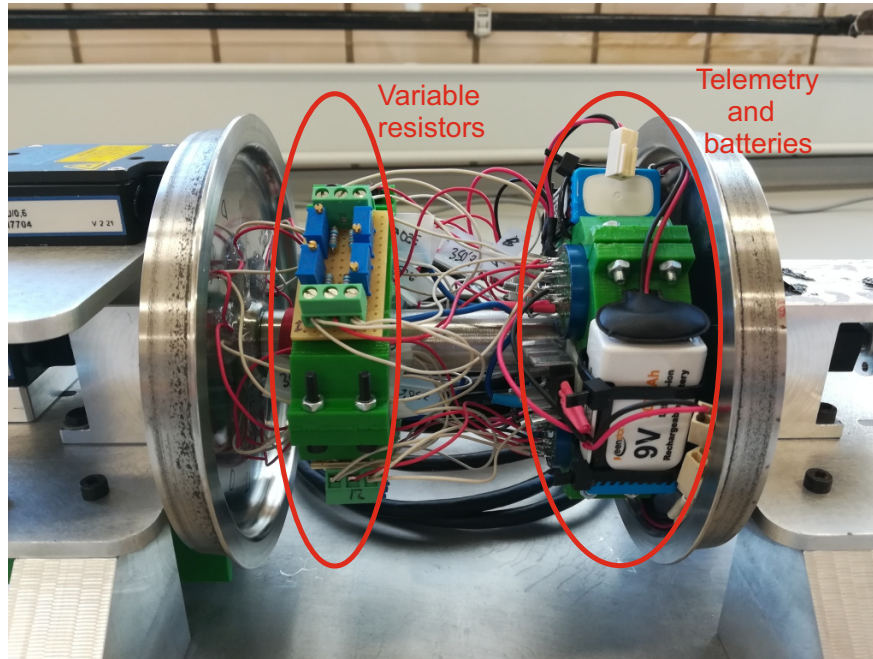


FIGURE 3.13: Final assembly of the scaled dynamometric wheelset

### 3.2.3 Lateral force estimation based on wheel-web radial strains

The methods proposed by Gómez in [100] and Gutiérrez-Lopez in [101] are based on some harmonic elimination techniques that have been successfully proved for measuring wheel-rail contact forces, tyre-road contact forces and applied moments respectively.

These methods allow the estimation of a different number of magnitudes depending on the number of strain gauges installed on the dynamometric wheels. However, for the purpose of this thesis, due to the reduced dimensions of the scaled wheelset, a maximum of twelve strain gauges can be used.

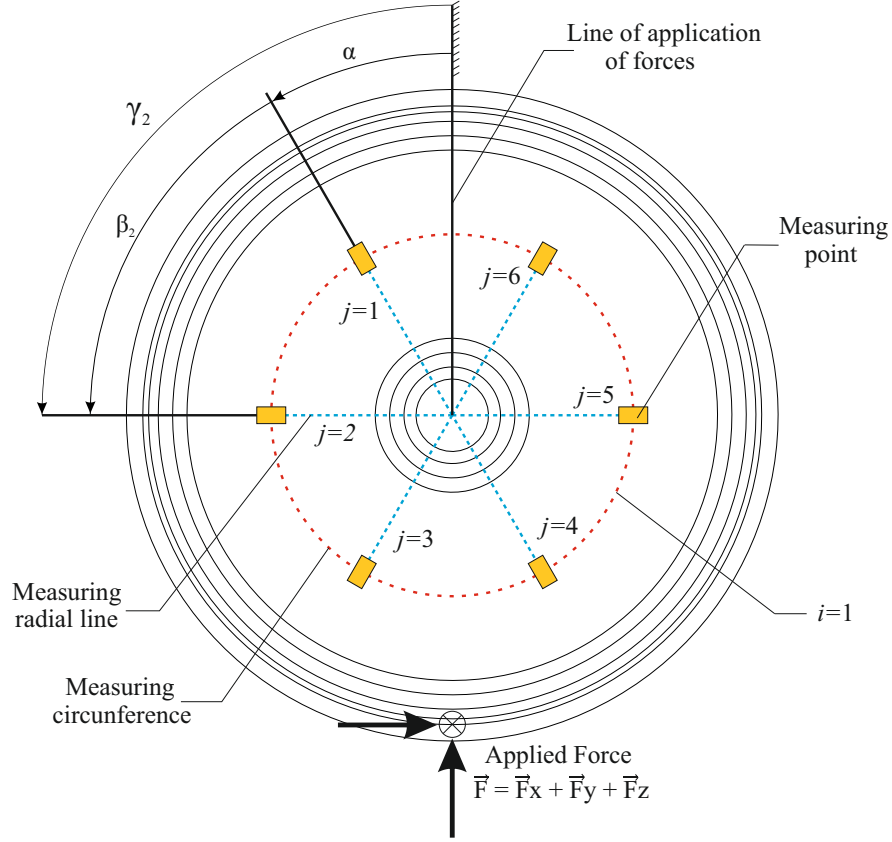


FIGURE 3.14: Measuring points, radial lines and measuring circumference

The method proposed hereafter is an application of the above mentioned methods to a scaled wheelset. In the algorithm formulation, a linear elastic model of the wheel, six strain bridges connected in half-bridge configuration (each of them with an active strain gauge installed on each side of the wheel), and a combination of lateral, vertical and longitudinal loads applied on the wheel-tread have been considered. Figure 3.14 shows a diagram of the instrumented wheel, where each measuring point represents one of the strain bridges present on the wheel-web.

The radial strain on measuring point  $j$  is given by:

$$\varepsilon_j(\gamma_j, t) = B_j^X(\gamma_j)F_X(t) + A_j^Y(\gamma_j)F_Y(t) + A_j^Z(\gamma_j)F_Z(t) \quad (3.3)$$

$$\gamma_j = \alpha + \beta_j \quad (3.4)$$

where  $F_X, F_Y$  and  $F_Z$  are the three components of the applied force on the wheel, and  $B_j^X(\gamma_j), A_j^Y(\gamma_j)$  and  $A_j^Z(\gamma_j)$  are influence functions of the rotated angle  $\gamma_j$  that show the strain due to unitary forces  $F_X, F_Y$  and  $F_Z$  on the measured strain  $\varepsilon_j$ . Variable  $\gamma_j$  is the angle between the measuring radial line  $j$  and the line of application of forces,  $\alpha$  is the angle between the reference radial line  $j = 1$  and the line of application of forces, and  $\beta_j$  is the angle between the measuring radial line  $j$  and the reference radial line.

As explained in [101], the influence functions are periodic, thus, Eq. (3.3) can be rewritten as a Fourier series expansion. It is important to note that  $A_j^Y(\gamma_j)$  and  $A_j^Z(\gamma_j)$  are symmetric influence functions and only cosine terms appear on them, while  $B_j^X(\gamma_j)$  are antisymmetric influence functions that only contain sine terms. This can be written in the following way:

$$\varepsilon_j(\gamma_j, t) = F_X(t) \sum_{k=0}^{\infty} B_k^X \sin(k\gamma_j) + F_Y(t) \sum_{k=0}^{\infty} A_k^Y \cos(k\gamma_j) + F_Z(t) \sum_{k=0}^{\infty} A_k^Z \cos(k\gamma_j) \quad (3.5)$$

Considering only the first  $n$  harmonics and rewriting Eq. (3.5) in matrix forms yields:

$$\varepsilon_j(\gamma_j, t) = \begin{bmatrix} 1 & \cos(\gamma_j) & \cos(2\gamma_j) & \cdots & \cos(n\gamma_j) \end{bmatrix} \begin{bmatrix} A_0^Y & A_0^Z \\ A_1^Y & A_1^Z \\ \vdots & \vdots \\ A_n^Y & A_n^Z \end{bmatrix} \begin{bmatrix} F_Y(t) \\ F_Z(t) \end{bmatrix} + \begin{bmatrix} 0 & \sin(\gamma_j) & \sin(2\gamma_j) & \cdots & \sin(n\gamma_j) \end{bmatrix} \begin{bmatrix} B_0^X \\ B_1^X \\ \vdots \\ B_n^X \end{bmatrix} \begin{bmatrix} F_X(t) \end{bmatrix} \quad (3.6)$$

This can be rewritten in compact form as:

$$\varepsilon_j(\gamma_j, t) = \mathbf{h}_{Sj}(\gamma_j)^T \mathbf{A}_S \mathbf{f}_S(t) + \mathbf{h}_{Aj}(\gamma_j)^T \mathbf{B}_A \mathbf{f}_A(t) \quad (3.7)$$

where vectors  $\mathbf{h}_{Sj}$  and  $\mathbf{h}_{Aj}$  that depend on the angular position  $\gamma_j$  and  $\mathbf{A}_S$  and  $\mathbf{B}_A$  are constant matrices depending on the wheel geometry. Equation (3.7) can be particularized for the case of study of this work, where six active strain bridges are installed on the instrumented wheel. The following expression is obtained:

$$\varepsilon(\gamma_j, t) = \mathbf{H}_S(\gamma_j) \mathbf{A}_S \mathbf{f}_S(t) + \mathbf{H}_A(\gamma_j) \mathbf{B}_A \mathbf{f}_A(t) \quad (3.8)$$

where:

$$\varepsilon(\gamma_j, t) = \begin{bmatrix} \varepsilon_1 & \varepsilon_2 & \cdots & \varepsilon_6 \end{bmatrix}^T \quad (3.9)$$

$$\mathbf{H}_S = \begin{bmatrix} \mathbf{h}_{S1}^T \\ \mathbf{h}_{S2}^T \\ \vdots \\ \mathbf{h}_{S6}^T \end{bmatrix} = \begin{bmatrix} 1 & \cos(\gamma_1) & \cos(2\gamma_1) & \cdots & \cos(n\gamma_1) \\ 1 & \cos(\gamma_2) & \cos(2\gamma_2) & \cdots & \cos(n\gamma_2) \\ \vdots & \vdots & \vdots & \ddots & \vdots \\ 1 & \cos(\gamma_n) & \cos(2\gamma_n) & \cdots & \cos(n\gamma_6) \end{bmatrix} \quad (3.10)$$

$$\mathbf{H}_A = \begin{bmatrix} \mathbf{h}_{A1}^T \\ \mathbf{h}_{A2}^T \\ \vdots \\ \mathbf{h}_{A6}^T \end{bmatrix} = \begin{bmatrix} 0 & \sin(\gamma_1) & \sin(2\gamma_1) & \cdots & \sin(n\gamma_1) \\ 0 & \sin(\gamma_2) & \sin(2\gamma_2) & \cdots & \sin(n\gamma_2) \\ \vdots & \vdots & \vdots & \ddots & \vdots \\ 0 & \sin(\gamma_n) & \sin(2\gamma_n) & \cdots & \sin(n\gamma_6) \end{bmatrix} \quad (3.11)$$

The values contained in Eq. (3.9) are the strains measured by each of the six strain bridges of the dynamometric wheelset. These signals are periodic with the angle rotated by wheel. They must be combined in such a way that four new signals are obtained:

- $E_{Si}$ : Signal that contains information of the first harmonic of the strain curves and depends linearly on the forces that produce symmetric strains ( $F_Y$  and  $F_Z$ ).
- $E_{Ai}$ : Signal that contains information of the first harmonic of the strain curves and depends linearly on the force that produce antisymmetric strains ( $F_X$ ).
- $E'_{Si}$ : Signal that contains information of the second harmonic of the strain curves and depends linearly on the forces that produce symmetric strains ( $F_Y$  and  $F_Z$ ).
- $E'_{Ai}$ : Signal that contains information of the second harmonic of the strain curves and depends linearly on the force that produce antisymmetric strains ( $F_X$ ).

Signals that depend on the first harmonic can be written as

$$E_S = \mathbf{x}_S^T \boldsymbol{\varepsilon} = \mathbf{x}_S^T \mathbf{H}_S(\gamma_j) \mathbf{A}_S \mathbf{f}_S(t) + \mathbf{x}_S^T \mathbf{H}_A(\gamma_j) \mathbf{B}_A \mathbf{f}_A(t) \quad (3.12)$$

$$E_A = \mathbf{x}_A^T \boldsymbol{\varepsilon} = \mathbf{x}_A^T \mathbf{H}_S(\gamma_j) \mathbf{A}_S \mathbf{f}_S(t) + \mathbf{x}_A^T \mathbf{H}_A(\gamma_j) \mathbf{B}_A \mathbf{f}_A(t) \quad (3.13)$$

where  $\mathbf{x}_S$  and  $\mathbf{x}_A$  are two unknown vectors of coefficients.

To guarantee the conditions enumerated above, vectors  $\mathbf{x}_S$  and  $\mathbf{x}_A$  must fulfil the following expressions:



$$\begin{aligned}
\mathbf{x}_S^T \mathbf{H}_S &= \begin{bmatrix} 0 & 1 & 0 & 0 & 0 & \cdots & 0 \end{bmatrix} \\
\mathbf{x}_S^T \mathbf{H}_A &= \begin{bmatrix} 0 & 0 & 0 & 0 & 0 & \cdots & 0 \end{bmatrix} \\
\mathbf{x}_A^T \mathbf{H}_S &= \begin{bmatrix} 0 & 0 & 0 & 0 & 0 & \cdots & 0 \end{bmatrix} \\
\mathbf{x}_A^T \mathbf{H}_A &= \begin{bmatrix} 0 & 1 & 0 & 0 & 0 & \cdots & 0 \end{bmatrix}
\end{aligned} \tag{3.14}$$

If Eqs. (3.14) are fulfilled, it yields:

$$E_S = \begin{bmatrix} A_1^Y & A_1^Z \end{bmatrix} \begin{bmatrix} F_Y(t) & F_Z(t) \end{bmatrix}^T \tag{3.15}$$

$$E_A = B_1^X F_X(t) \tag{3.16}$$

To calculate the unknown values of  $\mathbf{x}_S$  and  $\mathbf{x}_A$ , Eqs. (3.14) can be rewritten in the following way:

$$\begin{bmatrix} H_S^T \\ H_A^T \end{bmatrix} \mathbf{x}_S = \begin{bmatrix} 0 & 1 & 0 & \cdots & 0 & 0 & 0 & 0 & \cdots & 0 \end{bmatrix}^T \tag{3.17}$$

$$\begin{bmatrix} H_S^T \\ H_A^T \end{bmatrix} \mathbf{x}_A = \begin{bmatrix} 0 & 0 & 0 & \cdots & 0 & 0 & 1 & 0 & \cdots & 0 \end{bmatrix}^T \tag{3.18}$$

Equations (3.17) and (3.18) constitute two overdetermined system of equations. Considering there is not an unique solution for  $\mathbf{x}_S$  and  $\mathbf{x}_A$ , an optimization problem must be solved in this point. To that end, Eqs. (3.17) and (3.18) are partitioned as follows:

$$\begin{bmatrix} 1 & 1 & \cdots & 1 \\ \cos(\gamma_1) & \cos(\gamma_2) & \cdots & \cos(\gamma_6) \end{bmatrix} \begin{bmatrix} x_1^S \\ x_2^S \\ \vdots \\ x_6^S \end{bmatrix} = \begin{bmatrix} 0 \\ 1 \end{bmatrix} \Rightarrow \mathbf{R}_S \mathbf{X}_S = \mathbf{d} \tag{3.19}$$

$$\begin{bmatrix} \cos(2\gamma_1) & \cos(2\gamma_2) & \cdots & \cos(2\gamma_6) \\ \cos(3\gamma_1) & \cos(3\gamma_2) & \cdots & \cos(3\gamma_6) \\ \vdots & \vdots & \ddots & \vdots \\ \cos(n\gamma_1) & \cos(n\gamma_2) & \cdots & \cos(n\gamma_6) \\ \sin(\gamma_1) & \sin(\gamma_2) & \cdots & \sin(\gamma_6) \\ \sin(2\gamma_1) & \sin(2\gamma_2) & \cdots & \sin(2\gamma_6) \\ \vdots & \vdots & \ddots & \vdots \\ \sin(n\gamma_1) & \sin(n\gamma_2) & \cdots & \sin(n\gamma_6) \end{bmatrix} \begin{bmatrix} x_1^S \\ x_2^S \\ \vdots \\ x_6^S \end{bmatrix} = \begin{bmatrix} 0 \\ \vdots \\ 0 \\ 0 \\ \vdots \\ 0 \end{bmatrix} \Rightarrow \mathbf{M}_S \mathbf{X}_S = \mathbf{0} \quad (3.20)$$

$$\begin{bmatrix} 1 & 1 & \cdots & 1 \\ \sin(\gamma_1) & \sin(\gamma_2) & \cdots & \sin(\gamma_6) \end{bmatrix} \begin{bmatrix} x_1^A \\ x_2^A \\ \vdots \\ x_6^A \end{bmatrix} = \begin{bmatrix} 0 \\ 1 \end{bmatrix} \Rightarrow \mathbf{R}_A \mathbf{X}_A = \mathbf{d} \quad (3.21)$$

$$\begin{bmatrix} \cos(\gamma_1) & \cos(\gamma_2) & \cdots & \cos(\gamma_6) \\ \cos(2\gamma_1) & \cos(2\gamma_2) & \cdots & \cos(2\gamma_6) \\ \vdots & \vdots & \ddots & \vdots \\ \cos(n\gamma_1) & \cos(n\gamma_2) & \cdots & \cos(n\gamma_6) \\ \sin(2\gamma_1) & \sin(2\gamma_2) & \cdots & \sin(2\gamma_6) \\ \sin(3\gamma_1) & \sin(3\gamma_2) & \cdots & \sin(3\gamma_6) \\ \vdots & \vdots & \ddots & \vdots \\ \sin(n\gamma_1) & \sin(n\gamma_2) & \cdots & \sin(n\gamma_6) \end{bmatrix} \begin{bmatrix} x_1^A \\ x_2^A \\ \vdots \\ x_6^A \end{bmatrix} = \begin{bmatrix} 0 \\ \vdots \\ 0 \\ 0 \\ \vdots \\ 0 \end{bmatrix} \Rightarrow \mathbf{M}_A \mathbf{X}_A = \mathbf{0} \quad (3.22)$$

Thus, equations  $\mathbf{M}_S \mathbf{X}_S = \mathbf{0}$  and  $\mathbf{M}_A \mathbf{X}_A = \mathbf{0}$  must be solved while constraint equations,

$$\begin{aligned} \mathbf{R}_S \mathbf{X}_S &= \mathbf{d} \\ \mathbf{R}_A \mathbf{X}_A &= \mathbf{d} \end{aligned} \quad (3.23)$$

are fulfilled. The values of vectors  $\mathbf{x}_S$  and  $\mathbf{x}_A$  can be obtained by solving the following system of equations that correspond with the method of Lagrange multipliers:

$$\begin{bmatrix} \mathbf{M}_S^T \mathbf{M}_S & \mathbf{R}_S^T \\ \mathbf{R}_S & \mathbf{0} \end{bmatrix} \begin{bmatrix} \mathbf{x}_S \\ \lambda \end{bmatrix} = \begin{bmatrix} 0 \\ \mathbf{d} \end{bmatrix} \quad (3.24)$$

$$\begin{bmatrix} \mathbf{M}_A^T \mathbf{M}_A & \mathbf{R}_A^T \\ \mathbf{R}_A & \mathbf{0} \end{bmatrix} \begin{bmatrix} \mathbf{x}_A \\ \lambda \end{bmatrix} = \begin{bmatrix} 0 \\ \mathbf{d} \end{bmatrix} \quad (3.25)$$

The minimum error is obtained when:

$$\mathbf{x}_S = \frac{1}{3} \begin{bmatrix} \cos(\gamma_1) \\ \cos(\gamma_2) \\ \vdots \\ \cos(\gamma_6) \end{bmatrix} \quad (3.26)$$

$$\mathbf{x}_A = \frac{1}{3} \begin{bmatrix} \sin(\gamma_1) \\ \sin(\gamma_2) \\ \vdots \\ \sin(\gamma_6) \end{bmatrix} \quad (3.27)$$

Considering the measuring points disposition depicted in Fig. 3.14, the angular position  $\gamma_j$  can be written as:

$$\gamma_j = \alpha + (j - 1) \frac{\pi}{3} \quad (3.28)$$

Finally, substituting Eq. (3.26), (3.27) and (3.28) in equations (3.12) and (3.13), it yields:

$$E_S = \mathbf{X}_S^T \varepsilon = \frac{1}{3} \sum_{j=1}^6 (\varepsilon_j \cos(\gamma_j)) \quad (3.29)$$

$$E_A = \mathbf{X}_A^T \varepsilon = \frac{1}{3} \sum_{j=1}^6 (\varepsilon_j \sin(\gamma_j)) \quad (3.30)$$

For the signals that contains information of the second harmonic of the strain signal  $E'_S$  and  $E'_A$ , an identical procedure must be accomplished, with the exception of matrices  $\mathbf{R}_S$ ,  $\mathbf{M}_S$ ,  $\mathbf{R}_A$  and  $\mathbf{M}_A$  take now the following form:

$$\mathbf{R}_S = \begin{bmatrix} 1 & 1 & \cdots & 1 \\ \cos(2\gamma_1) & \cos(2\gamma_2) & \cdots & \cos(2\gamma_6) \end{bmatrix} \quad (3.31)$$

$$\mathbf{M}_S = \begin{bmatrix} \cos(\gamma_1) & \cos(\gamma_2) & \cdots & \cos(\gamma_6) \\ \cos(3\gamma_1) & \cos(3\gamma_2) & \cdots & \cos(3\gamma_6) \\ \vdots & \vdots & \ddots & \vdots \\ \cos(n\gamma_1) & \cos(n\gamma_2) & \cdots & \cos(n\gamma_6) \\ \sin(\gamma_1) & \sin(\gamma_2) & \cdots & \sin(\gamma_6) \\ \sin(2\gamma_1) & \sin(2\gamma_2) & \cdots & \sin(2\gamma_6) \\ \vdots & \vdots & \ddots & \vdots \\ \sin(n\gamma_1) & \sin(n\gamma_2) & \cdots & \sin(n\gamma_6) \end{bmatrix} \quad (3.32)$$

$$\mathbf{R}_A = \begin{bmatrix} 1 & 1 & \cdots & 1 \\ \sin(2\gamma_1) & \sin(2\gamma_2) & \cdots & \sin(2\gamma_6) \end{bmatrix} \quad (3.33)$$

$$\mathbf{M}_A = \begin{bmatrix} \cos(\gamma_1) & \cos(\gamma_2) & \cdots & \cos(\gamma_6) \\ \cos(2\gamma_1) & \cos(2\gamma_2) & \cdots & \cos(2\gamma_6) \\ \vdots & \vdots & \ddots & \vdots \\ \cos(n\gamma_1) & \cos(n\gamma_2) & \cdots & \cos(n\gamma_6) \\ \sin(\gamma_1) & \sin(\gamma_2) & \cdots & \sin(\gamma_6) \\ \sin(3\gamma_1) & \sin(3\gamma_2) & \cdots & \sin(3\gamma_6) \\ \vdots & \vdots & \ddots & \vdots \\ \sin(n\gamma_1) & \sin(n\gamma_2) & \cdots & \sin(n\gamma_6) \end{bmatrix} \quad (3.34)$$

By applying again the Lagrange multipliers method the following optimised vectors are obtained:

$$\mathbf{x}_S = \frac{1}{3} \begin{bmatrix} \cos(2\gamma_1) \\ \cos(2\gamma_2) \\ \vdots \\ \cos(2\gamma_6) \end{bmatrix} \quad (3.35)$$

$$\mathbf{x}_A = \frac{1}{3} \begin{bmatrix} \sin(2\gamma_1) \\ \sin(2\gamma_2) \\ \vdots \\ \sin(2\gamma_6) \end{bmatrix} \quad (3.36)$$

Taking the results of vectors  $x_S$  and  $x_A$  of (3.35) and (3.36), it results:

$$E'_S = \mathbf{X}_S^T \varepsilon = \frac{1}{3} \sum_{j=1}^6 (\varepsilon_j \cos(2\gamma_j)) \quad (3.37)$$

$$E'_A = \mathbf{X}_A^T \varepsilon = \frac{1}{3} \sum_{j=1}^6 (\varepsilon_j \sin(2\gamma_j)) \quad (3.38)$$

By substituting Eq. (3.3) in Eqs. (3.29), (3.30), (3.37) and (3.38), and considering just the influence of the amplitudes of the first and second harmonics,  $E_S$ ,  $E_A$ ,  $E'_S$  and  $E'_A$  can be rewritten as:

$$E_S \approx A_1^Y F_Y(t) + A_1^A F_Z(t) \quad (3.39)$$

$$E_A \approx B_1^X F_X(t) \quad (3.40)$$

$$E'_S \approx A_2^Y F_Y(t) + A_2^A F_Z(t) \quad (3.41)$$

$$E'_A \approx B_2^X F_X(t) \quad (3.42)$$

By rewriting Eqs. (3.40) to (3.42) in matrix form, the values of  $F_Y(t)$ ,  $F_Z(t)$  and  $F_X(t)$  can be easily obtained from:

$$\begin{bmatrix} A_1^Y & A_1^Z \\ A_2^Y & A_2^Z \end{bmatrix} \begin{bmatrix} F_Y(t) \\ F_Z(t) \end{bmatrix} = \begin{bmatrix} E_S \\ E_A \end{bmatrix} \quad (3.43)$$

$$\begin{bmatrix} B_1^X \\ B_2^X \end{bmatrix} \begin{bmatrix} F_X(t) \end{bmatrix} = \begin{bmatrix} E'_S \\ E'_A \end{bmatrix} \quad (3.44)$$

Equations (3.43) and (3.44) have been obtained only considering the influence of the amplitudes proportional to the first and second harmonics of the influence functions. More details of the complete method presented can be found in [101].

As a summary of the process described above, in order to calculate the lateral force applied on the wheel from the radial strain measured by the strain gauges the following steps must be completed:

1. Coefficients  $A_1^Y$ ,  $A_1^Z$ ,  $A_2^Y$  and  $A_2^Z$  must be obtained from the FEM (only in the first iteration).
2. The angle rotated by the wheel is obtained.
3. Terms  $E_S$ ,  $E_A$ ,  $E'_S$  and  $E'_A$  are obtained from Eqs. (3.29 - 3.30) and Eqs. (3.37 - 3.38).
4. Expressions (3.43) and (3.44) are evaluated and the forces are obtained.

### 3.2.4 Numerical validation of the radial strains method

The method presented here, has been validated using strain data from the FEM as follows: Figure 3.15 shows the synthesized radial strains measured by each of the six strain bridges when a combination of variable lateral and vertical loads are applied on the wheel. Note that each strain bridge experiences the applied load as a force that rotates around the wheel axle. That means, the magnitude measured by one strain bridge is maximized when the strain bridge is in the same measuring radius than

the point of application of the force (its nearest position). By solving the system of equations (3.43) the results depicted in Figs. 3.16 and 3.17 are obtained. As it can be observed, the applied lateral force has been satisfactorily estimated by the proposed method. However, a normal load does not have the same result as one can observe in Fig. 3.17. Functions shown in Fig. 3.18 explain the unsatisfactory vertical and longitudinal load measurements. As it can be observed, the magnitude of the radial strain measured along the measuring circumference where the strain gauges are installed is more than a thousand times bigger when a lateral load is applied in comparison to a normal load acting on the wheel. The reason is that the differential configuration of the strain bridges make them highly sensitive to the bending of the wheel, but any vertical load applied on the wheel is almost undetectable. Taking this into account, the coefficient matrix of system of equation (3.43) is bad conditioned because coefficients  $A_1^Y$  and  $A_2^Y$  are much larger than  $A_1^Z$  and  $A_2^Z$ . That explains why just the lateral load is correctly estimated by the algorithm. This fact does not compromise the final results of this study since the applied normal load on the instrumented wheelset has been satisfactorily measured by another procedure explained later.

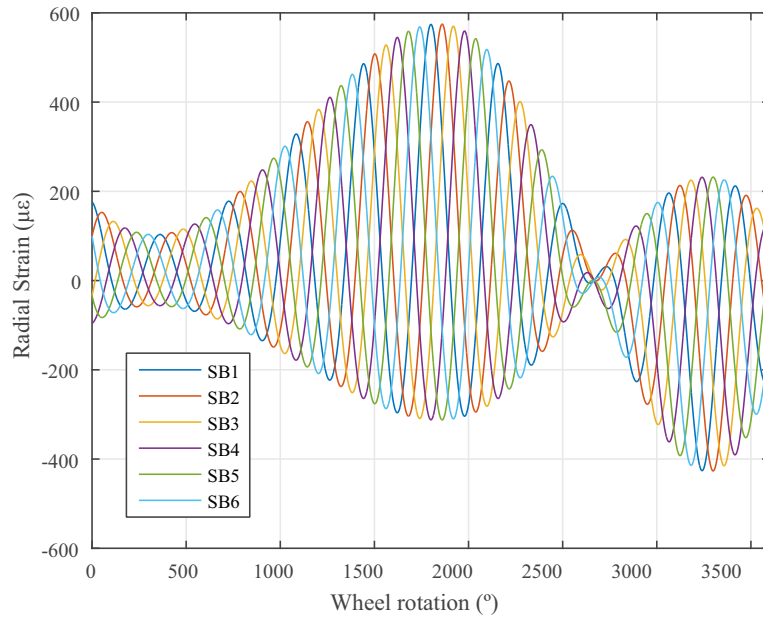


FIGURE 3.15: Synthesized strains when lateral and vertical loads are applied on the wheel

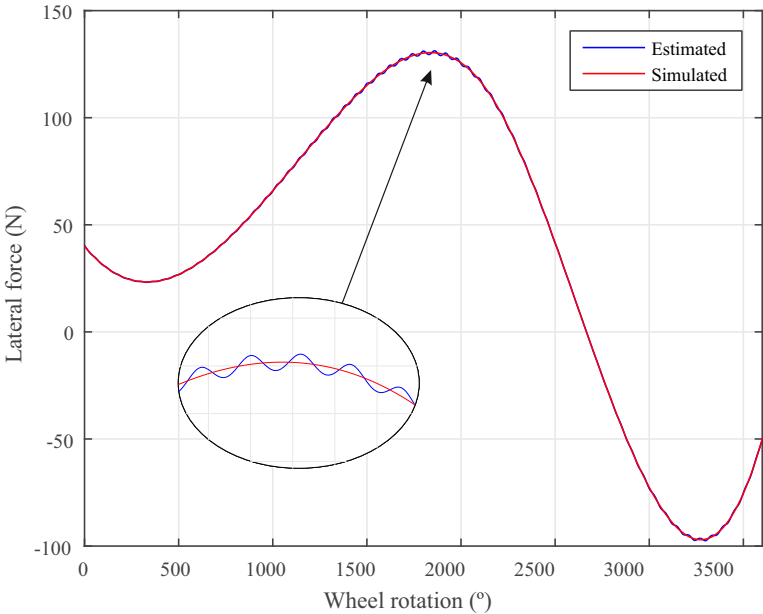


FIGURE 3.16: Simulated vs estimated applied lateral load

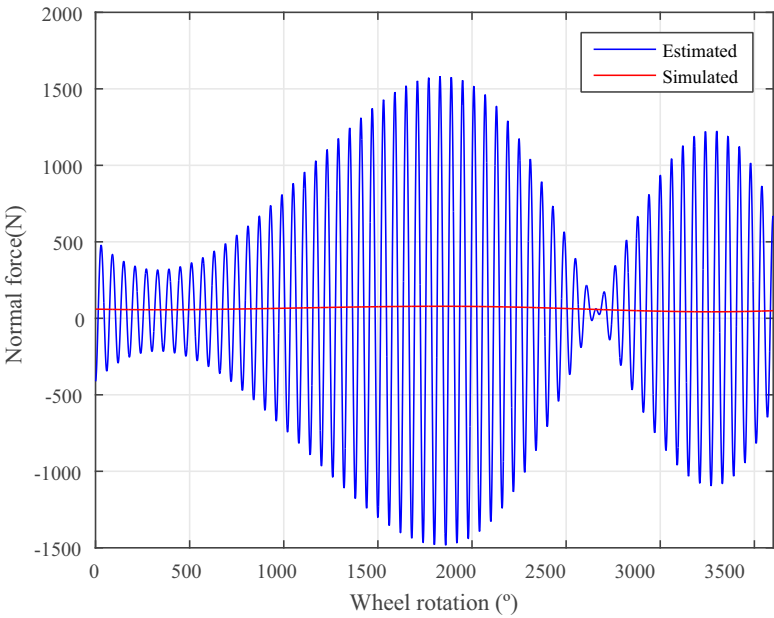


FIGURE 3.17: Simulated vs estimated applied vertical load



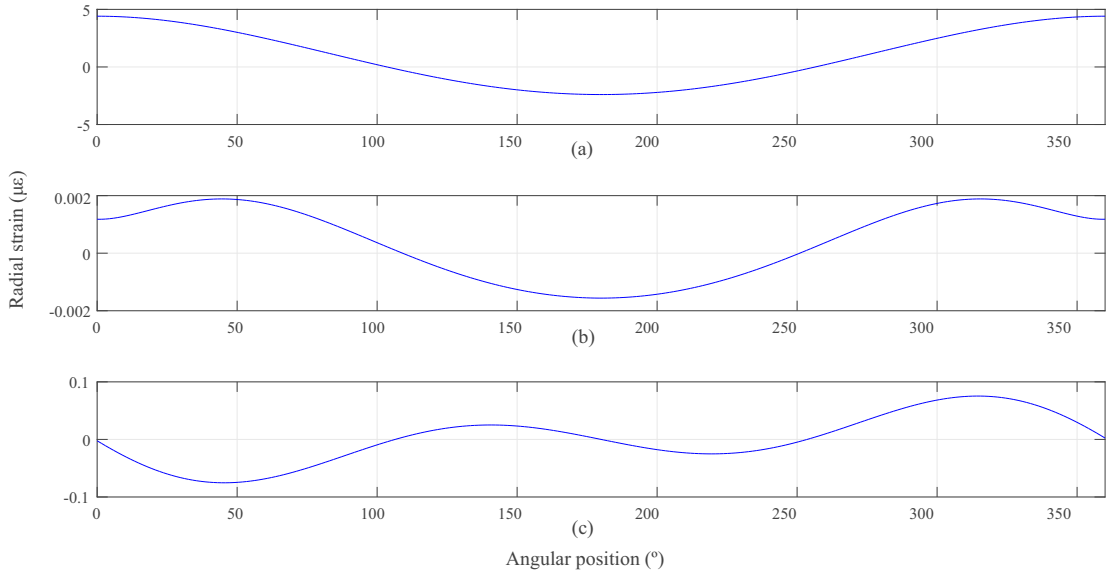


FIGURE 3.18: (a) Deformed shape when a unitary lateral load is applied on the wheel, (b) Deformed shape when a unitary vertical load is applied on the wheel, (c) Deformed shape when a unitary longitudinal load is applied on the wheel

### 3.3 Calibration of the scaled dynamometric wheelset

Before its commissioning, the dynamometric wheelset must be submitted to a calibration process. The goal is to analyse the response of the measuring instruments installed in the wheelset when different forces act on the wheels. In the railways industry there are two types of calibration facilities: static test benches [13] and dynamic test benches [14]. Figure 3.19 shows an example of dynamic calibration bench, also known as rolling rigs. Some of these machines can test a full scale dynamometric wheelset up to 300  $km/h$  while controlling vertical and lateral loads and the relative wheelset-rail yaw angle. The rails are two rings machined with a conventional UIC profile. With a sophisticated test rig controller, it is possible to reproduce straight and curve running conditions, including acceleration and braking.

Although a dynamic test bench is most straightforward facility to calibrate a dynamometric wheelset, their complexity and high price make them even prohibitive for some railways manufacturers. Static test benches, where the wheelset remains motionless

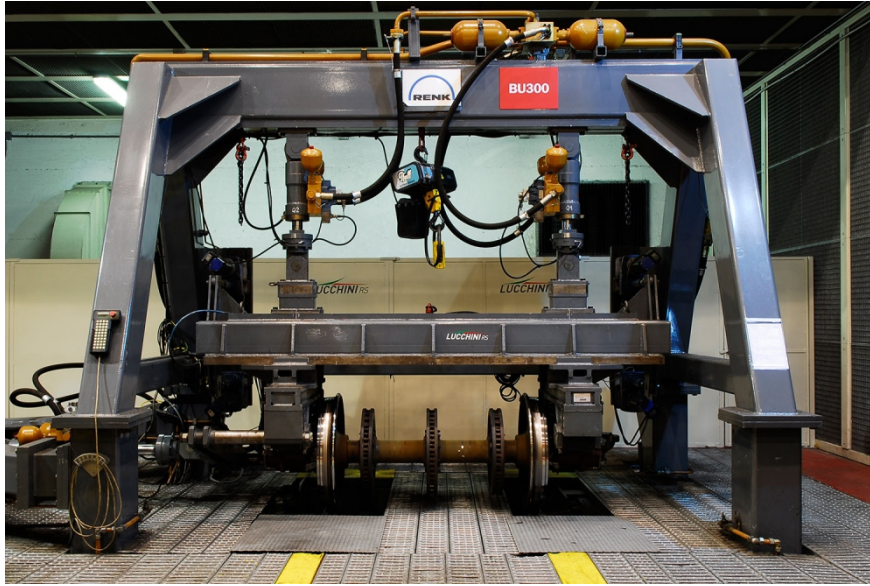


FIGURE 3.19: Luccini Rolling Rig

during the tests, are an alternative. In this PhD thesis the instrumented wheelset has been tested on a static scaled test bench.

### 3.3.1 Static calibration test bench

An scaled static calibration test bench has been fully designed and manufactured by the author. Figure 3.20 shows the preliminary design of the mentioned test bench. The goal was to develop a machine where the wheelset could be attached while applying controlled lateral and vertical forces on one the wheels.

Numerous tests have been carried out with the calibration bench in order to validate the FEM developed in ANSYS and to tune the involved sensors. In addition to the dynamometric wheelset instruments, the test bench has two load cells in charge of applying the lateral and vertical loads on the wheel (see Fig. 3.22). Figure 3.21 shows all the equipment required during the calibration tests.

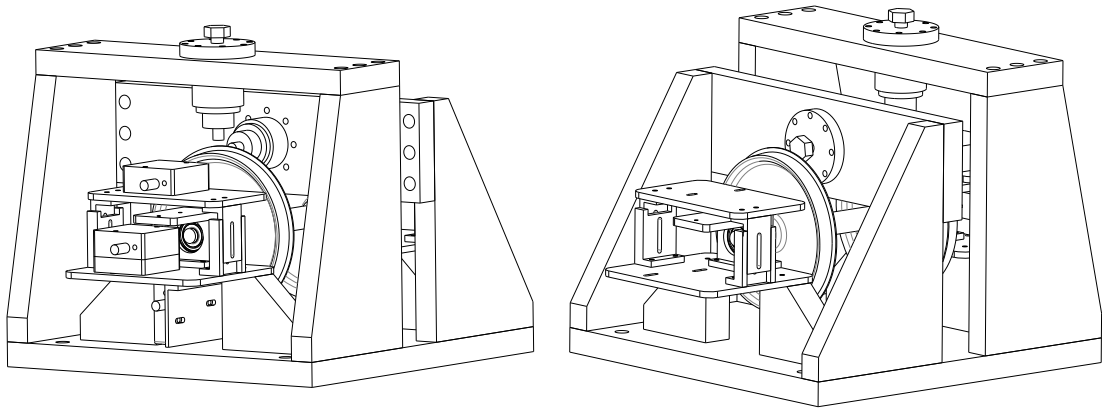


FIGURE 3.20: Scaled Static Test Bench

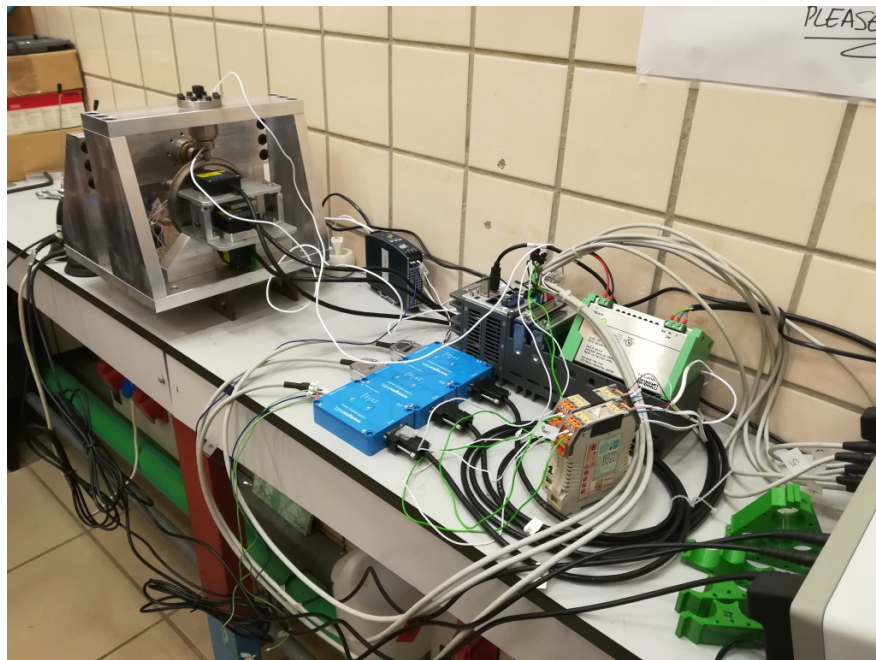


FIGURE 3.21: Calibration Test Bench Instrumentation

### 3.3.1.1 Strain gauges calibration in the test bench

The first step consist on electronically balance the strain gauges, getting a 0 V output at each of the six strain bridges when the wheel is unloaded. Then, the receiver (Fig. 3.12 (b)) gains must be adjusted to guarantee that every strain bridge provides the same output when an input load is applied on the wheel. Finally, in order to validate

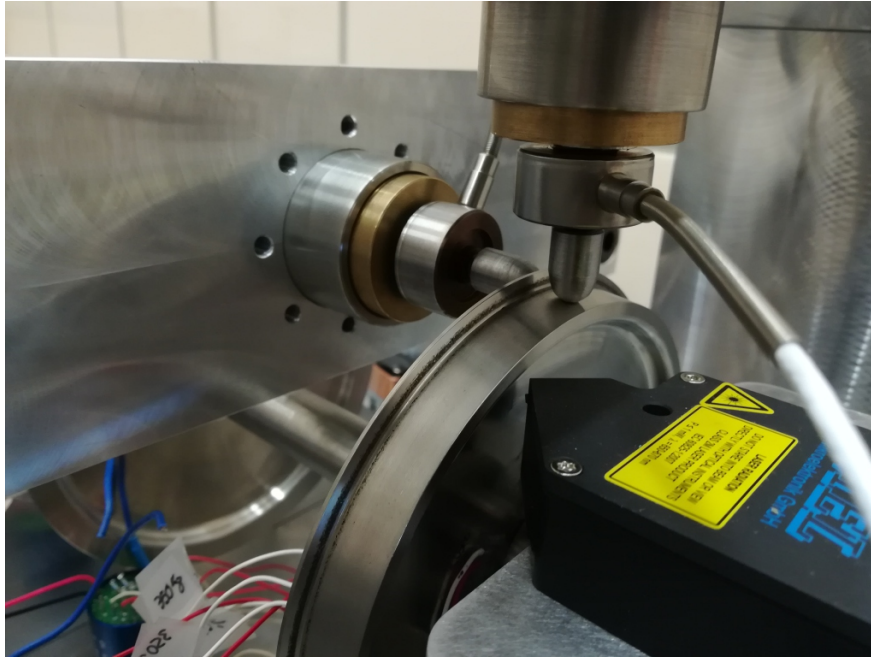


FIGURE 3.22: Test Bench Load Cells

the FEM of the wheel, the micro-strain / volts ratio has been established by means of an external strain gauge calibrator that automatically provides that ratio.

Figure 3.23 shows the FEM experimental validation. In this scenario a variable lateral load is applied on the central point of the wheel tread. Solid lines are the experimental data obtained from the calibration test bench while dashed lines are numerical results from the FEM. Different colours lines represent the strains measured by the six strain bridges. Solid and dashed yellow lines are the strains measured by the strain bridge closest to the point of application of the force. As it can be seen, there is a good accordance between both sets of data. These result validate the FEM developed in ANSYS. Hereafter the numerical results obtained from the FEM can be used for the algorithm that calculates the lateral contact force.

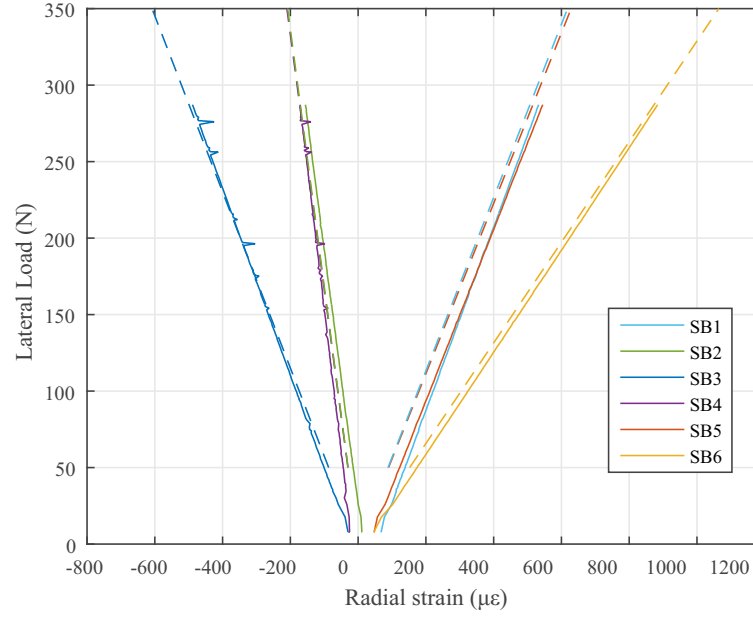


FIGURE 3.23: FEM Experimental Validation

Once the finite elements model developed in ANSYS has been validated, it can be used to easily check some of the assumptions made during the design stage. For instance, as explained in subsection 3.2.2, the strain gauges half-bridge configuration should make them blind to the normal load effect. That assumption makes sense when the vertical load is applied in the neutral axis of the wheel cross-section but not when it is displaced. Figure 3.24 shows the simulated strain obtained in one of the strain bridges during one wheel turn, being the normal load applied on the central point of the wheel tread (neutral axis). Different colour lines represent the strain measured when different lateral loads are applied on the wheel. Coloured lines of the same colour represent the strain measured in the strain bridge when five different values of normal load (from 0  $N$  to 700  $N$ ) are applied on the wheel, maintaining the same lateral load. The maximum strain difference between the 0  $N$  and 700  $N$  vertical load scenarios is 5  $\mu\epsilon$ . Taking into account a normal resolution of any strain gauge conditioner is around 1  $\mu\epsilon$ , vertical load effect can be neglected when the load applied is centred on the wheel tread.

A similar experiment has been carried out with the real scaled vehicle. The bogie has been positioned centred on the scaled track while the wheel normal load has been

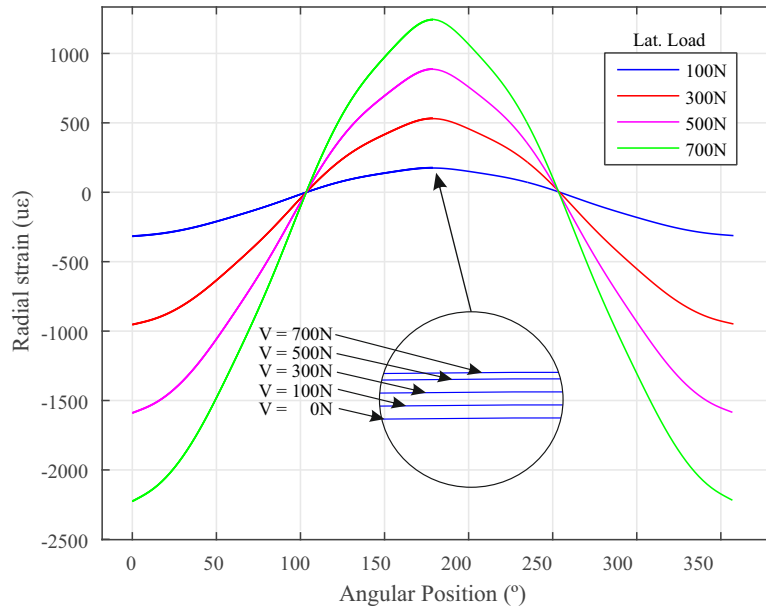


FIGURE 3.24: Effect of the Normal Load Applied on the Wheel

gradually augmented by adding extra weight on the bogie. Figure 3.25 shows on the left the bogie loaded with a calibrated 50 N weight and Fig. 3.25 shows on the right the vehicle loaded with 200 N. The measurements drawn from the strain gauges are shown in Fig. 3.26. Vertical red lines occur during the periods when the normal load applied on the wheels is changed by adding or removing a calibrated weight. The test starts and finishes with no extra weight on the vehicle. As it can be observed, there is not a significative change on the measured strain, the maximum strain difference detected during the experiment is less than  $5 \mu\epsilon$ . Based on these results and the previous FEM analysis, it can be concluded that the normal load applied on the instrumented wheel does not affect the measurements of the strain gauges.



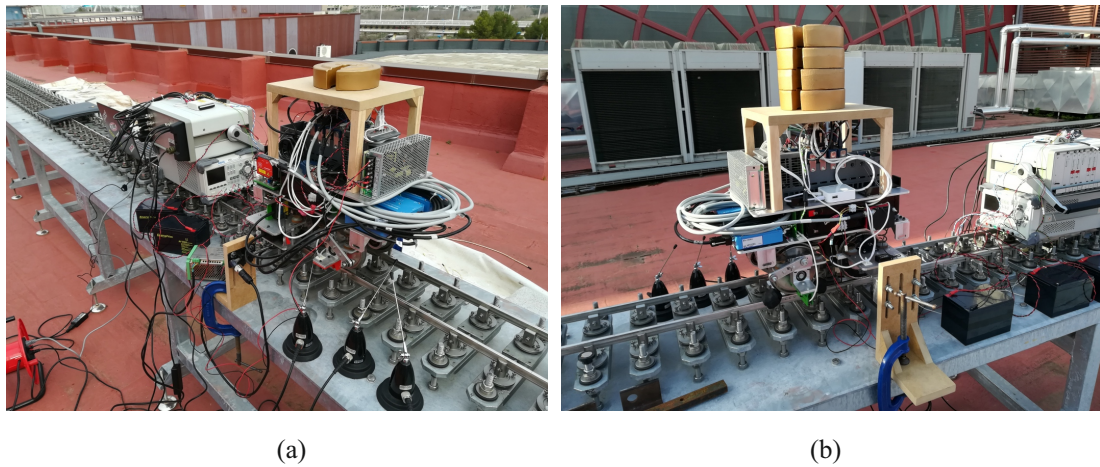


FIGURE 3.25: Normal load effect on the measured radial strains. Track experiment

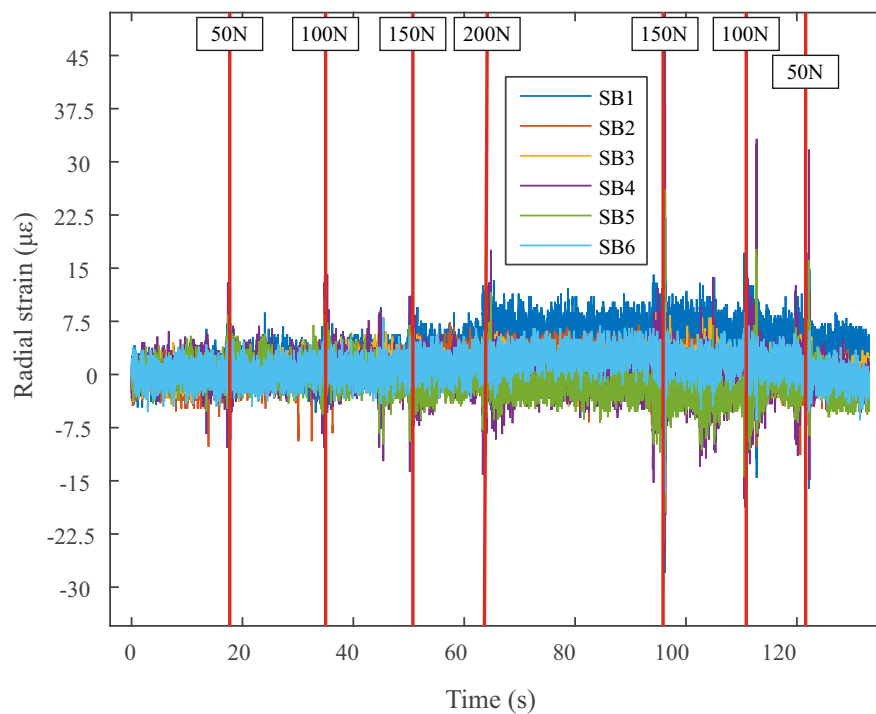


FIGURE 3.26: Normal load effect on the measured radial strains, experimental validation

To conclude the scaled dynamometric wheelset calibration, the influence of the point of application of the force on the wheel thread has also been analysed for the strain gauges. Several simulations have been carried out applying a combination of different

vertical, lateral and longitudinal loads. Those loads have been applied on three points of the wheel tread named as P1, P2 and P3 in Fig. 3.27. The goal of this analysis is to determine how the strain gauges and lateral lasers measurements change when the point of application of the force moves along the wheel tread.

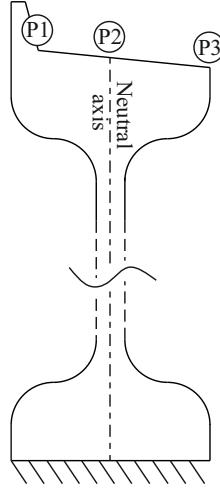


FIGURE 3.27: Points of application of the force in the wheel tread

Figure 3.28 shows the obtained results. For the sake of simplicity only strain bridge number 6 (see Fig. 3.14) is shown, but the conclusions can be extended to the other five. Orange, dark blue and yellow solid lines represent the radial strain measured by the strain bridge when a combination of a constant 60 N vertical load and a variable lateral loads are applied at point P1, P2 and P3, respectively. The line of application of the force coincides with radial line  $j = 6$  (see Fig. 3.14). The maximum uncertainty of the sensor is approximately  $\pm 2.5$  N. That correspond to a 4% error in the lateral load measurement using this technology. Again, longitudinal loads applied on the wheel tread do not affect the measured lateral force.



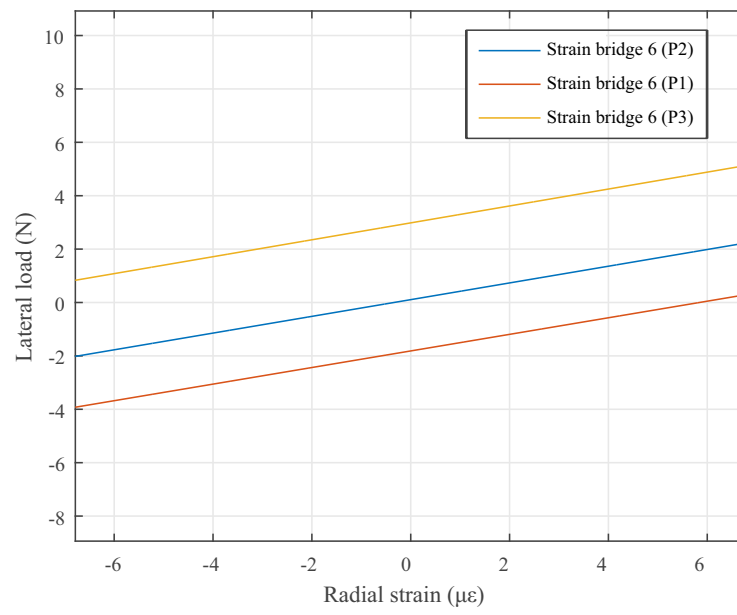


FIGURE 3.28: Influence of the contact point on the radial strain measurements



## Chapter 4

# Scaled Dynamometric Wheelset: Distance Lasers Approach

### 4.1 Dynamometric wheelset instrumented with non-contact distance sensors

In the previous chapter, the instrumentation of the scaled dynamometric wheelset with strain gauges has been presented. As it has been discussed, the strain gauges are a reliable method to measure the lateral contact force applied on the wheel. However the applied normal load cannot be obtained in such a straight forward way. To that end, a higher number of sensors and a more sophisticated installation procedure must be accomplished. In this PhD thesis due to the reduced dimensions of the instrumented wheelset and the limited number of input channels of the telemetry system, the vertical force measurement through out the radial strains has been refused. Nonetheless, there are also other instrumentation options used in the railways industry for the wheel/rail contact forces measurements.

The alternative to the strain gauges are the non-contact distance sensors based on laser or inductive technology. Unlike the strain gauges, these sensors do not need to be placed in rolling parts, but they are mounted in fixed parts such as the bearing

boxes. Their mission consists of measuring the deflection experimented by the wheel-web due to the forces acting on the wheel tread while the vehicle is running on the track. This technology has some advantages against strain gauges: On the one hand non wireless connections are needed since the sensors are not spinning with the wheel. On the other hand, lasers are a more enduring technology with less maintenance and easy to calibrate than strain gauges. Of course, they also have some drawbacks. For instance, due to the presence of mechanical parts such as the bearings between the sensors and the wheel-web, these sensors are also going to capture useless information. Housing clearance, lateral play and roll angle of the bearings are variables inherit to the measurement that must be considered in the force calculation algorithm in order to obtain a precise estimation.

In the scientific literature two main approaches can be found for the wheel-web lateral deflection measurement: inductive magnetic distance sensors or distance lasers. The first family was immediately dismissed because their minimum resolution is not small enough for the measurement of the tiny lateral deflection on the scaled system. Thus, distance laser technology has been finally chosen to measure the forces applied on the scaled wheelset. Vertical and lateral forces are going to be measured separately by two sets of distance lasers.

The first set consist of two sensors *MICRO-EPSILON optoNCDT-1302* mounted in both sides of the bogie frame front part, pointing towards the bearing boxes. Their measuring range can be established from 20 to 200 *mm* with a minimum resolution of 2  $\mu m$ . Figure 4.1 shows the mentioned sensors. They register the instantaneous deflection of the primary suspension of the dynamometric wheelset. Known the stiffness of the springs, the vertical force applied on the wheels can be easily obtained.

The measurement of the applied lateral force on the instrumented wheel requires a more sophisticated procedure than the normal force measurement. To that end, a second set consisting on three high precision distance lasers *MEL-M7L/0.5-10B* has been installed on the front left bearing box. The selected devices have a 500  $\mu m$  measuring range with a resolution up to 0.2  $\mu m$  and a maximum sampling rate of 54 *kHz*. For the sake of a better understanding, Fig. 4.2 shows an sketch of the lasers assembly in the vehicle. Lasers number one to three are rigidly attached to the front left bearing box. Several sliding mechanisms allow the precise positioning of the lasers in the radial and lateral



FIGURE 4.1: Vertical lasers mounting on the bogie frame

directions. The applied lateral force  $Q$  on the wheel tread is obtained as a combination of the measurement of the three lasers. Laser number two is pointing towards the axle central point. This sensor registers the relative lateral displacement of the wheelset with respect to the bearing box. Lasers one and three are pointing towards the wheel-web and they measure the lateral deflection experienced due to the applied lateral force  $Q$ . Figure 4.3 shows the final assembly of the instrumented wheelset, the high precision lateral lasers are numbered in red from one to three.

## 4.2 Lateral force estimation based on wheel-web deflections

The second method proposed for the lateral contact force estimation is based on the measurement of the wheel-web deflection with three high-precision lasers installed in the bearing box of the instrumented wheel, as explained above. Figure 4.2 on the left shows the positioning of the distance lasers. Parameters  $r_1$  and  $r_2$  are radial positions of the outer lasers while  $r_Q$  defines the radius of the point of application of the force. Figure 4.2 on right, shows coloured in red the deformed shape  $v(r)$  of the wheel when a lateral load  $Q$  is applied. The deflection experienced by the wheel is denoted as  $v(r_Q)$ . The model boundary condition establishes that the wheel hub is clamped to the surface in contact with the axle. As a result, deformed shape  $v(r)$  is obtained.

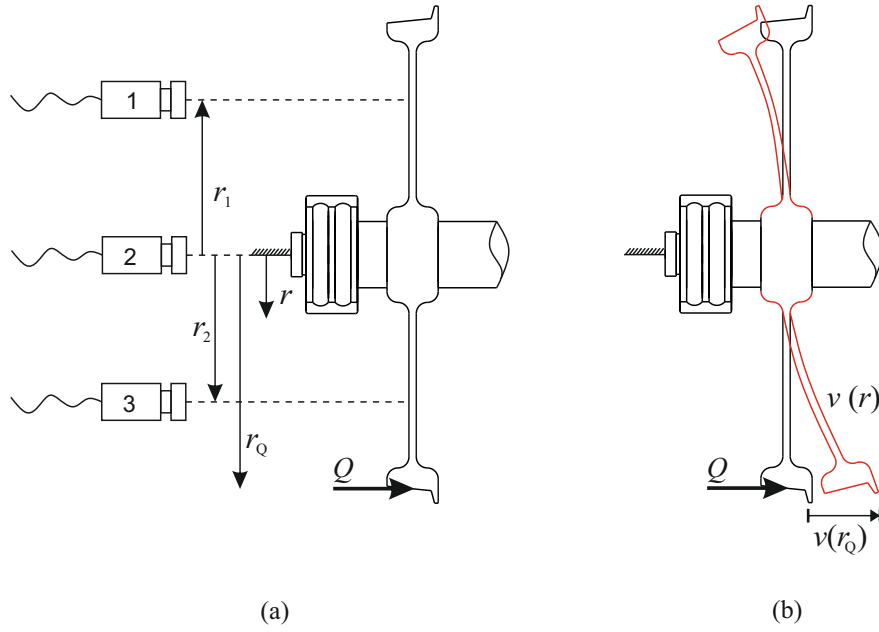


FIGURE 4.2: Lateral lasers mounting on the left bearing box

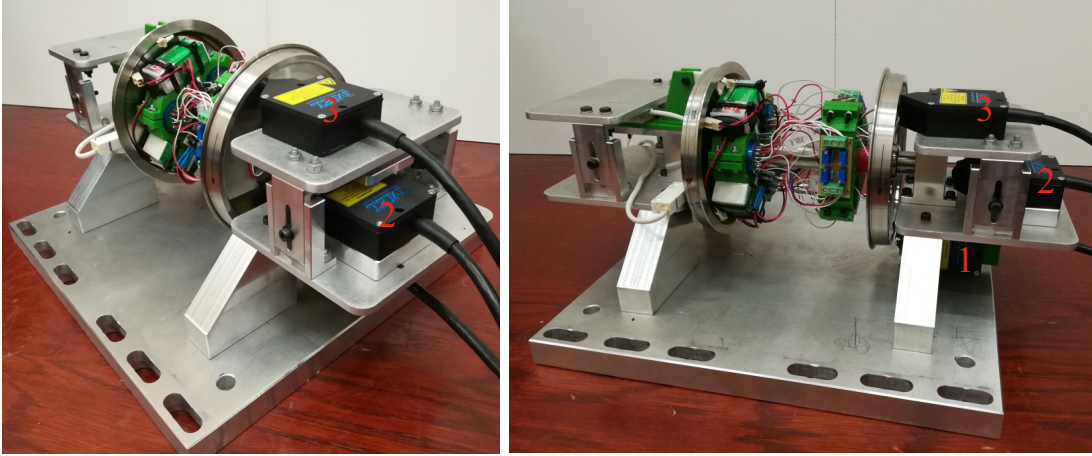


FIGURE 4.3: Final assembly of the dynamometric wheelset

Figure 4.4 shows the kinematic assumptions on which the method is based. The pale blue line represents the wheel reference diametrical plane of the instrumented wheel when no loads are applied on it. Assume that a lateral load  $Q$  is applied on the wheel contact patch. If the bearing has a certain play, the wheel reference diametrical plane sections moves laterally a distance  $y$ . If the bearing also allows some rotation  $\beta$  around  $O'$ , the wheel reference diametrical plane turns into the inclined green solid line.

Finally, due to the effect of the applied lateral load, the wheel acquires a deformed shape depicted with the solid magenta line. In the scenario presented so far, it is considered that the wheel-web surface, to which lasers 1 and 2 are pointing, is perfectly smooth, so that the deformed shaped will be independent of the wheelset rotation  $\theta$  around its axis. However, it has been proven that the scaled wheel web surface presents noticeable irregularities generated during the machining process and also the perpendicularity between the instrumented wheel and the axle is not perfect. This fact will be explained in detail in the next section.

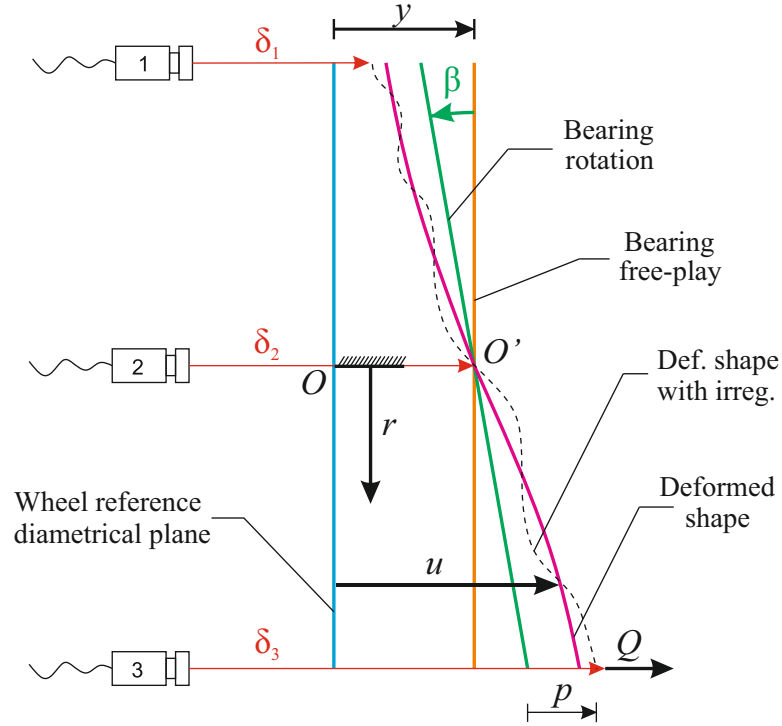


FIGURE 4.4: Laser based method kinematic assumptions

The lateral displacement of the wheel reference diametrical plane can be expressed as follows:

$$\begin{aligned}
u(r, t) &= y(t) + r\beta(t) + v(r)p(t) + \text{rug}(r, \theta(t)) = \\
&= \begin{bmatrix} 1 & r & v(r) \end{bmatrix} \begin{bmatrix} y \\ \beta \\ p \end{bmatrix} + \text{rug}(r, \theta(t)) = \\
&= \Phi(r)\mathbf{q} + \text{rug}(r, \theta(t))
\end{aligned} \tag{4.1}$$

where:

- $r$  and  $v(r)$  are the measuring radial distance (see Fig. 4.2) and the normalized deformed shaped experienced in that radial distance, respectively. The deformed shaped function  $v(r)$  is drawn from the FEM and depicted in Fig. 4.5.
- $y$  and  $\beta$  are the wheelset/axle-body relative lateral displacement and relative roll angle due to bearing play, and  $p$  is the displacement due to deformation at the point of application of the force.
- $\text{rug}(r, \theta(t))$  is the roughness function of the wheel. It depends on the rotated angle  $\theta$ , and it describes the wheel-web superficial roughness at a certain measuring radius  $r$ .

Evaluating Eq.(4.1) for the three lasers installed on the dynamometric wheelset, the following equations are obtained:

$$\begin{aligned}
u_1 &= \Phi(r_1)q + \text{rug}(r_1, \theta) \\
u_2 &= \Phi(r_2)q + \text{rug}(r_2, \theta) \\
u_3 &= \Phi(r_3)q + \text{rug}(r_3, \theta)
\end{aligned} \tag{4.2}$$

those equations can be used to find the bearing free-play  $y$ , bearing roll angle  $\beta$  and experienced deflection  $p$ . Once  $p(t)$  is obtained, the lateral force  $Q(t)$  is calculated as:

$$Q(t) = K_{FEM} \cdot p(t) \tag{4.3}$$



where  $K_{FEM}$  is the wheel lateral stiffness drawn from the FEM.

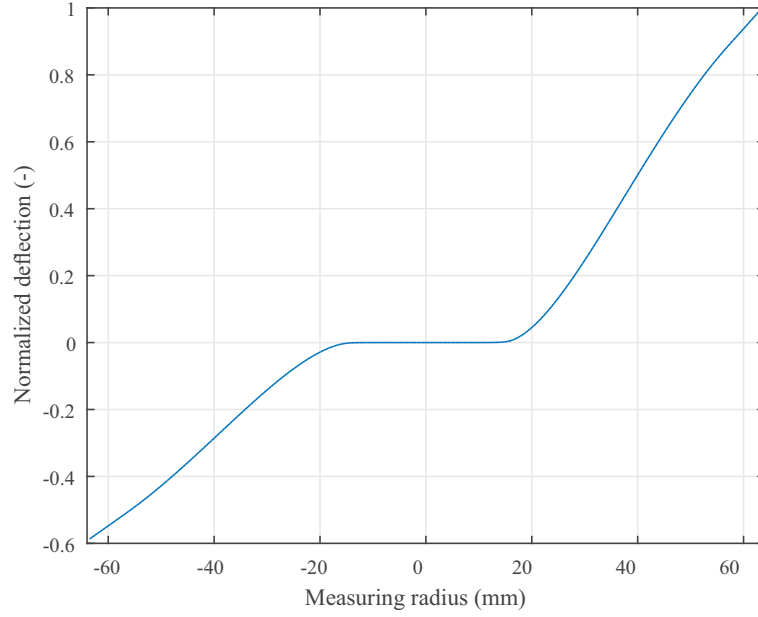


FIGURE 4.5: Deformed wheel web shaped when a unitary lateral load is applied

### 4.3 Primary suspension lasers calibration

As explained before, the normal load applied on the instrumented wheel is calculated through the deflections experienced by the primary suspension elements, which are measured by two distance lasers installed at both sides of the bogie frame. Due to the fact that the points of application of the forces on the wheel profiles are not aligned with the points of application of the suspension forces, the latter cannot be directly considered as applied vertical forces on the wheels. To that end, the applied vertical forces on the instrumented wheel can be easily calculated establishing balance of forces and torques at one contact point of the wheelset, knowing its geometry. In the scaled vehicle used in this research, the mentioned misalignment is not substantial, so the suspension force is approximately equal to the normal force on the wheel. It is assumed that the variation of the direction of application of the force due to the wheel conicity

is negligible to the normal force calculation. This is reasonable taking into account that the lateral displacement of the wheelset is not measured experimentally.

The wheelsets in the instrumented vehicle are connected to the bogie frame by four pairs of helical springs assembled in parallel (see Fig. 3.6). These springs have been previously tested on a general-purpose test machine obtaining an individual average stiffness of  $17.21 \text{ N/mm}$ . If the method proposed to measured the vertical load applied is valid, the same spring stiffness calculated with the test machine should be measured with the vertical lasers installed on the vehicle. Figures 4.6 and 4.7 show the experimental results obtained from the vertical lasers when the vehicle is loaded with known weights as depicted in Fig. 3.25. Pale blue lines on the graphs are the primary suspension displacements measured by the lasers during the test while dark blue lines represent the real spring stiffness measured in the test machine. As it can be observed, there is a good agreement between both methods, so that, it can be conclude that normal loads applied on the vehicle can be estimated by the measurement of primary suspension deflection.

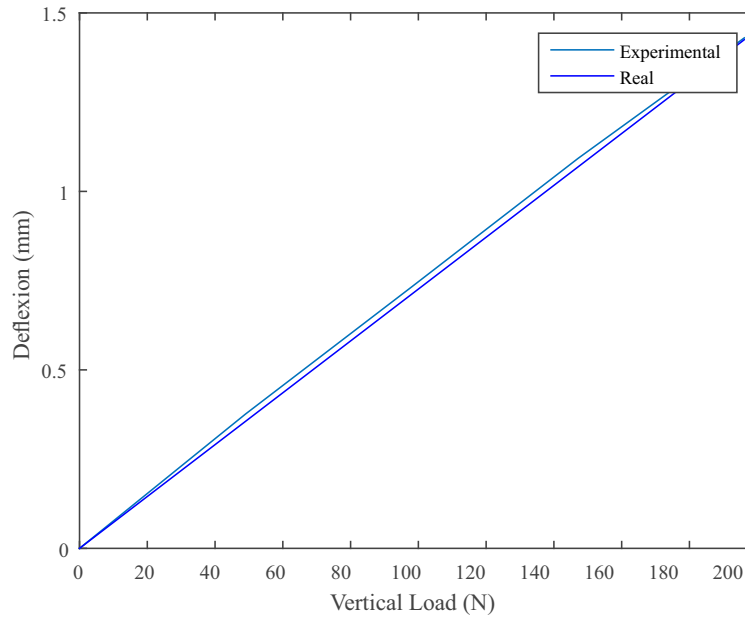


FIGURE 4.6: Right Side Vertical Laser Calibration

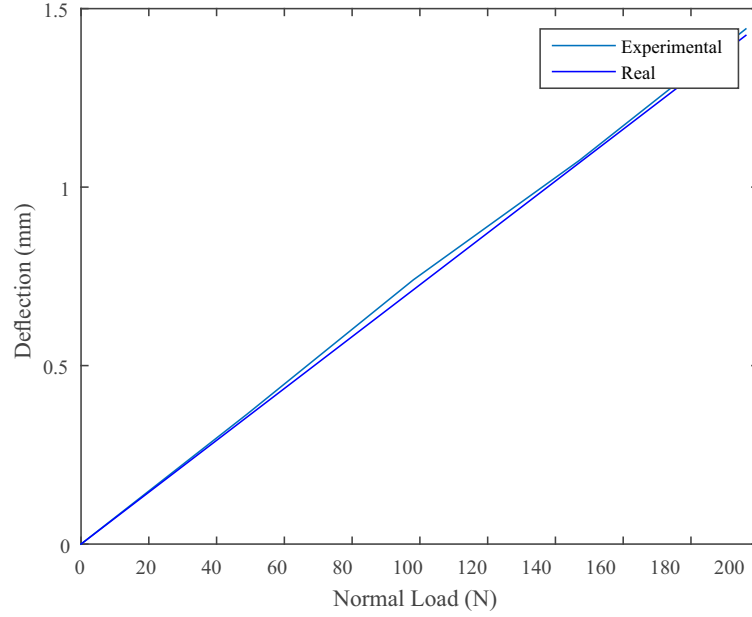


FIGURE 4.7: Left Side Vertical Laser Calibration

#### 4.4 Calibration of the lateral precision lasers

The lateral high precision lasers have been also tested in the calibration test bench in order to obtain a univocal relation between the instantaneous forces applied on the wheel and the deflections measured by these sensors. Figure 4.8 shows the comparison between the FEM simulation and the experimental measurements. As it can be observed, there is a good accordance between both sets of data. That means the FEM has been successfully developed and the numerical results drawn from it can be used in the lateral force estimation algorithm presented before in this chapter. Figure 4.8 shows the measurements of the lasers number one and three (see Fig 4.2) named as upper and lower respectively, after subtracting the measurement of laser number 2. Thus, measurement of laser number two is implicit on the graph. As mentioned before the central laser captures the axial play between the axel and the bearing box, thus magenta and green lines on the graph are the result of subtracting laser number two measurement to the measurement of lasers one and three respectively.

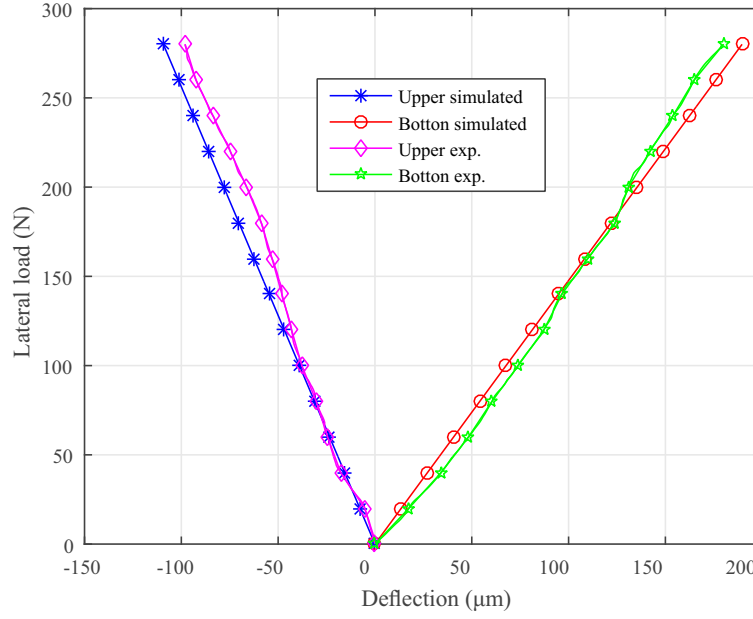


FIGURE 4.8: Lateral deflection vs applied lateral load, experimental validation

The influence of the point of application of the force on the experienced wheel-web deflection has also been analysed as done before with the strain gauges. Figure 4.9 shows the variation of the lateral deflection experienced by the wheel web when a combination of a 60 N vertical load and a variable lateral load  $Q$  are applied on points P1, P2 and P3 of the wheel tread (see Fig. 3.27). The value of the vertical load has been set to 60 N. It is known from the multibody dynamics simulation of the vehicle that the vertical load on the wheel fluctuates around that value (a quarter of the vehicle total mass). Dark blue, orange and yellow solid lines in Fig. 4.9 are the deflection measurements of the upper lateral laser when the load are applied on point P1, P2 and P3, respectively. Purple, green and pale blue lines are the bottom laser measurements at the same three points. It is observed an uncertainty of  $\pm 2.5$  N approximately in the lateral force, in both sensors measurements when the applied load moves from point P1 to P3. This is due to, when the vertical load is applied further from the neutral axis of the wheel web, a bending moment appears that produce a small lateral deflection even when no lateral loads are applied on the wheel. That uncertainty due to the variation of the contact point on the wheel tread corresponds to a 4% in the lateral force based on the lateral lasers measurements. This experiment has been also carried

out applying a longitudinal load at point P1, P2 and P3 within any variation on the measurements. Thus it can be said that the longitudinal loads do not affect the lateral force measurement.

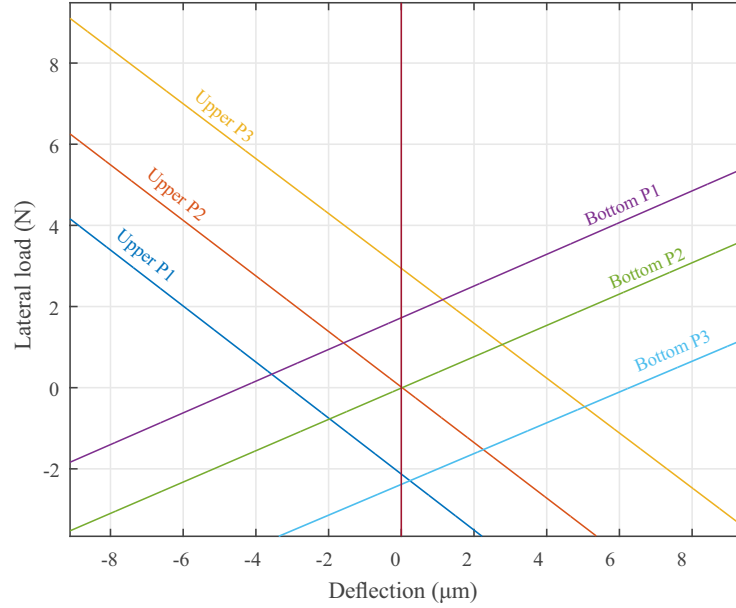


FIGURE 4.9: Influence of the contact point on the lateral lasers measurements

The angular position of the wheel  $\theta$  (see Fig. 4.10) should not be considered a priori during the contact forces measuring process since the lasers are installed on fixed parts of the vehicle as explained before in this chapter. In an scenario where no forces are applied on the wheel, the precision lasers should measure an almost constant value corresponding to the sensor offset and noise, even when the wheel is spinning. This assumption would be true provided that wheel and shaft were perfectly perpendicular to each other and the wheel web surface was totally smooth without any irregularity. However, experiments have shown that the previous assumption is wrong. The three lasers register a variable measurement when the wheel spins unloaded.

Figures 4.11 to 4.13 shows the deflection measured by the precision lasers when the wheel rotates unloaded. Coloured lines on the graphs represent the sensor measurement along one wheel turn. As it can be observed, there is a repetitive pattern in the measurements of the three lasers when no loads are applied on the wheel. That means the wheel web surface is not perfectly flat and the wheel and the shaft are not

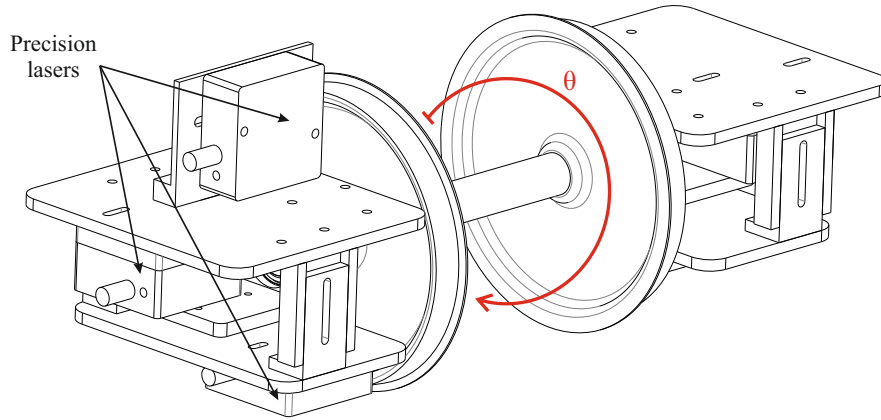


FIGURE 4.10: Lateral deflection vs applied lateral load, experimental validation

totally perpendicular to each other. For a correct measurement of the real deflection experimented by the wheel when a lateral load is applied on its tread, it is necessary to identify these patterns. Figures 4.14 to 4.16 shows the functions identified versus the absolute angular position of the wheel respect to the bearing box. These functions have been obtained in an experiment where the wheel has rotated unloaded one hundred times registering a deflection data per rotated degree on the wheel. Blue lines on Figs. 4.14 to 4.16 are the average of the data collected at each angular position. In view of the noisy shape of the graphs the pattern function have been filtered in order to obtain an smoother shape (orange lines on the graphs). This last set of functions are the roughness functions introduced as inputs in the system of equations (4.2).

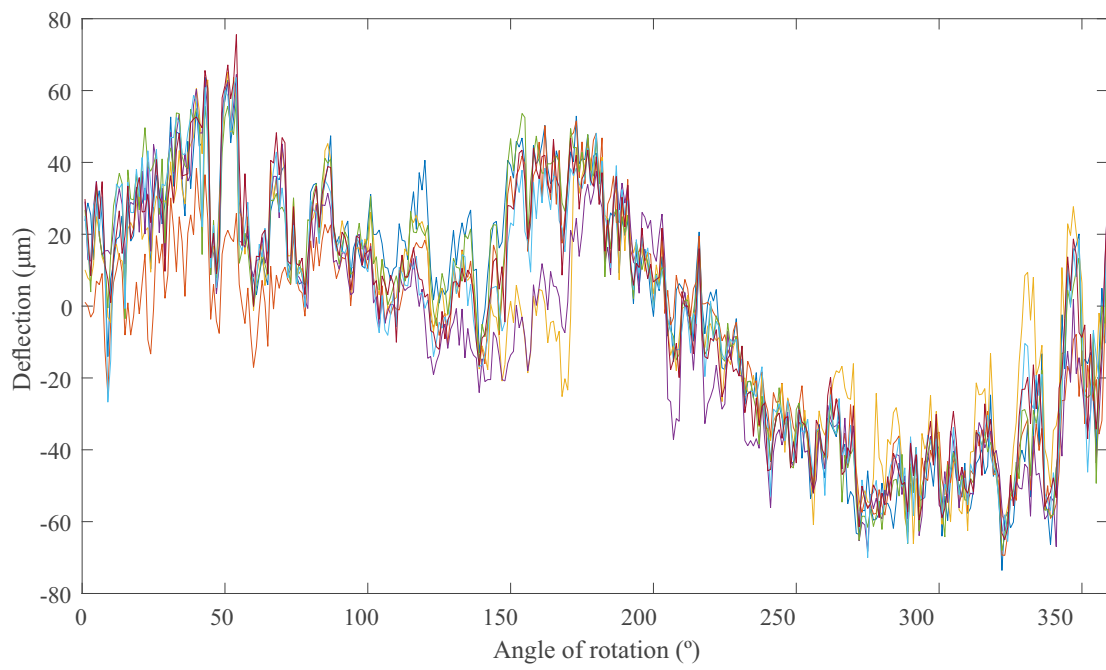


FIGURE 4.11: Upper Laser Raw Measurement

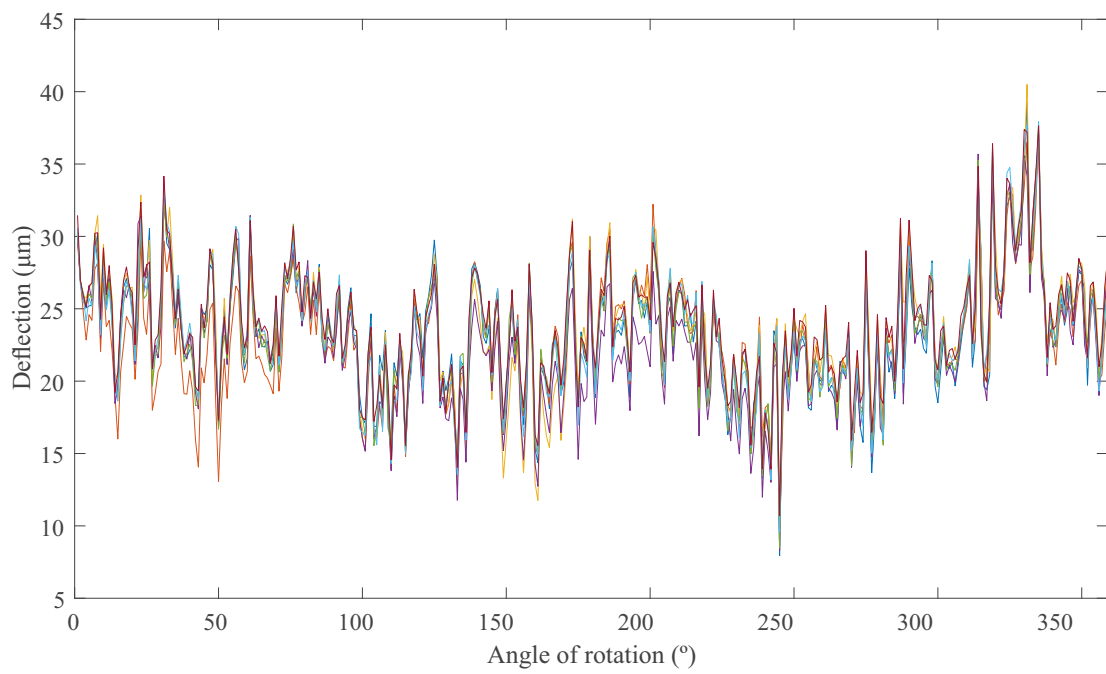


FIGURE 4.12: Central Laser Raw Measurement

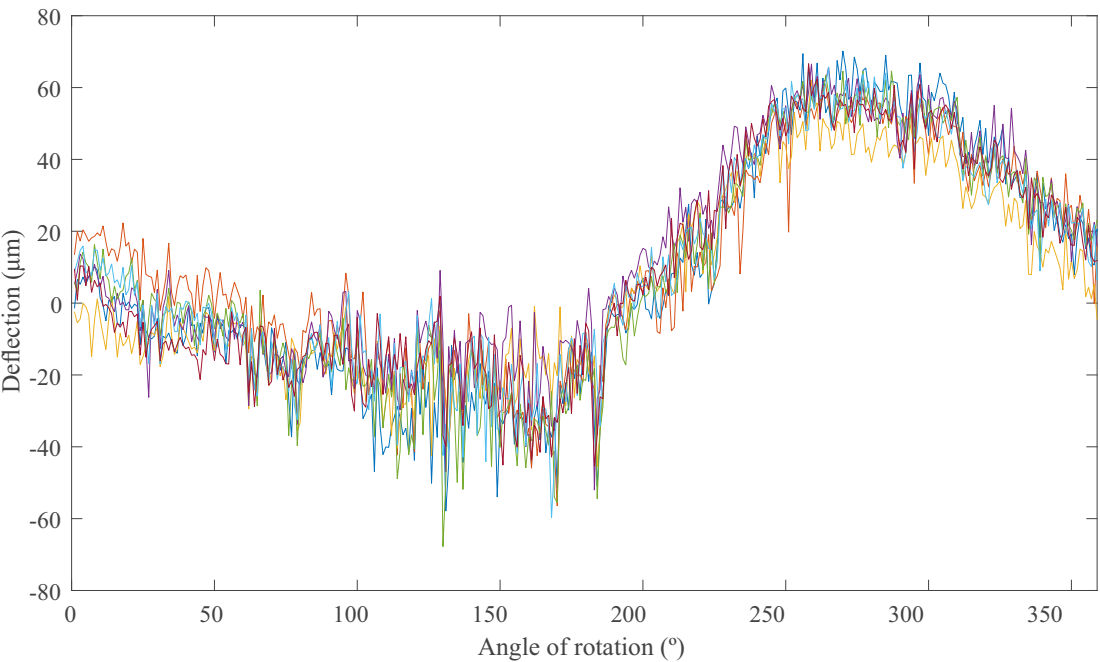


FIGURE 4.13: Bottom Laser Raw Measurement

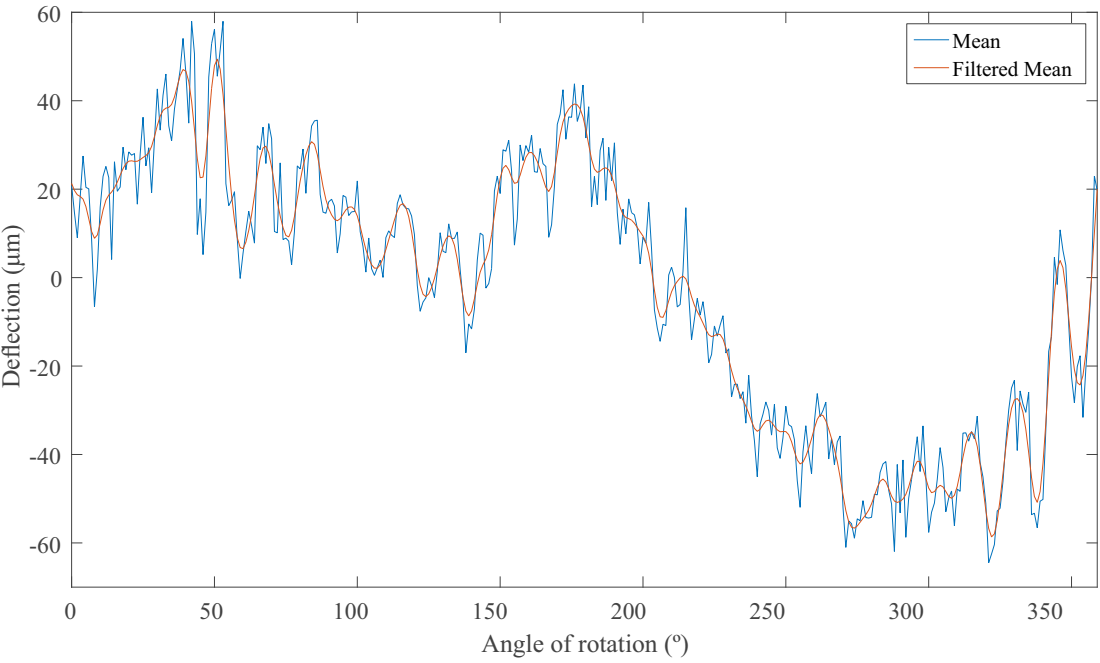


FIGURE 4.14: Upper Laser Irregularity Pattern



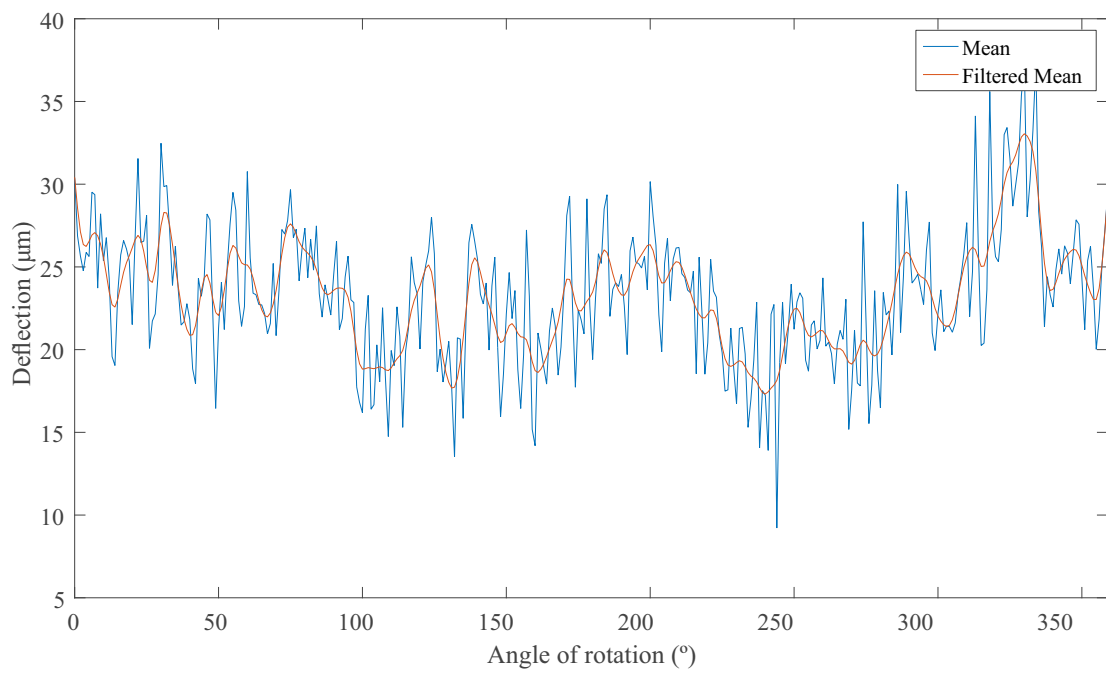


FIGURE 4.15: Central Laser Irregularity Pattern

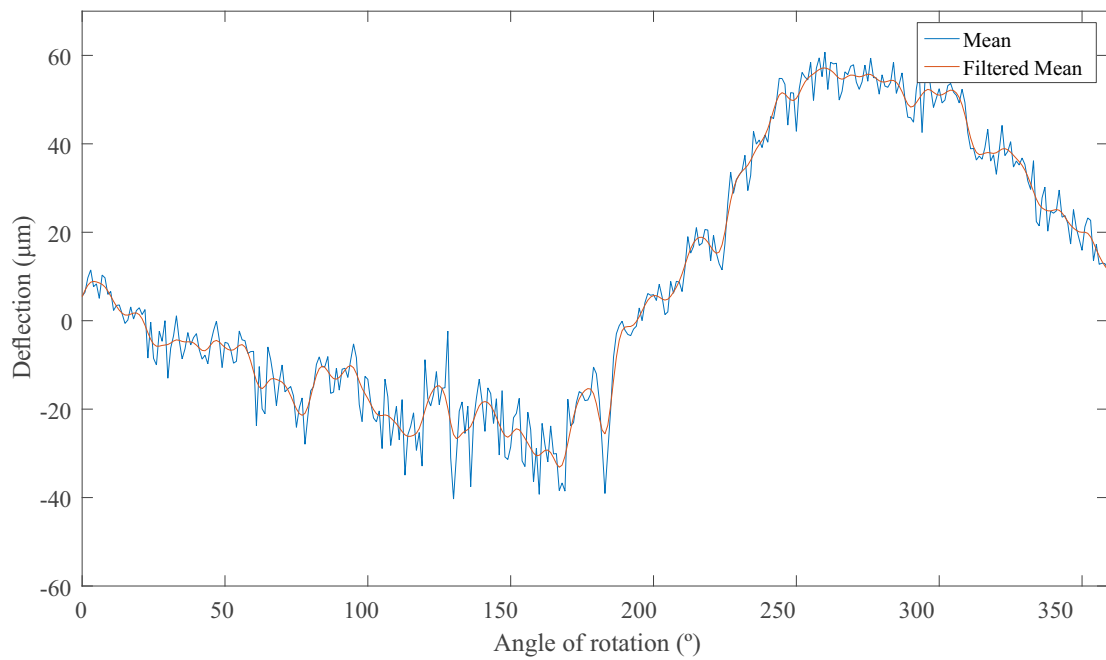


FIGURE 4.16: Bottom Laser Irregularity Pattern

Once the roughness functions have been identified, it is necessary to probe that removing this component from the lasers measurements the assumption that "*with no loads applied on the wheel the lasers must register an almost constant value*" is now fulfilled. To that end a last experiment has been carried out in the calibration test bench. In that trial the instrumented wheelset was spinning free while the three laser sensors recorded the deflection and no loads were applied. Figures 4.17 to 4.19 show the experimental results obtained during a test. Blue lines represent the raw measurements of the lasers and lines coloured in orange are the results once the roughness functions were subtracted from the raw data. As it can be observed, the irregularity correction reduces the static measurement of the lasers from dozens of microns to just a few microns. More precise data could not be obtained since there are some uncertainties very difficult to analyse such the vibrations induced by the wheelset rotation to the laser sensors. The vibration induced by the track when the instrumented vehicle is running on it also have a negative impact on the laser sensors measurements.

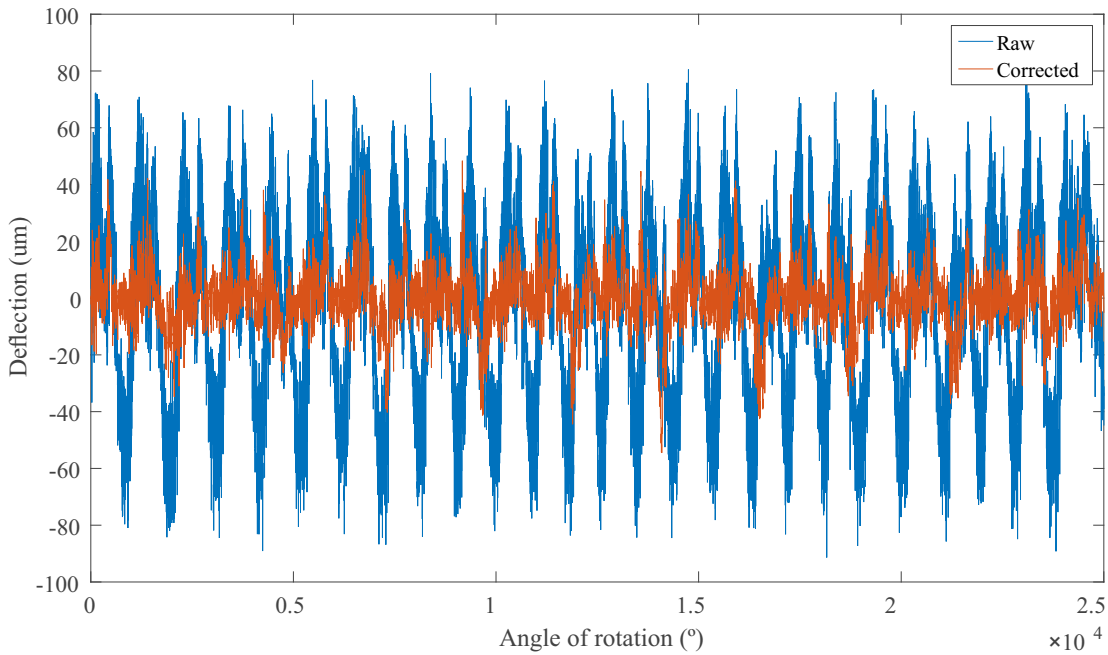


FIGURE 4.17: Upper Laser Raw and Corrected Measurement

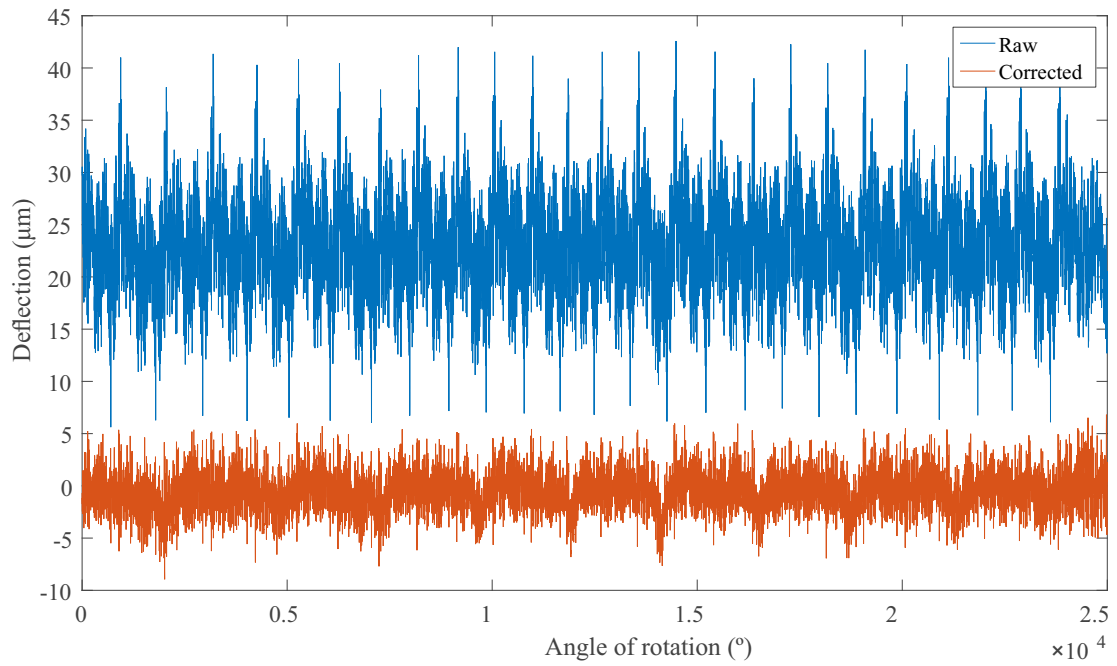


FIGURE 4.18: Central Laser Irregularity Pattern

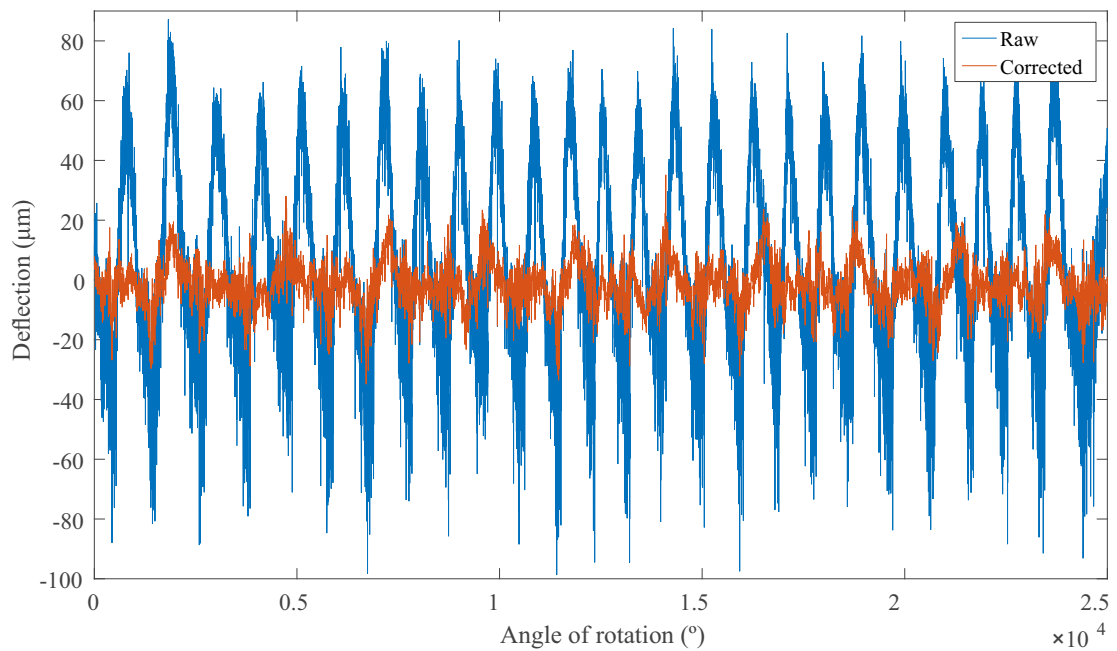


FIGURE 4.19: Bottom Laser Raw and Corrected Measurement



## Chapter 5

# Numerical Modelling

### 5.1 Introduction

Computational modelling represents an inexpensive and effective way to validate the dynamics of railroad vehicles. Nowadays, one can find acceptance norms for railways vehicle based on numerical simulation [102]. The European norm EN-14363 or the British norms GM/RT2141 and TT0088 are some of them. Other countries such as USA, Australia, Japan, China and Korea also allow the use of simulation for vehicle approval. The success of this process lies in the development of a precise and efficient computational model of the multibody system. From an economical point of view the numerical modelling represent the optimal solution to analyse and validate the performance of a railway vehicle. Any railways manufacturer wants to have a fast and precise simulation software that allow their engineers to analyse the dynamic performance of new designs reducing as much as possible expensive field tests.

The Department of Mechanical Engineering at the University of Seville have been working over a decade in the development of high efficient and precise dynamics computational models of different types of railway vehicles. In this chapter two different computational formulations of a railway vehicle are going to be presented. The scaled vehicle used in this PhD thesis has been modelled using both computational approaches and their numerical results will be compared with the experimental measurement obtained

with the actual vehicle. The first approach presented is a a multibody model of a rail-way vehicle with weakly coupled vertical and lateral dynamics is presented. The second one is a non-linear full 3D coupled dynamic model.

## 5.2 Multibody model with weakly coupled vertical and lateral dynamics

In this section a simplified model based on the assumption of weakly coupled lateral and vertical dynamics is presented. The development of this model has not been part of this PhD thesis. A more detailed description of the model can be found in [103]. Longitudinal dynamics is solved separately although its effects are implicit in the lateral and vertical dynamics formulations. The wheel/rail contact problem is solved using the so called knife-edge-contact approach and the concept of equivalent conicity. The track geometry is introduced as an input of the model, also dealing with track irregularities. One of the key points of the presented model is its simplicity, make it real time capable. Its simple formulation is possible thanks to the lateral and vertical dynamics decoupling and multiple linearisation in the equations of motion.

### 5.2.1 Coordinates and frames in the multibody model

As it is well known, in railways multibody modelling is convenient to formulate the equations of motion of the vehicle with respect to an intermediate frame (neither inertial nor body fixed) that is the so called *Track Frame* (TF). In the movement of the TF, it is assumed to keep its X axis tangent to the track centre line. It is important to note that for the TF definition no track irregularities are considered.

In the reduced model formulation a main TF has been defined. It is called *Vehicle Track Frame* (VTF),  $\langle X^{vt} Y^{vt} Z^{vt} \rangle$ , that moves together with the vehicle at the same forward speed along the track. Figure 5.1 shows coloured in purple the mentioned VTF together with other reference frames common in the railroad modelling. The VTF must be positioned with respect to the *Global Frame* (GF),  $\langle X Y Z \rangle$ , depicted in red in the figure, being its position and orientation a function of the arc-length coordinate

$s^{vt}$ . Every body that constitute the entire vehicle have its own TF, named *Body Track Frame* (BTiF),  $\langle X^{bti} Y^{bti} Z^{bti} \rangle$ . This frame, coloured in orange in the figure is assumed to follow the gross motion of body  $i$  along the track, and it is positioned at  $s = s^{vt} + s^i$ . Taking into account that the longitudinal dynamics of the vehicle is not considered in this reduced model, the longitudinal relative position between the bodies  $s^i$  will always remain constant. Finally, each body  $i$  has a *Body Frame* (BiF),  $\langle X^i Y^i Z^i \rangle$ , attached to the centre of mass of the body (depicted in dark green in Fig. 5.1).

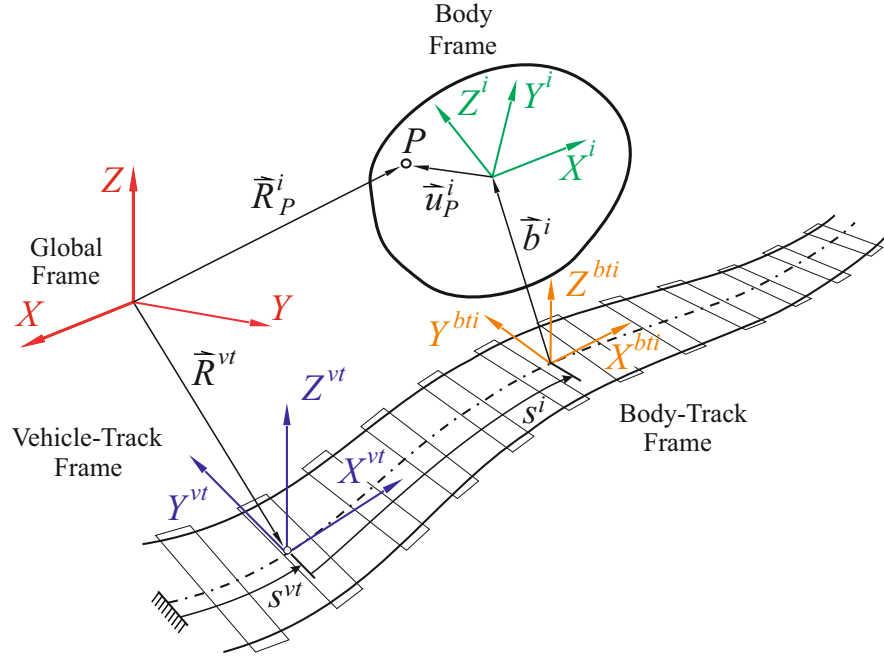


FIGURE 5.1: Frames of reference used in the railroad modelling

Among the different bodies that constitute a railroad vehicle, wheelsets must be treated in a different way. First because its kinematics differs in a way from the other bodies, and second due to the wheel/rail contact phenomenon takes place on it. So then, the following reference frames depicted in Fig. 5.2 must be defined to describe the wheelset kinematics:

- *Wheelset-Track Frame* (WTiF),  $\langle X^{wti} Y^{wti} Z^{wti} \rangle$ , coloured in grey in the figure.
- *Wheelset Frame* (WiF),  $\langle X^{wi} Y^{wi} Z^{wi} \rangle$ , coloured in green in the figure.

- *Wheelset-Intermediate Frame* (WliF),  $\langle X^{wIi} Y^{wIi} Z^{wIi} \rangle$ , coloured in dark blue in the figure. This reference frame has the peculiarity of keeping its  $X^{wIi}$  parallel to the horizontal plane. That means no pitch rotation is allowed. This is interesting because the orientation of the WliF with respect to the WTiF can be defined using small angles and also because the definition of the contact points in the WliF experiments small variations along time.
- *Left Wheel Profile Frame* and *Right Wheel Profile Frame* (LPiF and RPiF),  $\langle X^{lpi} Y^{lpi} Z^{lpi} \rangle$  and  $\langle X^{rpi} Y^{rpi} Z^{rpi} \rangle$ . They are located approximately at the centre of both wheels and they are obtained after a rotation  $\alpha$  (the equivalent conicity) of the WliF around  $X$  axis.

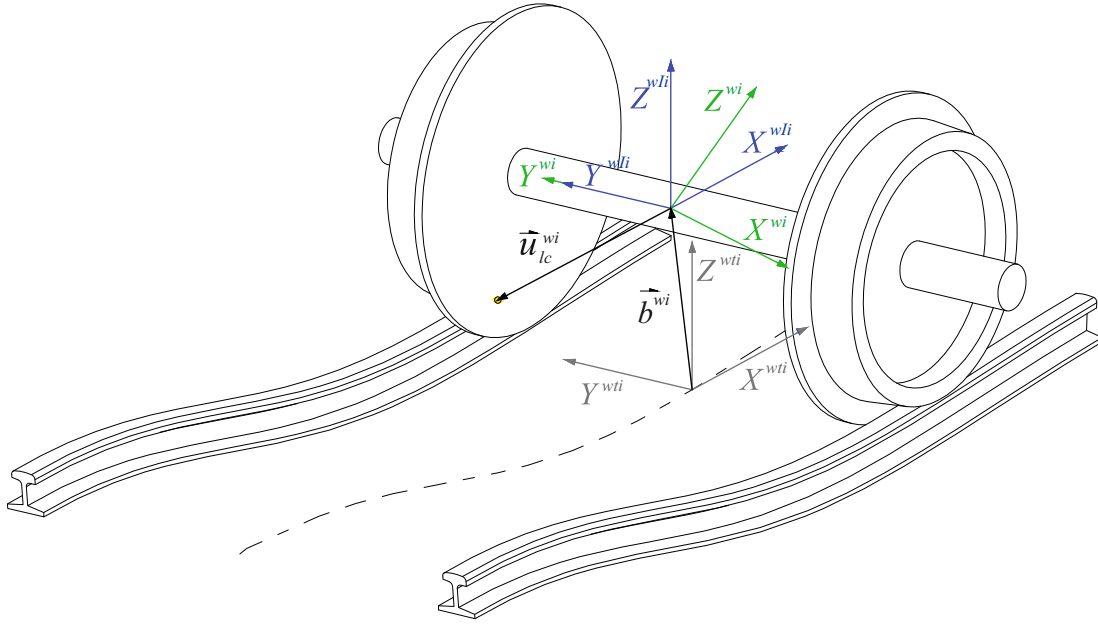


FIGURE 5.2: Wheelset-track frame, wheelset frame and wheelset intermediate frame

Finally, rails must also be precisely defined. Figure 5.3 shows a sketch of the rails and the two necessary reference frames. They are named as *Left Rail-Head Frame* (LRF) and *Right Rail-Head Frame* (RRF),  $\langle X^{lr} Y^{lr} Z^{lr} \rangle$  and  $\langle X^{rr} Y^{rr} Z^{rr} \rangle$ . These frames have an orientation with respect to the TF defined for each value of the arc-length coordinate  $s^t$ .



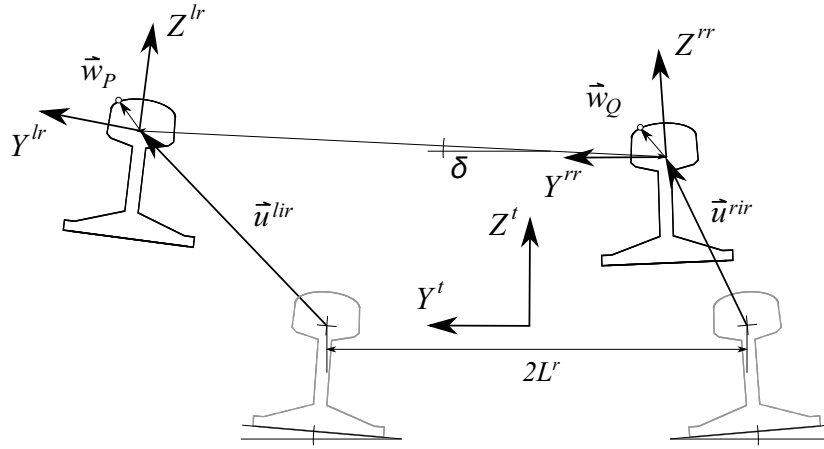


FIGURE 5.3: Rail-head frames

### 5.2.2 Kinematics notation of the multibody model

In this section the kinematics of the different elements that constitute the simulation model is presented. For a correct kinematics description of the problem is important to describe unequivocally and precisely every single element of the system. Hereafter the following notation is going to be used for the kinematics description of the reduced model:

1.  $\vec{R}$  is a position vector whose origin is located at the GF.
2.  $\vec{r}$  is a position vector whose origin is located at the VTF.
3.  $\vec{b}$  is a position vector whose origin is located at the BTiF or the WTiF in case of wheelsets.
4.  $\vec{u}$  is a position vector whose origin is located at the BiF (WiF or WliF in case of a wheelset).
5. Bold symbols without diacritic like  $\mathbf{v}$ , are 3 x 1 column matrices whose elements are the component of vector  $\vec{v}$  in the GF.
6. Bold symbols with "bar" diacritic like  $\bar{\mathbf{v}}$ , are 3 x 1 column matrices whose elements are the component of the vector  $\vec{v}$  in the VTF.

7. Bold symbols with "arc" diacritic like  $\widehat{\mathbf{v}}$ , are 3 x 1 column matrices whose elements are the component of the vector  $\vec{v}$  in the BTiF (WTiF in case of a wheelset or TF in case of rails cross-sections).
8. Bold symbols with "hat" diacritic like  $\hat{\mathbf{v}}$ , are 3 x 1 column matrices whose elements are the component of the vector  $\vec{v}$  in the BiF (WliF in case of a wheelset body).
9. Bold symbols with "inverted arc" diacritic like  $\check{\mathbf{v}}$ , are 3 x 1 column matrices whose elements are the component of the vector  $\vec{v}$  in the WiF.
10. Bold symbols with "tilde" diacritic like  $\tilde{\mathbf{v}}$ , are 3 x 1 column matrices whose elements are the component of the vector  $\vec{v}$  in the wheel profile frame (LPiF or RPiF).

Concerning to the matrices notation, a symbol like  $\mathbf{A}^2$  represents a rotation matrix that projects the components of a vector given in frame B<sub>2</sub>F to the global frame. In case of using two superscripts like  $\mathbf{A}^{wt3, wI3}$ , it means the matrix that projects the components of a vector given in the WI<sub>3</sub>F to WT<sub>3</sub>F.

### 5.2.3 Kinematics of the track

The position of an arbitrary point of the track centreline is written as:

$$\mathbf{R}^t(s) = \begin{bmatrix} R_x^t(s) & R_y^t(s) & R_z^t(s) \end{bmatrix}^T \quad (5.1)$$

where  $s$  is an arbitrary arc-length.

The track ideal CL is described by the horizontal and the vertical profile both defined by a set of different length and geometry sections. In the horizontal profile description three different kind of sections can be found: straights, transitions and curves. The vertical profile is described just by two types of sections: straight and transitions. The different sections in the horizontal and vertical profile are connected by vertices. It is important to note that the horizontal and vertical vertices do not have to necessary coincide. The track centre line is fully described by the following geometric parameters:

- Horizontal curvature  $\rho_h$
- Vertical curvature  $\rho_v$
- Twist curvature  $\rho_{tw}$
- Spatial-derivative of horizontal curvature  $\rho_h'$
- Vertical slope  $\alpha_v$

Table 5.1 shows the values of the above mentioned parameters for the horizontal profile description, where  $R_h$  stands for curve radius,  $f_{lin}(s)$  is a linear function of the arc-length coordinate that is zero at the straight end and one at the curved end.  $\varphi_P$  is the cant angle at the curved section and  $L_{ht}$  is the length of the transition section. Table 5.2 shows an equivalent description for the vertical profile, where  $\alpha_{v1}$  and  $\alpha_{v2}$  are the slopes of the straight section before and after the transition, and  $L_{vt}$  is the length of the transition section.

TABLE 5.1: Horizontal profile description

Section	$\rho_h$	$\rho_{tw}$	$\rho_h'$
Straight	0	0	0
Circular	$1/R_h$	0	0
Transition	$f_{lin}(s)(1/R_h)$	$f_{lin}(s)\varphi_P$	$1/(L_{ht}R_h)$

TABLE 5.2: Vertical profile description

Section	$\alpha_v$	$\rho_v$
Straight	Constant	0
Transition	$\alpha_{v1} + f_{lin}(s)(\alpha_{v2} - \alpha_{v1})$	$(\alpha_{v2} - \alpha_{v1})/L_{vt}$

Every point of the track centreline described by Eq. 5.1 has an associate TF whose orientation with respect to the GF are given by the Euler angles of yaw  $\psi^t$  (heading angle), roll  $\phi^t$  (cant angle) and pitch  $\theta^t$  (vertical slope), corresponding to a rotation sequence Z-X-Y (see Fig. 5.4). It is important to note that the pitch and roll angles normally takes small values, that means the orientation matrix of the TF with respect

to the GF can be linearised as:

$$\mathbf{A}^t(s) \cong \begin{bmatrix} \cos(\psi^t) & -\sin(\psi^t) & \varphi^t \sin(\psi^t) + \theta^t \cos(\psi^t) \\ \sin(\psi^t) & \cos(\psi^t) & \theta^t \sin(\psi^t) - \varphi^t \cos(\psi^t) \\ -\theta^t & \varphi^t & 1 \end{bmatrix} \quad (5.2)$$

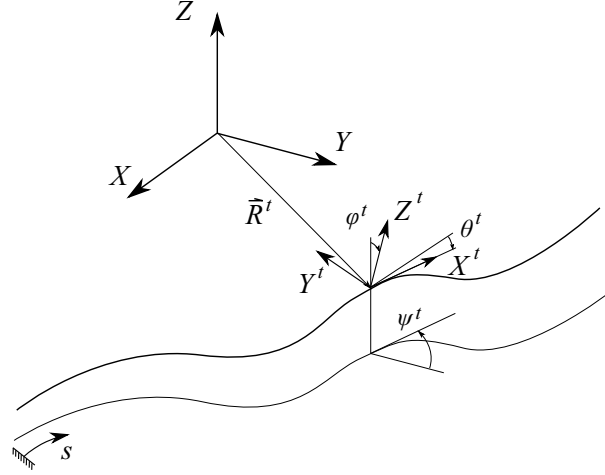


FIGURE 5.4: Track frame at centreline

The velocity and acceleration of an arbitrary body that moves along the track CL following the same orientation that the TF are written as:

$$\widehat{\mathbf{R}}^t = \begin{bmatrix} V & 0 & 0 \end{bmatrix}^T, \quad \widehat{\mathbf{R}}^t = \begin{bmatrix} \dot{V} & \rho_h V^2 & -\rho_v V^2 \end{bmatrix}^2 \quad (5.3)$$

In a similar manner, the angular velocity and angular acceleration are given by:

$$\widehat{\boldsymbol{\omega}}^t = \begin{bmatrix} \rho_{tw} V & \rho_v V & \rho_h V \end{bmatrix}^T, \quad \widehat{\boldsymbol{\alpha}}^t = \begin{bmatrix} \rho_{tw} \dot{V} & \rho_v \dot{V} & \rho_h \dot{V} + \rho_h' V^2 \end{bmatrix}^T \quad (5.4)$$

#### 5.2.4 Kinematics of the rail head centrelines

For the definition of the rail head centreline in the reduced model an arbitrary track with irregularities is going to be considered. As explained in Chapter 2, track irregularities are deviations of the rail cross-sections from the design positions (see Fig. 5.3).

Irregularity vectors of left and right rails are defined as:

$$\bar{\mathbf{r}}^{lir}(s) = \begin{bmatrix} 0 & r_y^{lir}(s) & r_z^{lir}(s) \end{bmatrix}^T, \quad \bar{\mathbf{r}}^{rir}(s) = \begin{bmatrix} 0 & r_y^{rir}(s) & r_z^{rir}(s) \end{bmatrix}^T \quad (5.5)$$

The components of vectors above, allow the definition of the four track irregularities present on an arbitrary track named as: track gauge  $\xi_g$ , lateral alignment  $\xi_a$ , cross-level  $\xi_{cl}$  and vertical profile  $\xi_{vp}$ . Their expressions are:

$$\begin{aligned} \xi_g &= (r_y^{lir} - r_y^{rir}), & \xi_a &= (r_y^{lir} + r_y^{rir})/2 \\ \xi_{cl} &= (r_z^{lir} - r_z^{rir}), & \xi_{vp} &= (r_z^{lir} + r_z^{rir})/2 \end{aligned} \quad (5.6)$$

### 5.2.5 Kinematics of arbitrary vehicle bodies

An arbitrary body of the vehicle can be described by the following set of generalized coordinates:

$$\mathbf{q}^i = \begin{bmatrix} y^i & z^i & \varphi^i & \theta^i & \psi^i \end{bmatrix}^T \quad (5.7)$$

The position and orientation of an arbitrary BiF with respect to its BTiF is described as:

$$\widehat{\mathbf{b}}^i = \begin{bmatrix} 0 & y^i & z^i \end{bmatrix}^T, \quad \mathbf{A}^{bti,i} = \begin{bmatrix} 1 & -\psi^i & \theta^i \\ \psi^i & 1 & -\varphi^i \\ -\theta^i & \varphi^i & 1 \end{bmatrix} \quad (5.8)$$

where  $\widehat{\mathbf{b}}^i$  is the position vector and  $\mathbf{A}^{bti,i}$  is the rotation matrix assuming small angle approximation.

Figure 5.5 shows the kinematic representation of an arbitrary vehicle body that moves on an irregular track. The position of an arbitrary point  $P$  of body  $i$  in the GF can be written as:

$$\mathbf{R}_P^i(s^{vt}, \mathbf{q}^i) = \mathbf{R}^{vt} + \mathbf{A}^{vt} \bar{\mathbf{r}}_P^i \quad (5.9)$$

where,  $\mathbf{R}^{vt}$  and  $\mathbf{A}^{vt}$  are the position and orientation matrix of the VTF, and  $\bar{\mathbf{r}}_P^i$  is the position of point  $P$  expressed in the VTF. This latter term can be expanded as:

$$\bar{\mathbf{r}}_P^i(s^{vt}, \mathbf{q}^i) = \bar{\mathbf{r}}^{bti}(s^{vt}) + \mathbf{A}^{vt,bti}(s^{vt}) \left[ \widehat{\mathbf{b}}^i + \mathbf{A}^{bti,i} \hat{\mathbf{u}}_P^i \right] \quad (5.10)$$



### 5.2.7 Wheel-rail contact kinematics constraints

In the wheel-rail contact scenario there are normally two surfaces involved, the wheel and the rail head profiles. Although this approach has been used in railways simulations for decades and it represents one of the most precise ways to describe the wheel-rail contact problem it has some drawbacks from the computational efficiency point of view. Firstly because it requires to solve the wheel-rail contact constraint each time step during the dynamic simulation and secondly because when the flange contact occurs the contact point position in the wheel and the rail suddenly changes. Integrators find difficulties when dealing with these situations, reducing their efficiency as a result. However, when the wheelset is running centred on the track the values of the coordinates that describe the position of the contact point vary smoothly, that is not a problem for the integrator.

Several approaches can be used to minimize these effects and make the simulation as efficient as possible. As it is well known, one common approach is the use of contact lookup tables, or the use of elastic methods to deal with the flange contact scenario. In the reduced model presented in this chapter an alternative solution to the wheel-rail contact problem has been used. In this new contact approach the rail cross-sections are considered dimensionless, having been reduced to a single point. Furthermore the wheel profiles are assumed to be bi-conical.

The approximation of the wheel-rail contact point are located in the  $\langle Y^{wIi}, Z^{wIi} \rangle$  plane is used. Figure 5.6 shows a sketch of the planar wheel-rail contact scenario. The wheel-rail contact is assumed as a point-to-curve constraint, where the curve is the wheel's tread profile (assumed in this case as a straight line) and the rail head cross-section is assumed to be the single point. On the one hand, the position of the left and right contact points on the WTiF are given by the following expression:

$$\widehat{\mathbf{b}}_{lc}^{wi} = \widehat{\mathbf{b}}^{wi} + \mathbf{A}^{wti,wIi} \hat{\mathbf{u}}_{lc}^{wi}, \quad \widehat{\mathbf{b}}_{rc}^{wi} = \widehat{\mathbf{b}}^{wi} + \mathbf{A}^{wti,wIi} \hat{\mathbf{u}}_{rc}^{wi} \quad (5.13)$$

where  $\widehat{\mathbf{b}}^{wi}$  and  $\mathbf{A}^{wti,wIi}$  are the position vector and rotation matrix of the WLiF with respect to the WTiF, expressed as:

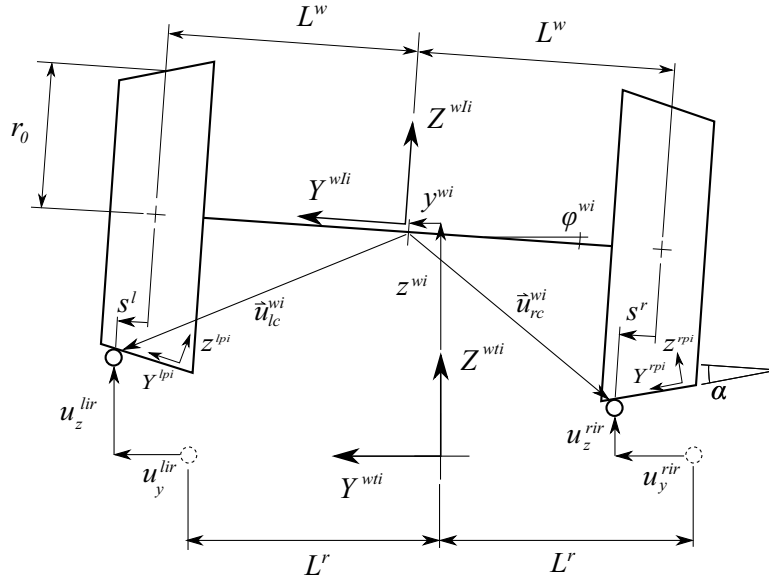


FIGURE 5.6: Geometry of wheelset-track knife-edge contact constraints

$$\widehat{\mathbf{b}}_{lc}^{wi} = \begin{bmatrix} 0 & y^{wi} & z^{wi} \end{bmatrix}^T, \quad \mathbf{A}^{wti,wli} = \begin{bmatrix} 1 & -\psi^{wi} & 0 \\ \psi^{wi} & 1 & -\varphi^{wi} \\ 0 & \varphi^{wi} & 1 \end{bmatrix} \quad (5.14)$$

In Eq. 5.13  $\hat{\mathbf{u}}_{lc}^{wi}$  and  $\hat{\mathbf{u}}_{rc}^{wi}$  are the position of the left and right contact point in the WliF, whose expressions are:

$$\hat{\mathbf{u}}_{lc}^{wi} = \begin{bmatrix} 0 & L^w + s^l & -r_0 + \alpha s^l \end{bmatrix}^T, \quad \hat{\mathbf{u}}_{rc}^{wi} = \begin{bmatrix} 0 & -L^w + s^r & -r_0 + -\alpha s^l \end{bmatrix}^T \quad (5.15)$$

where  $\alpha$  is the wheel profile conicity,  $r_0$  is the nominal radius and  $s^l$  and  $s^r$  are the wheel-profile coordinates.

On the other hand the positions of the left and right rails expressed in the TF are:

$$\widehat{\mathbf{b}}^{lir} = \begin{bmatrix} 0 & L^r + r_y^{lir} & r_z^{lir} \end{bmatrix}^T, \quad \widehat{\mathbf{b}}^{rir} = \begin{bmatrix} 0 & -L^r + r_y^{rir} & r_z^{rir} \end{bmatrix}^T \quad (5.16)$$

where  $r_y^{lir}$ ,  $r_z^{lir}$ ,  $r_y^{rir}$  and  $r_z^{rir}$  are the components of the irregularity vector  $r^{irr}(s)$ , whose elements are drawn from Eqs. 5.6. The parameters  $L^w$  and  $L^r$  used in the equations



above, are the wheelset half-wide and rails half-wide respectively. In the reduced model formulation both parameters take the same value.

Assuming now that the position vector of the contact point on the wheel coincides with the position vector of the rail the following vectorial expressions are obtained:

$$\begin{aligned}\vec{b}_{lc}^{wi} - \vec{b}^{lr} &= 0 \\ \vec{b}_{rc}^{wi} - \vec{b}^{rr} &= 0\end{aligned}\tag{5.17}$$

Rewritten Eqs. 5.17 in matrix form one obtains:

$$\begin{aligned}\widehat{\mathbf{b}}^{wi} \mathbf{A}^{wti, wIi} \hat{u}_{lc}^{wi} - \widehat{\mathbf{b}}^{lr} &= 0 \\ \widehat{\mathbf{b}}^{wi} \mathbf{A}^{wti, wIi} \hat{u}_{rc}^{wi} - \widehat{\mathbf{b}}^{rr} &= 0\end{aligned}\tag{5.18}$$

Equations 5.18 represent a set of six constraints equations functions of the wheelset coordinates  $\mathbf{q}^{wi}$ , the track irregularities  $\mathbf{u}^{irr}$  and the two contact parameters on the wheel ( $s^l$  and  $s^r$ ). Assuming that the contact take place at plane  $\langle Y^{wti}, Z^{wti} \rangle$  the yaw angle  $\psi^{wi}$  must be equal to zero. In fact, the first term in vectorial equations 5.17 are:

$$\psi^{wi}(L^w + s^l) = 0, \quad \psi^{wi}(-L^w + s^l)\tag{5.19}$$

which are only fulfilled when  $\psi^{wi} = 0$ .

Considering only the second and third term of Eqs. 5.18, one gets:

$$\begin{aligned}y^{wi} + (1 - \alpha\varphi^{wi})s^l + r_0\varphi^{wi} - r_y^{lir} &= 0 \\ z^{wi*} + (\varphi^{wi} + \alpha)s^l + L^w\varphi^{wi} - r_z^{lir} &= 0 \\ y^{wi} + (1 + \alpha\varphi^{wi})s^r + r_0\varphi^{wi} - r_y^{rir} &= 0 \\ z^{wi*} + (\varphi^{wi} - \alpha)s^r - L^w\varphi^{wi} - r_z^{rir} &= 0\end{aligned}\tag{5.20}$$

where,  $z^{wi*} = z^{wi} - r_0$  is a small-valued variable created to guarantee the correct coefficient matrix conditioning. The solution of the system of equations must provides the values of  $\mathbf{p}^{wi} = [z^{wi*} \quad \varphi^{wi} \quad s^l \quad s^r]^T$ . The constraints equations in 5.20 (hereafter named  $\mathbf{C}^{kec}(\mathbf{p}^{wi})$ ) is non-linear so it requires an iterative procedure to solve them.

Considering that the values of all coordinates can be assumed to be small, an analytical approximation can be obtained. This solution consists on considering the exact solution to the exact equations the first iteration of the Newton-Raphson algorithm given a relatively accurate initial estimation. That provides a solution to Eqs. 5.20 such as:

$$\mathbf{p}^{wi} = \mathbf{p}_0^{wi} - (\mathbf{C}_p^{kec})^{-1} \mathbf{C}^{kec}(\mathbf{p}_0^{wi}) \quad (5.21)$$

where,

$$\mathbf{p}_0^{wi} = \left[ \frac{u_z^{lr} + u_z^{rr} + \alpha(u_y^{lr} - u_y^{rr})}{2} \quad 0 \quad u_y^{lr} - y^{wi} \quad u_y^{rr} - y^{wi} \right]^T \quad (5.22)$$

and,

$$\mathbf{C}_p^{kec} = \begin{bmatrix} 0 & r_0 - \alpha s^l & 1 - \alpha \varphi^{wi} & 0 \\ 1 & L^w + s^l & \varphi^{wi} + \alpha & 0 \\ 0 & r_0 + \alpha s^r & 0 & 1 + \alpha \varphi^{wi} \\ 1 & -L^w + s^r & 0 & \varphi^{wi} - \alpha \end{bmatrix} \quad (5.23)$$

Once the reduced set of coordinates  $\mathbf{p}^{wi}$  is obtained, its first and second time derivatives can be obtained as follows:

$$\dot{\mathbf{C}}_p^{kec} = \begin{bmatrix} 0 & -\alpha \dot{s}^l & -\alpha \dot{\varphi}^{wi} & 0 \\ 0 & \dot{s}^l & \dot{\varphi}^{wi} & 0 \\ 0 & \alpha \dot{s}^r & 0 & \alpha \dot{\varphi}^{wi} \\ 0 & \dot{s}^r & 0 & \dot{\varphi}^{wi} \end{bmatrix}, \quad \mathbf{C}_t^{kec} = \begin{bmatrix} \dot{y}^{wi} - \dot{u}_y^{lr} \\ -\dot{u}_z^l r \\ \dot{y}^{wi} - \dot{u}_y^{rr} \\ -\dot{u}_z^{rr} \end{bmatrix}, \quad \dot{\mathbf{C}}_t^{kec} = \begin{bmatrix} \ddot{y}^{wi} - \ddot{u}_y^{lr} \\ -\ddot{u}_z^l r \\ \ddot{y}^{wi} - \ddot{u}_y^{rr} \\ -\ddot{u}_z^{rr} \end{bmatrix} \quad (5.24)$$

### 5.2.8 Generalized coordinates of the equations of motion

One of the main reasons of the computational high efficiency of the reduced model is the independent calculation of the vertical and lateral dynamics of the vehicle. Thus, the entire set of generalized coordinates can be written as:

$$\mathbf{q} = \left[ \mathbf{q}_V^{nw^T} \quad \mathbf{q}_L^T \right]^T \quad (5.25)$$

where,  $\mathbf{q}_V^{nw}$  are the generalized coordinates associated with the vertical dynamics of non-wheelset bodies and  $\mathbf{q}_L$  are the generalized coordinates associated with the lateral dynamics of the vehicle.

Assuming that the vehicle consists of  $p$  non-wheelset bodies and  $q$  wheelsets, vertical and lateral coordinates can be splited as:

$$\begin{aligned}\mathbf{q}_V^{nw} &= \begin{bmatrix} \mathbf{q}_V^{nw1^T} & \dots & \mathbf{q}_V^{nwp^T} \end{bmatrix}^T \\ \mathbf{q}_L &= \begin{bmatrix} \mathbf{q}_L^{nw^T} & \mathbf{q}_L^{w^T} \end{bmatrix}^T = \begin{bmatrix} \mathbf{q}_L^{nw1^T} & \dots & \mathbf{q}_L^{nwp^T} & \mathbf{q}_L^{w1^T} & \dots & \mathbf{q}_L^{wq^T} \end{bmatrix}^T\end{aligned}\quad (5.26)$$

where,

$$\begin{aligned}\mathbf{q}_V^{nwi} &= \begin{bmatrix} z^{nwi} & \varphi^{nwi} & \theta^{nwi} \end{bmatrix}^T, \quad \mathbf{q}_L^{nwi} = \begin{bmatrix} y^{nwi} & \psi^{nwi} \end{bmatrix}^T, \quad i = 1, \dots, p \\ \mathbf{q}_V^{wi} &= \begin{bmatrix} z^{wi} & \varphi^{wi} \end{bmatrix}^T, \quad \mathbf{q}_L^{wi} = \begin{bmatrix} y^{wi} & \psi^{wi} \end{bmatrix}^T, \quad i = 1, \dots, q\end{aligned}\quad (5.27)$$

The set of coordinates  $\mathbf{q}_V^{wi}$  is not considered in the set of generalized coordinates of  $\mathbf{q}$  in Eq. 5.25 because they are functions of the lateral coordinates  $\mathbf{q}_L^{wi}$  due to the contact constraints. This leads to a set of  $n = 5p + 2q$  generalized coordinates to describe the vehicle dynamics.

It is important to note that even if the longitudinal coordinate  $s^{vt}$  that describes the longitudinal dynamics of the vehicle has not been included in  $\mathbf{q}$ , the variation of  $s^{vt}$  is introduced as input in the model through out the forward velocity profile. The reduced model also accounts for the influence of the longitudinal motion in the transverse dynamics of the vehicle using generalized forces that depend on  $ds^{vt}/dt$  and  $d^2s^{vt}/dt^2$ .

### 5.2.9 Equations of motion of vertical dynamics

The equations of motion of the vertical dynamics are:

$$\mathbf{M}_V^{nw} \ddot{\mathbf{q}}_V^{nw} + \mathbf{C}_V^{s,nw} \dot{\mathbf{q}}_V^{nw} + \mathbf{K}_V^{s,nw} \mathbf{q}_V^{nw} = \mathbf{Q}_V^{ForIn} - \mathbf{C}_V^{s,w} \dot{\mathbf{q}}_V^w - \mathbf{K}_V^{s,w} \mathbf{q}_V^w + \mathbf{Q}_V^{grav} + \mathbf{Q}_{V0}^s \quad (5.28)$$

where  $\mathbf{M}_V^{nw}$  is the mass matrix, assembled as:

$$\mathbf{M}_V^{nw} = \begin{bmatrix} \mathbf{M}_V^{nw1} & & \\ & \ddots & \\ & & \mathbf{M}_V^{nwp} \end{bmatrix}, \quad \mathbf{M}_V^{nwi} = \begin{bmatrix} m^{nwi} & 0 & 0 \\ 0 & I_\varphi^{nwi} & I_\varphi^{nwi} \\ 0 & I_\varphi^{nwi} & I_\theta^{nwi} \end{bmatrix}, \quad i = 1, \dots, p \quad (5.29)$$

Terms  $\mathbf{C}_V^{s,nw}$ ,  $\mathbf{K}_V^{s,nw}$ ,  $\mathbf{C}_V^{s,w}$  and  $\mathbf{K}_V^{s,w}$  in Eq. 5.28 are the suspension damping and stiffness matrices associated with the vertical dynamics of the non-wheelsets and wheelsets bodies respectively. These matrices are computed symbolically though out the deformation energy  $U_{def}$  and Rayleigh dissipation function  $F_{Ray}$  associated with the suspension elements:

$$\begin{aligned} F_{Ray}(\mathbf{q}_V^{nw}, \mathbf{q}_V^w, \dot{\mathbf{q}}_V^{nw}, \dot{\mathbf{q}}_V^w) &= \sum_i \frac{1}{2} c_i \dot{l}_{i,V}^2 \\ U_{def}(\mathbf{q}_V^{nw}, \mathbf{q}_V^w) &= \sum_i \frac{1}{2} k_i \Delta l_{i,V}^2 \\ i &= 1, \dots, n_s \end{aligned} \quad (5.30)$$

Finally, terms  $\mathbf{Q}_V^{ForIn}$  is the vector of generalized forces due to the forward motion in the vertical direction,  $\mathbf{Q}_V^{grav}$  is the generalized gravity force vector and  $\mathbf{Q}_{V0}^s$  contains the constant terms that appear in the generalized suspension forces:

$$\mathbf{Q}_V^{ForIn} = \begin{bmatrix} \mathbf{Q}_{V,1}^{ForIn} \\ \vdots \\ \mathbf{Q}_{V,p}^{ForIn} \end{bmatrix}, \quad \mathbf{Q}_{V,i}^{ForIn} = \begin{bmatrix} m^i \rho(\dot{s}^{vt})^2 \\ -I_\varphi^i \rho_{tw} \ddot{s}^{vt} - I_{\varphi\theta}^i \rho_v \ddot{s}^{vt} \\ -I_\theta^i \rho_v \ddot{s}^{vt} - I_{\varphi\theta}^i \rho_{tw} \ddot{s}^{vt} \end{bmatrix}, \quad i = 1, \dots, p \quad (5.31)$$

where  $\rho_v$  and  $\rho_{tw}$  are the vertical and twist curvatures.

$$\mathbf{Q}_V^{grav} = \begin{bmatrix} \mathbf{Q}_{V,1}^{grav} \\ \vdots \\ \mathbf{Q}_{V,p}^{grav} \end{bmatrix}, \quad \mathbf{Q}_{V,i}^{grav} = \begin{bmatrix} -m^i g \\ 0 \\ 0 \end{bmatrix}, \quad i = 1, \dots, p \quad (5.32)$$

### 5.2.10 Equations of motion of lateral dynamics

The equation of motion for the lateral dynamics of the railway vehicle are:

$$\mathbf{M}_L \ddot{\mathbf{q}}_L + (\mathbf{C}_L^s + \mathbf{C}_L^c) \dot{\mathbf{q}}_L + (\mathbf{K}_L^s + \mathbf{K}_L^c) \mathbf{q}_L = \mathbf{Q}_L^{ForIn} + \mathbf{Q}_{L0}^s + \mathbf{Q}_{L0}^c + \mathbf{Q}_L^{grav} \quad (5.33)$$

where  $\mathbf{M}_L$  is the mass matrix built as:

$$\mathbf{M}_L = \begin{bmatrix} \mathbf{M}_L^1 & & \\ & \ddots & \\ & & \mathbf{M}_L^n \end{bmatrix}, \quad \mathbf{M}_L^i = \begin{bmatrix} m^i & 0 \\ 0 & I_\psi^i \end{bmatrix}, \quad i = 1, \dots, p+q \quad (5.34)$$

being  $I_\psi^i$  the yaw moment of inertia of body  $i$ .

Terms  $\mathbf{C}_L^s$ ,  $\mathbf{K}_L^s$ ,  $\mathbf{C}_L^c$  and  $\mathbf{K}_L^c$  in Eq. 5.33 are the constant damping and stiffness matrices associated with the suspensions and contact forces acting on the wheelset in the lateral direction respectively. These matrices are computed symbolically in a similar manner than the equivalent matrices for the vertical dynamics. Furthermore  $\mathbf{Q}_L^{ForIn}$  is the vector of generalized inertia forces due to the forward motion, vectors  $\mathbf{Q}_{L0}^s$  and  $\mathbf{Q}_{L0}^c$  contains terms that appear in the generalized suspension forces and in the generalized contact forces when the lateral coordinates and velocities are zero.  $\mathbf{Q}_L^{grav}$  is the vector of generalized gravitational forces in the lateral direction.

The generalized force vector  $\mathbf{Q}_L^{ForIn}$  is given by:

$$\mathbf{Q}_L^{ForIn} = \begin{bmatrix} \mathbf{Q}_{L,1}^{ForIn} \\ \vdots \\ \mathbf{Q}_{L,p+q}^{ForIn} \end{bmatrix}, \quad \mathbf{Q}_{L,i}^{ForIn} = \begin{bmatrix} -m^i \rho_h \dot{s} v t^2 \\ -I_\psi^i [\rho_h \ddot{s} v t + \rho_h' \dot{s} v t^2] \end{bmatrix}, \quad i = 1, \dots, p+q \quad (5.35)$$

where  $\rho_h$  is the horizontal curvature.

The generalized gravitational force vector is given by:

$$\mathbf{Q}_L^{grav} = \begin{bmatrix} \mathbf{Q}_{L,1}^{grav} \\ \vdots \\ \mathbf{Q}_{L,p}^{grav} \end{bmatrix}, \quad \mathbf{Q}_{L,i}^{grav} = \begin{bmatrix} -m^i g \varphi^t \\ 0 \end{bmatrix}, \quad i = 1, \dots, p \quad (5.36)$$

where  $\varphi^t$  is the cant angle.

### 5.2.11 Wheel rail contact forces

Wheel/rail contact forces play a fundamental role in the railroad vehicle performance. For that reason they must be correctly included in the formulation of the model. Figure 5.7 shows an sketch of the wheelset free body diagram with all possible forces acting on it. As it can be observed, the wheels have been modelled with two bi-conical surfaces. The first one corresponds to the wheel tread, with nominal conicity  $\alpha$ , and the second corresponds to the flange with a larger conicity  $\beta$ . In the figure,  $\vec{F}_l^n$  and  $\vec{F}_r^n$  are the left and right tread normal contact forces,  $\vec{F}_l^{creep}$  and  $\vec{F}_r^{creep}$  are the left and right tread tangential contact forces,  $\vec{F}_{lf}^n$  and  $\vec{F}_{rf}^n$  are the flange normal contact forces.  $\vec{F}_l^{susp}$  and  $\vec{F}_r^{susp}$  are the forces transmitted to the wheelset by the primary suspension through the bearing boxes. The figure also includes the gravitational force and the inertia forces and rotary inertia torques.

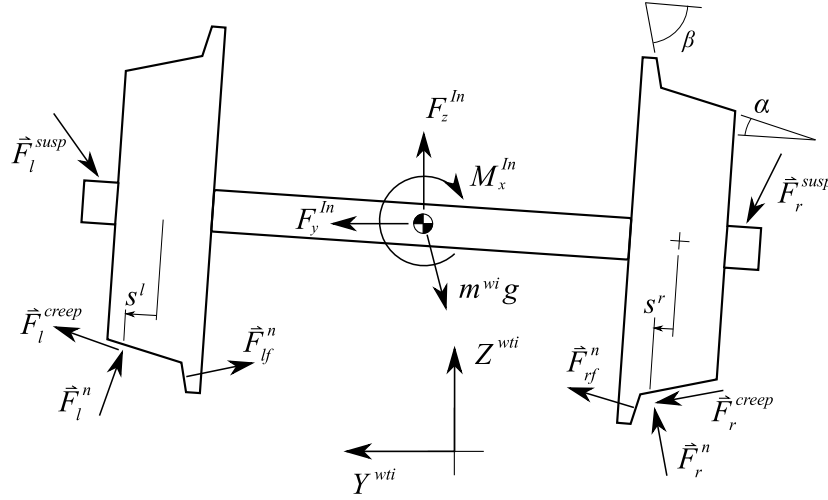


FIGURE 5.7: Forces and torque on a wheelset

The generalized inertia forces associated with the forward motion is computed as follows:

$$\begin{aligned} F_y^{In} &= F_y^{TranIn} + F_y^{ForIn} = -m^{wi}\ddot{y}^{wi} - m^{wi}\rho_h(\dot{s}^{vt})^2 \\ F_z^{In} &= F_z^{TranIn} + F_z^{ForIn} = -m^{wi}\ddot{z}^{wi} + m^{wi}\rho_h(\dot{s}^{vt})^2 \\ M_x^{In} &= M_x^{TranIn} + M_x^{ForIn} = -I_\varphi^{wi}\ddot{\varphi}^{wi} - I_\varphi^{wi}\rho_{tw}(\dot{s}^{vt})^2 + I_\theta^{wi}\rho_h\frac{(\dot{s}^{vt})^2}{r_0} \end{aligned} \quad (5.37)$$

where *TranIn* stands for "inertia due to the transverse motion with respect to the track" and *ForIn* stands for "inertia forces due to the forward motion along the track".

The generalized contact forces acting on the wheelset in the lateral direction are:

$$\mathbf{Q}_L^c = \mathbf{Q}_L^{creep} + \mathbf{Q}_L^{flange} + \mathbf{Q}_L^{normal} \quad (5.38)$$

where the tread tangential, flange normal and tread normal contact forces are considered.  $\mathbf{Q}_L^c$  is computed symbolically in a preprocessing stage and linearised using Taylor series approximation as follows:

$$\mathbf{Q}_L^c \approx \mathbf{Q}_{L0}^c - \mathbf{C}_L^c \dot{\mathbf{q}}_L - \mathbf{K}_L^c \mathbf{q}_L \quad (5.39)$$

where  $\mathbf{Q}_{L0}^c$  is the value of  $\mathbf{Q}_L^c$  in the reference configuration and

$$\mathbf{C}_L^c = -\frac{\partial \mathbf{Q}_L^c}{\partial \dot{\mathbf{q}}_L^T}, \quad \mathbf{K}_L^c = -\frac{\partial \mathbf{Q}_L^c}{\partial \mathbf{q}_L^T} \quad (5.40)$$

The calculation of the tread tangential contact forces follows the Kalker's creep linear theory [104] that stands:

$$\begin{bmatrix} F_x^{creep} \\ F_y^{creep} \\ M_z^{creep} \end{bmatrix} = - \begin{bmatrix} f_{11} & 0 & 0 \\ 0 & f_{22} & f_{23} \\ 0 & -f_{23} & f_{33} \end{bmatrix} \begin{bmatrix} \xi_x \\ \xi_y \\ \xi_z \end{bmatrix} \quad (5.41)$$

where  $F_x^{creep}$ ,  $F_y^{creep}$  and  $M_z^{creep}$  are the components of the force and torque due to the contact tangential stresses in a frame associated with the contact area.  $\xi_x$ ,  $\xi_y$  and  $\xi_z$  are the *creepages* defined as:  $\xi_x = [\tilde{\mathbf{v}}_c^{wi}]_x/V$ ,  $\xi_y = [\tilde{\mathbf{v}}_c^{wi}]_y/V$  and  $\xi_z = [\tilde{\omega}^{wi}]_z/V$ , being  $\tilde{\mathbf{v}}_c^{wi}$  is the rigid body velocity of the contact point,  $\tilde{\omega}^{wi}$  is the angular velocity of the

wheelset and  $V$  the wheelset centre of mass forward velocity. The vectors of tangential contact forces and torques are:

$$\tilde{\mathbf{F}}^{creep} = \begin{bmatrix} F_x^{creep} \\ F_y^{creep} \\ 0 \end{bmatrix}, \quad \tilde{\mathbf{M}}^{creep} = \begin{bmatrix} 0 \\ 0 \\ M_z^{creep} \end{bmatrix} \quad (5.42)$$

It is important to note that  $\tilde{\mathbf{F}}^{creep}$ ,  $\tilde{\mathbf{M}}^{creep}$ ,  $\tilde{\mathbf{v}}_c^{wi}$  and  $\tilde{\omega}^{wi}$  must be expressed in the local contact frame of each wheel (LCiF or RCiF).

After calculating the position of the left and right contact points their velocities can be evaluated in the WTiF as follows:

$$\begin{aligned} \dot{\mathbf{R}}_{lc}^{wi} &= \dot{\mathbf{R}}^{wti} + (\widehat{\omega}^{wti} \wedge \widehat{\mathbf{b}}^{wi}) + \dot{\mathbf{b}}^{wi} + \mathbf{A}^{wti,wIi}(\hat{\omega}^{wi} \wedge \hat{\mathbf{u}}_{lc}^{wi}) \\ \dot{\mathbf{R}}_{rc}^{wi} &= \dot{\mathbf{R}}^{wti} + (\widehat{\omega}^{wti} \wedge \widehat{\mathbf{b}}^{wi}) + \dot{\mathbf{b}}^{wi} + \mathbf{A}^{wti,wIi}(\hat{\omega}^{wi} \wedge \hat{\mathbf{u}}_{rc}^{wi}) \end{aligned} \quad (5.43)$$

where,

$$\dot{\mathbf{R}}^{wti} = \begin{bmatrix} \dot{s}^v \\ 0 \\ 0 \end{bmatrix}, \quad \dot{\mathbf{b}}^{wi} = \begin{bmatrix} 0 \\ \dot{y}^{wi} \\ \dot{z}^{wi} \end{bmatrix}, \quad (5.44)$$

and

$$\hat{\omega}^{wi} = (\mathbf{A}^{wti,wIi})^T \widehat{\omega}^{wti} + \hat{\omega}^{wti,wi}, \quad \hat{\omega}^{wti,wi} = \begin{bmatrix} \dot{\phi}^{wi} \\ \dot{s}^{vt}/r_0 \\ \dot{\psi}^{wi} \end{bmatrix} \quad (5.45)$$

As mentioned before the velocities of the contact points must be expressed in the local contact frame of each wheel (LCiF and RCiF), that leads to:

$$\begin{aligned} \mathbf{v}^{lc} &= (\mathbf{A}^{wti,lpi})^T \dot{\mathbf{R}}_{lc}^{wi}, \quad \mathbf{v}^{rc} = (\mathbf{A}^{wti,rpi})^T \dot{\mathbf{R}}_{rc}^{wi} \\ \omega^{lc} &= (\mathbf{A}^{wti,lpi})^T (\widehat{\omega}^{wti} + \mathbf{A}^{wti,wIi} \hat{\omega}^{wti,wi}), \\ \omega^{rc} &= (\mathbf{A}^{wti,rpi})^T (\widehat{\omega}^{wti} + \mathbf{A}^{wti,wIi} \hat{\omega}^{wti,wi}) \end{aligned} \quad (5.46)$$



where  $\mathbf{A}^{wti, lpi}$  and  $\mathbf{A}^{wti, rpi}$  are the orientation matrices of the LPiF and RPiF with respect to the WTiF computed as:

$$\begin{aligned} \mathbf{A}^{wti, lpi} &= \mathbf{A}^{wti, wli} \mathbf{A}^{wli, lpi}, \quad \mathbf{A}^{wti, rpi} = \mathbf{A}^{wti, wli} \mathbf{A}^{wli, rpi}, \\ \mathbf{A}^{wli, lpi} &= \begin{bmatrix} 1 & 0 & 0 \\ 0 & 1 & -\alpha \\ 0 & \alpha & 1 \end{bmatrix}, \quad \mathbf{A}^{wli, rpi} = \begin{bmatrix} 1 & 0 & 0 \\ 0 & 1 & \alpha \\ 0 & -\alpha & 1 \end{bmatrix}, \end{aligned} \quad (5.47)$$

Finally, the tangential contact forces and torques with respect to the origin of the WLiF projected to the WTiF are:

$$\begin{aligned} \widehat{\mathbf{F}}_l^{creep} &= \mathbf{A}^{wti, lpi} \tilde{\mathbf{F}}_l^{creep}, \\ \widehat{\mathbf{F}}_r^{creep} &= \mathbf{A}^{wti, rpi} \tilde{\mathbf{F}}_r^{creep}, \\ \widehat{\mathbf{M}}_l^{creep} &= \mathbf{A}^{wti, wli} [\hat{\mathbf{u}}_{lc}^{wi} \wedge (\mathbf{A}^{wli, lpi} \tilde{\mathbf{F}}_l^{creep})] + \mathbf{A}^{wti, lpi} \tilde{\mathbf{M}}_l^{creep}, \\ \widehat{\mathbf{M}}_r^{creep} &= \mathbf{A}^{wti, wli} [\hat{\mathbf{u}}_{rc}^{wi} \wedge (\mathbf{A}^{wli, rpi} \tilde{\mathbf{F}}_r^{creep})] + \mathbf{A}^{wti, rpi} \tilde{\mathbf{M}}_r^{creep} \end{aligned} \quad (5.48)$$

The non-linear generalized creep force vector is obtained as:

$$\begin{aligned} \mathbf{Q}_L^{creep} &= \begin{bmatrix} \mathbf{0} & \dots & \mathbf{0} & (\mathbf{Q}_{L1}^{creep})^T & \dots & (\mathbf{Q}_{Lq}^{creep})^T \end{bmatrix}^T \\ \mathbf{Q}_{Li}^{creep} &= \left[ (\hat{F}_l^{creep})_y + (\hat{F}_r^{creep})_y \quad (\hat{M}_l^{creep})_z + (\hat{M}_r^{creep})_z \right]^T, \quad i = 1, \dots, q \end{aligned} \quad (5.49)$$

To conclude with the wheel/rail contact forces calculation, the flange contact forces must be established. They have been computed using an elastic approach, where the contact forces are functions of the indentation and velocity of indentation:

$$\begin{aligned} f_{lf}^n &= k_f (\delta_{lf})^{n_f} + c_f \dot{\delta}_{lf} |\delta_{lf}|, \\ f_{rf}^n &= k_f (\delta_{rf})^{n_f} + c_f \dot{\delta}_{rf} |\delta_{rf}| \end{aligned} \quad (5.50)$$

where  $\delta_{lf}$  and  $\delta_{rf}$  are approximations of the left or right indentations,  $k_f$ ,  $c_f$  and  $n_f$  are a stiffness, damping and exponent constants. The indentations are calculated as:

$$\delta_{lf} = \begin{cases} -s^l - h & \text{if } s^l < -h \\ 0 & \text{if } s^l \geq -h \end{cases} \quad (5.51)$$

$$\delta_{rf} = \begin{cases} s^r - h & \text{if } s^r > h \\ 0 & \text{if } s^l \leq h \end{cases} \quad (5.52)$$

where  $h$  is the clearance between the flange and the rail when the wheelset is centred on the track.

The normal flange contact forces projected into the WTiF are given by:

$$\widehat{F}_{lf}^n = f_{lf}^n \begin{bmatrix} 0 \\ -\sin(\beta + \varphi_{max}^{wi} + \varphi^{irr}) \\ \cos(\beta + \varphi_{max}^{wi} + \varphi^{irr}) \end{bmatrix}, \quad \widehat{F}_{rf}^n = f_{rf}^n \begin{bmatrix} 0 \\ \sin(\beta + \varphi_{max}^{wi} + \varphi^{irr}) \\ \cos(\beta + \varphi_{max}^{wi} + \varphi^{irr}) \end{bmatrix} \quad (5.53)$$

where  $\varphi_{max}^{wi}$  is the roll angle of the wheelset when left flange contact takes place in an irregularity-free track.

The flange tangential contact forces are modelled as Coulomb friction forces in the longitudinal direction as:

$$\widehat{F}_{lf}^t = \mu_f f_{lf}^n \begin{bmatrix} 1 \\ 0 \\ 0 \end{bmatrix}, \quad \widehat{F}_{rf}^t = \mu_f f_{rf}^n \begin{bmatrix} 1 \\ 0 \\ 0 \end{bmatrix} \quad (5.54)$$

where  $\mu_f$  is the wheel/rail friction coefficient.

The torques of the flange contact forces with respect to the origin of the WLiF projected into the WTiF are:

$$\begin{aligned} \widehat{F}_{lf} &= \mathbf{A}^{wti,wLi} \hat{u}_{lf}^{wi} \wedge (\widehat{F}_{lf}^n + \widehat{F}_{lf}^t), \\ \widehat{F}_{rf} &= \mathbf{A}^{wti,wLi} \hat{u}_{rf}^{wi} \wedge (\widehat{F}_{rf}^n + \widehat{F}_{rf}^t) \end{aligned} \quad (5.55)$$

The generalized flange force vector is obtained as:

$$\begin{aligned} \mathbf{Q}_L^{flange} &= \begin{bmatrix} \mathbf{0} & \dots & \mathbf{0} & (\mathbf{Q}_{L1}^{flange})^T & \dots & (\mathbf{Q}_{Lq}^{flange})^T \end{bmatrix}^T \\ \mathbf{Q}_{Li}^{flange} &= \left[ (\widehat{\mathbf{F}}_{lf}^n)_y + (\widehat{\mathbf{F}}_{rf}^n)_y + (\widehat{\mathbf{F}}_{lf}^t)_y + (\widehat{\mathbf{F}}_{rf}^t)_y \quad (\widehat{\mathbf{F}}_{lf}^n)_z + (\widehat{\mathbf{F}}_{rf}^n)_z \right]^T, \end{aligned} \quad (5.56)$$

$$i = 1, \dots, q$$

The tread contact forces can be written in the WTiF as:

$$\begin{aligned}\widehat{\mathbf{F}}_l^n &= f_l^n \begin{bmatrix} 0 \\ -\sin(\varphi^{wi} + \alpha) \\ \cos(\varphi^{wi} + \alpha) \end{bmatrix} \approx \begin{bmatrix} 0 \\ -\varphi^{wi} - \alpha \\ 1 \end{bmatrix}, \\ \widehat{\mathbf{F}}_r^n &= f_r^n \begin{bmatrix} 0 \\ -\sin(\varphi^{wi} - \alpha) \\ \cos(\varphi^{wi} - \alpha) \end{bmatrix} \approx \begin{bmatrix} 0 \\ -\varphi^{wi} + \alpha \\ 1 \end{bmatrix}\end{aligned}\quad (5.57)$$

where  $f_l^n$  and  $f_r^n$  are the norms of the left and right normal contact forces. In order to calculate the treads' normal contact forces (the reaction forces associated with the KEC constraints) a balance of forces in the vertical direction and torques in the longitudinal direction must be established:

$$\begin{aligned}f_l^n + f_r^n + \sum (\widehat{\mathbf{F}}^{wi})_z &= 0 \\ f_l^n(L^w + s^l) - f_r^n(L^w - s^r) + \sum (\widehat{\mathbf{F}}^{wi})_x &= 0\end{aligned}\quad (5.58)$$

where

$$\begin{aligned}\sum (\widehat{\mathbf{F}}^{wi})_z &= F_z^{ln} + (\widehat{\mathbf{F}}_l^{susp} + \widehat{\mathbf{F}}_r^{susp} + \widehat{\mathbf{F}}_l^{creep} + \widehat{\mathbf{F}}_r^{creep} + \widehat{\mathbf{F}}_{lf}^n + \widehat{\mathbf{F}}_{rf}^n)_z \\ \sum (\widehat{\mathbf{M}}^{wi})_x &= M_x^{ln} + (\widehat{\mathbf{F}}_l^{susp} + \widehat{\mathbf{F}}_r^{susp} + \widehat{\mathbf{F}}_l^{creep} + \widehat{\mathbf{F}}_r^{creep} + \widehat{\mathbf{F}}_l^n + \widehat{\mathbf{F}}_r^n)_x\end{aligned}\quad (5.59)$$

Then, solving the following system of equations the tread normal contact forces are obtained

$$\begin{bmatrix} 1 & 1 \\ L^w + s^l & -L^w + s^r \end{bmatrix} \begin{bmatrix} f_l^n \\ f_r^n \end{bmatrix} = \begin{bmatrix} -\sum (\widehat{\mathbf{F}}^{wi})_z \\ -\sum (\widehat{\mathbf{M}}^{wi})_x \end{bmatrix}\quad (5.60)$$

The generalized tread normal force vector is obtained as:

$$\begin{aligned}\mathbf{Q}_L^{normal} &= \begin{bmatrix} \mathbf{0} & \dots & \mathbf{0} & (\mathbf{Q}_{L1}^{normal})^T & \dots & (\mathbf{Q}_{Lq}^{normal})^T \end{bmatrix}^T, \\ \mathbf{Q}_{Li}^{normal} &= \begin{bmatrix} (\widehat{\mathbf{F}}_l^n)_y + (\widehat{\mathbf{F}}_r^n)_y & (\widehat{\mathbf{F}}_l^n)_z + (\widehat{\mathbf{F}}_r^n)_z \end{bmatrix}^T, \\ i &= 1, \dots, q\end{aligned}\quad (5.61)$$

where,

$$\widehat{\mathbf{F}}_l^n = \mathbf{A}^{wti, wIi} \hat{\mathbf{u}}_{lc}^{wi} \wedge \widehat{\mathbf{F}}_l^n, \quad \widehat{\mathbf{F}}_r^n = \mathbf{A}^{wti, wIi} \hat{\mathbf{u}}_{rc}^{wi} \wedge \widehat{\mathbf{F}}_r^n, \quad (5.62)$$

### 5.3 Full 3D railroad multibody model

In this section a non-linear tridimensional multibody formulation for the dynamic analysis of railway vehicles is presented. The development of this model has not been part of this PhD thesis. A more detailed description of the model formulation can be found in [105]. Unlike the reduced model presented in the previous section, vertical, lateral and longitudinal dynamics are taken into account. This formulation can be used to model an arbitrary vehicle, compromising a set of rigid bodies connected by suspension elements among themselves, running on a rigid track with arbitrary geometry. The formulation is designed to be computationally efficient and physically meaningful, being adequate to perform typical analysis required in the railway industry such as: running stability, ride comfort, steady curving, safety analysis...

#### 5.3.1 Coordinates and frames

An adequate coordinate selection plays a fundamental role in the multibody model computational efficiency and ease of implementation. In railroad multibody modelling three main types of coordinates can be found: absolute reference coordinates, relative vehicle-track frame coordinates and relative body-track frame coordinates.

The reduced model presented in the previous section is based on vehicle-track frame coordinates description. This approach has the advantage that, due to the fact that there is an unique VTF, the total number of coordinates involved is smaller than using relative body-track frame coordinates formulation. In this formulation formulation of the entire vehicle depends on a single coordinate  $s^{vt}$ . In addition, the use of a single VTF also eases the definition of the suspension forces. However wheel/rail contact forces are more difficult to compute because wheel-to-track relative position coordinates are not among the generalized coordinates. In the relative body-track frame formulation, each body  $i$  has it own longitudinal formulation.

Figure 5.8 shows a sketch of the kinematics of the bodies of a railway vehicle using relative body-track frame coordinates. As it can be observed, there is a Body Track Frame (BTiF) that follows each body  $i$  along the track centre line. Each body  $i$  has its own Body Frame (BiF) whose relative position with respect to the BTiF is given by:

$$\widehat{\mathbf{r}}^i = \begin{bmatrix} 0 & r_y & r_z \end{bmatrix}^T \quad (5.63)$$

Thus, the set of coordinates that describes each body  $i$  of the vehicle is:

$$\mathbf{q}^i = \begin{bmatrix} s^i & r_y^i & r_z^i & (\Phi^i)^T \end{bmatrix}^T = \begin{bmatrix} s^i & r_y^i & r_z^i & \varphi^i & \theta^i & \psi^i \end{bmatrix}^T \quad (5.64)$$

where  $s^i$  is the arc-length coordinate,  $r_y^i$  and  $r_z^i$  are the relative BiF to BTiF position and  $\Phi^i$  is the BiF to BTiF frame orientation. Therefore, the set of coordinates for all vehicle bodies is:

$$\mathbf{q} = \begin{bmatrix} \mathbf{q}^2 & \dots & \mathbf{q}^{nb} \end{bmatrix}^T \quad (5.65)$$

where  $nb$  stands for number of bodies.

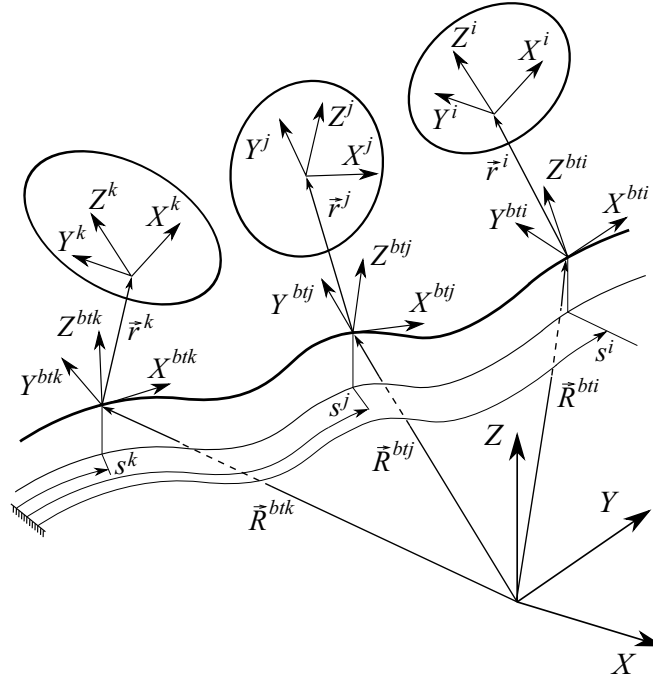


FIGURE 5.8: Kinematics of the bodies of a railway vehicle with relative body-track frame coordinates

In the multibody formulation presented in this section, the railroad vehicle is modelled as a set of  $nch$  open-chain mechanism interconnected by suspension elements. Figure 5.9 shows two chain mechanisms (coloured in green and blue respectively) interconnected by a suspension element. The green chain consists of three bodies while the blue chain includes four bodies. On each chain a base body must be selected that not necessary must be the nearest to the track. The kinematics of an arbitrary chain is described by the position and orientation of the base body together with a set of orientation coordinates  $\theta^i$  that describes the relative orientation between the bodies belonging to the same chain. Therefore, each chain is described by:

$$\mathbf{q}^i = \begin{bmatrix} \mathbf{q}_t^i & \Phi^i \end{bmatrix}^T, \quad i = 1, \dots, nch \quad (5.66)$$

where,

$$\mathbf{q}_t^i = \begin{bmatrix} s^i & r_y^i & r_z^i & \varphi^i & \theta^i & \psi^i \end{bmatrix}^T \quad (5.67)$$

The use of these relative orientation coordinates  $\Phi^i$  represent a drawback on a scenario with long vehicles and sharp curves. The magnitude of the relative orientation angles can be large enough that kinematic linearisation due to small-angles assumption was not recommendable.

The set of coordinates used for the whole vehicle is given by:

$$\mathbf{q} = \begin{bmatrix} \mathbf{q}^1 & \dots & \mathbf{q}^{nch} \end{bmatrix}^T \quad (5.68)$$

### 5.3.2 Kinematics of the track

The description of the track kinematics in the non-linear 3D model is equivalent to the one used in the reduced model. The main difference lies in the fact that in the 3D model the wheel-rail contact geometry is not simplified as in the reduced model. Remember that the reduced model considers the rail cross-section dimensionless. Irregularities are also modelled in the same way as in the reduced model formulation. Equations 5.5 and 5.6 can be extended to the coupled dynamics model formulation.

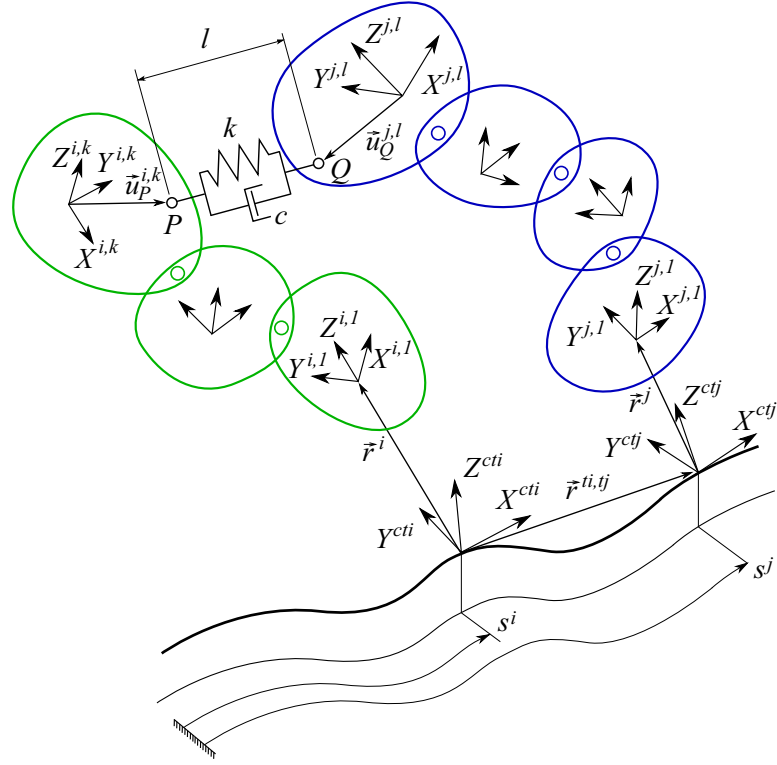


FIGURE 5.9: Railroad vehicle as a set of open-chain mechanisms

The orientation of the rail head frames (LRF and RRF) with respect to the track frame are given by:

$$\mathbf{A}^{t,lr} = \begin{bmatrix} 1 & 0 & 0 \\ 0 & \cos(\beta + \delta) & -\sin(\beta + \delta) \\ 0 & \sin(\beta + \delta) & \cos(\beta + \delta) \end{bmatrix}, \quad (5.69)$$

$$\mathbf{A}^{t,lr} = \begin{bmatrix} 1 & 0 & 0 \\ 0 & \cos(-\beta + \delta) & -\sin(-\beta + \delta) \\ 0 & \sin(-\beta + \delta) & \cos(-\beta + \delta) \end{bmatrix}$$

where  $\beta$  is the orientation angle of the rail profiles (see Fig. 5.3) and  $\delta = (r_z^{lir} - r_z^{rir})$  is the linearised angle due to irregularity.

The position vectors of the left and right contact points on the rails named as  $Q$  and  $P$  respectively are:

$$\begin{aligned}\vec{R}_Q^{lr} &= \vec{R}^t + \vec{r}^{lr} + \vec{r}^{lir} + \vec{u}_Q^{lr} \\ \vec{R}_P^{rr} &= \vec{R}^t + \vec{r}^{rr} + \vec{r}^{rir} + \vec{u}_P^{rr}\end{aligned}\quad (5.70)$$

Those vectors can be expressed in the GF as:

$$\begin{aligned}\mathbf{R}_Q^{lr} &= \mathbf{R}^t + \mathbf{A}^t(\widehat{\mathbf{r}}^{lr} + \widehat{\mathbf{r}}^{lir} + \mathbf{A}^{t,lr}\hat{\mathbf{u}}_Q^{lr}), \\ \mathbf{R}_P^{rr} &= \mathbf{R}^t + \mathbf{A}^t(\widehat{\mathbf{r}}^{rr} + \widehat{\mathbf{r}}^{rir} + \mathbf{A}^{t,rr}\hat{\mathbf{u}}_Q^{rr})\end{aligned}\quad (5.71)$$

where,

$$\hat{\mathbf{u}}_Q^{lr} = \begin{bmatrix} 0 & s_2^{lr} & h^r(s_2^{lr}) \end{bmatrix}^T, \quad \hat{\mathbf{u}}_P^{rr} = \begin{bmatrix} 0 & s_2^{rr} & h^r(s_2^{rr}) \end{bmatrix}^T \quad (5.72)$$

being  $h^r$  the function that describes the rail head (see Fig. 5.10) and  $s_2^{lr}$  and  $s_2^{rr}$  are the rail surface coordinates. Those equations have not sense in the reduced formulation due to the rail cross-section geometry is simplified.

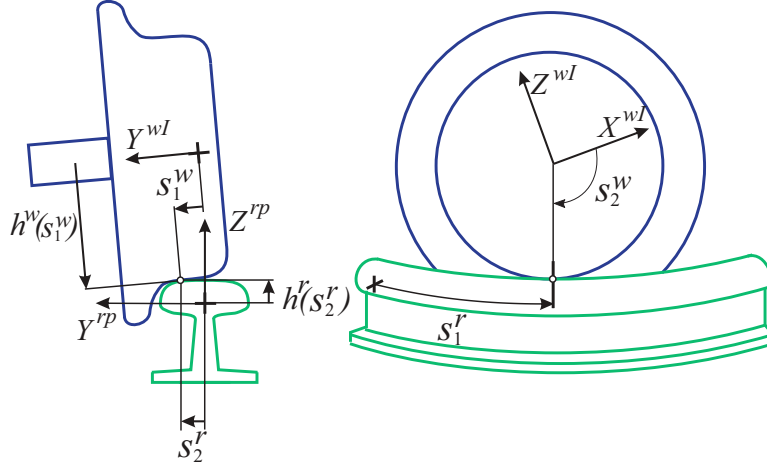


FIGURE 5.10: Wheel profile and rail profile geometry

### 5.3.3 Kinematics of the vehicle

As mentioned before, in the coupled dynamics model formulation the vehicle is defined by chain of bodies. To formulate the kinematics equations of the model it is necessary



to define the positions, velocities and accelerations of interest points of the vehicle as functions of coordinates  $\mathbf{q}$ . All the formulation described below can be developed using general purpose symbolic programs.

The position of an arbitrary point  $P$  that belongs to body  $j$  of chain  $i$  is given by the following vectorial expression:

$$\vec{R}_P^j = \vec{R}^{cti} + \vec{r}^i + \vec{w}^{i,j} + \vec{u}_P^j \quad (5.73)$$

where  $\vec{R}^{cti}$  is the global position of the chain  $i$  track frame,  $\vec{r}^i$  is the relative position of the base body of chain  $i$  with respect to its chain track frame,  $\vec{w}^{i,j}$  is the relative position vector of body  $j$  with respect to its base body  $i$  and  $\vec{u}_P^j$  is the local position vector of point  $P$  in body  $j$ . Eq. 5.73 can be projected in the GF as:

$$\mathbf{R}_P^j = \mathbf{R}^{cti} + \mathbf{A}^{cti}(\bar{\mathbf{r}}^i + \mathbf{A}^{cti,i}(\hat{\mathbf{w}}^{i,j} + \mathbf{A}^{i,j} \hat{\mathbf{u}}_P^j)) \quad (5.74)$$

The position  $\mathbf{R}^{cti}$  and orientation matrix  $\mathbf{A}^{cti}$  are functions of the arc-length coordinate  $s^{cti}$ , while  $\bar{\mathbf{r}}^i$  and  $\mathbf{A}^{cti,i}$  depends on the coordinates  $\mathbf{q}_t^i$  (Eq. 5.67). Vector  $\hat{\mathbf{w}}^{i,j}$  and orientation matrix  $\mathbf{A}^{i,j}$  are functions of the joint relative coordinates  $\boldsymbol{\theta}^i$ .

The velocity and acceleration of point  $P$  are given by:

$$\dot{\vec{R}}_P^j = \dot{\vec{R}}^{cti} + \dot{\vec{r}}^i + \vec{\omega}^{cti} \times \vec{r}^i + \dot{\vec{w}}^{i,j} + \vec{\omega}^i \times \vec{w}^{i,j} + \vec{\omega}^j \times \vec{u}_P^j \quad (5.75)$$

$$\begin{aligned} \ddot{\vec{R}}_P^j = & \ddot{\vec{R}}^{cti} + \ddot{\vec{r}}^i + \vec{\alpha}^{cti} \times \vec{r}^i + \vec{\omega}^{cti} \times (\vec{\omega}^{cti} \times \vec{r}^i) + 2\vec{\omega}^{cti} \times \dot{\vec{r}}^i + \\ & + \ddot{\vec{w}}^{i,j} + \vec{\alpha}^i \times \vec{w}^{i,j} + \vec{\omega}^i \times (\vec{\omega}^i \times \vec{w}^{i,j}) + 2\vec{\omega}^i \times \dot{\vec{w}}^{i,j} + \vec{\alpha}^j \times \vec{u}_P^j + \\ & \vec{\omega}^j \times (\vec{\omega}^j \times \vec{u}_P^j) \end{aligned} \quad (5.76)$$

where "prima" next to a vector means the time-derivative of the vector as observed from the moving frame,  $\vec{\omega}^{cti}$ ,  $\vec{\omega}^i$  and  $\vec{\omega}^j$  are the angular velocity of the chain-track frame, the chain's base body  $i$  and the body  $j$  of the chain respectively. Terms  $\vec{\alpha}^{cti}$ ,  $\vec{\alpha}^i$  and  $\vec{\alpha}^j$  are the corresponding angular accelerations.

The kinematics description of a wheelset body in the full 3D model is equivalent to the description done in the reduced model. Six generalized coordinates are required to

describe the kinematics of wheelset  $i$ :

$$\mathbf{q}_t^{wi} = \begin{bmatrix} s^{wi} & \bar{r}_y^{wi} & \bar{r}_z^{wi} & \bar{\varphi}^{wi} & \bar{\theta}^{wi} & \bar{\psi}^{wi} \end{bmatrix}^T \quad (5.77)$$

Figure 5.2 shows the reference frames required for the kinematic description. The orientation of the wheelset body frame with respect to the wheelset track frame  $i$  is given by the following matrix that has been linearised assuming small angles:

$$\mathbf{A}^{wti,wi} = \mathbf{A}^{wti,wIi} \mathbf{A}^{wIi,wi} \approx \begin{bmatrix} 1 & -\bar{\psi}^{wi} & 0 \\ \bar{\psi}^{wi} & 1 & -\bar{\varphi}^{wi} \\ 0 & \bar{\varphi}^{wi} & 1 \end{bmatrix} \begin{bmatrix} c\bar{\theta}^{wi} & 0 & s\bar{\theta}^{wi} \\ 0 & 1 & 0 \\ -s\bar{\theta}^{wi} & 0 & c\bar{\theta}^{wi} \end{bmatrix} \quad (5.78)$$

For the calculation of the relative angular velocity of body  $i$  with respect to its chain track frame, the following convection is accepted:

$$\bar{\omega}^{cti,i} = \mathbf{A}^{cti,i} \hat{\omega}^{cti,i} = \begin{bmatrix} 1 & \bar{\psi}^i & -\bar{\theta}^i \\ -\bar{\psi}^i & 1 & \bar{\varphi}^i \\ \bar{\theta}^i & -\bar{\varphi}^i & 1 \end{bmatrix} \begin{bmatrix} \dot{\bar{\varphi}}^i \\ \dot{\bar{\theta}}^i \\ \dot{\bar{\psi}}^i \end{bmatrix} \quad (5.79)$$

Using this expression, the absolute velocity of the base body of chain  $i$  is given by:

$$\hat{\omega}^i = \hat{\omega}^{cti} + \hat{\omega}^{cti,i} = (\mathbf{A}^{cti,i})^T \bar{\omega}^{cti} + \hat{\omega}^{cti,i}, \quad (5.80)$$

The translational velocity of the centre of mass of body  $j$  defined as  $\bar{\mathbf{R}}_G^j$  and the angular velocity  $\widehat{\omega}^j$  can be written as follows:

$$\begin{aligned} \bar{\mathbf{R}}_G^j &= \mathbf{H}^j \dot{\mathbf{q}}^{ci}, \\ \widehat{\omega}^j &= \mathbf{G}^j \dot{\mathbf{q}}^{ci} \end{aligned} \quad (5.81)$$

where,  $\mathbf{H}^j$  and  $\mathbf{G}^j$  are the velocity transformation matrices which are functions of the coordinates  $\mathbf{q}^{ci}$  and the track geometry. Those matrices can be computed symbolically

as follows:

$$\begin{aligned}\mathbf{H}^i &= \frac{\partial \bar{\mathbf{R}}_G^j}{\partial \dot{\mathbf{q}}^{ci}}, \\ \mathbf{G}^j &= \frac{\partial \widehat{\boldsymbol{\omega}}^j}{\partial \dot{\mathbf{q}}^{ci}}\end{aligned}\tag{5.82}$$

The translational and angular acceleration can be written as:

$$\begin{aligned}\bar{\mathbf{R}}_G^j &= \mathbf{H}^j \ddot{\mathbf{q}}^{ci} + \dot{\mathbf{H}}^j \dot{\mathbf{q}}^{ci} = \mathbf{H}^j \ddot{\mathbf{q}}^{ci} + \mathbf{h}^j, \\ \widehat{\boldsymbol{\omega}}^j &= \mathbf{G}^j \ddot{\mathbf{q}}^{ci} + \dot{\mathbf{G}}^j \dot{\mathbf{q}}^{ci} = \mathbf{G}^j \ddot{\mathbf{q}}^{ci} + \mathbf{g}^j\end{aligned}\tag{5.83}$$

#### 5.3.4 Contact constraints

In the formulation of the wheel-rail contact constraints, it is established that the point of contact on the wheel coincides with the point of contact on the rail. The non-linear full 3D model uses a similar formulation for the wheel-rail contact constraints to the one used in the reduced model presented in the previous section. The main difference lies in the fact that the 3D model uses the Knife Edge Contact (KEC) constraint formulation with equivalent wheel profiles. A detailed description of this formulation is presented in [106]. In this formulation the real wheel profiles are substituted with the so-called equivalent wheel profiles. The wheelset with the equivalent profiles has the same relative kinematics than the wheelset with real profiles. In that case, the transition of the contact point between the wheel thread and the flange is totally smooth. In this formulation the rail cross-section is considered dimensionless, which reduces the number of coordinates required to formulate the computational model. The use of the KEC with equivalent wheel-profiles facilitates the integrator's work, because it does not have to deal with abrupt changes in position of the contact point on the wheel between consecutive integration steps, as it may happen when flange contact appears in the real profile. All this improves the computational efficiency of the model. Figure 5.11 shows an example of a real wheel profile and its equivalent profile using the mentioned formulation.

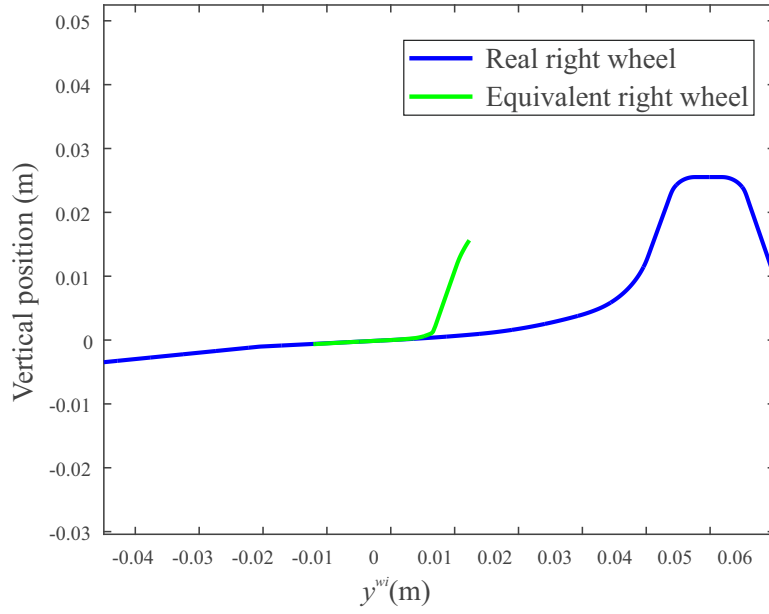


FIGURE 5.11: Real and equivalent wheel profiles

### 5.3.5 Equations of motion

As explained before in this section, the railroad vehicle in the full 3D model is modelled as a set of chains of bodies interconnected by suspension elements. After the description of the vehicle's kinematics the next step in the multibody analysis consist on solving the equations of motion. Those equations are the results of assembly the equation of motion of each individual chain with the addition of the generalized forces due to the suspension elements that connect these chains.

The Newton-Euler equations for an arbitrary solid  $j$  of chain  $i$  can be written as:

$$\begin{bmatrix} \mathbf{m}^i & \mathbf{0} \\ \mathbf{0} & \hat{\mathbf{I}}^j \end{bmatrix} \begin{bmatrix} \bar{\mathbf{a}}_G^j \\ \hat{\boldsymbol{\alpha}}^j \end{bmatrix} = \begin{bmatrix} \bar{\mathbf{F}}^j \\ \hat{\mathbf{M}}^j \end{bmatrix} + \begin{bmatrix} \mathbf{0} \\ -\hat{\boldsymbol{\omega}}^j \wedge \bar{\mathbf{I}}^j \hat{\boldsymbol{\omega}}^j \end{bmatrix}, \quad j = 1, 2, \dots, nbi, \quad (5.84)$$

where  $\mathbf{m}^i$  is the mass matrix of body  $j$ ,  $\hat{\mathbf{I}}^j$  is the inertia matrix expressed in the body frame,  $\bar{\mathbf{F}}^j$  and  $\hat{\mathbf{M}}^j$  are the applied forces and torques on the body, respectively. Assuming that chain  $i$  consist of  $nbi$  bodies, the Newton-Euler equations assembly of

the entire chain of bodies yields:

$$\begin{bmatrix} \mathbf{m}^1 & & & \\ & \bar{\mathbf{I}}^1 & & \\ & & \ddots & \\ & & & \mathbf{m}^{nbi} \\ & & & & \hat{\mathbf{I}}^{nbi} \end{bmatrix} \begin{bmatrix} \bar{\mathbf{a}}_G^1 \\ \hat{\boldsymbol{\alpha}}^1 \\ \vdots \\ \bar{\mathbf{a}}_G^{nbi} \\ \hat{\boldsymbol{\alpha}}^{nbi} \end{bmatrix} = \begin{bmatrix} \bar{\mathbf{F}}^1 \\ \hat{\mathbf{M}}^1 \\ \vdots \\ \bar{\mathbf{F}}^{nbi} \\ \hat{\mathbf{M}}^{nbi} \end{bmatrix} + \begin{bmatrix} \mathbf{0} \\ -\hat{\boldsymbol{\omega}}^1 \wedge \hat{\mathbf{I}}^1 \hat{\boldsymbol{\omega}}^1 \\ \vdots \\ \mathbf{0} \\ -\hat{\boldsymbol{\omega}}^{nbi} \wedge \hat{\mathbf{I}}^{nbi} \hat{\boldsymbol{\omega}}^{nbi} \end{bmatrix} \quad (5.85)$$

This is a system of  $6 \times nbi$  equations that can be written in compact form as:

$$\hat{\mathbf{M}}^i \hat{\mathbf{a}}^i = \hat{\mathbf{Q}}_{app}^i + \hat{\mathbf{Q}}_v^i \quad (5.86)$$

$$\hat{\mathbf{a}}^i = \begin{bmatrix} \bar{\mathbf{a}}_G^1 \\ \hat{\boldsymbol{\alpha}}^1 \\ \vdots \\ \bar{\mathbf{a}}_G^{nbi} \\ \hat{\boldsymbol{\alpha}}^{nbi} \end{bmatrix} = \begin{bmatrix} \mathbf{H}^1 \\ \mathbf{G}^1 \\ \vdots \\ \mathbf{H}^{nbi} \\ \mathbf{G}^{nbi} \end{bmatrix} \ddot{\mathbf{q}}^i + \begin{bmatrix} \mathbf{h}^1 \\ \mathbf{g}^1 \\ \vdots \\ \mathbf{h}^{nbi} \\ \mathbf{g}^{nbi} \end{bmatrix} = \mathbf{L}^i \ddot{\mathbf{q}}^i + \mathbf{l}^i \quad (5.87)$$

Introducing Eq. (5.87) into Eq. (5.86) and pre-multiplying by  $(\mathbf{L}^i)^T$  it yields:

$$(\mathbf{L}^i)^T \hat{\mathbf{M}}^i \mathbf{L}^i \ddot{\mathbf{q}}^i = (\mathbf{L}^i)^T \hat{\mathbf{Q}}_{app}^i + (\mathbf{L}^i)^T (\hat{\mathbf{Q}}_v^i - \hat{\mathbf{M}}^i (\mathbf{L}^i)^T \mathbf{l}^i) \quad (5.88)$$

Newly, writing Eq. (5.88) in compact form it is obtained:

$$\mathbf{M}^i \ddot{\mathbf{q}}^i = \mathbf{Q}_{app}^i + \mathbf{Q}_v^i \quad (5.89)$$

The vector of generalized forces  $\mathbf{Q}_{app}^i$  does not include reaction forces in those chains that not include wheels since  $\mathbf{q}^i$  is assumed to be free of constraints. In the case of wheelset bodies, wheel/rail contact constraints must be accounted for.

Once the equations of motion for a single chain of bodies have been defined, the equations of motions for the entire vehicle are:

$$\begin{bmatrix} \mathbf{M}^1 & & \\ & \ddots & \\ & & \mathbf{M}^{nch} \end{bmatrix} \begin{bmatrix} \ddot{\mathbf{q}}^1 \\ \vdots \\ \ddot{\mathbf{q}}^{nch} \end{bmatrix} = \begin{bmatrix} \mathbf{Q}_{app}^1 \\ \vdots \\ \mathbf{Q}_{app}^{nch} \end{bmatrix} + \begin{bmatrix} \mathbf{Q}_v^1 \\ \vdots \\ \mathbf{Q}_v^{nch} \end{bmatrix} + \mathbf{Q}_{susp} + \mathbf{Q}_{reacc}^{wr} \quad (5.90)$$

where,  $\mathbf{Q}_{susp}$  is the vector of generalized suspension forces and  $\mathbf{Q}_{reacc}^{wr}$  is the vector of generalized forces due to wheel-rail contact constraints  $\mathbf{C}^{wr}(\mathbf{q}) = 0$ . Reaction forces are accounted for using the Lagrange multiplier method. To that end, the equations of motion are augmented with the wheel-rail contact constraints, as follows:

$$\begin{bmatrix} \mathbf{M} & (\mathbf{C}_q^{wr})^T \\ \mathbf{C}_q^{wr} & \mathbf{0} \end{bmatrix} \begin{bmatrix} \ddot{\mathbf{q}} \\ \boldsymbol{\lambda}^{wr} \end{bmatrix} = \begin{bmatrix} \mathbf{Q}_{app} + \mathbf{Q}_v + \mathbf{Q}_{susp} \\ -\dot{\mathbf{C}}_q^{wr} \dot{\mathbf{q}} \end{bmatrix} \quad (5.91)$$

where  $\mathbf{C}_q^{wr}$  is the jacobian of the wheel/rail contact constraints and  $\boldsymbol{\lambda}^{wr}$  are the Lagrange multipliers associated with the wheel-rail contact constraints.

Reaction forces due to the wheel-rail contact are not calculated in the 3D model as it is done in the reduced model. The resultant forces acting on both wheels depend on the tangential and normal force on the wheel thread and the flange. The 3D model uses an hybrid method for the calculation of the wheel-rail contact forces. This method is the result of a combination between the constraint and the elastic method. Constraints are applied on the thread region while the elastic method is used when flange contact appears. In that moment, a force proportional to the indentation and the velocity of indentation between the wheel and the rail is introduced in the model. It is assumed that the tangential forces are a function of pseudo-slip speeds (creepages) following the Polach model [38]. The Polach method is valid not just in the micro sliding region as Kalker's creep forces formulation, but it is also valid in the transition and gross sliding regions.

## 5.4 Scaled vehicle modelling

The multibody model of the scaled vehicle used in this PhD thesis consist of three rigid bodies, name as bodies 1 to 3. Bodies 1 and 2 are the rear and front wheelset respectively, while body 3 represents the bogie frame. Both wheelset are connected to the bogie frame through the primary suspension. It consists on 8 helical springs, distributed in pairs connecting each bearing box with the bogie frame. All bodies' masses have been measured experimentally, while inertia tensors have been drawn from a CAD software. The suspension stiffness have been characterized in a test machine, obtaining the actual stiffness of one of the helical spring. Figure 5.12 shows the geometry of the modelled vehicle. Four traction rods connect the wheelsets with the bogie frame. The model formulation allows the introduction as input a synthesized or experimental velocity profile. This velocity is imposed to the rear wheelset, body 1, that powers the vehicle. Tables 5.3 to 5.6 summarized initial positions, masses, inertia parameters of each rigid body of the vehicle and the main characteristics and positions of the suspension elements. The ideal track input parameters are described in Tables 2.5 and 2.7.

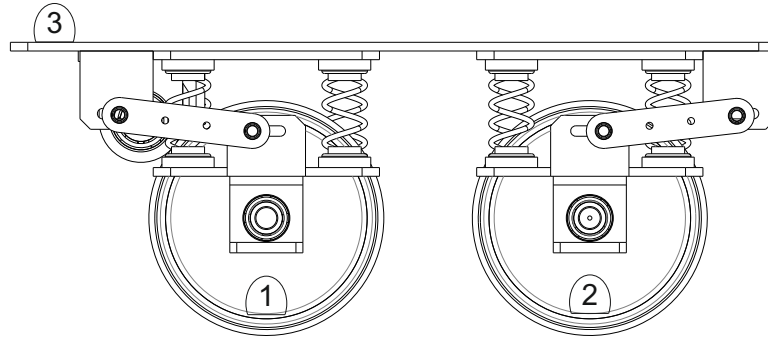


FIGURE 5.12: Multibody model main elements

TABLE 5.3: Body frames initial position and orientation

<b>Body</b>	$R_x$ (m)	$R_y$ (m)	$R_z$ (m)	$\varphi$ (rad)	$\theta$ (rad)	$\psi$ (rad)
1	0.000	0.000	0.000	0.000	0.000	0.000
2	0.185	0.000	0.000	0.000	0.000	0.000
3	0.093	0.000	0.098	0.000	0.000	0.000

TABLE 5.4: Mass and inertia properties of bodies

<b>Body</b>	$m$ (kg)	$I_{xx}$ (kg·m <sup>2</sup> )	$I_{yy}$ (kg·m <sup>2</sup> )	$I_{zz}$ (kg·m <sup>2</sup> )
1	2.210	0.0191	0.0040	0.0188
2	4.315	0.0590	0.0085	0.0588
3	17.475	0.0190	0.0530	0.0510

TABLE 5.5: Primary suspension elements

<i>No.</i>	$i$	$j$	$l_0$ (m)	$k$ (N/m)	$c$ (N·s/m)	$\hat{\mathbf{u}}^i$ (m)	$\hat{\mathbf{u}}^j$ (m)
1	1	3	0.050	7500	2.52	[ 0.045 -0.097 0.035]	[-0.048 -0.097 -0.014]
2	1	3	0.050	7500	2.52	[-0.045 -0.097 0.035]	[-0.014 -0.097 -0.014]
3	1	3	0.050	7500	2.52	[ 0.045 0.097 0.035]	[-0.048 0.097 -0.014]
4	1	3	0.050	7500	2.52	[-0.045 0.097 0.035]	[-0.138 0.097 -0.014]
5	2	3	0.050	7500	2.52	[ 0.045 -0.097 0.035]	[ 0.138 -0.097 -0.014]
6	2	3	0.050	7500	2.52	[-0.045 -0.097 0.035]	[ 0.048 -0.097 -0.014]
7	2	3	0.050	7500	2.52	[ 0.045 0.097 0.035]	[ 0.138 0.097 -0.014]
8	2	3	0.050	7500	2.52	[-0.045 0.097 0.035]	[ 0.048 0.097 -0.014]

TABLE 5.6: Traction rods

<i>No.</i>	$i$	$j$	$l_0$ (m)	$k$ (N/m)	$\hat{\mathbf{u}}^i$ (m)	$\hat{\mathbf{u}}^j$ (m)
1	1	3	0.077	$5 \cdot 10^5$	[ 0.000 -0.127 0.050]	[-0.179 -0.127 -0.039]
2	1	3	0.077	$5 \cdot 10^5$	[ 0.000 0.127 -0.039]	[-0.179 0.127 -0.039]
3	2	3	0.077	$5 \cdot 10^5$	[ 0.000 -0.127 0.050]	[ 0.179 -0.127 -0.039]
4	2	3	0.077	$5 \cdot 10^5$	[ 0.000 0.127 0.050]	[ 0.179 0.127 -0.039]



## Chapter 6

# Comparison Between Measured and Simulated Wheel-Rail Contact Forces

### 6.1 Simulation to experiment comparison

After the manufacturing, instrumentation and calibration, the scaled dynamometric wheelset has been tested in a real scenario in order to validate its functionality as a wheel/rail contact force measurement system. To that end, the instrumented wheelset has been installed in a scaled railway vehicle designed by the Department of Mechanical and Manufacturing Engineering of the University of Seville and tested in the 5 inches gauge scaled track presented in Chapter 2. Several experiments have been carried out and the obtained accelerations, angular velocities and contact forces have been compared with the numerical results drawn from the two computational multibody models of the scaled vehicle presented in Chapter 5. The final goal of this section is to compare the vertical and lateral force measurements obtained with the two measuring procedures presented in this PhD thesis, the strain gauges and distance lasers. The experiments are also compared with the simulated results.

### 6.1.1 Vehicle instrumentation for the experiments

The vehicle used during the experiments is a single bogie consisting of two wheelsets and a bogie frame connected by a suspension elements. The rear wheelset is driven by a chain transmission powered by a 30 W *Phidget* DC motor. The front axle is the dynamometric wheelset. There are also two traction rods (see Fig. 6.3) connecting the rear axle with the bogie frame. These rods allow a smoother power transmission to the traction wheelset reducing notoriously longitudinal vibrations in the vehicle.

Figures 6.1 to 6.3 shows three different views of the instrumented bogie on the scaled track. As it can be noticed, the vehicle has numerous sensors and other electronic devices installed on it. In addition to the sensors of the dynamometric wheelset (see Chapters 3 and 4) the vehicle has two high precision Inertial Measurement Units (IMUs) one installed on the left bearing box of the instrumented wheelset (see Fig. 6.3) and the other centred on the bogie frame. These sensors register accelerations and angular velocities on the three axes. The vehicle have been also equipped with high precision encoders that register the instantaneous angular position and velocity of both axes. A set of magnets (see Fig. 6.4) have been installed along the scaled track. These magnets act like beacons which are detected by two inductive magnetic sensors installed under the bearing boxes of the rear wheelset (see Figs. 6.2 and 6.3). The beacons together with both precision encoder are used as inputs of the vehicle's odometer that precisely located the vehicle on the track. The vehicle is controlled by a Real Time (RT) computer *NI-cRIO-9035* of *National Instruments* installed on the bogie frame (see Fig. 6.2). The RT computer also acquires the sensors' data. The control and data acquisition system has been fully programmed on *LabVIEW 2017*. Figure 6.5 shows the user control interface. Three lead acid batteries power the vehicle electric system. Table 6.1 summarizes the electronic instruments equipped on the vehicle.

TABLE 6.1: Instruments equipped on the vehicle

Instrument	Function
NI-cRIO-9035	Vehicle control
MEL-M7L/0.5-10B Precision Lasers	Lateral force measurement
$\mu\epsilon$ optoNCDT-1302 Precision Lasers	Vertical force measurement
LORD MicroStrain 3DM-GX4-25 IMU	Inertial measurements
Phidget quadrature encoder 40 CPR	Rear axle encoder
Kubler quadrature encoder 360 PPR	Front axle encoder
Inductive magnetic sensors	Beacon detection
Power source (24V)	Electrical supply
TP-Link WiFi Router	Computer wireless communication
Lead acid batteries	Electrical supply

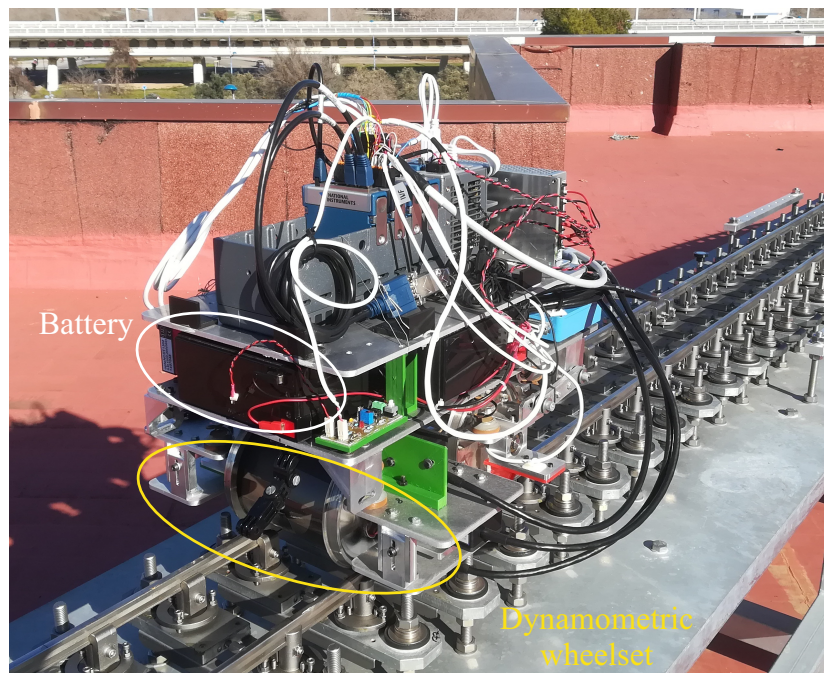


FIGURE 6.1: Instrumented scaled bogie on the track. Front view

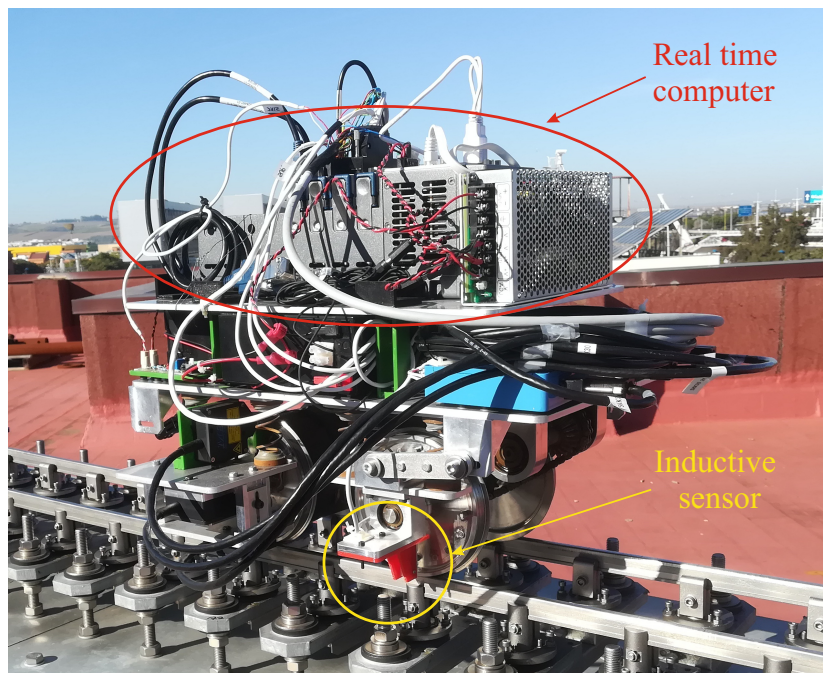


FIGURE 6.2: Instrumented scaled bogie on the track. Left side view

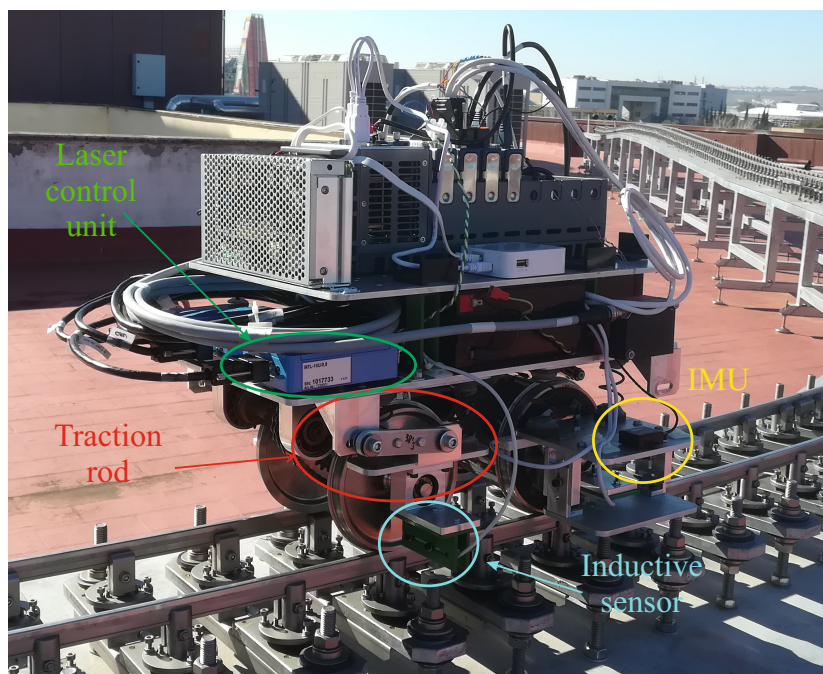


FIGURE 6.3: Instrumented scaled bogie on the track. Right side view



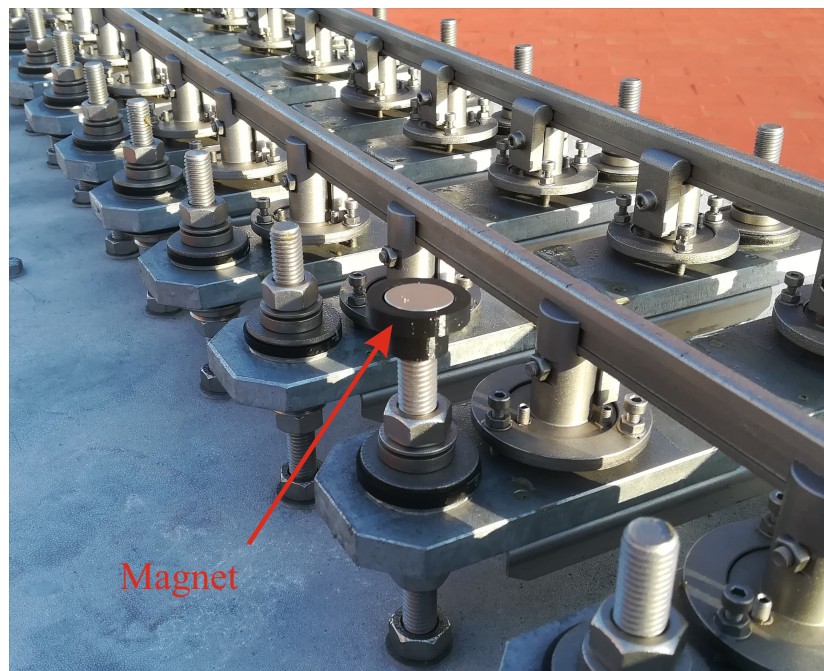


FIGURE 6.4: Track beacons

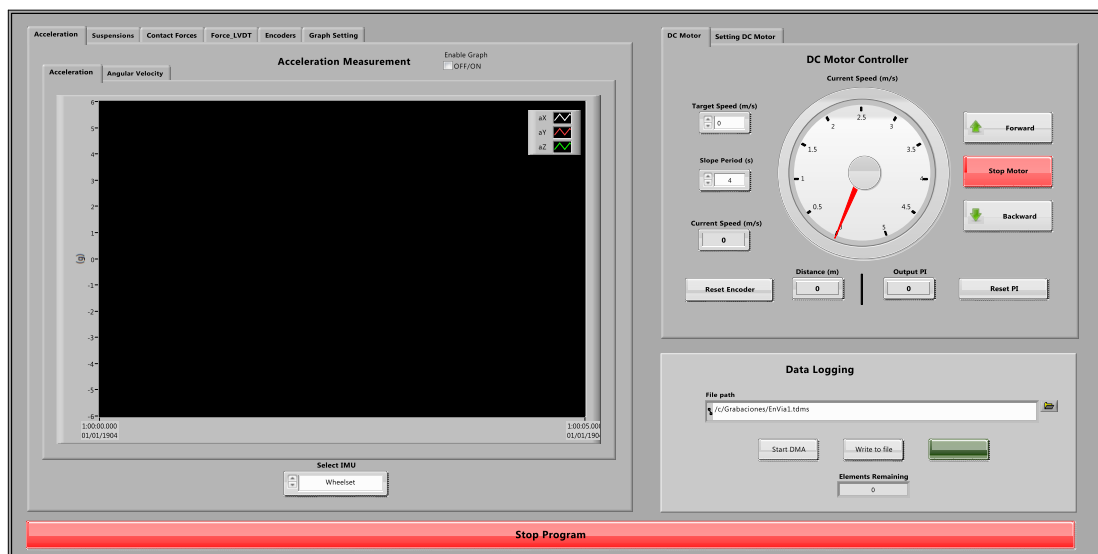


FIGURE 6.5: LabVIEW user control interface

### 6.1.2 Experiments on the track

In this section, the measurement obtained from several experiment on the track are going to be presented. A total of six experiments have been carried out. They can be divided into two groups of three experiments each. The first group are the experiments where the vehicle moves forward on the track, and, the second group are the experiments where the vehicles moves backwards. It is important to note that the instrumented wheelset is always the leading axle. That means, the vehicle is turned around in the backwards rides. This is important because, as presented in Chapter 2, the experimental scale track is an open circuit consisting of a straight section, one curve to the right with 24 m radius, a straight section, one curve to the left with 6 m radius and a final straight section. They are connected by transition sections of variable curvature. Thus, when the vehicles moves forward or backwards the instrumented wheel (the front wheelset left wheel) interacts in a different manner with the track as will be shown later.

The forward rides have been named as experiments 1, 2 and 3, where the vehicles moves with average velocities of 1.7 m/s, 2 m/s and 2.5 m/s respectively. The backward rides are experiments named 4, 5 and 6, where the vehicle moves with average velocities of 1.5 m/s, 2 m/s and 2.5 m/s. Taking into account that temperature affects the track geometry, both the track measurements (see Section 2) and the experimental campaign were carried out in similar temperature conditions.

### 6.1.3 Forward movement experiments

The results obtained from the experiments are linear accelerations, angular velocities and contact forces measurement mainly, besides the odometer position and forward velocity calculation. Due to the fact that the measured accelerations and angular velocities have similar patterns in all the experiments, the results of a single experiment are shown in this subsection and compared with the simulation results drawn from the computational model. The wheel-rail contact force experimental measurements obtained with both approaches, main goal of this PhD thesis, will be presented on each experiment.

The experimental accelerations and angular velocities shown in Figs. 6.7 to 6.18 correspond to experiment number 3. This is the experiment where the vehicle reaches the fastest velocity and therefore the largest acceleration and angular velocities are obtained. Figure 6.6 shows the longitudinal velocity profile of the vehicle during the experiment versus the longitudinal coordinate  $s$  of the track centre line (TCL). The fluctuations of the velocity between 5 m and 25 m are due to the PI control action.

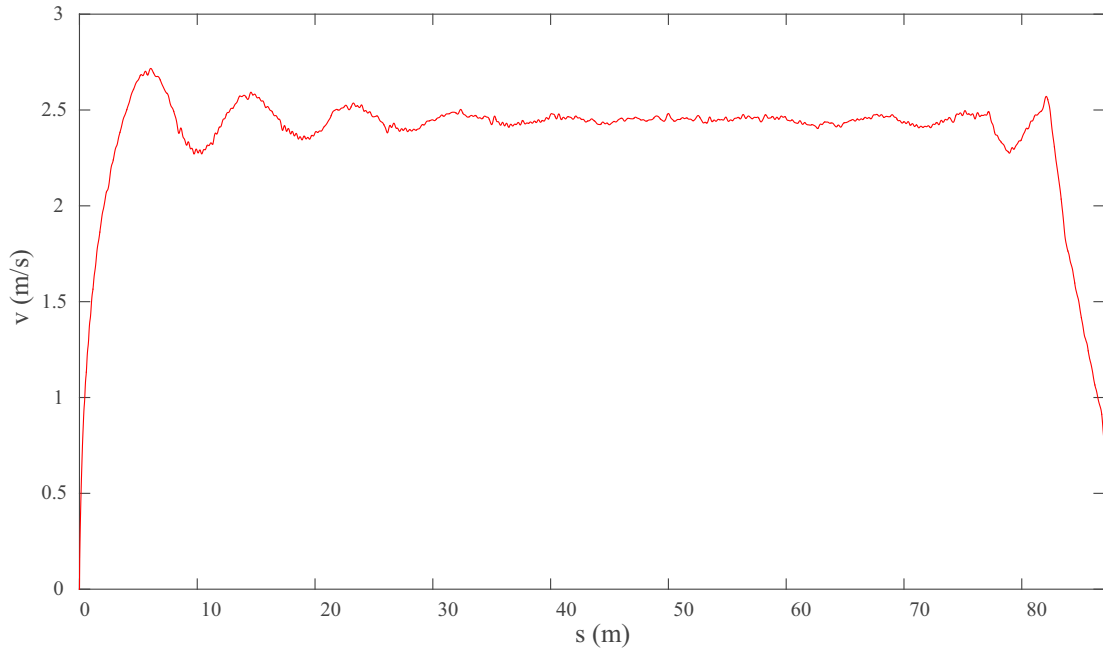


FIGURE 6.6: Forward velocity profile in Experiment 3

Figures 6.7 to 6.9 show the accelerations in the longitudinal, lateral and vertical directions of the instrumented wheelset, respectively, measured by the IMU, compared with the numerical data drawn from the computational models. Figure 6.7 shows a comparison between the experimental and simulated longitudinal accelerations of the instrumented wheelset. It is observed how the 3D model does not reproduce correctly the experiment like the reduced model does. Larger fluctuations are observed in the 3D model results. This is due to the absence of traction rods in the 3D model construction. Those results show how the traction rods can highly reduce the longitudinal oscillations of the wheelset. In Fig. 6.8, it can be observed the variation of the lateral acceleration experienced by the wheelset while negotiating both curves. The large radius curve is located between  $s = 21$  m and  $s = 50$  m, and the sharp radius curve located between

$s = 53$  m and  $s = 62$  m. Figures 6.10 to 6.12 shows the angular velocities experienced by the wheelset. Similar conclusion can be reached in Figs. 6.8 and 6.12. It is important to note that, the pitch angular velocity is not correctly reproduced by any of the simulation models as it can be seen in Fig. 6.11, where the experimental data shows larger fluctuations. This is due to the fact that, the bearing boxes have not been modelled as independent rigid bodies. That means, their real kinematics can not be reproduced by any of both multibody models. As it can be observed in Fig. 5.12, two helical springs connect each bearing box with the bogie frame. Thus, the bearing box, where the IMU is installed, can experience in a real scenario a small pitch movement that is not considered in the simulation models.

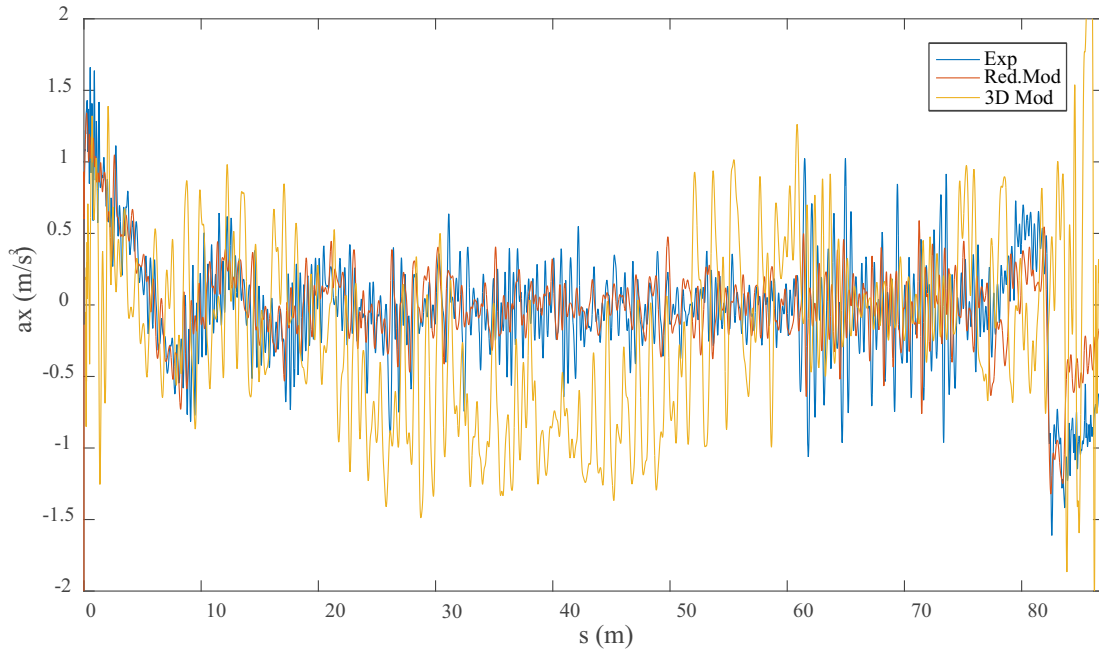
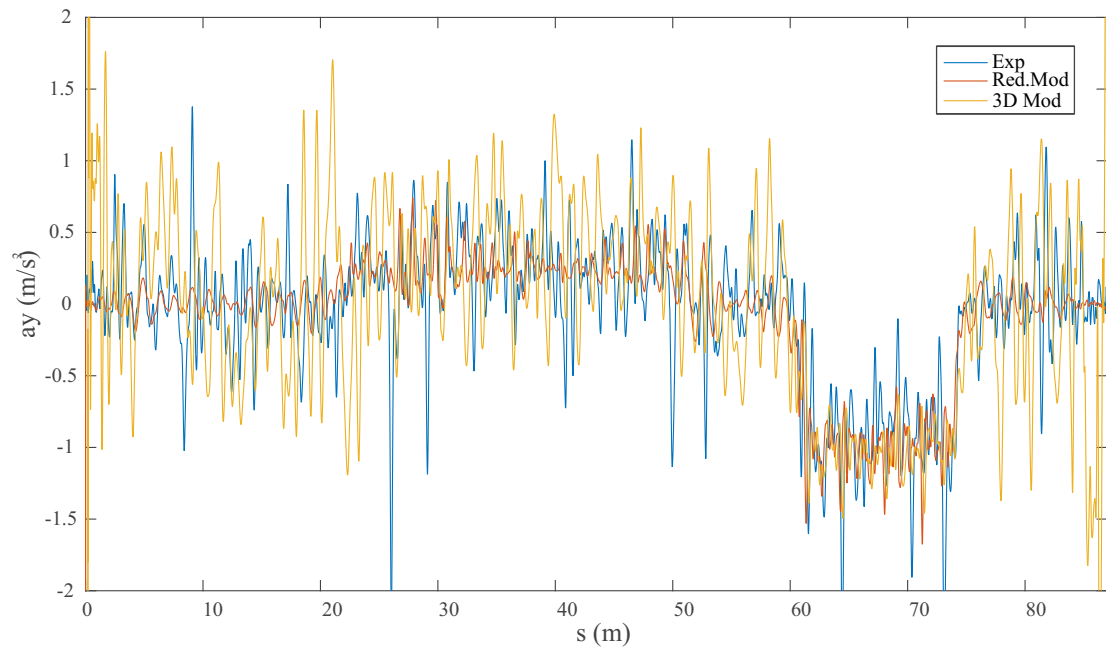
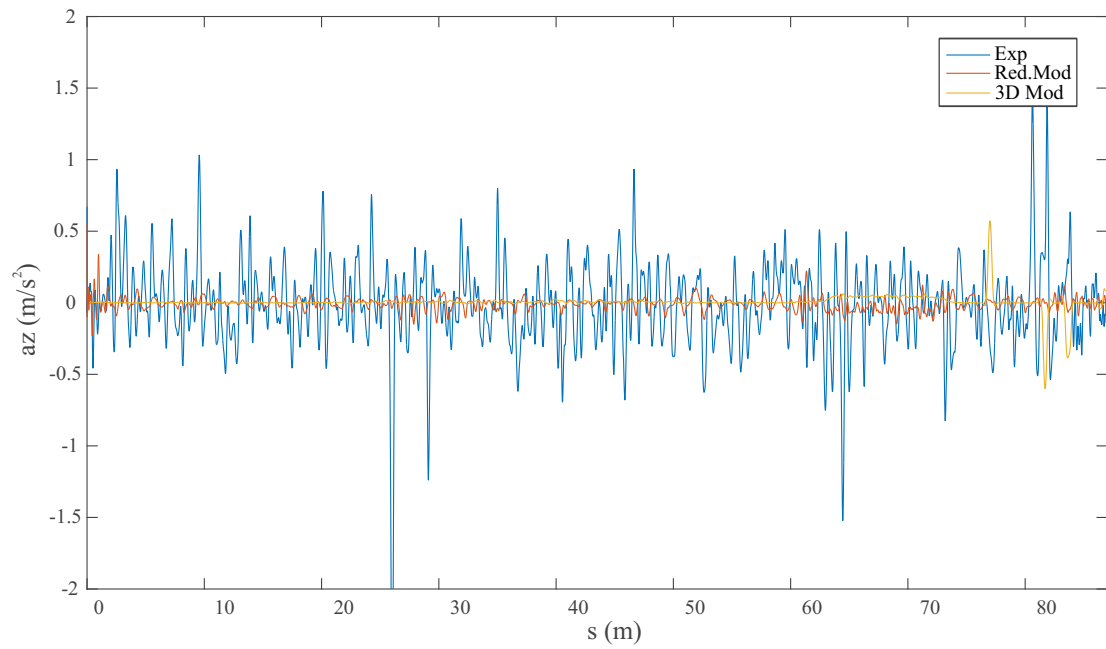
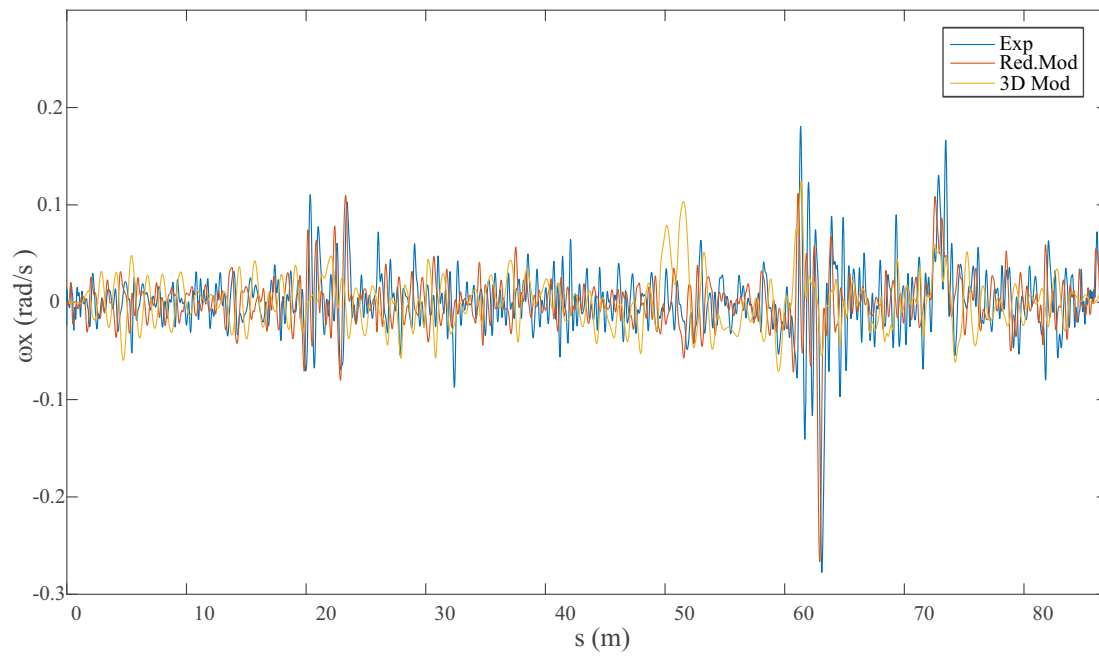
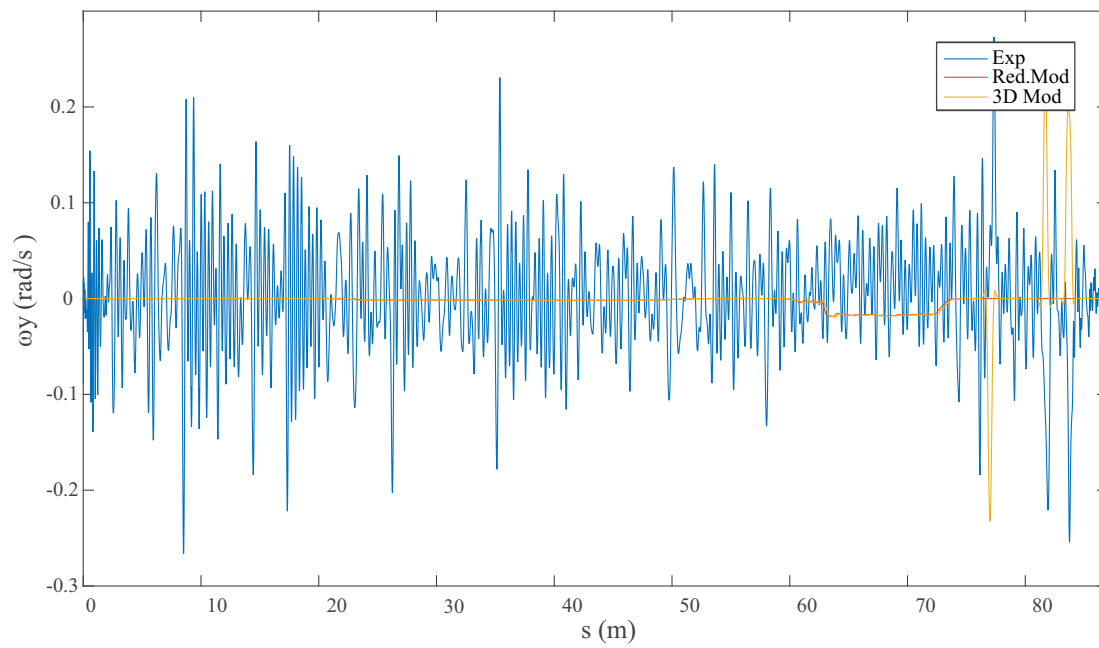
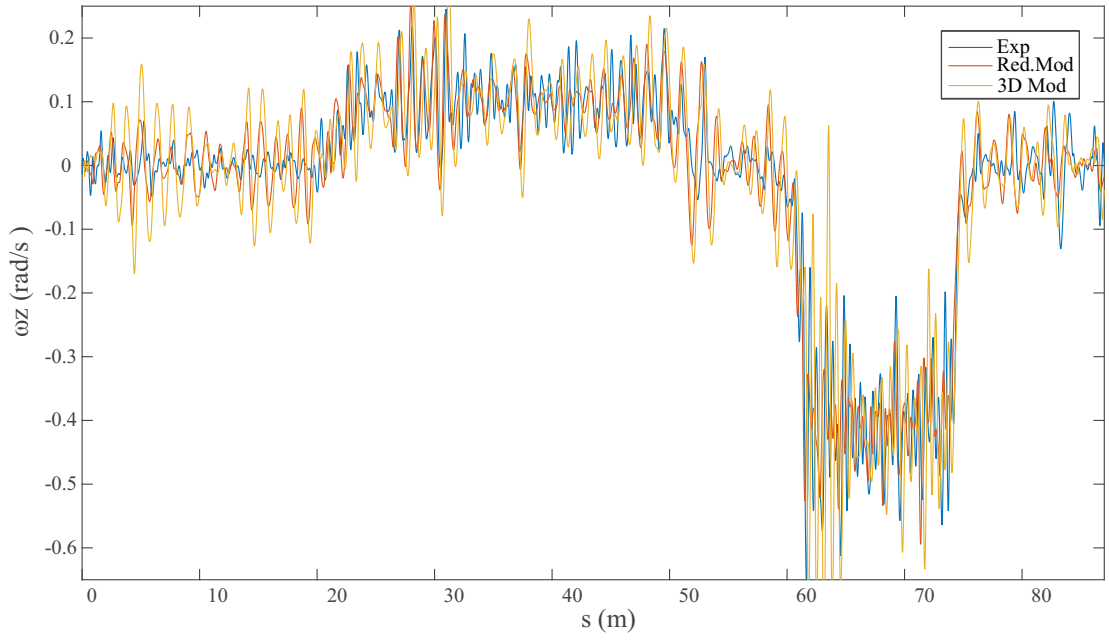


FIGURE 6.7: Longitudinal acceleration  $a_x$  of the instrumented wheelset

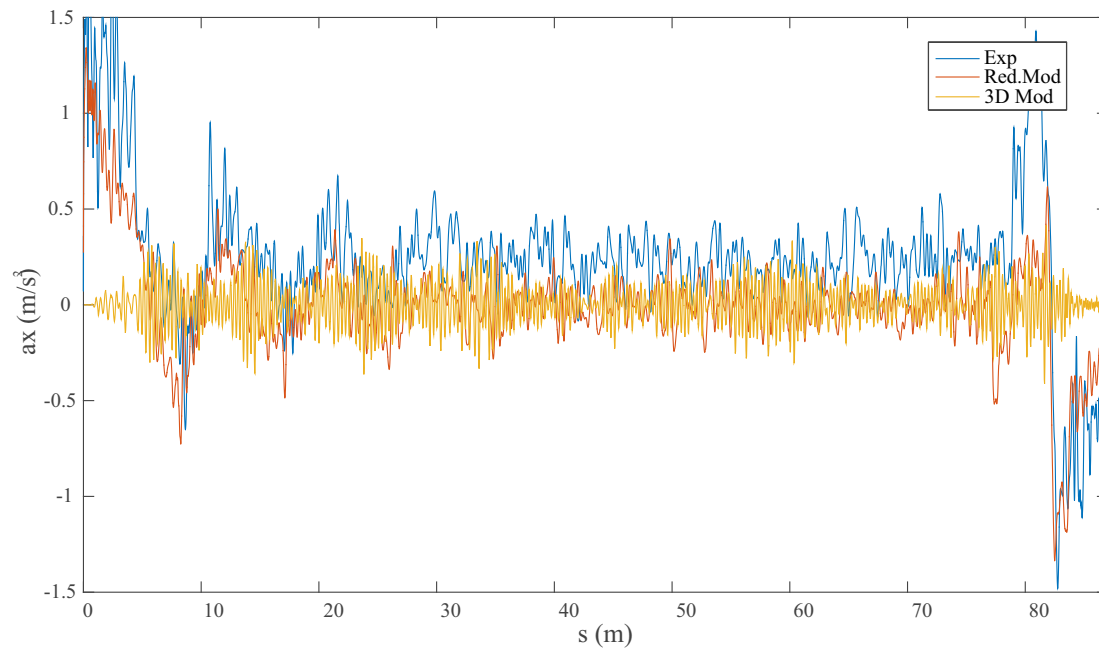
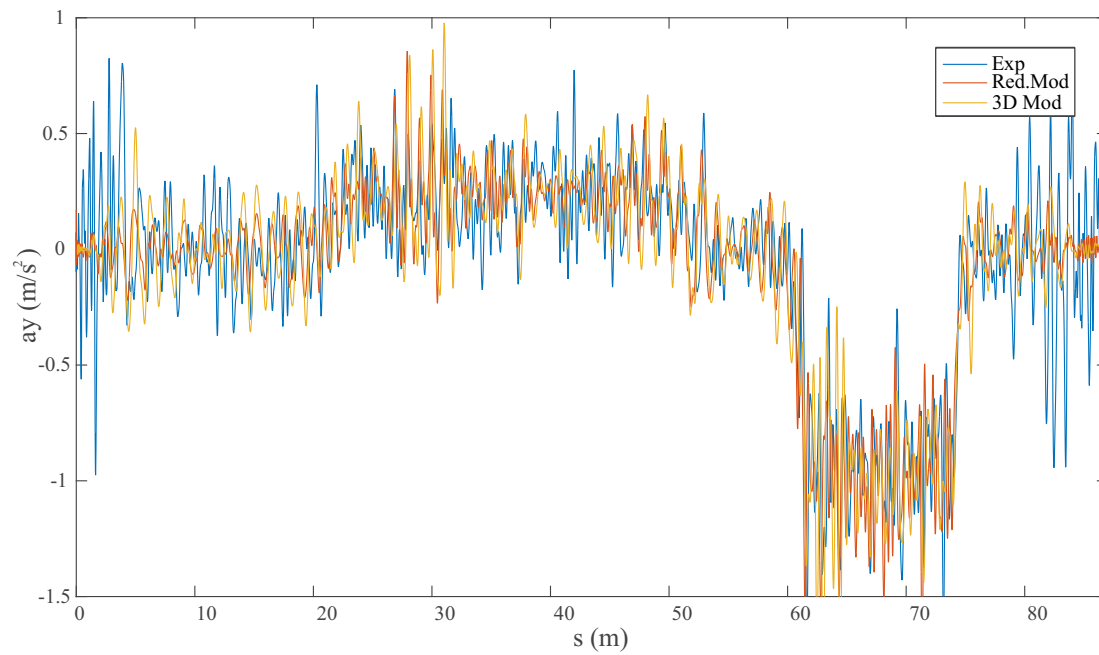


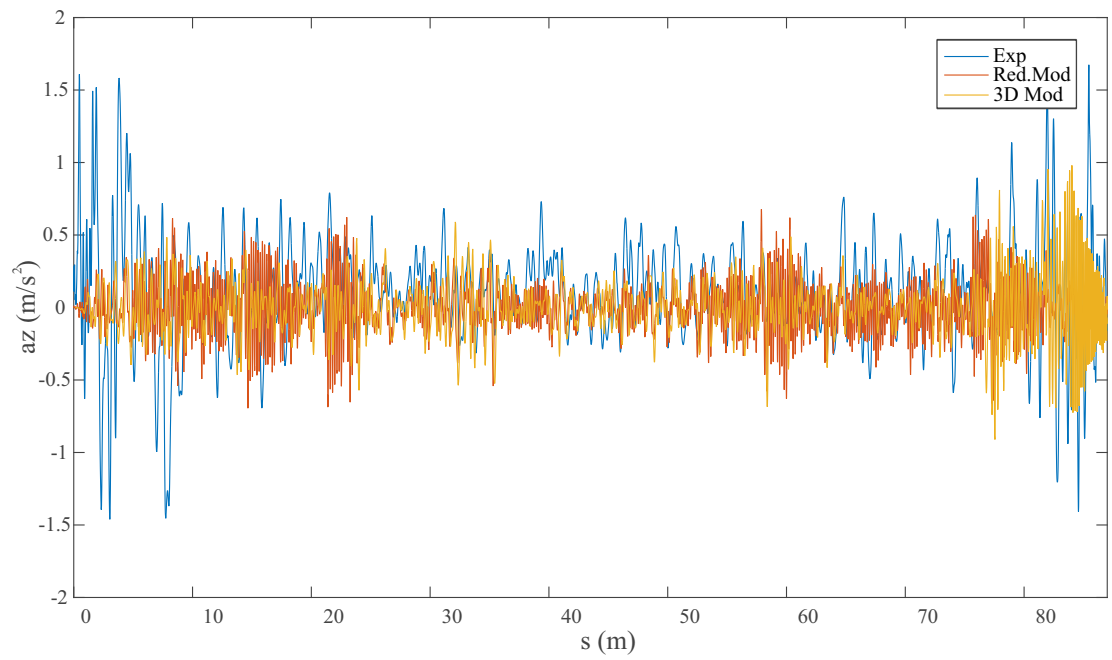
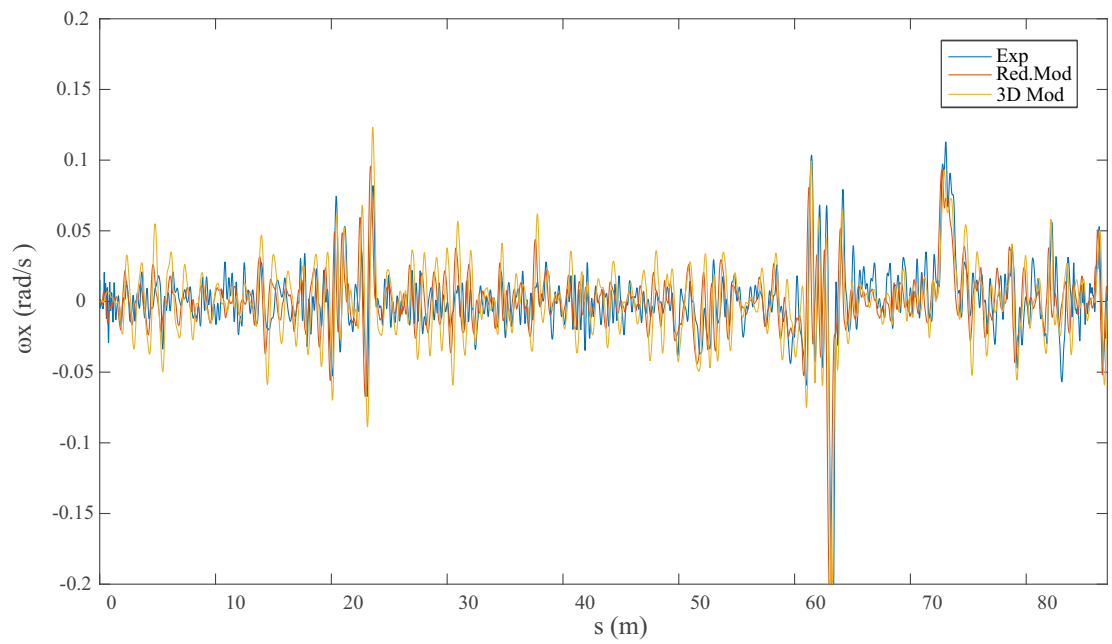
FIGURE 6.8: Lateral acceleration  $a_y$  of the instrumented wheelsetFIGURE 6.9: Vertical acceleration  $a_z$  of the instrumented wheelset

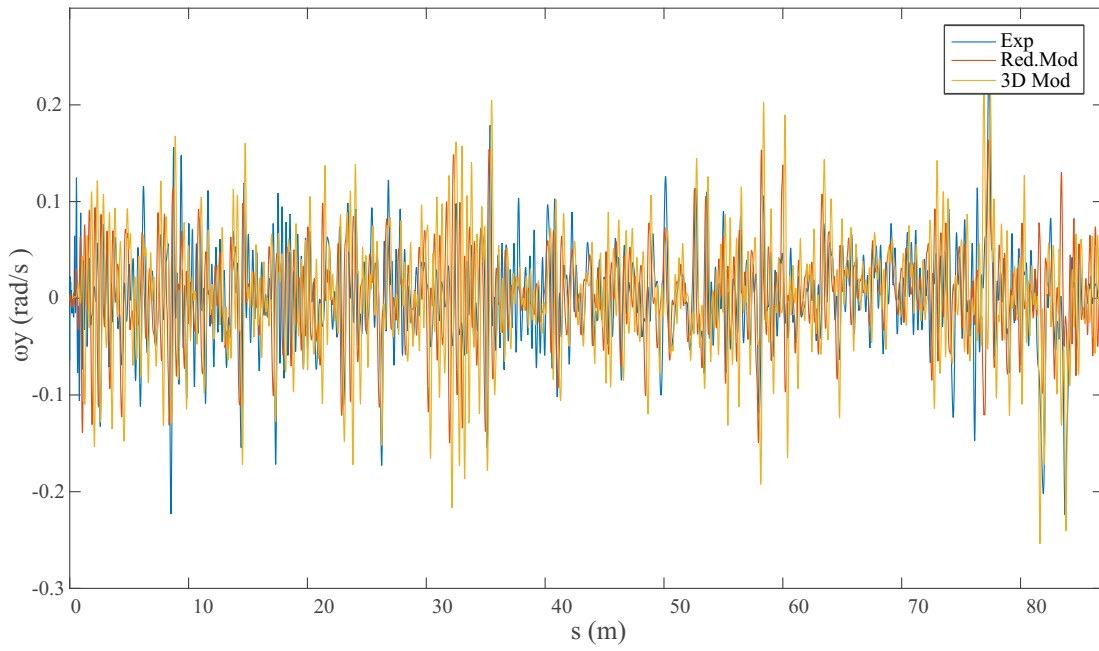
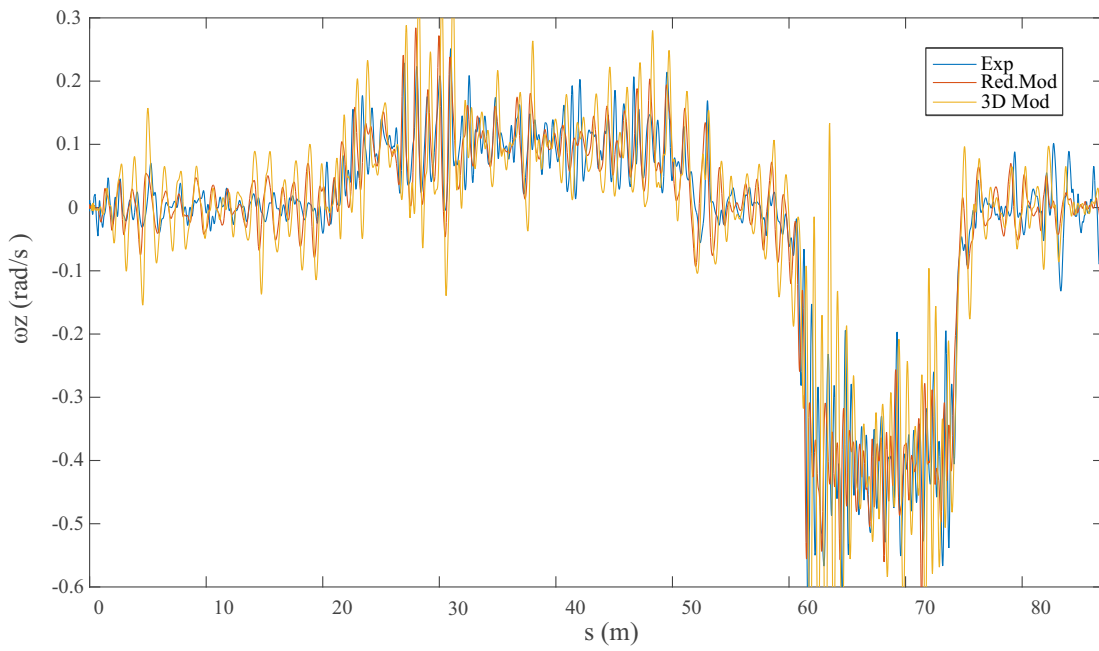
FIGURE 6.10: Angular velocity  $\omega_x$  of the instrumented wheelsetFIGURE 6.11: Angular velocity  $\omega_y$  of the instrumented wheelset

FIGURE 6.12: Angular velocity  $\omega_z$  of the instrumented wheelset

Similar results are obtained from the IMU installed on the bogie frame (see Figs. 6.13 to Figs. 6.18). The inertial magnitudes measured by both IMUs are very similar due to the stiffness of the suspension elements.

FIGURE 6.13: Longitudinal acceleration  $a_x$  of the bogie frameFIGURE 6.14: Longitudinal acceleration  $a_y$  of the bogie frame

FIGURE 6.15: Vertical acceleration  $a_z$  of the bogie frameFIGURE 6.16: Angular velocity  $\omega_x$  of the bogie frame

FIGURE 6.17: Angular velocity  $\omega_y$  of the bogie frameFIGURE 6.18: Angular velocity  $\omega_z$  of the bogie frame

To conclude this epigraph, the force measurements obtained in the three experiments

where the vehicle moves in the forward direction are shown below. The two lateral force measurement techniques, strain gauges and precision distance lasers developed in this PhD thesis, are compared among them, and at the same time with the two computational models results. Applied vertical force measurements on the instrumented wheel are also shown and compared with the computational results.

As it can be observed in Fig. 6.20, corresponding to experiment 1, the normal force applied on the wheel measured by the vertical lasers approximately reproduces the computational results. The differences between both model estimations is due to the model assumptions.

Figure 6.21 shows the comparison between the lateral force measured by the lateral distance lasers and the strain gauges compared with the simulation results. In order to have a clearer view of them, Fig. 6.22 shows the same graph lines on independent charts. The differences between both computational models are again observed. Experimental measurements (see Fig. 6.22 (c) and (d)) also show different tendencies. The strain gauges approach, Fig. 6.22 (d), shows a reasonable agreement with the reduced model and the expected results. It is observed how the lateral force increases when the vehicle negotiates both curves. In the large radius curve both the reduced model and the strain gauges show the same instantaneous impacts. Those impacts are due to track irregularities. The precision lasers do not detect so clearly the increase in the lateral force in the first curve. When the vehicle negotiates the sharp radius curve a continuous flange contact appears. That is correctly reproduced by the reduced model, the strain gauges and the laser sensors. A video recording of the wheel-rail contact made during the experiment shows how this continuous flange contact actually appears. Figure Fig. 6.19 shows a video frame of the instrumented wheelset when the vehicles passes the small radius curve.

Moving on experiment two, the same conclusions are obtained from the normal force measurements Fig. 6.23. However, in the lateral force measurement a slight difference is observed. In this experiment, the distance lasers are able to detect when the vehicle negotiates the large radius curve. It is true that, the instantaneous flange impacts of the wheel against the rail are not noticed by the lasers as the strain gauges are able to do. The mean value of the lateral force approximately coincides for both set of sensors.

In the experiment number three, the last one in forward direction, the vertical force is again satisfactory measured and it approximately coincides with the numerical results. The lateral force is also measured satisfactory with the strain gauges, whose measurements are similar to both computational models. Nonetheless, the distance lasers fail again. The measurement of the lateral force in the large radius curve does not agree with the other graph lines. Finally, the force experienced by the wheel in the small radius curve is satisfactory measured by both approaches, as it was observed in the previous experiments.

In the light of the obtained results in the forward movement experiments, it can be said that the normal force applied on the instrumented wheel can be measured through the deflection of the primary suspension and a simple balance of forces and torques on the wheelset. The lateral force has been satisfactory measured by the strain gauges in the three experiments described above. In addition, the measurements have a good level of accordance with the computational results. However, the distance lasers do not show the same robustness than the strain gauges. Although they are able to correctly measure the lateral force when the vehicle passes the small radius curve, they fail measuring the lateral force in the large radius curve in two of the three experiments. The possible reasons that lead to this situation are discussed later in this chapter.

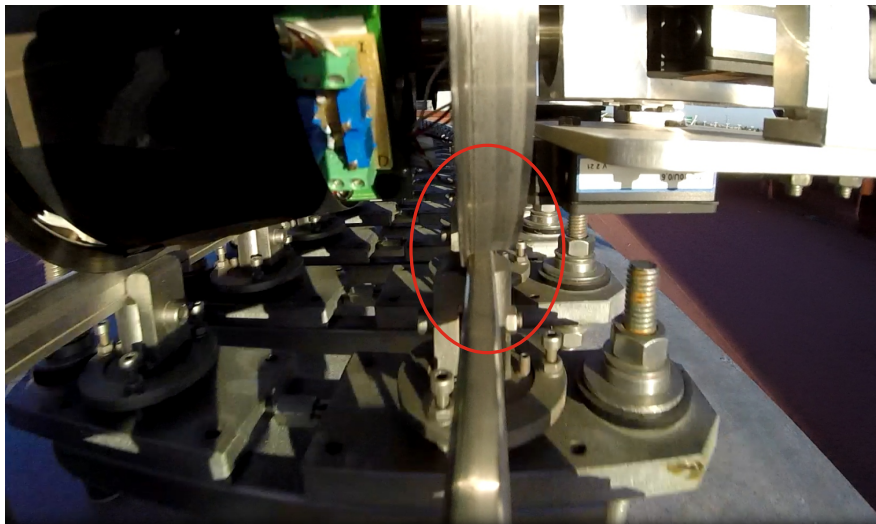


FIGURE 6.19: Continuous flange contact in the sharp radius curve



### 6.1.3.1 Experiment 1 contact force measurements

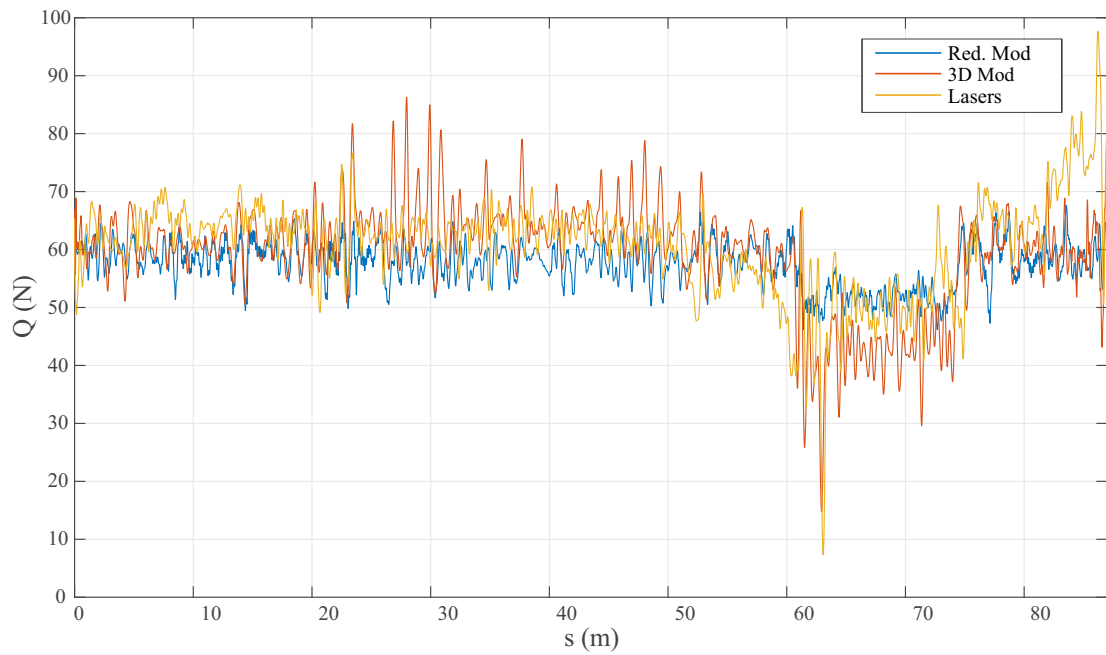


FIGURE 6.20: Normal force experiment 1, methods comparison

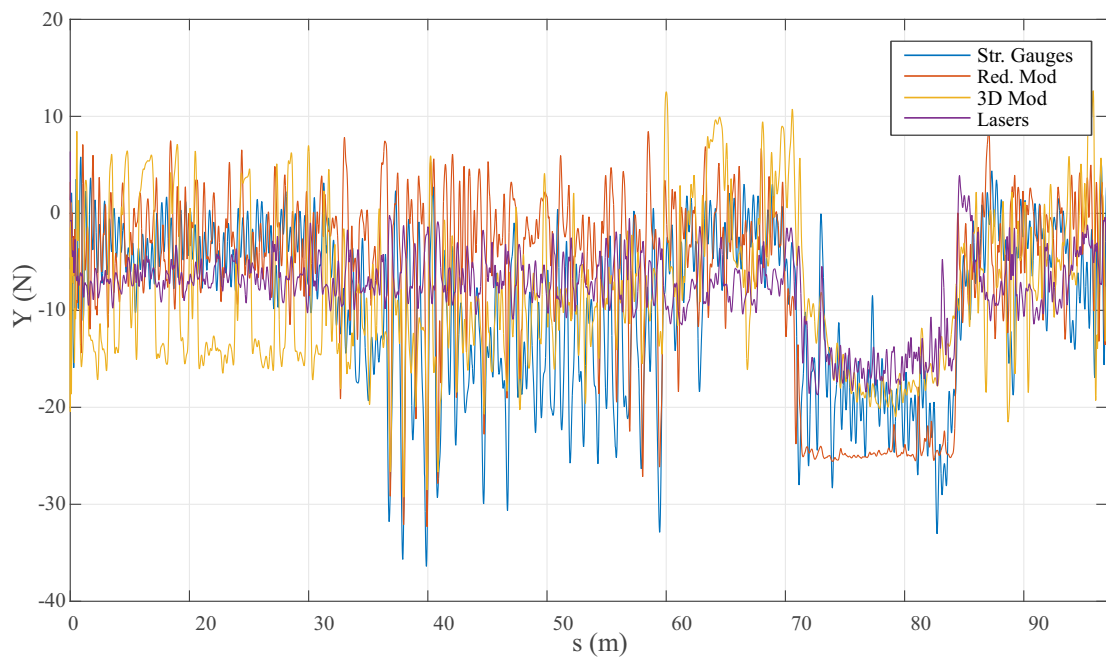


FIGURE 6.21: Lateral force experiment 1, methods comparison

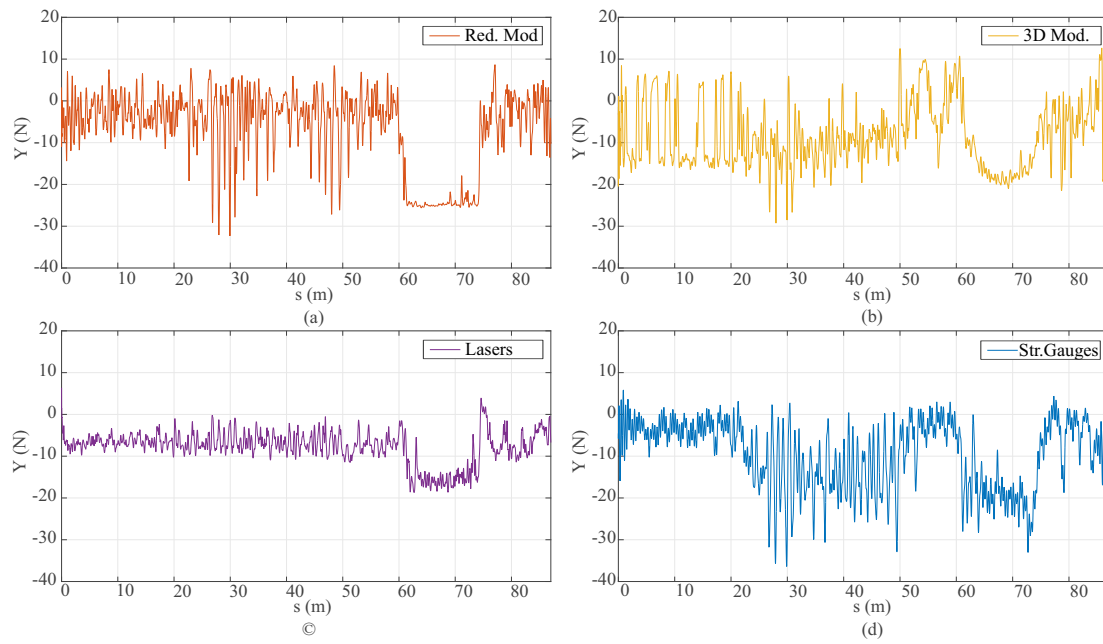


FIGURE 6.22: Lateral force experiment 1, methods comparison

### 6.1.3.2 Experiment 2 contact force measurements

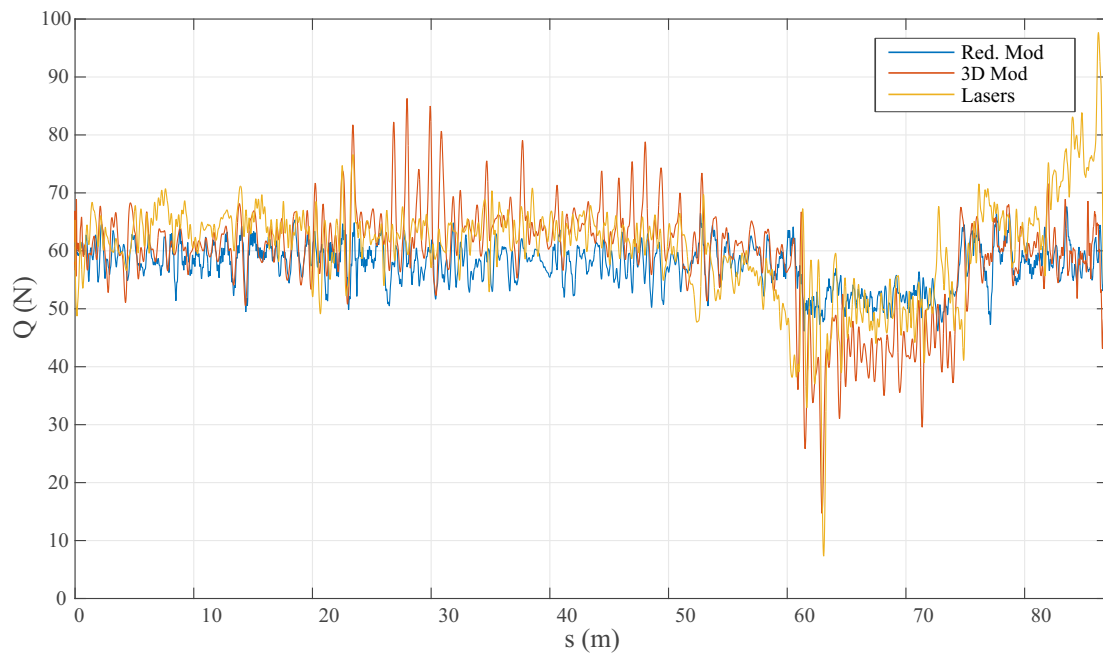


FIGURE 6.23: Normal force experiment 2, methods comparison

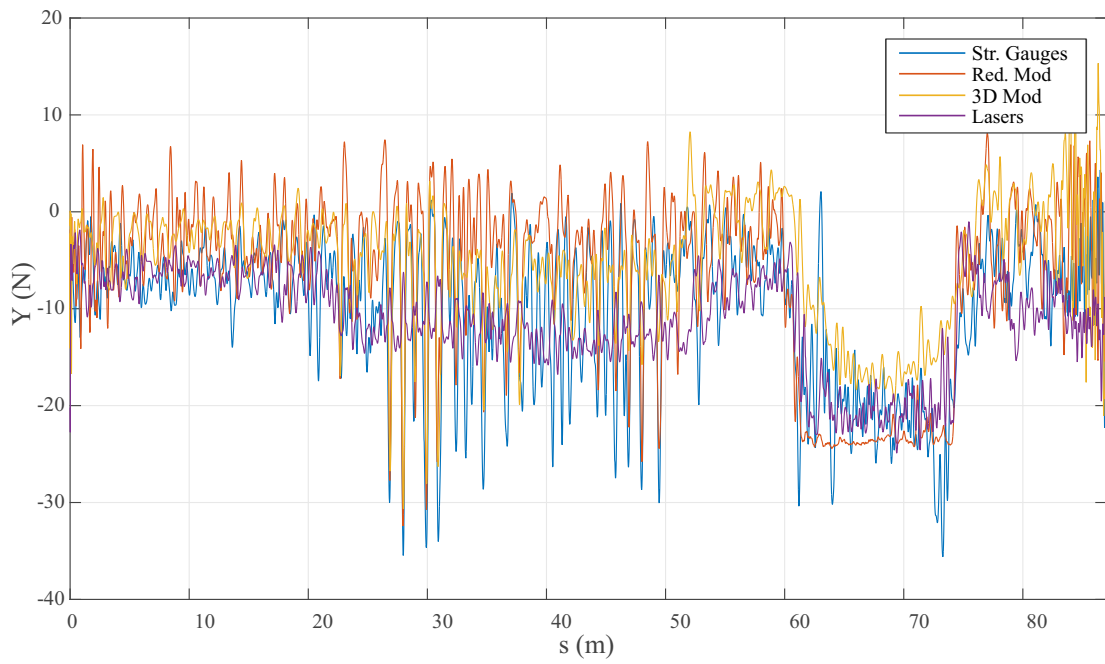


FIGURE 6.24: Lateral force experiment 2, methods comparison

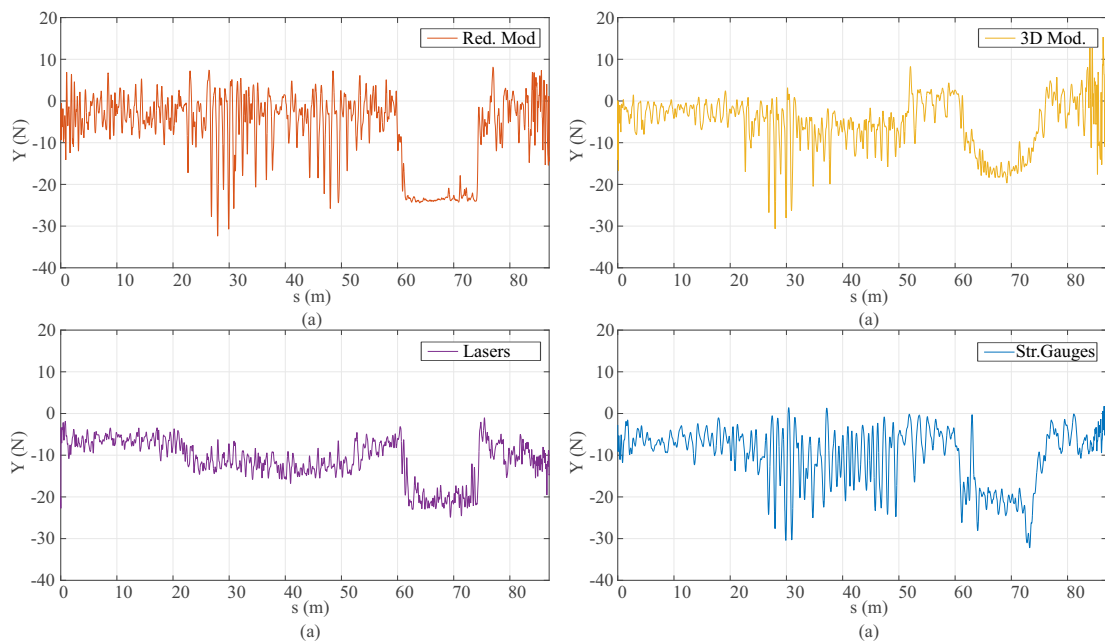


FIGURE 6.25: Lateral force experiment 2, methods comparison

### 6.1.3.3 Experiment 3 contact force measurements

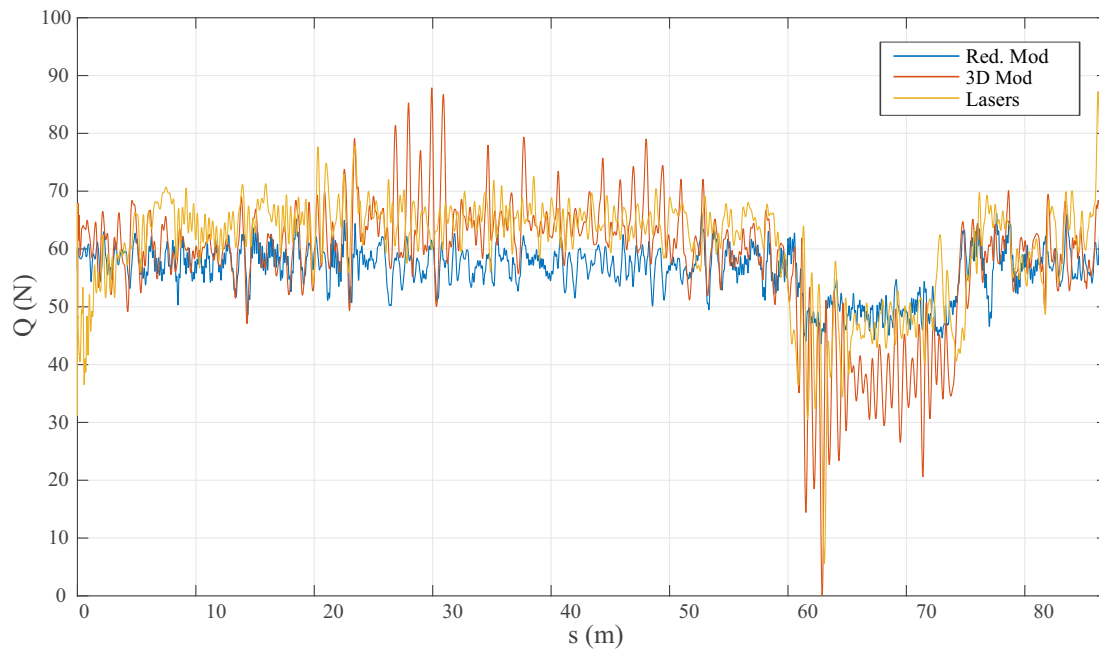


FIGURE 6.26: Normal force experiment 3, methods comparison

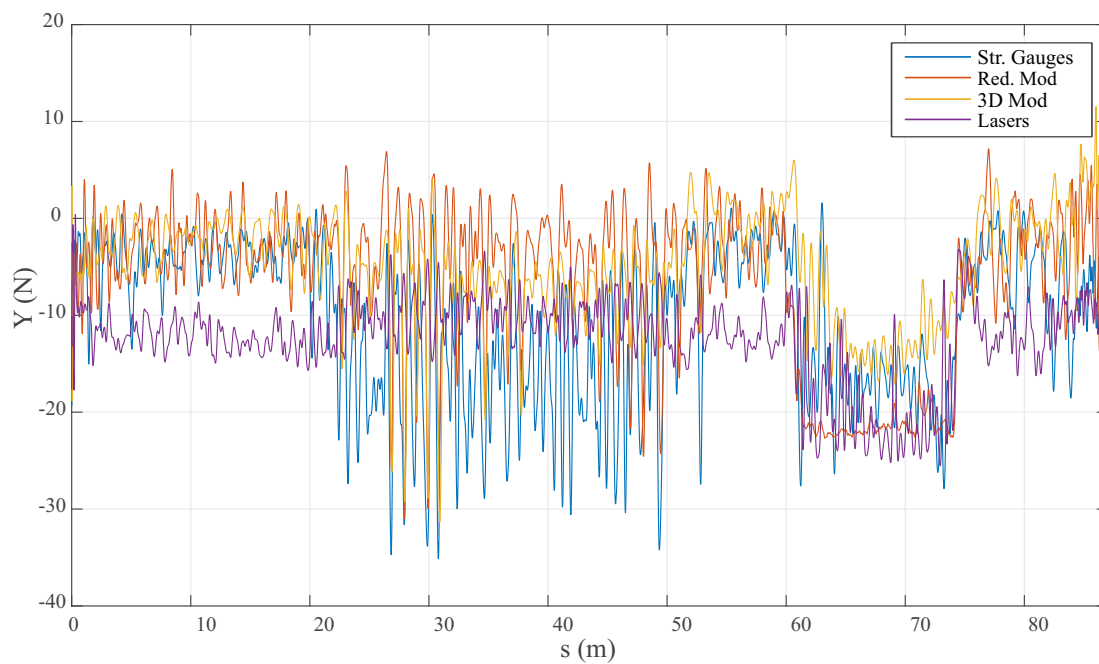


FIGURE 6.27: Lateral force experiment 3, methods comparison

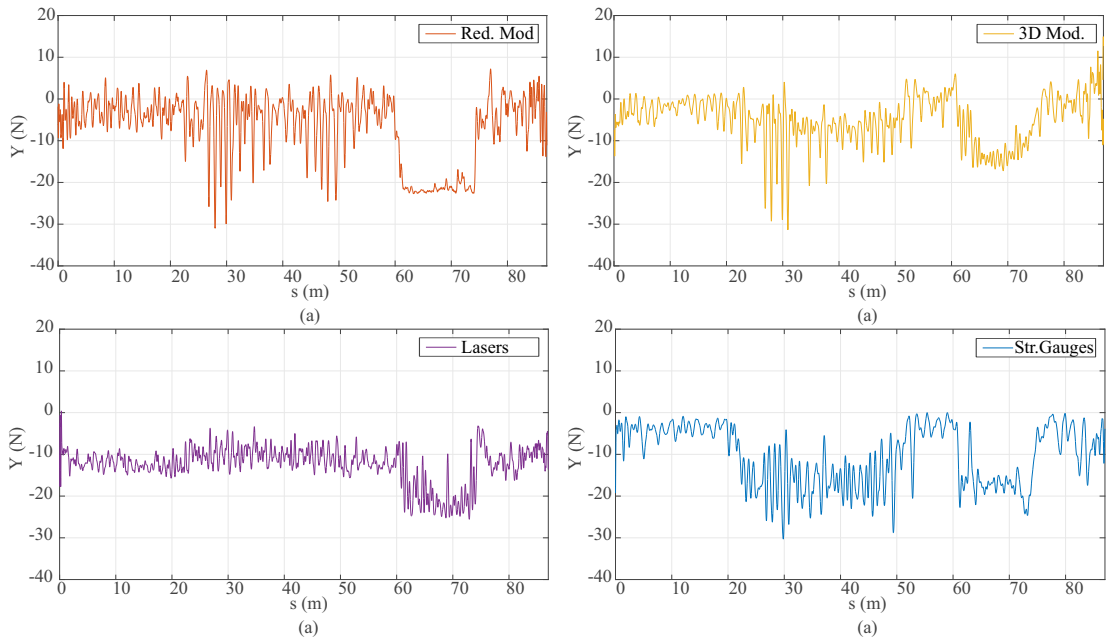


FIGURE 6.28: Lateral force experiment 3, methods comparison

#### 6.1.4 Backward movement experiments

Equivalent experiments have been carried out with the vehicle running in the backward direction of the track. In these experiments the instrumented wheel (left wheel of the leading wheelset) interacts in a different manner with the track with respect to the forward movement experiments presented before. Figures 6.30 to 6.41 show the linear accelerations and angular velocities measured by the IMUs installed on the vehicle. Those results correspond to experiment number 6 where the vehicle reaches an average forward velocity of 2.5 m/s. It is important to note that, in those experiments the vehicle starts its movement at coordinate  $s = 87$  m and it stops at  $s = 0$  m. The results obtained are similar to the analysed in the forward movement experiments. There is again a good agreement between the measured magnitudes and the numerical results drawn from the reduced computational model.

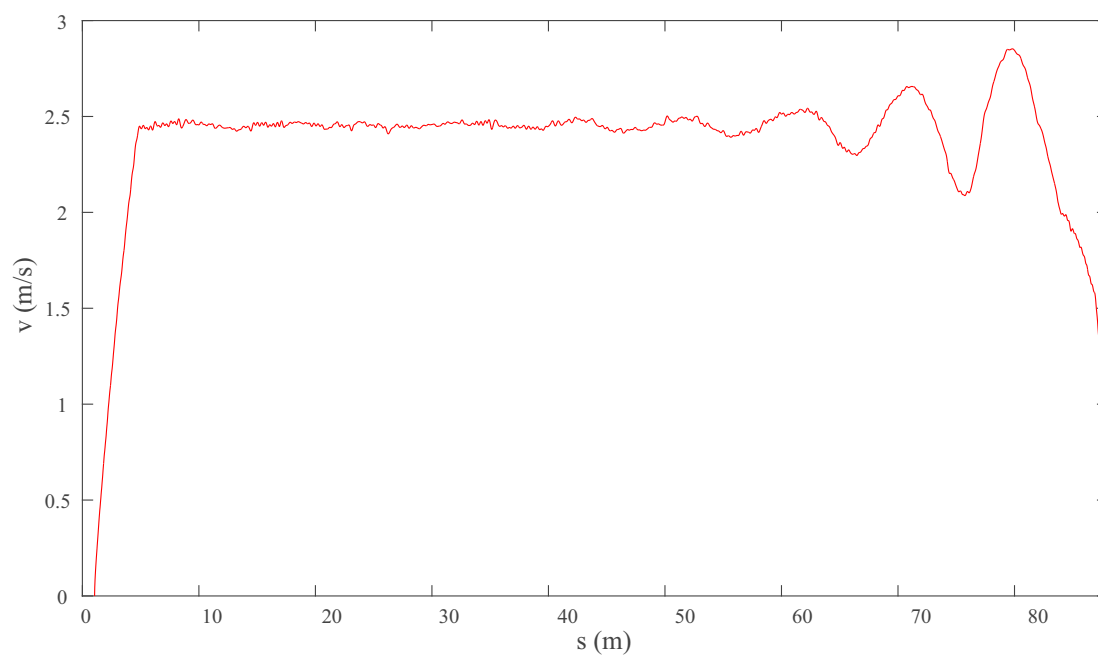
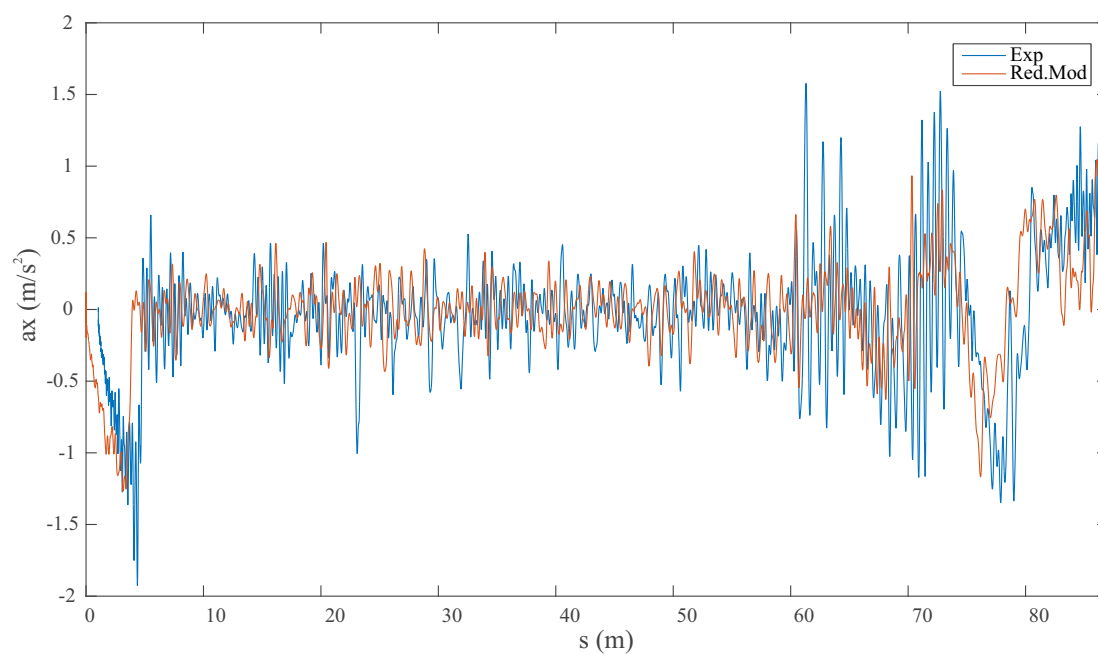
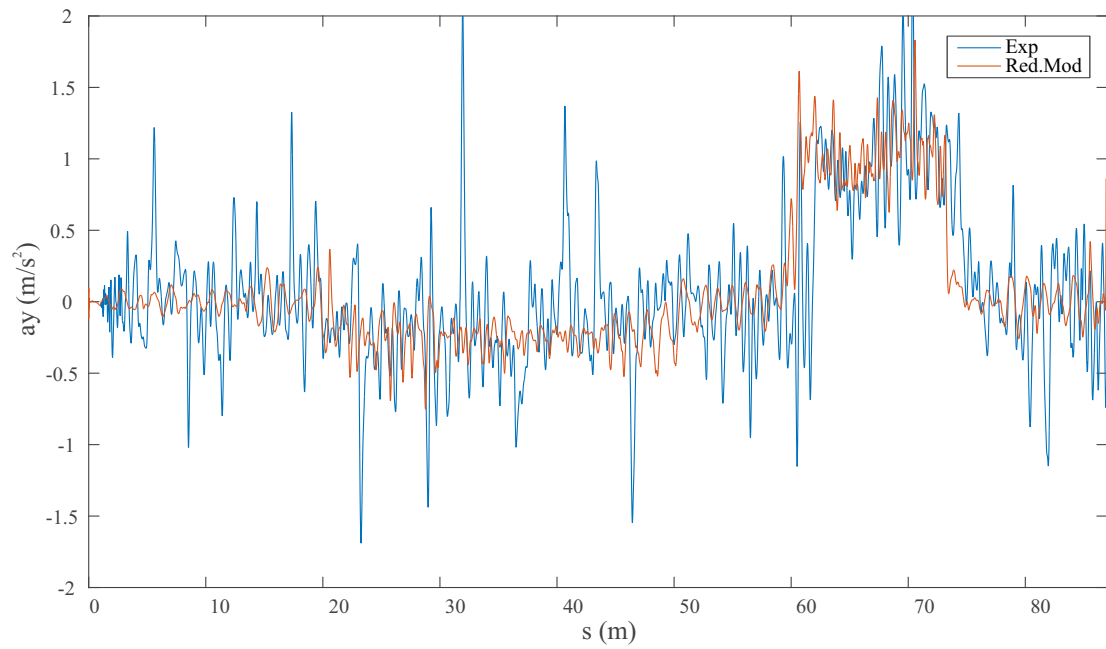
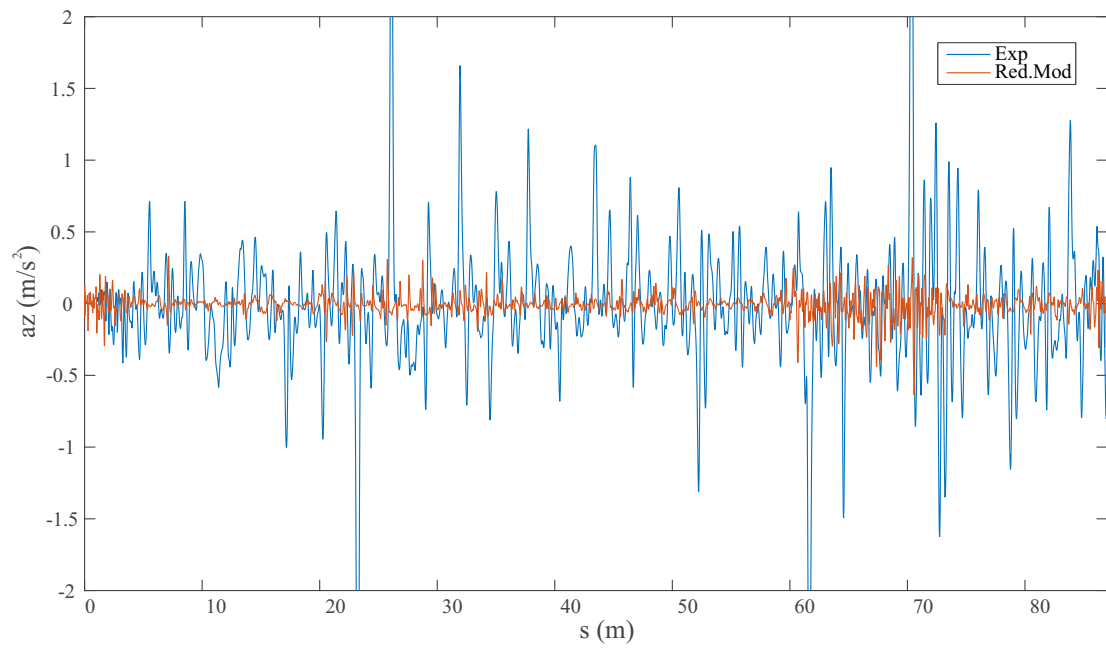
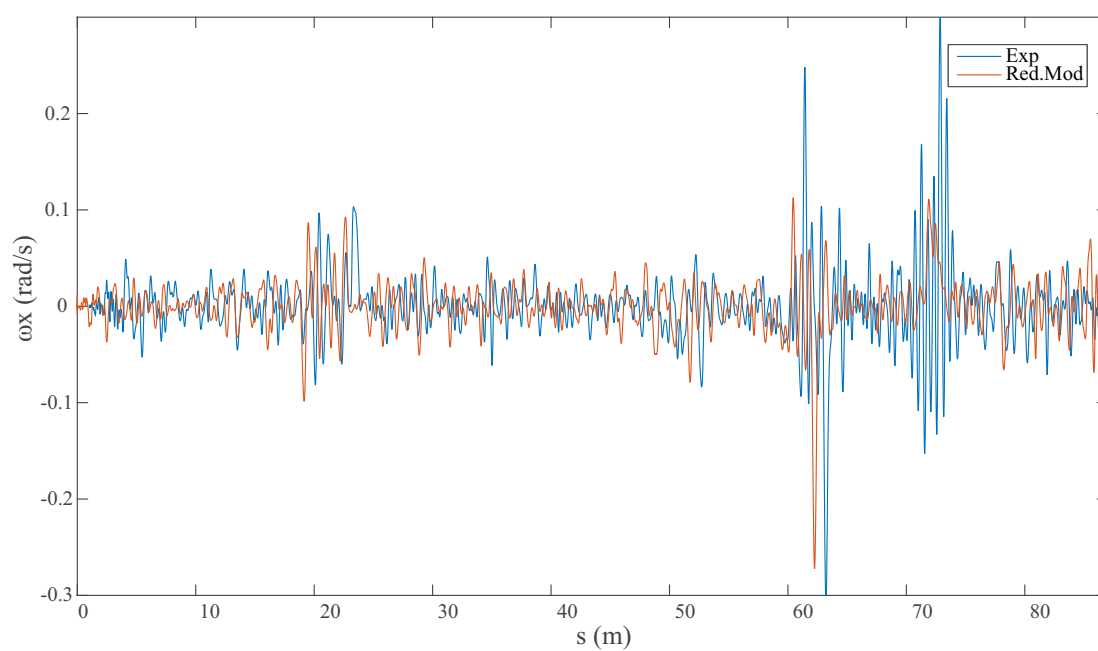
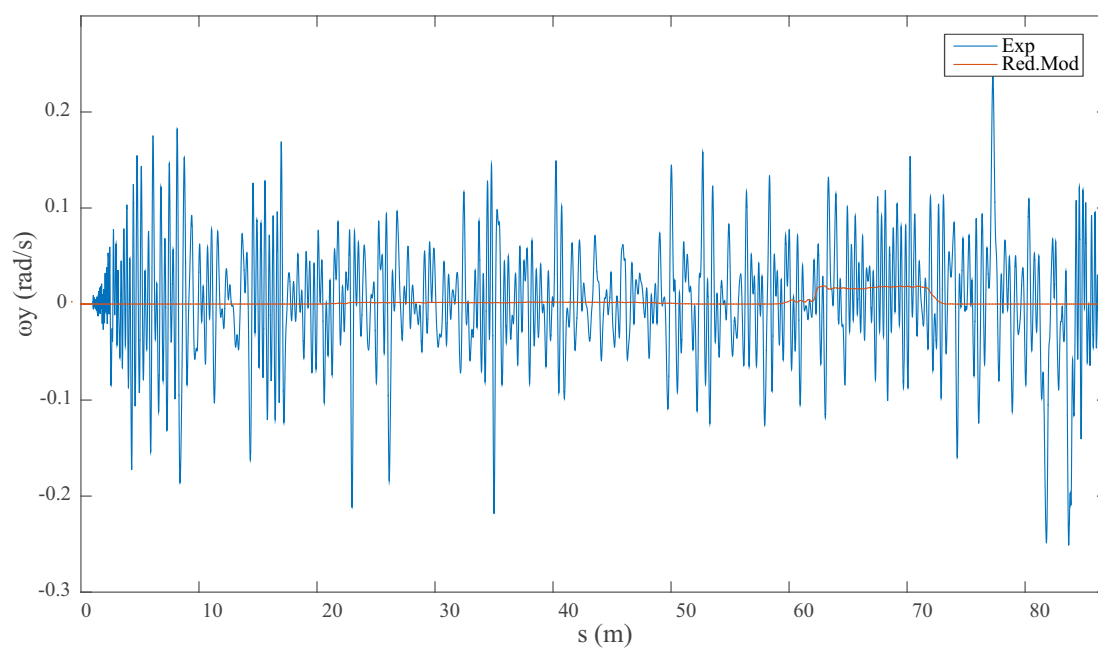


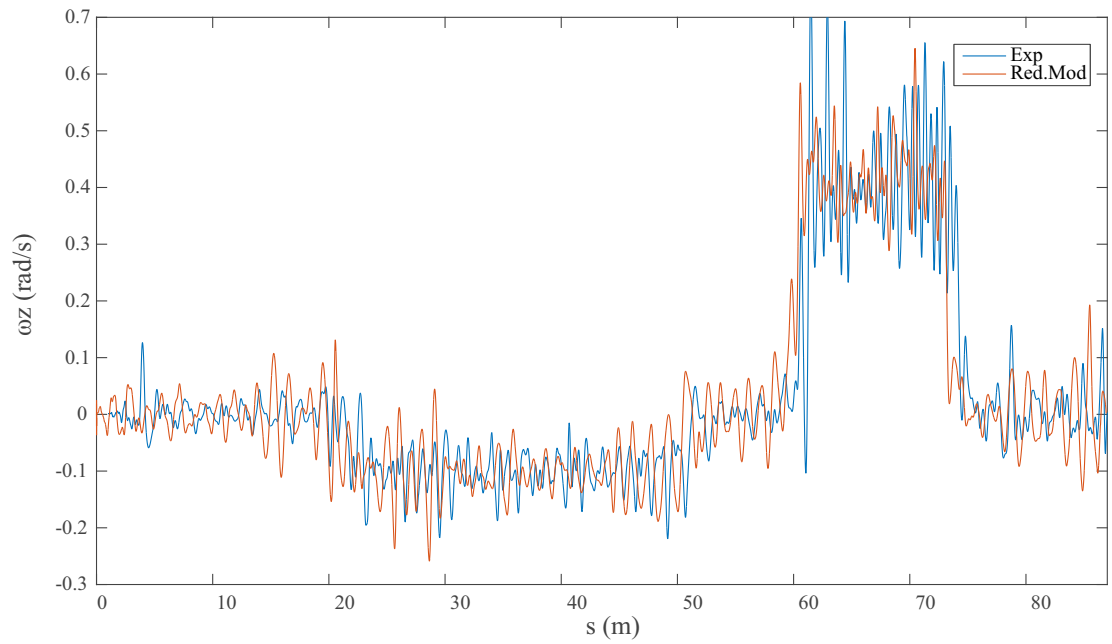
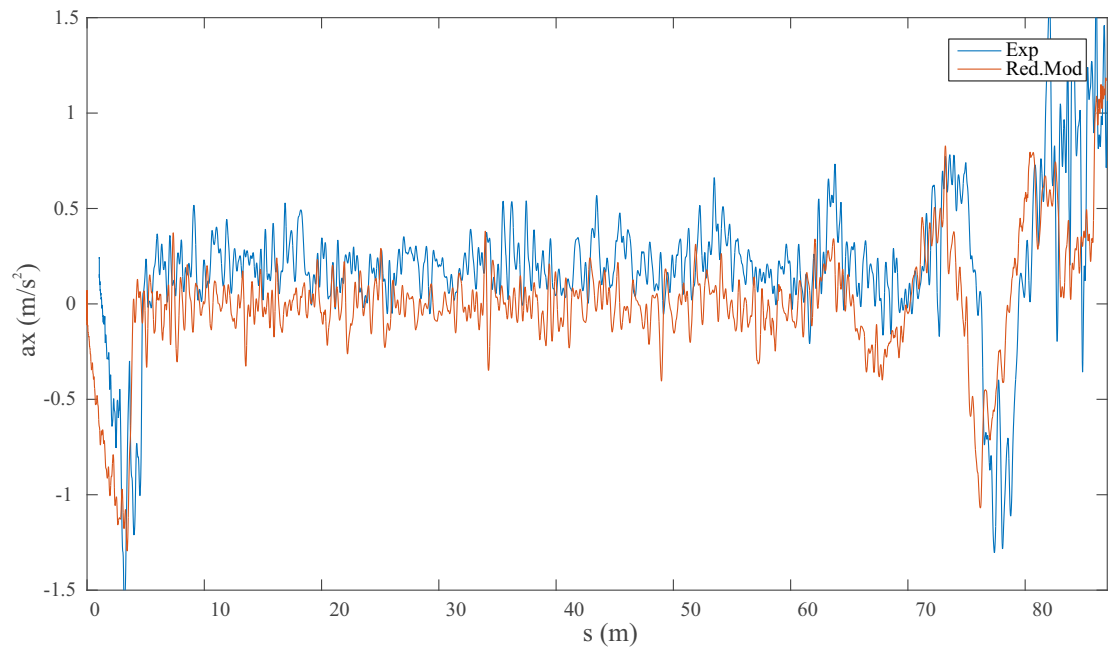
FIGURE 6.29: Forward velocity profile in experiment 6

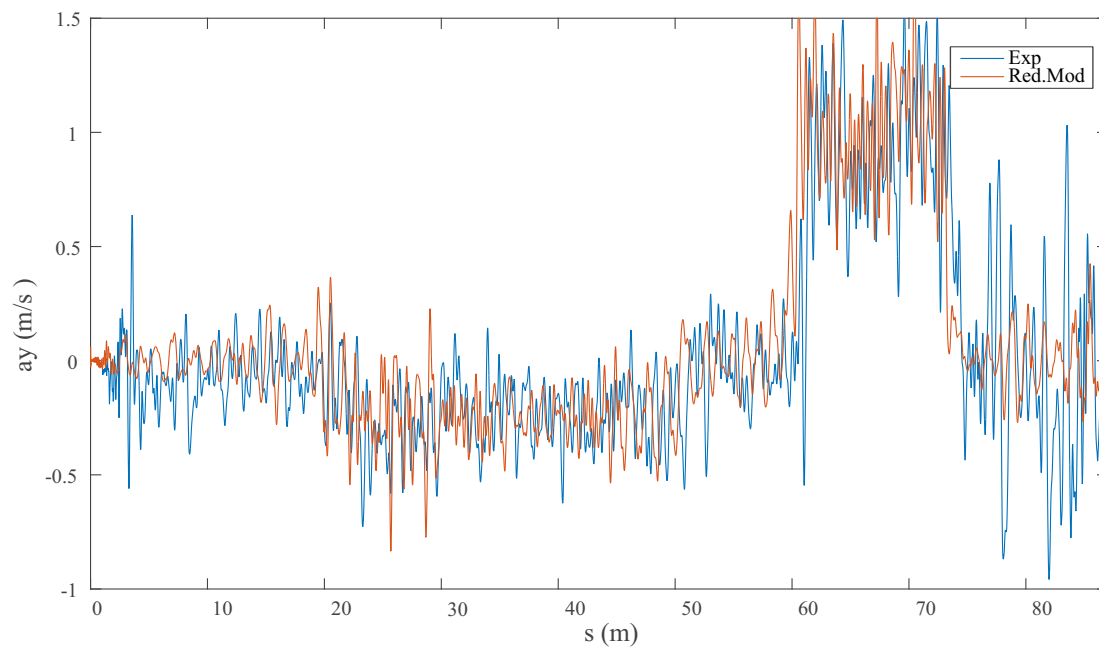
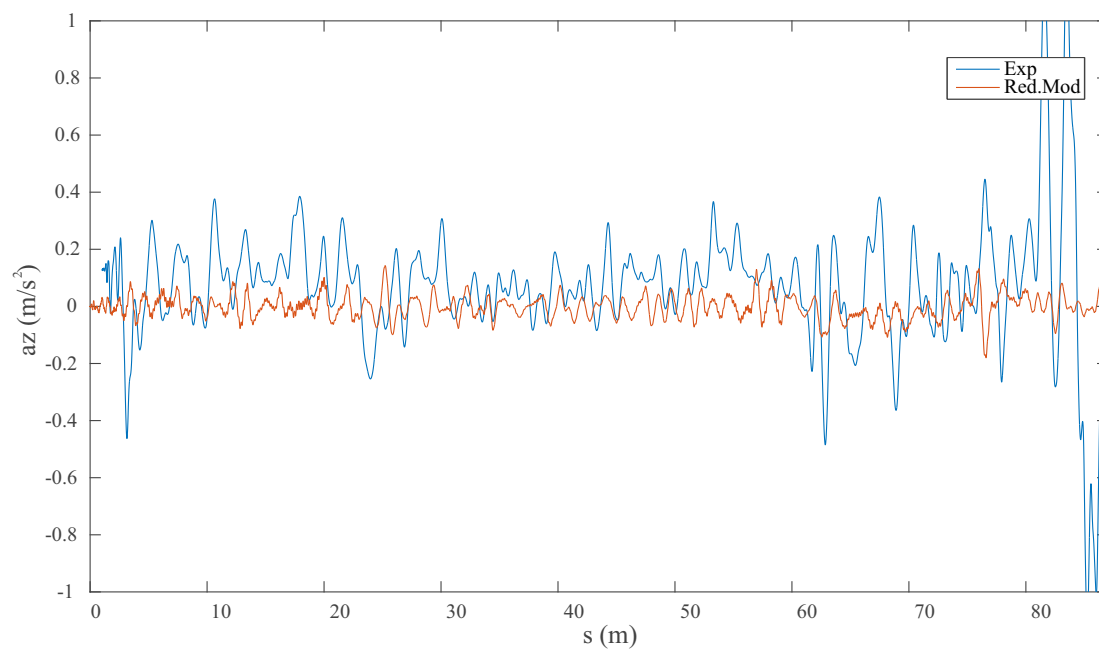
FIGURE 6.30: Longitudinal acceleration  $a_x$  of the instrumented wheelset

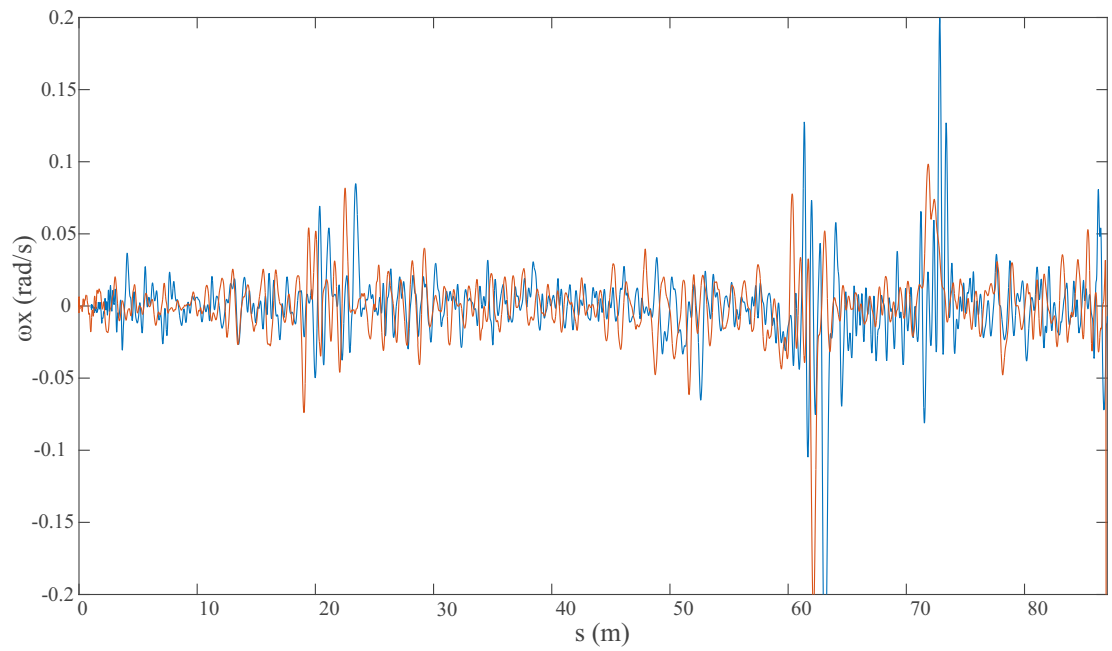
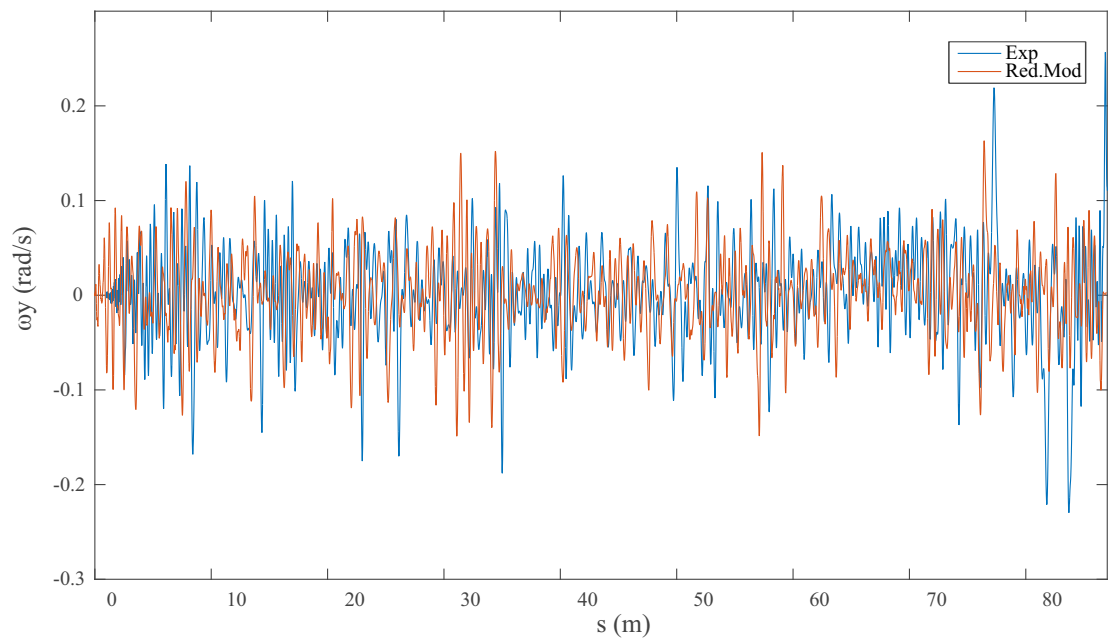
FIGURE 6.31: Lateral acceleration  $a_y$  of the instrumented wheelsetFIGURE 6.32: Vertical acceleration  $a_z$  of the instrumented wheelset

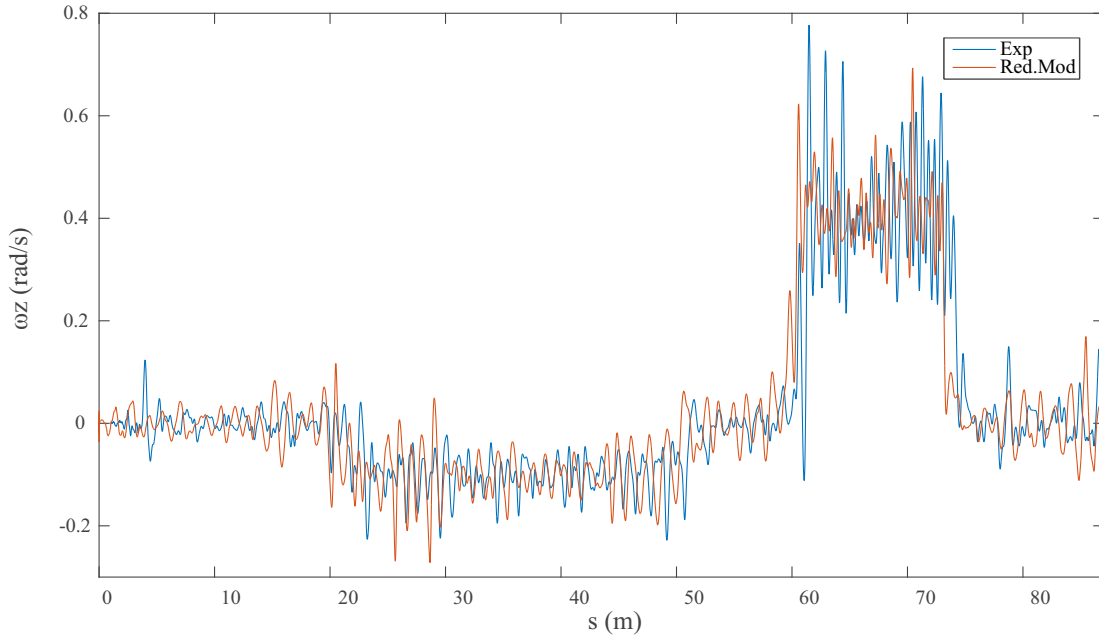
FIGURE 6.33: Angular velocity  $\omega_x$  of the instrumented wheelsetFIGURE 6.34: Angular velocity  $\omega_y$  of the instrumented wheelset



FIGURE 6.35: Angular velocity  $\omega_z$  of the instrumented wheelsetFIGURE 6.36: Longitudinal acceleration  $a_x$  of the bogie frame

FIGURE 6.37: Lateral acceleration  $a_y$  of the bogie frameFIGURE 6.38: Vertical acceleration  $a_z$  of the bogie frame

FIGURE 6.39: Angular velocity  $\omega_x$  of the bogie frameFIGURE 6.40: Angular velocity  $\omega_y$  of the bogie frame

FIGURE 6.41: Angular velocity  $\omega_z$  of the bogie frame

The contact force measurement results obtained with the instrumented wheelset are shown below. The normal force measured in experiments 4 to 6 (Figs. 6.42 to 6.48) has been satisfactorily estimated through the proposed method. It must be pointed out that, in the normal force experimental measurements it can be observed force peaks larger than in the simulated signal. To the author's opinion, this is due to vibrations experienced by the laser sensors and the measuring surfaces where they are pointing towards. Those vibrations introduce these incorrect measurements in the signal. One of the conclusion drawn from this research is that, laser sensors have shown a fantastic performance under laboratory conditions, but they are not as robust as expected in a real scenario.

Analysing the measured lateral force, one can observed at a glance that, the average lateral force in the sharp radius curve is almost twice the force measured at the same section when the vehicles moves forward. The reason is that, when the vehicle is running in backward direction and it negotiates the small radius curve, the continuous flange contact appears in the instrumented wheel. It is also observed how the maximum average lateral force in the three experiments that appears in the small radius curve increases with the forward speed. This differs from the same results obtained in the

forward movement experiments. In those experiments the maximum average force in the small radius curve decreases with the forward velocity of the vehicle. Table 6.2 summarized the these results for the complete set of experiments. That different trend between forward and backward experiments is due to the wheel that experiences flange contact: the instrumented wheel in the inverse direction and the non-instrumented wheel in the normal direction of the travel. The steady curving behaviour of railroad vehicles is a complete non-linear phenomenon that depends on several factors, such as curve radius, forward velocity, geometry of the vehicle, wheel conicity, etc. Under these conditions the decrease of one component of the force when the forward velocity increases is perfectly possible.

Concerning the measurements obtained with the strain gauges and precision lasers in the complete vehicle ride, one can observe how the strain gauges approach fits better with the computational results drawn from the reduced model than the precision lasers measurements. In fact, it can be observed in the three experiments (Figs. 6.43 to 6.50) how the precision lasers measure a higher lateral force in the small radius curve than the strain gauges or the computational model.

TABLE 6.2: Second curve average lateral force

Direction	Velocity	Simulation	Lasers	Strain gauges
Normal	1.5 m/s	24.16 N	21.84 N	21.66 N
	2.0 m/s	23.92 N	20.56 N	20.16 N
	2.5 m/s	22.06 N	19.10 N	18.60 N
Inverse	1.5 m/s	32.29 N	33.44 N	33.56 N
	2.0 m/s	34.03 N	36.81 N	37.02 N
	2.5 m/s	35.73 N	37.23 N	38.20 N

If one compares the performance of both set of sensors installed on the dynamometric wheelset, the strain gauges and the precision lasers, it can be said that the lateral force measurement based on strain gauges performs better. In fact, in the six experiments carried out with the strain gauges, the obtained measurements have a good agreement with the computational results. The same conclusion does not apply to the measurement with precision lasers, where different tendencies appear in the forward

and backward experiments. Nonetheless, the six experiments with the lasers have in common that the sensors satisfactorily measure the lateral force when the vehicle negotiates the sharp radius curve. In addition, taking a look on the lateral force measurement of the precision lasers in the backward experiments, one can observe how the three line graphs (see Fig. 6.44 (b), Fig. 6.50 (b) and Fig. 6.50 (b)) show the same tendency. However, this does not happen in the forward experiments where the precision lasers measurements do not agree further from the small radius curve (see Fig. 6.22 (c), Fig. 6.25 (c) and Fig. 6.28 (c)). This could be explained by an incorrect model assumptions when developing the lateral force calculation algorithm based on the precision lasers. That has led to a non-fully efficient measuring procedure based on the lateral deflection experiences by the wheel.

It seems that, when the vehicle moves backwards and it negotiates the small radius curve first, the high value of the force experienced by the wheel due to the flange impact with the outer rail makes the wheel get stuck into an unusual position, such that the stiffness of the assembly wheel and bearing box changes. To the author's opinion, the mechanical system consisting on the bearing box itself, the bearing, the snap rings and the axle has certain elasticity that it is lost when the wheel gets stuck after a strong impact against the rail. Of course this is just speculation, and the truth is that, it has not been possible to identify this phenomenon during the calibration process. It is true that, experiment 2 has an extraordinary accordance between the distance lasers and the strain gauges and computational model. Of course it is not enough to consider the proposed method as robust. In experiment 2 the wheel experiences conditions very similar to the test conditions reproduced in the static calibration process accomplished, drawing a correct lateral force estimation. In light of the obtained results, and considering that one of the experiment 2 has been quite satisfactory, the author considers that the lateral force measurement method based on the lateral deflection is not entirely effective. It requires a further analysis and probably some changes in the model assumptions. Due to the research deadline this study has not been accomplished.

#### 6.1.4.1 Experiment 4 contact force measurements

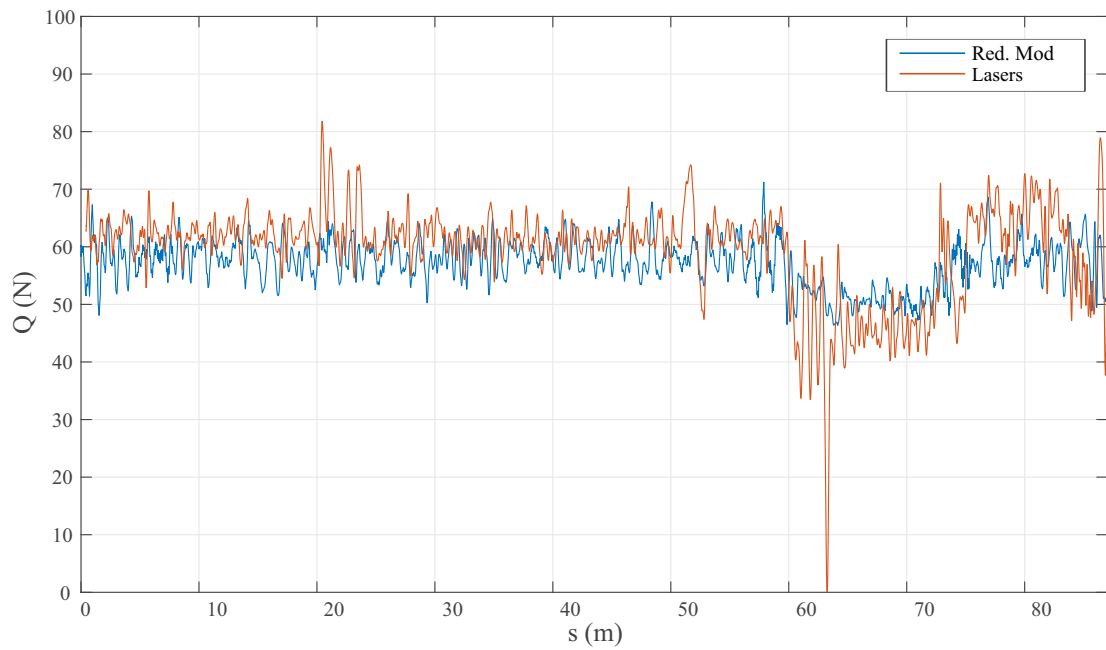


FIGURE 6.42: Normal force experiment 4, methods comparison

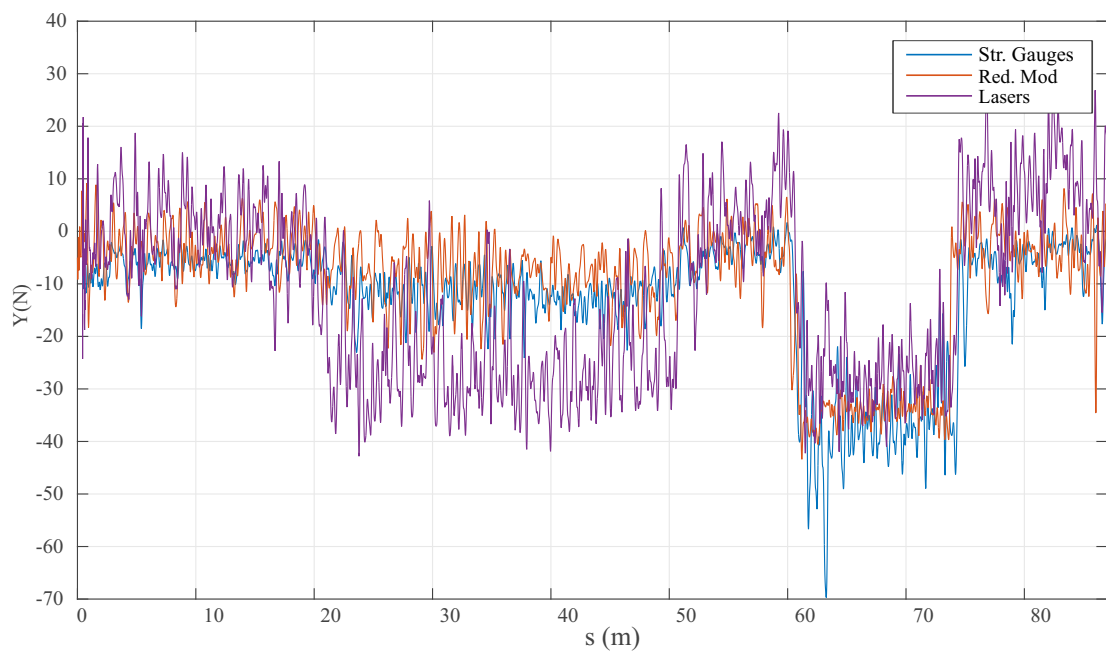


FIGURE 6.43: Lateral force experiment 4, methods comparison

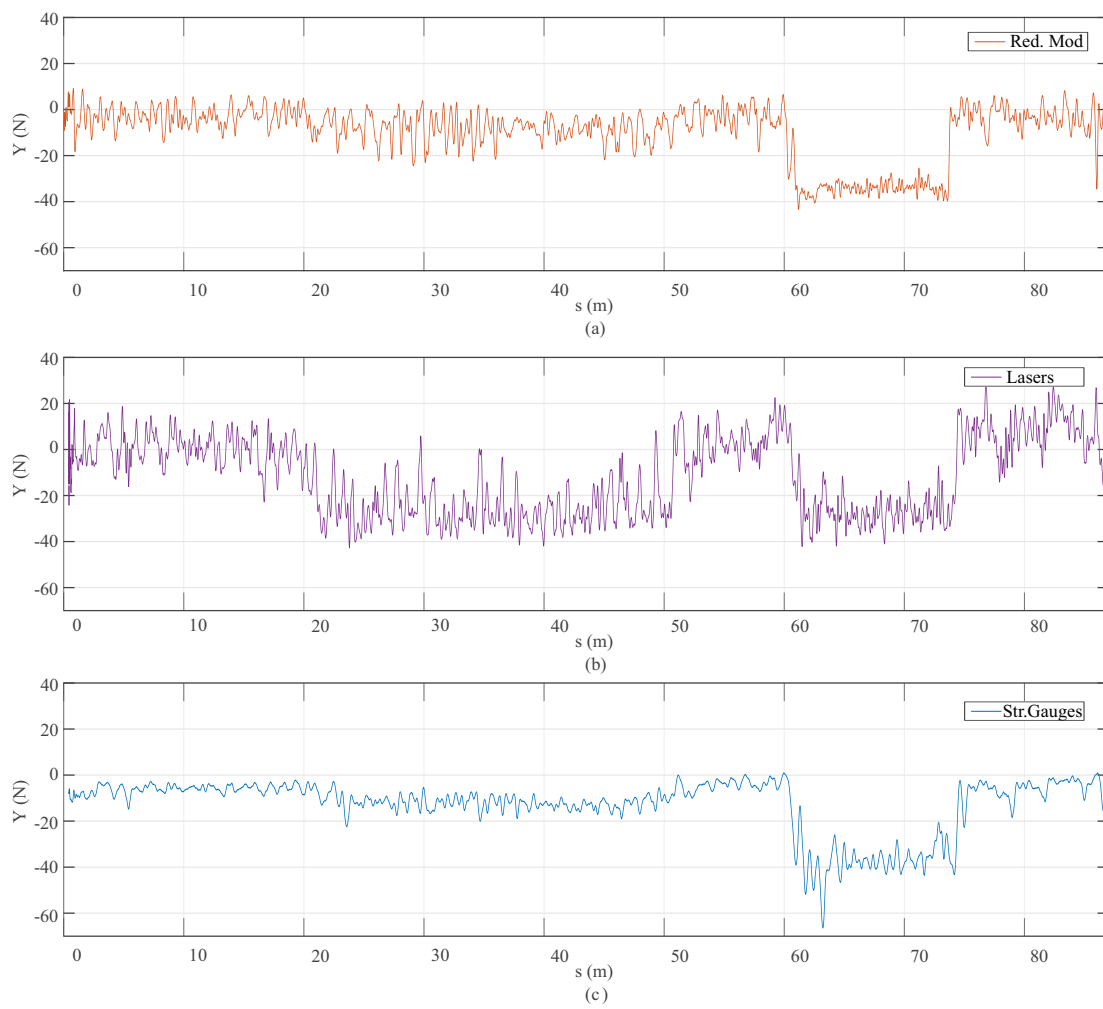


FIGURE 6.44: Lateral force experiment 4, methods comparison



### 6.1.4.2 Experiment 5 contact force measurements

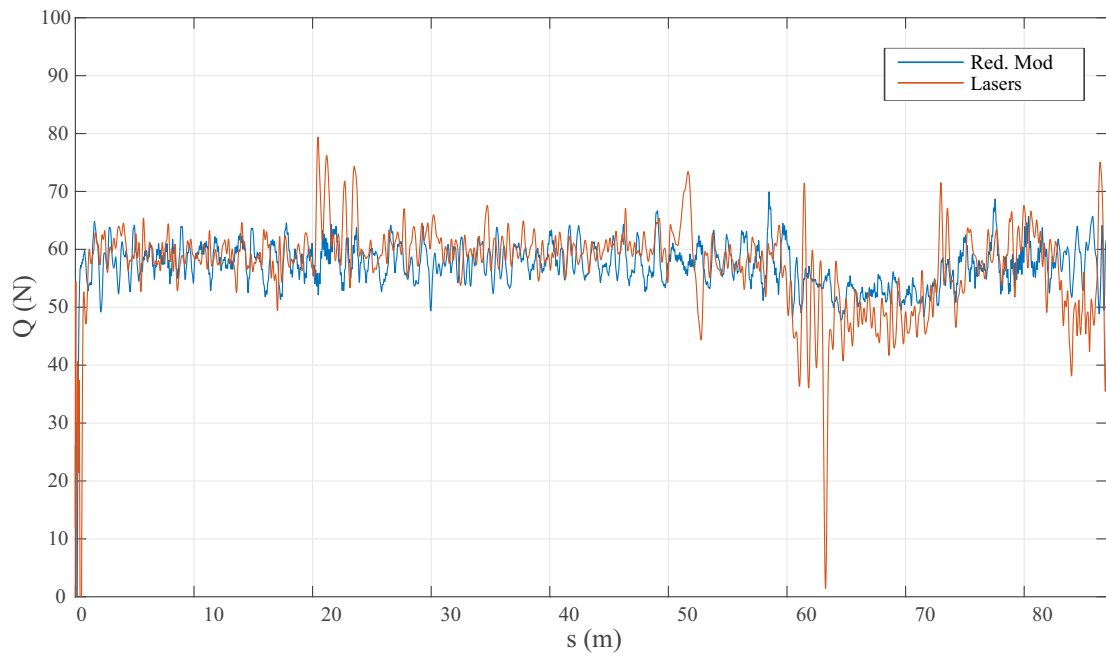


FIGURE 6.45: Normal force experiment 5, methods comparison

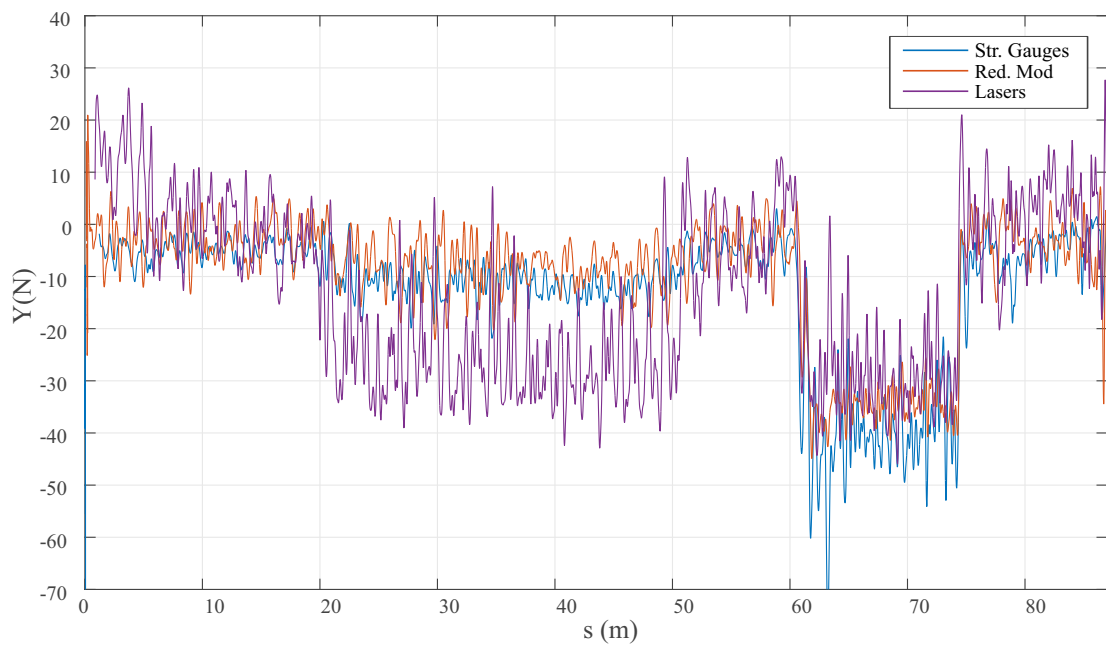


FIGURE 6.46: Lateral force experiment 5, methods comparison

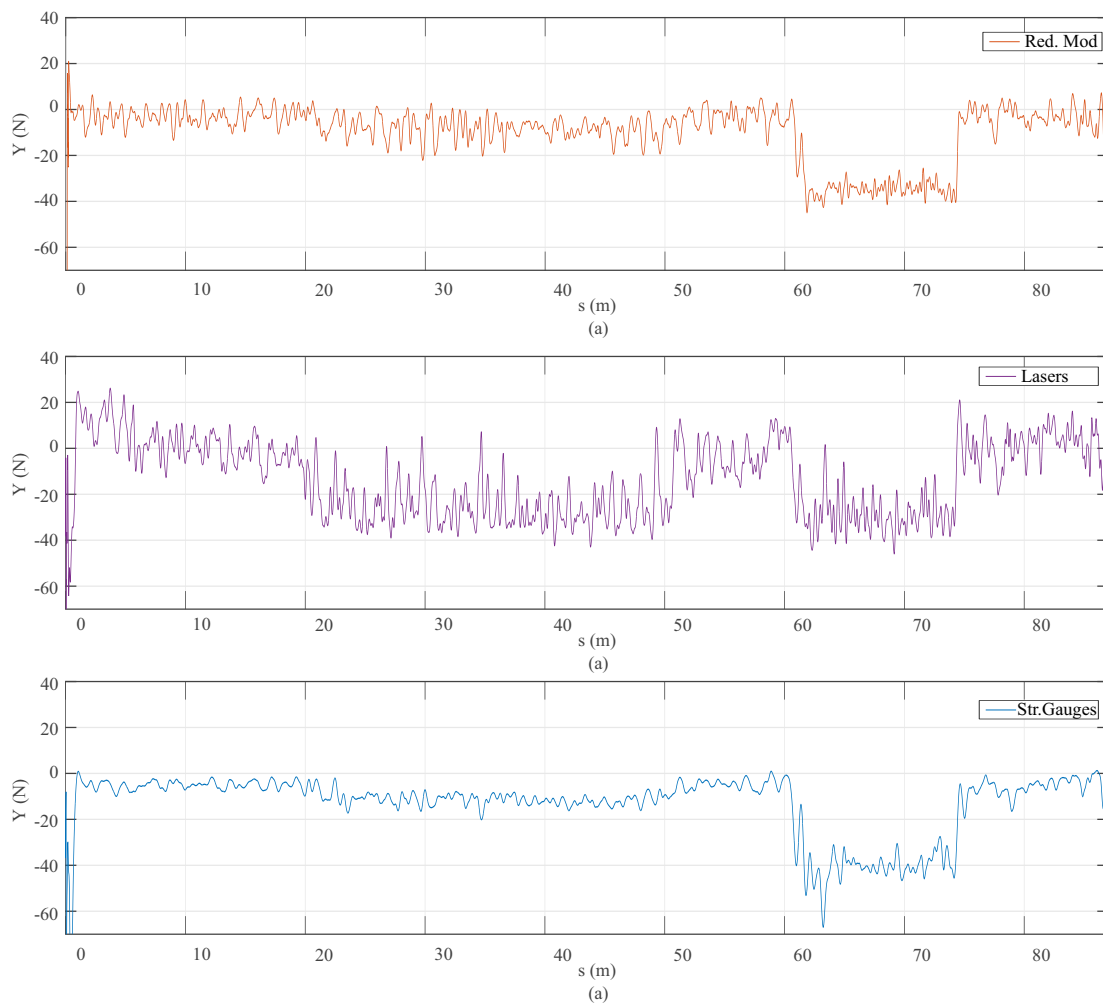


FIGURE 6.47: Lateral force experiment 5, methods comparison

## 6.1.4.3 Experiment 6 contact force measurements

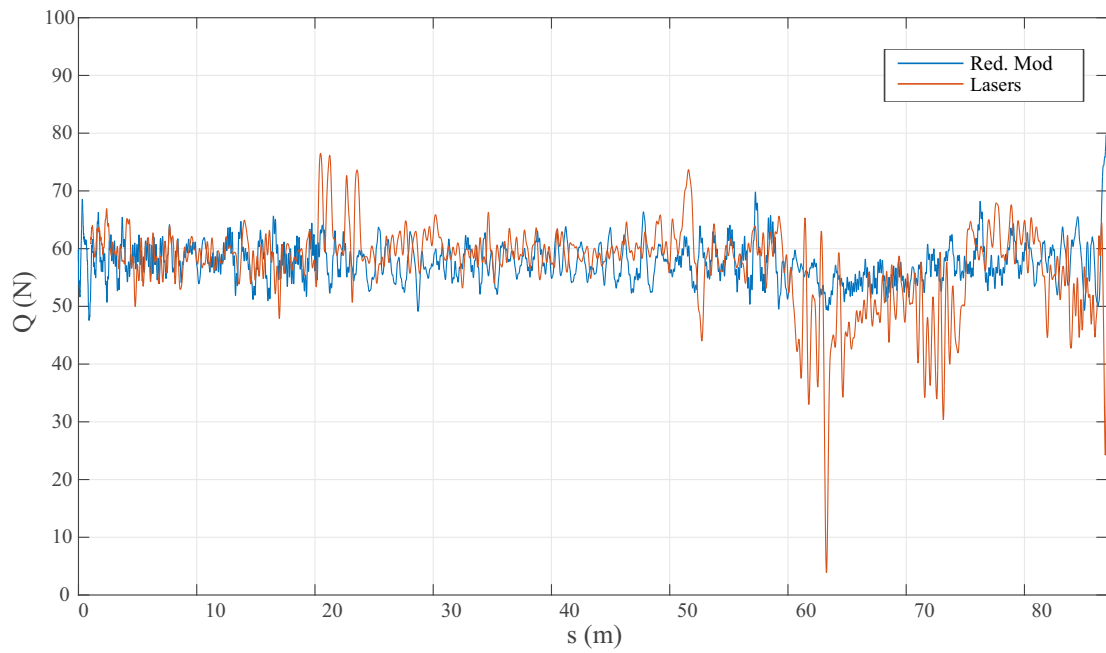


FIGURE 6.48: Normal force experiment 6, methods comparison

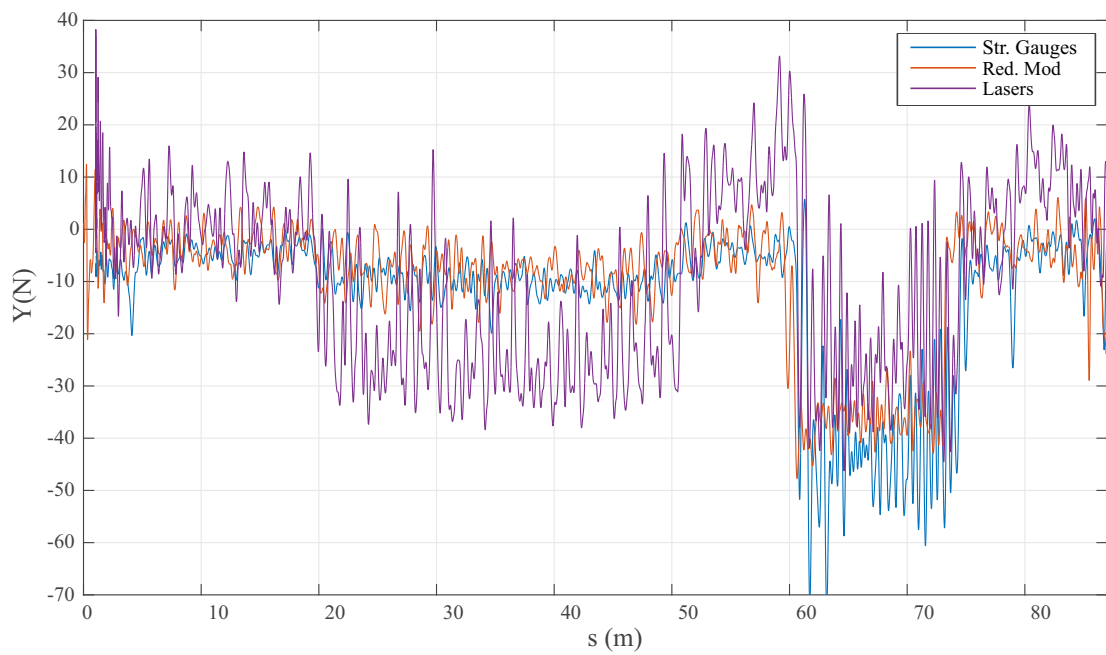


FIGURE 6.49: Lateral force experiment 6, methods comparison

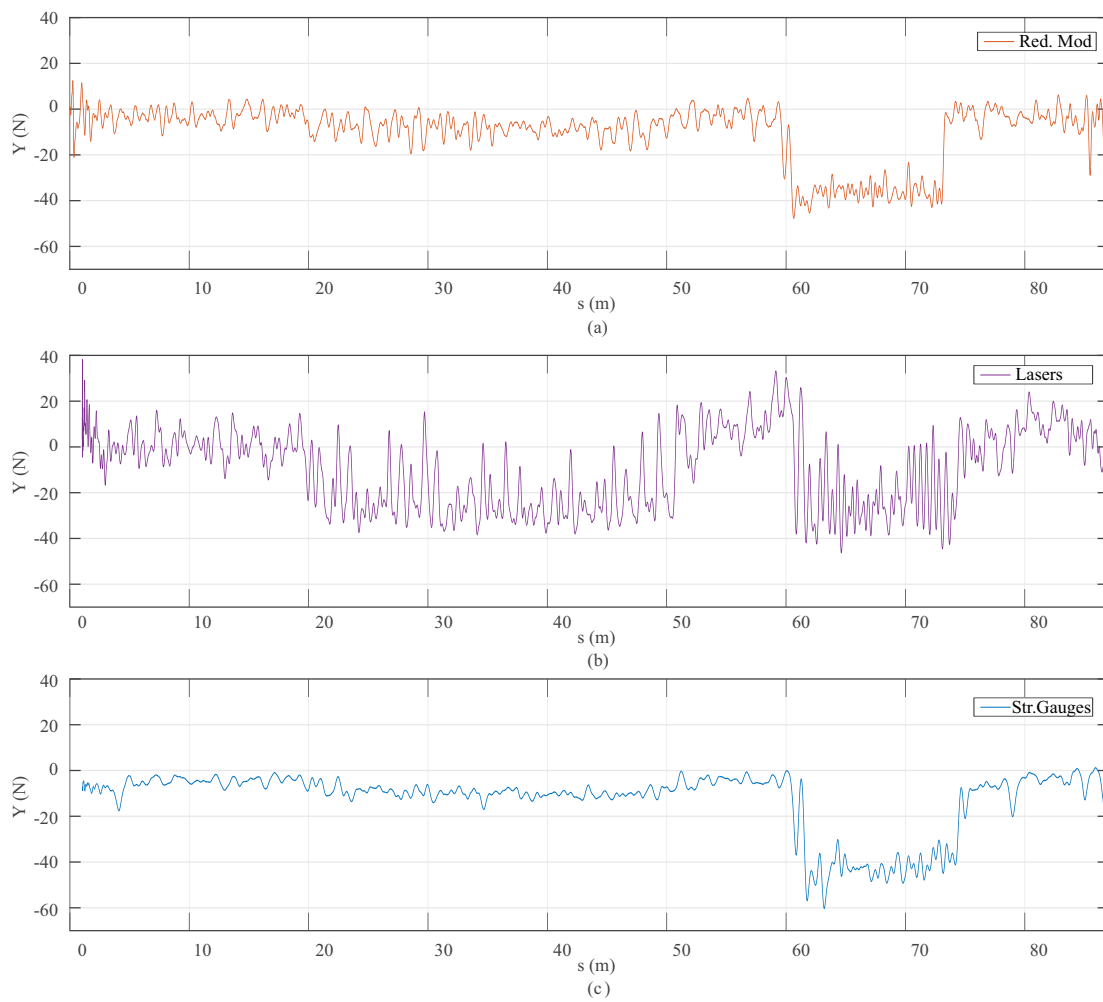


FIGURE 6.50: Lateral force experiment 6, methods comparison

# Chapter 7

## Closure

### 7.1 Closure

#### 7.1.1 Summary

The main purpose of this PhD thesis has been the development of a scaled dynamometric wheelset for the measurement of wheel/rail contact forces on a scaled railway vehicle. The dynamometric wheelset has been instrumented with two different technologies for the measurement of applied forces: strain gauges and precision distance lasers. The system has been tested on a experimental scaled track built at the rooftop of the School of Engineering at the University of Seville.

The thesis has begun in Chapter 1 with an state of the art review of the main technologies uses in the railways industry for the measurement of the wheel/rail contact forces. Showing off the latest research on this subject present in the literature.

In Chapter 2, the experimental scaled track has been measured with an innovative technique in order to precisely determine its geometry. An optimization software for the ideal track centre line identification has also been developed. Track irregularities are obtained as output of the optimization software.

The dynamometric wheelset design, instrumentation and calibration have been presented in detail in Chapters 3 and 4. The calibration process has been accomplished on

a scaled static test bench developed by the author. In that bench, controlled vertical and lateral loads are applied on the instrumented wheelset and the experimental results are compared with simulation drawn from a FEM of the instrumented wheel created in ANSYS. Two algorithms for the calculation of the applied lateral force on the instrumented wheel have been proposed. The first one estimates the applied lateral force by the measurement of the radial strain on the wheel-core. The second one determines the applied lateral force through the deflection experienced by the wheel-web. Vertical forces are obtained measuring the deflection of the primary suspension and establishing a balance of forces on the wheelset.

Two railroad computational multibody models have been presented in Chapter 5. The first one assumed a weakly couple vertical and lateral dynamics while the latter is a full non-linear 3D model. The force measurements obtained in a experimental campaign on the scaled track have been compared with the numerical results drawn from the two computational models.

### 7.1.2 Conclusions

In view of the obtained results, it can be said that the strain gauges are a better choice for the lateral contact force measurement since their results prove to be more precise compared to the numerical simulation than the precision distance lasers. The strain gauges measure satisfactory the lateral force applied on the wheel in all the experiments carried out with the dynamometric wheelset. Vertical forces on the wheel have been also correctly measured through the precision vertical lasers obtaining meaningful force results.

However, from a practical point of view, strain gauge use is more sophisticated than using distance lasers. On the one hand, strain gauges require a careful installation to guarantee their correct functioning. An imprecise installation of the sensors on the wheel-core or inappropriate soldering of wires will result in an incorrect force measurement. On the other hand, if strain gauges are installed on both sides of the wheel core, it is also necessary to drill into the wheel to wire the sensors. This can jeopardize the security of the wheel if it is not done correctly. In addition, the strain gauges need very expensive telemetry systems to transfer the information from the rotating wheelset to

the data acquisition system. Brush connectors are another valid alternative to telemetry but they normally introduce considerable noise on the signals. Additionally, they are expensive to manufacture. It is also important to note that, signal processing in the strain gauge method is more sophisticated compared to the precision laser approach. Due to the fact that strain gauges rotate with the wheel, harmonics will appear on the acquired signals and the force calculation algorithm must be able to remove a large part of those harmonics in order to obtain a precise force measurement.

On the other hand, distance lasers are installed on non-rotating parts of the vehicle, so they do not need wireless communication. That greatly reduces instrumentation costs even though a single precision laser sensor is more expensive than a complete set of strain gauges. Laser setup is also easier as they only need to be fixed to the bearing box and pointed towards the wheel-web. The only requisite is to position them at a certain offset distance from the measurement surface. That can be easily done, for instance, with a simple slider mechanism. In some cases, as the one studied in this paper, the wheel surface might have a surface irregularity pattern, but it can be easily registered during system calibration and later removed from the signal. A clear drawback of distance lasers against strain gauges is the fact that to guarantee a correct performance of the system lasers' lenses, they must be always free of dust. A simple solution could be a pressurized air jet coming from the vehicle pressurized air system directed towards the sensor lens actuating at regular intervals.

The wheel-rail contact force measurement methods presented in this thesis have been applied to a scaled vehicle. Nonetheless, they can be extended to a full-scaled system, always provided that an equivalent preliminary FEM study of the wheelset geometry, instrumentation and calibration process is done. Taking into account that the scaled vehicle used for testing does not exactly reproduce the dynamics of a real bogie, the conclusions drawn from this thesis related to vehicle dynamics response and force magnitudes and frequency analysis must not be directly applied to a full-scaled vehicle. However, all the results obtained about instrument setup, uncertainties and precisions can be fully extended to a larger system. Furthermore, considering that the radial strains, wheel web lateral bending and primary suspension deflections in a real vehicle will be larger, these methods will work even better. The author's opinion after carrying out this research, is such that, non-contact distance measurement sensors applied

to vertical and lateral wheel-rail contact forces measurement are an interesting choice against traditional dynamometric wheelsets instrumented with strain gauges. Particularly considering the ease of installation and use of non-contact distance measurement sensors.

Finally, the utilization of scale systems represents an easy, inexpensive and safe way to validate different railway computational models, wheel-rail contact force estimation methods or new running safety criteria for instance. The modelling techniques, results and conclusions drawn from a scaled system might then be extended with caution to full scale vehicles. As a future line of research, the presented work can be applied to a full scale system in order to compare both instrumentation technologies when applied loads on the wheels are much larger. In that scenario, researchers hope to find an equivalent performance of both technologies although it is yet to be proven.

### 7.1.3 Publications

As part of this PhD thesis the candidate contribute in the following journal and conference papers.

#### 7.1.3.1 Journal papers

- Pedro Urda, Sergio Muñoz, Javier F. Aceituno and José L. Escalona. *Wheel-rail contact force measurement using strain gauges and distance lasers on a scaled railway vehicle*. Mechanical Systems and Signal Processing. Under Review.
- Sergio Muñoz, Javier F. Aceituno, Pedro Urda and José L. Escalona. *Multi-body model of railroad vehicles with weakly coupled vertical and lateral dynamics*. Mechanical System and Signal Processing. 115:570-592, 2019.
- Jose L. Escalona, Javier F. Aceituno, P. Urda, and O. Balling. *Railroad multibody simulation with the knife-edge-equivalent wheel-rail constraint equations*. Multi-body Systems Dynamics. 2019



### 7.1.3.2 Conference papers

- Pedro Urda, Sergio Muñoz, Javier F. Aceituno and José L. Escalona. *A novel procedure to measure wheel-rail contact forces in an instrumented scale railway vehicle* The Fourth International Conference on Railway Technology RAILWAYS 2018. Sitges, Barcelona.
- Pedro Urda, Sergio Muñoz, Javier F. Aceituno and José L. Escalona. *Estimación de fuerzas de contacto rueda carril en vehículo instrumentado a escala*. XXII Congreso Nacional de Ingeniería Mecánica 2018. Madrid, Madrid.
- Pedro Urda, Sergio Muñoz, Javier F. Aceituno and José L. Escalona. *Wheel-rail contact force measurement on a scaled railway vehicle: comparison between numerical and experimental data*. ECCOMAS Multibody Dynamics Conference 2019. Duisburg, Germany.



# Bibliography

- [1] G. Diana, F. Cheli, S. Bruni, and A. Collina. Interaction between railroad superstructure and railway vehicles. *Vehicle System Dynamics*, 23(sup1):75–86, 1994. doi: 10.1080/00423119308969506. URL <https://doi.org/10.1080/00423119308969506>.
- [2] Christopher P. Ward, Roger M. Goodall, and Roger Dixon. Contact force estimation in the railway vehicle wheel-rail interface. *IFAC Proceedings Volumes*, 44(1):4398 – 4403, 2011. ISSN 1474-6670. doi: <https://doi.org/10.3182/20110828-6-IT-1002.02904>. URL <http://www.sciencedirect.com/science/article/pii/S1474667016443004>. 18th IFAC World Congress.
- [3] Lai Wei, Jing Zeng, Pingbo Wu, and Hao Gao. Indirect method for wheel-rail force measurement and derailment evaluation. *Vehicle System Dynamics*, 52(12):1622–1641, 2014. doi: 10.1080/00423114.2014.953180. URL <https://doi.org/10.1080/00423114.2014.953180>.
- [4] Francesco Braghin, Stefano Bruni, and Giorgio Diana. Experimental and numerical investigation on the derailment of a railway wheelset with solid axle. *Vehicle System Dynamics*, 44(4):305–325, 2006. doi: 10.1080/00423110500337494. URL <https://doi.org/10.1080/00423110500337494>.
- [5] H. Weinstock. Wheel climb derailment criteria for evaluation of rail vehicle safety. *Proceedings of the ASME Winter Annual Meeting, Paper 84 - WA/RT-1*, 1984.
- [6] J.A. Elkins and H. Wu. New criteria for flange climb derailment. *ASMEE/IEEE Joint Railroad Conference*, 2000.

- [7] M.J. Nadal. Theorie de la stabilite des locomotives - part ii. *Movement de Lacet. Annales des Mines*, 10:232–255, 1896.
- [8] Vijay Garg and Rao Dukkipati. *Dynamics of railway vehicle systems*. Academic Press, 2012.
- [9] EN-14363:2016. Railway applications. testing and simulation for the acceptance of running characteristics of railway vehicles. running behaviour and stationary test.
- [10] Gabriele Cazzulani, Egidio Di Gialleonardo, Stefano Bionda, Marco Bassetti, Pietro Crosio, and Francesco Braghin. A new approach for the evaluation and the improvement of the metrological characteristics of an instrumented wheelset for the measure of wheel-rail contact forces. *Proceedings of the Institution of Mechanical Engineers, Part F: Journal of Rail and Rapid Transit*, 231(4):381–393, 2017. doi: 10.1177/0954409716631785. URL <https://doi.org/10.1177/0954409716631785>.
- [11] Braghin-F. Cazzulani G.-Di Gialleonardo E. Bionda, S. Improvements fo the estimation of wheel-rail contact forces using instrumented wheel-sets (conference paper).
- [12] G Diana, F Resta, F Braghin, Marco Bocciolone, Egidio Di Gialleonardo, and Pietro Crosio. Methodology for the calibration of dynamometric wheel-sets for the measurement of the wheel-rail contact forces. 67:9–21, 01 2012.
- [13] Egidio Di Gialleonardo, G Diana, Resta F, Braghin F, Marco Bocciolone, and Pietro Crosio. Design of a new full scale test-rig for the calibration of instrumented wheelsets. 05 2011.
- [14] Francesco Braghin, Stefano Bruni, and Giorgio Diana. Experimental and numerical investigation on the derailment of a railway wheelset with solid axle. *Vehicle System Dynamics*, 44(4):305–325, 2006. doi: 10.1080/00423110500337494. URL <https://doi.org/10.1080/00423110500337494>.
- [15] N. Bosso, A. Gugliotta, and A. Somà. Dynamic behavior of a railway wheelset on a roller rig versus tangent track. *Shock and Vibration*, 11(3-4):467–492, 2004. doi: <https://doi.org/10.1155/2004/280673>.

- [16] E. González, C. Prados, V. Antón, and B. Kennes. Grail-2: Enhanced odometry based on gnss. *Procedia - Social and Behavioral Sciences*, 48:880–887, 2012. doi: 10.1016/j.sbspro.2012.06.1065.
- [17] A. Matsumoto, Y. Sato, H. Ohno, M. Tomeoka, K. Matsumoto, J. Kurihara, T. Ogino, M. Tanimoto, Y. Kishimoto, Y. Sato, and T. Nakai. A new monitoring method of train derailment coefficient. In *2006 IET International Conference On Railway Condition Monitoring*, pages 136–140, 2006.
- [18] Yu Boronenko, A. Orlova, A. Iofan, and S. Galperin. Effects that appear during the derailment of one wheelset in the freight wagon: simulation and testing. *Vehicle System Dynamics*, 44(sup1):663–668, 2006. doi: 10.1080/00423110600882787. URL <https://doi.org/10.1080/00423110600882787>.
- [19] Werner Hubacher and Patrik Scheiber. Derailment detector systems for cff/sbb rolling stock. 31:31–37, 09 2000.
- [20] Jing Zeng and Pingbo Wu. Study on the wheel/rail interaction and derailment safety. *Wear*, 265(9):1452 – 1459, 2008. ISSN 0043-1648. doi: <https://doi.org/10.1016/j.wear.2008.01.031>. URL <http://www.sciencedirect.com/science/article/pii/S0043164808001683>. Contact Mechanics and Wear of Rail/Wheel Systems - CM2006.
- [21] Stefano Bruni, Roger Goodall, T. X. Mei, and Hitoshi Tsunashima. Control and monitoring for railway vehicle dynamics. *Vehicle System Dynamics*, 45(7-8):743–779, 2007. doi: 10.1080/00423110701426690. URL <https://doi.org/10.1080/00423110701426690>.
- [22] Goodall-R. Charles, G. and R. Dixon. Wheel-rail profile estimation. *Conference on Railway Condition Monitoring*, 2006.
- [23] K. Goda and R. Goodall. Fault-detection-and-isolation system for a railway vehicle bogie. *Vehicle System Dynamics*, 41:468–476, 2004.
- [24] Goodall-R. Li, P. and V. Kadiramanathan. Estimation of parameter in a linear state space model using a rao-backwellised particle filter. *IEE Proceedings-Control Theory and Application*, 151(6):727–738, 2004.

- [25] Goodall-R. Weston P.-Ling C.S. Goodman C. Li, P. and C. Roberts. Estimation of railway vehicle suspension parameters for condition monitoring. *Control Engineering Practice*, 15:43–55, 2006.
- [26] Y. Hayashi, T. Kojima, H. Tsunashima, and Y. Marumo. Real time fault detection of railway vehicles and tracks. In *2006 IET International Conference On Railway Condition Monitoring*, pages 20–25, 2006.
- [27] G. Charles and R. Goodall. Low adhesion estimation. *International Conference on Railway Condition Monitoring*, pages 96–97, 2006.
- [28] S. Bruni, F. Cheli, A. Collina, and F. Resta. Road test data procedures for evaluating the hunting instability threshold of a railway vehicle from on board measurements. *Vehicle System Dynamics*, 33(sup1):168–179, 1999. doi: 10.1080/00423114.1999.12063079. URL <https://doi.org/10.1080/00423114.1999.12063079>.
- [29] F. Xia, C. Cole, and P. Wolfs. A method for setting wagon speed restrictions based on wagon responses. *Vehicle System Dynamics*, 44(sup1):424–432, 2006. doi: 10.1080/00423110600872465. URL <https://doi.org/10.1080/00423110600872465>.
- [30] R W Ngigi, C Pislaru, A Ball, and F Gu. Modern techniques for condition monitoring of railway vehicle dynamics. *Journal of Physics: Conference Series*, 364:012016, may 2012. doi: 10.1088/1742-6596/364/1/012016. URL <https://doi.org/10.1088%2F1742-6596%2F364%2F1%2F012016>.
- [31] Fujie Xia, Colin Cole, and Peter Wolfs. Grey box-based inverse wagon model to predict wheel-rail contact forces from measured wagon body responses. *Vehicle System Dynamics*, 46(sup1):469–479, 2008. doi: 10.1080/00423110801993102. URL <https://doi.org/10.1080/00423110801993102>.
- [32] L. Ljung. *System identification: Theory for the user*. Prentice Hall, 1987.
- [33] R. Isermann and M. Munchhof. *Identification of dynamics system. An introduction with applications*. Springer, 2011.

- [34] Andrews-A.P Grewal, M.S. *Kalman Filtering: Theory and practice*. Prentice Hall, 1993.
- [35] G. Charles, R. Goodall, and R. Dixon. Model-based condition monitoring at the wheel-rail interface. *Vehicle System Dynamics*, 46(sup1):415–430, 2008. doi: 10.1080/00423110801979259. URL <https://doi.org/10.1080/00423110801979259>.
- [36] Andrew Smyth and Meiliang Wu. Multi-rate kalman filtering for the data fusion of displacement and acceleration response measurements in dynamic system monitoring. *Mechanical Systems and Signal Processing*, 21:706–723, 02 2007. doi: 10.1016/j.ymssp.2006.03.005.
- [37] Goodall-R.M. Dixon R. Ward, C.P. Contact force estimation in the railway vehicle wheel-rail interface. *18th IFAC Word Congress*, 2011.
- [38] O. Polach. Creep forces in simulations of traction vehicles running on adhesion limit. *Wear*, 258:992–1000, 2005. ISSN 00431648.
- [39] Frank Naets, Roland Pastorino, Javier Cuadrado, and Wim Desmet. Online state and input force estimation for multibody models employing extended kalman filtering. *Multibody System Dynamics*, 32, 10 2013. doi: 10.1007/s11044-013-9381-8.
- [40] Association of American Railroads. Railroad wheel dynamometer. *The American Society of Mechanical Engineers*, 1988.
- [41] Coenraad Esveld. *Modern Railway Track*. [s.n.], 1989.
- [42] Michael J.M.M. Steenbergen. Quantification of dynamic wheel-rail contact forces at short rail irregularities and application to measured rail welds. *Journal of Sound and Vibration*, 312(4):606 – 629, 2008. ISSN 0022-460X. doi: <https://doi.org/10.1016/j.jsv.2007.11.004>. URL <http://www.sciencedirect.com/science/article/pii/S0022460X07008942>.
- [43] Per Gullers, Lars Andersson, and Roger Lunden. High-frequency vertical wheel-rail contact forces. field measurements and influence of track irregularities. *Wear*, 265(9):1472 – 1478, 2008. ISSN 0043-1648. doi: <https://doi.org/10.1016/j.wear.2008.02.035>. URL <http://www.sciencedirect.com/science/article/>

- [pii/S0043164808001713](#). Contact Mechanics and Wear of Rail/Wheel Systems - CM2006.
- [44] Jens C.O. Nielsen. High-frequency vertical wheel-rail contact forces-validation of a prediction model by field testing. *Wear*, 265(9):1465 – 1471, 2008. ISSN 0043-1648. doi: <https://doi.org/10.1016/j.wear.2008.02.038>. URL <http://www.sciencedirect.com/science/article/pii/S0043164808001701>. Contact Mechanics and Wear of Rail/Wheel Systems - CM2006.
- [45] Lars-Ove Jonsson, Nils Nilstam, and Ingemar Persson. Using simulations for approval of railway vehicles: a comparison between measured and simulated track forces. *Vehicle System Dynamics*, 46(sup1):869–881, 2008. doi: 10.1080/00423110802037123. URL <https://doi.org/10.1080/00423110802037123>.
- [46] Yan Quan Sun, Colin Cole, and Maksym Spiryagin. Monitoring vertical wheel-rail contact forces based on freight wagon inverse modelling. *Advances in Mechanical Engineering*, 7(5):1687814015585431, 2015. doi: 10.1177/1687814015585431. URL <https://doi.org/10.1177/1687814015585431>.
- [47] Majid Mehrpouya and Hamid Ahmadian. Estimation of applied forces on railway vehicle wheelsets from measured vehicle responses. *International Journal of Vehicle Structures Systems*, 1, 11 2009. doi: 10.4273/ijvss.1.4.23.
- [48] Fujie Xia, Colin Cole, and Peter Wolfs. An inverse railway wagon model and its applications. *Vehicle System Dynamics*, 45(6):583–605, 2007. doi: 10.1080/00423110601079151. URL <https://www.tandfonline.com/doi/abs/10.1080/00423110601079151>.
- [49] Delta Rail. *Vampier User Manual*.
- [50] Yu Ren and Jianzheng Chen. A new method for wheel-rail contact force continuous measurement using instrumented wheelset. *Vehicle System Dynamics*, 57(2):269–285, 2019. doi: 10.1080/00423114.2018.1460853. URL <https://doi.org/10.1080/00423114.2018.1460853>.
- [51] Lai Wei, Jing Zeng, Pingbo Wu, and Hao Gao. Indirect method for wheel-rail force measurement and derailment evaluation. *Vehicle System Dynamics*, 52(12):



- 1622–1641, 2014. doi: 10.1080/00423114.2014.953180. URL <https://doi.org/10.1080/00423114.2014.953180>.
- [52] Marco Boccione Francesco Braghin Egidio Di Gialleonardo, Stefano Bionda. A hybrid method for the integration between an instrumented wheelset and the measure of the deflection of the primary suspension.
- [53] Monica Malvezzi, Enrico Meli, Stefano Falomi, and Andrea Rindi. Determination of wheel-rail contact points with semianalytic methods. *Multibody System Dynamics*, 20(4):327–358, Nov 2008.
- [54] Hiroyuki Sugiyama, Kohei Araki, and Yoshihiro Suda. On-line and off-line wheel/rail contact algorithm in the analysis of multibody railroad vehicle systems. *Journal of Mechanical Science and Technology*, 23(4):991–996, Apr 2009. ISSN 1976-3824. doi: 10.1007/s12206-009-0327-2. URL <https://doi.org/10.1007/s12206-009-0327-2>.
- [55] Jose L. Escalona and Javier F. Aceituno. Multibody simulation of railway vehicles with contact lookup tables. *International Journal of Mechanical Sciences*, 155:571 – 582, 2019. ISSN 0020-7403. doi: <https://doi.org/10.1016/j.ijmecsci.2018.01.020>. URL <http://www.sciencedirect.com/science/article/pii/S0020740317302485>.
- [56] Hiromichi Kanehara and Takehiko Fujioka. Measuring rail/wheel contact points of running railway vehicles. *Wear*, 253(1):275 – 283, 2002. ISSN 0043-1648. doi: [https://doi.org/10.1016/S0043-1648\(02\)00114-X](https://doi.org/10.1016/S0043-1648(02)00114-X). URL <http://www.sciencedirect.com/science/article/pii/S004316480200114X>. CM2000 S.I.
- [57] Richard L. Higgins Duane E. Otter, Magdy A. El-Sibaie. A design for next generation load measuring wheelsets.
- [58] J.A. Elkins and A. Carter. Testing and analysis techniques for safety assessment of rail vehicles: The state-of-the-art. *Vehicle System Dynamics*, 22(3-4):185–208, 1993. doi: 10.1080/00423119308969026. URL <https://doi.org/10.1080/00423119308969026>.
- [59] Karl Hoffmann. *An Introduction to Stress Analysis and Transducer Desing using Strain Gauges*. HBM, 2003.

- [60] Feng Yu and Michael T Hendry. A new strain gauge configuration on the rail web to decouple the wheel-rail lateral contact force from wayside measurement. *Proceedings of the Institution of Mechanical Engineers, Part F: Journal of Rail and Rapid Transit*, 0(0):0954409718822870, 0. doi: 10.1177/0954409718822870. URL <https://doi.org/10.1177/0954409718822870>.
- [61] H. Kanehara and K. Ohno. Development of a continuous measuring system for contact position between wheel and rail toward clarification of derailment mechanism. *East Technical Review*, 2003.
- [62] E. Gomez, J.G. Gimenez, and A. Alonso. Method for the reduction of measurement errors associated to the wheel rotation in railway dynamometric wheelsets. *Mechanical Systems and Signal Processing*, 25(8):3062 – 3077, 2011. ISSN 0888-3270. doi: <https://doi.org/10.1016/j.ymssp.2011.05.006>. URL <http://www.sciencedirect.com/science/article/pii/S0888327011002020>.
- [63] J. Zhang, S. Zhou, and C. Huang. A new method for the fault diagnosis of the train wheelset based on characteristic spectrum analysis. In *Proceedings of the 29th Chinese Control Conference*, pages 3988–3992, July 2010.
- [64] Erick Gomez, Asier Alonso, José Gimenez Ortiz, and Jordi Vinolas. *Railway Dynamometric Wheelsets: A Comparison of Existing Solutions and a Proposal for the Reduction of Measurement Errors*, volume 148, pages 261–284. 01 2012. ISBN 9783642279621. doi: 10.1007/978-3-642-27963-8\_25.
- [65] E. Gomez, J.G. Giménez, and A. Alonso. Es 2 334 529 a1.
- [66] E. García, J.A. Fernández, L. Baeza, and F.J. Fuenmayor. Es 2 436 692 b1 método de determinación de las fuerzas en el contacto rueda carril en vehículos ferroviarios.
- [67] Maria D. Gutierrez-Lopez, Javier Garcia de Jalon, and Adrian Cubillo. A novel method for producing low cost dynamometric wheels based on harmonic elimination techniques. *Mechanical Systems and Signal Processing*, 52-53:577 – 599, 2015. ISSN 0888-3270. doi: <https://doi.org/10.1016/j.ymssp.2014.06.010>. URL <http://www.sciencedirect.com/science/article/pii/S0888327014002374>.

- [68] Jennifer M. Bastiaan. Physical validation testing of a smart tire prototype for estimation of tire forces. In *WCX World Congress Experience*. SAE International, apr 2018. doi: <https://doi.org/10.4271/2018-01-1117>. URL <https://doi.org/10.4271/2018-01-1117>.
- [69] Pedro Ponce Cruz. *Inteligencia artificial con aplicaciones a la ingeniería*. AlphaOmega, 2016.
- [70] L. et al. Dingqing. Development of performance-based track geometry inspection. 7th international heavy haul conference, ihha inc., brisbane, australia, june 2001, pp. 461–465.
- [71] Z Sharif-Khodaei, M Ghajari, and M H Aliabadi. Determination of impact location on composite stiffened panels. *Smart Materials and Structures*, 21(10):105026, aug 2012. doi: 10.1088/0964-1726/21/10/105026. URL <https://doi.org/10.1088/0964-1726/21/10/105026>.
- [72] Mazdak Ghajari, Zahra Sharif Khodaei, M.H. Aliabadi, and Alfonso Apicella. Identification of impact force for smart composite stiffened panels. *Smart Materials and Structures*, 22:085014, 07 2013. doi: 10.1088/0964-1726/22/8/085014.
- [73] Akira Matsumoto, Yasuhiro Sato, Hiroyuki Ohno, Makoto Shimizu, Jun Kurihara, Masao Tomeoka, Takuya Saitou, Yohei Michitsuji, Masuhisa Tanimoto, Yoshi Sato, and Masaaki Mizuno. Continuous observation of wheel/rail contact forces in curved track and theoretical considerations. *Vehicle System Dynamics*, 50(sup1):349–364, 2012. doi: 10.1080/00423114.2012.669130. URL <https://doi.org/10.1080/00423114.2012.669130>.
- [74] Akira Matsumoto, Yasuhiro Sato, Hiroyuki Ohno, Masao Tomeoka, Kosuke Matsumoto, Jun Kurihara, Tomohisa Ogino, Masuhisa Tanimoto, Yasushi Kishimoto, Yoshi Sato, and Takuji Nakai. A new measuring method of wheel-rail contact forces and related considerations. *Wear*, 265(9):1518 – 1525, 2008. ISSN 0043-1648. doi: <https://doi.org/10.1016/j.wear.2008.02.031>. URL <http://www.sciencedirect.com/science/article/pii/S0043164808001749>. Contact Mechanics and Wear of Rail/Wheel Systems - CM2006.

- [75] Federico Cheli, Roberto Corradi, G Diana, and Alan Facchinetti. Validation of a numerical model for the simulation of tramcar vehicle dynamics by means of comparison with experimental data. *Journal of Computational and Nonlinear Dynamics - J COMPUT NONLINEAR DYN*, 2, 10 2007. doi: 10.1115/1.2754306.
- [76] A. Chudzikiewicz. Selected elements of the contact problems necessary for investigating the rail vehicle system. *Advanced railway vehicle system dynamics, WNT, Warszawa (1991)*.
- [77] A. Chudzikiewicz. Load identification methods based on parametric models for mechanical structures. *8th IEEE international conference on methods and models in automation and robotics*, pages 203–209, 2002.
- [78] Song Ying, Wang Zhi-Chen, and Du Yan-liang. Continuous measurement of lateral wheel/rail interaction force based on pvdf strain sensing technology, 2013.
- [79] Andrea Bracciali and Paolo Folgarait. New sensor for lateral and vertical wheel-rail forces measurements. 2004.
- [80] Joao Carlos Eloi de Jesus Pombo and Jorge Alberto Cadete Ambrosio. *A multi-body methodology for railway dynamics applications*. Ph.D. thesis, Instituto de Engenharia Mecanica, Lisboa, 2004.
- [81] Andreas Simonis and Christian Schindler. Measuring the wheel-rail forces of a roller coaster. *Journal of Sensors and Sensor Systems*, 7:469–479, 09 2018. doi: 10.5194/jsss-7-469-2018.
- [82] Javier F. Aceituno, Rosario Chamorro, Daniel Garcia-Vallejo, and Jose L. Escalona. On the design of a scaled railroad vehicle for the validation of computational models. *Mechanism and Machine Theory*, 115:60 – 76, 2017. ISSN 0094-114X. doi: <https://doi.org/10.1016/j.mechmachtheory.2017.04.015>. URL <http://www.sciencedirect.com/science/article/pii/S0094114X17300897>.
- [83] A.B. DE-solver. *GENESYS User's Manual, release 0103, Ostersund, Sweden*. 2001.
- [84] S. Handal P. Klauser, N. Wilson and M. Dembosky. *Users Manual for NUCARS. Version 2.1, SD-043-(rev 9/95). Association of American Railroads*. 1995.

- [85] P. Fissete. *Robotran Release 3.0 - User Manual*. 1998.
- [86] MD MDI. *ADAMS/RAIL 9.1 - Technical Manual*, Ann Arbor, Michigan. 1995.
- [87] R.R. Ryan. *ADAMS-Multibody system analysis software. Multibody Systems Handbokk*, Springer. 1990.
- [88] W. Rulka and A. Eichberger. *Simpack an analysis and design tool for mechanical systems*, volume 22. 1993.
- [89] L. Mauer G. Schupp, H. Netter and M. Gretzschel. *Multibody system simulation of railway vehicles with SIMPACK*, volume 31. 1999.
- [90] A.A. Shabana. *Computational dynamics. John Wiley and Sons*. 2009.
- [91] José L. Escalona, Javier F. Aceituno, Pedro Urda, and Ole Balling. Railroad multibody simulation with the knife-edge-equivalent wheel-rail constraint equations. *Multibody System Dynamics*, 2019.
- [92] Ahmed A. Shabana, Khaled E. Zaazaa, JosÃ© L. Escalona, and Jalil R. Sany. Development of elastic force model for wheel/rail contact problems. *Journal of Sound and Vibration*, 269(1):295 – 325, 2004. doi: [https://doi.org/10.1016/S0022-460X\(03\)00074-9](https://doi.org/10.1016/S0022-460X(03)00074-9).
- [93] Javier F Aceituno, Rosario Chamorro, Sergio Muñoz, and José L Escalona. An alternative procedure to measure railroad track irregularities. application to a scaled track. *Measurement*, 137:417–427, 2019. doi: <https://doi.org/10.1016/j.measurement.2019.01.025>.
- [94] José L Escalona and Javier F Aceituno. Multibody simulation of railway vehicles with contact lookup tables. *International Journal of Mechanical Sciences*, 155: 571–582, 2019. doi: <https://doi.org/10.1016/j.ijmecsci.2018.01.020>.
- [95] V. Garg. *Dynamics of railway vehicle systems*. Elsevier.
- [96] European Standard EN 12299. Railway applications - ride comfort for passengers - measurement and evaluation. submitted to cen members for enquiry. 2009.
- [97] Department of Transportation Federal Railroad Administration. Track safety standards, part 213, subpart g, class of track 6 and higher.

- 
- [98] A.D. Kerr. *Fundamentals of railway track engineering*. Simmons Boardman Pub Co, 2003.
- [99] Lai Wei, Jing Zeng, Pingbo Wu, and Hao Gao. Indirect method for wheel-rail force measurement and derailment evaluation. *Vehicle System Dynamics*, 52(12):1622–1641, 2014. doi: 10.1080/00423114.2014.953180. URL <https://doi.org/10.1080/00423114.2014.953180>.
- [100] E. Gomez, J.G. Giménez, and A. Alonso. Method for the reduction of measurement errors associated to the wheel rotation in railway dynamometric wheelsets. *Mechanical Systems and Signal Processing*, 25(8):3062 – 3077, 2011. ISSN 0888-3270. doi: <https://doi.org/10.1016/j.ymssp.2011.05.006>. URL <http://www.sciencedirect.com/science/article/pii/S0888327011002020>.
- [101] María D. Gutiérrez-López, Javier García de Jalón, and Adrián Cubillo. A novel method for producing low cost dynamometric wheels based on harmonic elimination techniques. *Mechanical Systems and Signal Processing*, 52-53:577 – 599, 2015. ISSN 0888-3270. doi: <https://doi.org/10.1016/j.ymssp.2014.06.010>. URL <http://www.sciencedirect.com/science/article/pii/S0888327014002374>.
- [102] O. Polach and J. Evans. Simulations of running dynamics for vehicle acceptance: Application and validation. *The 2nd International Conference on Railway Technology: Research, Development and Maintenance (RAILWAYS 2014)*.
- [103] Sergio Muñoz, Javier F Aceituno, Pedro Urda, and José L Escalona. Multi-body model of railway vehicles with weakly coupled vertical and lateral dynamics. *Mechanical Systems and Signal Processing*, 115:570–592, 2019. doi: <https://doi.org/10.1016/j.ymssp.2018.06.019>.
- [104] K.L. Johnson. *Contact Mechanics*. Cambridge University Press, Cambridge, UK, 1985.
- [105] Jose L. Escalona. A multibody formulation for the dynamic analysis of railway vehicles.
- [106] Jose L. Escalona, Javier F. Aceituno, P. Urda, and O. Balling. Railroad multi-body simulation with the knife-edge-equivalent wheel-rail constraint equations. *Multibody Systems Dynamics*.